NASA CONTRACTOR REPORT

NASA CR-2597

NASA CR-2597

DESIGN, FABRICATION AND ACOUSTIC TESTS OF A 36 INCH (0.914 METER) STATORLESS TURBOTIP FAN

E. G. Smith, D. L. Stempert, and W. R. Uhl

Prepared by
GENERAL ELECTRIC COMPANY
Cincinnati, Ohio 45215
for Ames Research Center

NATIONAL AERONAUTICS AND SPACE ADMINISTRATION • WASHINGTON, D. C. • SEPTEMBER 1975

1. Report No.	2. Government Accession No.	3. Recipient's Catalog No.
NASA CR-2597		

4. Title and Subtitle	5. Report Date
Design, Fabrication and Acoustic Tests of a 36 Inch (0.914 Meter) Statorless Turbotip Fan	SEPTEMBER 1975
	6. Performing Organization Code

7. Author(s)	8. Performing Organization Report No.
EG Smith DL Stempert WR Uhl	R74AEG334
	10. Work Unit No.

9. Performing Organization Name and Address	11. Contract or Grant No.
General Electric Company Cincinnati, Ohio 45215	NAS2-5462
	13. Type of Report and Period Covered
12. Sponsoring Agency Name and Address	Final Contract Report
National Aeronautics and Space Administration Washington, D.C. 20546	14. Sponsoring Agency Code

15. Supplementary Notes

16. Abstract

This is the final report covering the design, fabrication and acoustic tests of the LF336/E Statorless Turbotip Fan. The LF336/E is a 36 inch (0.914 meter) diameter fan designed to operate in a rotor-alone configuration. Design features required for modification of the existing LF336/A rotor-stator fan into the LF336/E statorless fan configuration are discussed.

Tests of the statorless fan identified an aerodynamic performance deficiency due to inaccurate accounting of the fan exit swirl during the aerodynamic design. This performance deficiency, related to fan exit static pressure levels, produced about a 20 percent thrust loss. A study was then conducted for further evaluation of the fan exit flowfields typical of statorless fan systems. This study showed that through proper selection of fan design variables such as pressure ratio, radius ratio and swirl distributions, performance of a statorless fan configuration could be improved with levels of thrust approaching the conventional rotor-stator fan system.

Acoustic measurements were taken for the statorless fan system at both General Electric and NASA, and when compared to other lift fan systems, showed noise levels comparable to the quietest lift fan configuration which included rotor-stator spacing and acoustic treatment.

The statorless fan system was also used to determine effects of rotor leading edge serrations on noise generations. A cascade test program identified the serration geometry based on minimum pressure losses, wake turbulence levels and noise generations. Tests of the fan with these serrated leading edges showed broadband noise reductions consistent with role of rotor fluctuating pressure reductions due to addition of serrated leading edges.

17. Key Words (Suggested by Author(s))	18. Distribution Statement
Fan, Serrated Blades, Acoustics, Base Pressures, Rotor - above noise	Unclassified - Unlimited STAR Category 07

19. Security Classif. (of this report)	20. Security Classif. (of this page)	21. No. of Pages	22. Price*
Unclassified	Unclassified	182	$7.00

For sale by the National Technical Information Service, Springfield, Virginia 22161

CONTENTS

CONTENTS

LIST OF TABLES

LIST OF FIGURES

LIST OF FIGURES

LIST OF FIGURES

LIST OF FIGURES

LIST OF FIGURES

INTRODUCTION

The LF336 lift fan has been involved in a continuous series of aerodynamic and acoustic test programs since the hardware was first designed and manufactured in 1968. The LF336 system is a 36 inch (0.914 m) diameter turbotip lift fan driven by the exhaust gases of the J85-5 engine. The initial configuration was designed to the requirements of a fan-in-wing configuration, including a shallow inlet bellmouth and close rotor to stator spacing. This fan configuration was subjected to numerous static and cross-flow testing at the facilities of General Electric and NASA Ames Research Center.

During the mid-1960 time frame, the noise generation of aircraft propulsion systems began to receive emphasis. The LF336 fan was an available propulsion system that could be easily modified to include acoustic features, and consequently was diverted towards applications in acoustic technology development programs. The fan configuration was initially modified to study the effects of rotor to stator spacing, blade to vane ratio and inner-stage suppression, Reference 1. These tests were then followed by a program for investigation of the aero-acoustic performance of multiple splitter exhaust suppressors, Reference 2.

Technology studies, as reported in Reference 3, identified the statorless fan as a possible lift fan propulsion concept. These preliminary studies showed that for equal thrust, the statorless fan required about the same installation volume of conventional fan, had about the same thrust to weight ratio, but had a larger diameter rotor. The statorless fan concept also offers the possibility of being an attractive low noise propulsion system. Conventional fan noise is dominated by noise generated from rotor-stator aerodynamic interaction. Other contributors to the overall noise are rotor noise and jet noise. The statorless fan system tends to optimize at low pressure ratios, thus jet noise levels would be low. Elimination of the exit guide vane row eliminates the source of rotor-stator interaction noise. Thus, a statorless fan system has the potential of being a low noise propulsion component that is competitive with conventional rotor-stator fans with acoustic suppression.

To provide a statorless fan research vehicle, the LF336 fan was modified to a statorless fan configuration. This activity was initiated by General Electric under contract to NASA Ames Research Center. The program was directed towards the design, manufacture and test of a statorless fan system derived from the existing LF336 fan. The configuration was assigned the LF336/E designation where the "E" designation represents the fifth modification of the basic fan.

The program also included an investigation of the effects on noise generation with serrated leading edges on the rotor blades. Investigations by NASA and General Electric had indicated that significant noise reductions can be achieved by serrating the leading edge of rotor blades. The acoustic tests of the LF336/E statorless fan provided an excellent opportunity for investigations of serrated rotor acoustic performance without the presence of a stator. The serrated shape used in the fan configuration was developed during the cascade program, Reference 4.

This report is a complete summary of the LF336/E statorless fan program, including design, fabrication, acoustic studies, and auxiliary studies of serrated leading edges and hub base pressure. The text of the report is divided into three parts. Part I covers the preliminary studies that established the statorless fan configuration, the design modifications to the LF336 fan and the tests to determine aerodynamic, mechanical and acoustic performance of the LF336/E statorless fan. Part II covers that phase of the program directed toward the study of noise suppression characteristics of serrated leading edges on rotor blades. The initial cascade tests that established the serration configuration are described. The acoustic performance of the fan configuration incorporating the serrations is then presented and compared to the unserrated rotor acoustic performance. Part III presents the results of an analytical and experimental program for investigation of hub base pressures typical of both the conventional and statorless fan configurations. The results of this study is then applied to the definition of a revised statorless fan configuration that would not experience the low thrust performance as experienced by the demonstrator LF336/E statorless fan.

PART I - STATORLESS FAN STUDY

PRELIMINARY DESIGN STUDIES

Major effort during the initial studies of statorless fans was directed towards the selection of a lift fan cycle consistent with the following objectives:

- The statorless fan configuration shall utilize LF336/A fan hardware and components wherever possible. The LF336/A is a conventional rotor-outlet guide vane lift fan system that is described in Reference 1 and is shown in Figure I-1.
- The cycle selection shall consider typical propulsion system optimization parameters such as lift-to-weight, installation size and transient response during thrust modulation.
- Since the fan system is intended to investigate the noise characteristics of the statorless lift fan concept, the cycle selection shall reflect requirements for minimum overall noise generation.

Parametric Study

As a first step in the optimization procedure, a simplified parametric study investigated effects of parameters such as hub radius raatio, tip speed, rotor hub slope, and hub loading. The fan tip flowpath and diameter was held identical to the LF336/A fan to permit future utilization of the existing fan front frame, turbine carriers and scroll systems.

The study varied each of the four design parameters given above and evaluating their effects on fan pressure ratio, flow, lift, power and other significant performance parameters. For this study, the fan rotor exit axial velocity profile was assumed to vary with a 0.2 power, N, of the fan radius. For N equal zero, the exit velocity would be uniform and for N equal unity, the velocity profile would vary linearly with radius. The other significant base point variables selected for the study were:

- Tip Speed, U_T = 1050 feet per second (320 meters per second)
- Hub Loading Coefficient, C_F = 0.40
- Hub Slope, $\Delta\overline{R}$ = 0.032

The results of this study for variation of fan tip speed, hub loading and hub slope are shown in Figure I-2.

These data are presented in parametric form and will be used as the basis of the optimization study to be described later. However, based on this analysis alone, certain conclusions can be drawn concerning the trends for optimization of statorless lift fan propulsion systems:

- The maximum thrust per unit frontal area is inherently lower for a statorless fan as compared to the conventional rotor-outlet guide vane system.

- Statorless fan systems require high tip speeds and tip relative Mach numbers. Tip relative Mach numbers less than unity are impractical for fans with pressure ratios considered here.

- The hub radius ratio for statorless fans should not exceed 0.55 since very little thrust increase is obtained at higher radius ratios.[1]

- Hub slope has a strong effect on rotor hub loading. Increased hub slope can be used to produce significant increases in fan performance.[1]

- Higher tip speeds may be possible for a tip turbine statorless fan since the power requirements are lower than a conventional fan system at the same diameter. The lower power requirements produce smaller or shorter buckets in the turbine.

Comparison of Statorless and Conventional Fan Designs

The second phase of the design studies used the results of the parametric design studies to determine performance and dimensions of statorless fan systems. For comparison, conventional rotor-stator fan performance and dimensions were also evaluated. The gas generator selected for this analysis was a scaled J97-GE-100 turbojet. This generator, with established short time VTO ratings, is representative of an advanced gas generator system that matches the gas flow requirements of the turbotip lift fan system. The fan turbine inlet gas conditions used for these studies are given in Table I-I. These gas conditions are representative of the engine three-second rating condition, comparable to the case where maximum aircraft control or fan system design lift is required.

The fan design parameters, such as radius ratio, efficiency, and specific flow, were selected based on a fan design tip speed of 1060 feet/sec (323 meters/sec). The fan design parameters are shown graphically in Figure I-3 for the

[1] These design criteria were established without concern for low hub base pressures as observed during later tests of the LF336/E fan. Including the effects of low base pressures, the criteria is significantly altered and produced trends towards the lowest possible radius ratio. The effects of this new criteria will be discussed later in Part III of this report.

range of fan pressure ratios of statorless fan systems. Similar design parameters for a conventional fan system also with a design fan tip speed of 1060 feet per second (323 meters/sec) are included for comparison. The penalties of the statorless fan system in terms of lower efficiency, lower specific flow and higher radius ratio are shown. These differences in design parameters are traceable to the effects of residual fan exit swirl.

Using the previously defined design parameters and fan turbine inlet gas conditions, a family of statorless and conventional fan systems were sized. The results of this sizing study in terms of fan tip diameter and ideal thrust are also shown in Figure I-3. Comparing the two fan systems on an equal thrust basis at the same level of gas generator energy, the data indicates that a statorless fan with a 1.25 pressure ratio will develop the same thrust as a conventional fan with about a 1.33 pressure ratio. The difference in fan pressure ratios is required to compensate for the lower fan efficiency of the statorless system. A comparison of fan size shows the attendant change in diameter from 62 to 52 inches (1.57 to 1.32 meters). This increase in fan size is the penalty required for reduced fan thickness and possibly equal or reduced fan noise generation. Such a comparison of noise levels will be made in a later section of the report, based on actual noise measurement of both the statorless and conventional turbotip lift fan systems.

Optimization Study

The optimization study performed to select a statorless fan cycle was based on the previously described parametric data. The study was directed towards optimization of the fan system with respect to the following parameters:

- System, fan plus gas generator, thrust-to-weight ratio.
- System thrust per unit frontal area.
- Lift unit transient response during control thrust changes.
- Fan tip speed limitations as established by the onset of multiple pure tone noise generation.

For this section of the study, two of the statorless design variables previously discussed were held constant. The hub loading parameter, C_F, was fixed at a level of 0.40, consistent with accepted moderate aerodynamic design risk, and the hub slope was also selected at a value of 0.032. The primary variables remaining were then fan tip speed, fan radius ratio and fan design pressure ratio.

System Thrust-to-Weight

The effects of statorless fan design variables such as tip speed and radius ratio were factored into an analysis of system thrust-to-weight. Lacking a detailed weight analysis, certain assumptions were made to determine the weight of the components for this study:

- Fan weight was estimated in two ways. One method assumed the lift unit would maintain constant lift-to-weight for the range of tip speeds investigated. The other method assumed a constant lift unit weight for a given size as established by a 20:1 lift-to-weight ratio for the base point configuration of 1060 feet per second (823 meters/sec) tip speed and 1.25 pressure ratio. The latter case is probably the more accurate estimation method.

- An allowance of 35 percent of the fan weight was included for installation effects such as closures, louvers and mounting hardware.

- The gas generator weight was estimated based on the energy required to operate the fan unit. The technology level of the YJ97-GE-100 engine was used for this case where the engine weight to power ratio developed in the fan turbine is 0.10 lb/HP (.060 kg/kW).

- A gas generator installation factor of 20 percent was assumed.

- The total fan thrust, including the turbine exhaust flow, was assumed 15 percent higher than the fan only thrust as given in the parametric study data.

The variation of system lift-to-weight obtained using the above assumptions is given in Figure I-4. The two radically different cases of fan unit weight indicate the same trends of higher thrust-to-weight for lower pressure ratio and higher tip speeds. The effects of tip speed seem to be less pronounced in the low pressure ratio regions. At high pressure ratios, a higher tip speed is required to improve the fan efficiency and total thrust.

Thrust Per Unit Frontal Area

Overall planform area, at a given thrust level is significant parameter that is related to ease of installing a lift unit in an aircraft system. The fan installation planform area, except for allowances for scroll geometry, is directly related to the fan thrust per unit area. This parameter was calculated from the parametric data and is shown in Figure I-4. Again, an allowance of 15 percent residual turbine thrust is included in these data.

These data indicate a desire to select high tip speeds for maximum disk loading. However, at tip speeds between 950 and 1150 feet per second (290 and 350 meters/sec), there is very little to gain by going to pressure ratios above 1.2 to 1.25.

Lift Unit Response

Another parameter included in the optimization study is the ability of the lift unit to respond rapidly to changes of energy as required by the aircraft

attitude control system. This parameter is usually presented as a time constant for a step change of rotor input energy. The general expression of speed time constant is:

$$\tau = (2\pi/60)\ (J_o\ N_{DP})\ (T_{DP})\ (K + 1)$$

where

J_o = rotor polar moment of inertia

N_{DP} = design point RPM

T_{DP} = design point turbine torque

K = ratio of locked rotor torque to design point torque

The statorless fan parametric data was used to evaluate the rotor turbine torque at the design point speed. The fan size was obtained by scaling all of the data to a 10,000 pound (44,500 N) lift level with a 15 percent allowance for turbine residual thrust. In addition, a "K" value of 1.8 was assumed based on typical values for tip turbine designs. The rotor inertia levels were evaluated based on an empirical correlation of the inertias of previously designed advanced lift fan rotor systems. The empirical correlation used for this analysis was as follows:

$$J_o = 0.027\ (D_{FT})^{4.1} \quad - - - D_{FT} \text{ in feet}$$

$$J_o = 0.000207\ (D_{FT})^{4.1} \quad - - - D_{FT} \text{ in meters}$$

where

D_{FT} = fan tip diameter as obtained from the scaled parametric data.

The results of the optimization study are shown in Figure I-4. Time response is presented as a function of fan pressure ratio and tip speed. The results show a desire to maintain high fan pressure ratios with the lowest possible tip speed.

Present V/STOL handling criteria specify the need of system thrust response time constants of less than 0.2 seconds. This then implies that a reasonable maximum fan time constant would be in the order of 0.3 second. For this level of response, some form of lead compensation or thrust spoiling method will be required to achieve an overall time constant of 0.2 second or less.

Noise Generation

The statorless fan type of propulsion unit will be required to meet low noise generation criteria and certain restrictions must be included in the design selection to minimize noise generation. One important source of increased noise

level is onset of multiple pure tones at high tip speeds. Correlation of existing data has shown that a rapid rise in noise generation occurs when the tip rotational speed exceeds a Mach number of one. This establishes a limit on the rotational tip speed of about 1050 to 1100 feet per second (320 to 335 meters per sec). Further reductions of fan tip speed are desirable for further reductions of rotor noise generation. In addition, a limit on the jet velocity generated noise also exists. For this study, a typical fan pressure ratio of 1.25 has been selected as the maximum tolerable jet noise condition.

Design Point Selection

The two major parameters optimized during selection of the statorless fan cycle were system thrust-to-weight and disk loading. The fan design variables were fan tip speed and fan pressure ratio. Fan radius ratio is then a dependent variable as established by the selected hub loading, the fan pressure ratio and the design tip speed. Constraints such as fan response, multiple pure tone noise generation and jet noise floor also influenced the design selection.

Figure I-5 shows the boundaries established by these criteria, and indicates that the optimum statorless lift fan configuration can be selected which will satisfy both the maximum thrust-to-weight and disk loading criteria. The selected design point parameters are:

Pressure Ratio = 1.25
Tip Speed = 1060 feet per second (323 meters per second)
Radius Ratio = 0.57
Hub Loading = 0.4
Hub Slope = 0.064
Profile Factor, N = 0.2

A hub slope of 0.064, as compared to 0.032, is a desirable feature because of increased performance and a lower risk aerodynamic design. The trends presented in the optimization studies apply equally as well for the low and high slope hubs; only the overall levels of thrust-to-weight and disk loading will improve.

LF336 Design Considerations

The previous study has shown that the optimum cycle for a statorless fan system should have a design pressure ratio of 1.25 with a tip speed of 1060 ft/sec (323 m/sec). The LF366 statorless fan system is to be derived from the existing LF336/A system. The fan design shall utilize existing hardware wherever possible. Since existing tip turbine hardware will be used in the demonstrator LF336/E fan, the fan tip speed will be limited to 89.6 percent of design. The fan system at this speed will develop about 80 percent of the design thrust level. This level of thrust is representative of nominal rated operation of lift fans, as presently defined for advanced remote and integral lift systems. The nominal or 80 percent lift level is also established as the

"Noise Rating" point. Operation to the maximum or 100 percent level represents the maximum control or maneuver condition where the 25 percent excess lift is used to generate aircraft control moments, and thus is basically a short-time operating point. The statorless fan configuration derived through modification of the LF336/A fan was identified as the LF336/E lift fan system.

The design approach used in the LF336/E fan system was then established as follows:

- Perform and optimize the detailed aerodynamic design at the 1.25 pressure ratio, 1060 ft/sec (323 m/sec) design point.
- Design the rotor system mechanically for operation at the design point. The integrated aero-mechanical design thus reflects any compromise in design dictated by this higher design rotational speed.
- The fan system can then be tested throughout the complete speed range up to the nominal or 80 percent of design thrust level. This will provide both aerodynamic and acoustic performance excluding the 80 to 100 percent thrust range of short time duration reserved for aircraft attitude control.

FAN DESIGN

The design of the statorless fan configuration was derived based on maximum utilization of components from the already developed and tested LF336/A fan configuration. These restraints established design parameters such as fan tip diameter and tip slope. The existing turbine design was also retained to permit use of the fan scroll and tip turbine carrier assemblies. The rotor frame, hub and bearing configurations were incorporated into the statorless fan design. Based on these criteria, the components requiring redesign and modification for the LF336/E fan were limited to the rotor blading, the rotor disk and the inlet bulletnose flowpath.

Aerodynamic

The considerations discussed in the previous sections led to the selection of a fan with the aerodynamic parameters and objective design point performance presented in Table I-II. The total pressure ratio shown is based on full recovery of the meridional velocity component at the fan exit but no recovery of the tangential component. The total pressure ratio based on full recovery of the exit velocity would be 1.325. The design static pressure ratio is slightly greater than unity because the fan flowpath convergence causes a vena-contracta effect at the fan exit. The design static pressure is approximately ambient at the hub and tip of the rotor exit plane.[2] The fan efficiency listed is also based on recovery of only the meridional velocity component.

The rotor inlet specific flow for this fan is not particularly high at 35.2 lb/sec ft^2 (172 kg/sec m^2) because of the rather large area convergence across the rotor. This should help to alleviate any rotor choke problems which may have otherwise occurred. The hub work coefficient is also rather low and is a direct result of the selected tip speed, radius ratio and pressure ratio. This would be a general characteristic of all statorless lift fans as light loading is required to keep exit swirl losses from becoming excessive.

For this fan, the average exit swirl angle is 27 degrees. If exit louvers are to be used with this fan for thrust vectoring, they should be designed to accommodate this swirl angle. Also, as this fan is throttled, the swirl angle can be expected to increase to about 36 degrees for a 10 percent flow reduction and to about 43 degrees for a 20 percent flow reduction.

---

[2] These design criteria were later shown to be invalid during fan testing. Effects of revised criteria will be described later in Part III of this report.

Aerodynamic Design Procedure

The first step in the design was to lay out a tentative hub flowpath consistent with the above objectives. The tip flowpath of the original LF336 fan was retained through the rotor. Downstream of the rotor free streamline boundaries were assumed for both hub and tip. The General Electric Wing Fan Flow computer program (WFF) was then used to determine an axisymmetric solution to the compressible fluid flow within this flowpath. This program is capable of handling flows with or without blade rows, variable total pressure and entropy profiles and leaned and/or swept blade rows. The theory is a modification and extension of the equations derived in Reference 5 by Katsanis. Program output consists primarily of the complete definition of the axisymmetric flowfield from which blade loading parameters and flowpath velocity distributions can be determined.

A number of hub flowpaths and downstream free streamline boundaries were tried before a satisfactory design was achieved while at the same time satisfying conditions of constant static pressure along the downstream free jet boundaries. The final flowpath arrived at by this procedure is shown in Figure I-6. Velocity diagrams at the blade leading and trailing edges were determined from this axisymmetric flowfield.

The next step in the design procedure was to define a detailed blade geometry which would actually produce these desired velocity diagrams at good efficiency and simultaneously meet mechanical requirements of flexural and torsional stiffness, and cross-sectional area distribution. Airfoil coordinates were generated in the following manner. First, an airfoil was constructed in a plane using a multiple circular arc mean line, the cylindrical projections of the leading and trailing edge air angles on a streamline, specified chord, maximum thickness, incidence angle, deviation angle, edge thickness and a quarter sine wave thickness distribution. This planar section was then positioned so that it was normal to a radial line from the fan axis through its mid-chord point. The planar section was then projected back to the stream surface by rays parallel to this radial line. Stream surface coordinates were thus generated. Finally, these three-dimensional sections were located on a stacking axis and their coordinates interpolated to obtain cylindrical section coordinates at desired radii for mechanical analysis and manufacturing drawings.

As illustrated in Figure I-7, the meanline is composed of two circular arcs and its shape is controlled by the leading and trailing edge angles along with two other parameters called arc-length-ratio and arc-radius-ratio. Arc-length-ratio is the ratio of the arc length of the leading meanline arc to the total meanline length. Arc-radius-ratio is the ratio of the radius of curvature of the trailing meanline arc to the radius of curvature of the leading meanline arc. By varying incidence and these ratios, the chordwise camber distribution may be varied to obtain the desired choke margin.

Chord, maximum thickness and edge thickness are strongly influenced by mechanical requirements of flexural and torsional stiffness and cross-sectional area distributions. A thickening of the blade tip area is required

to obtain a satisfactory blend into the bucket carrier attachment tang. In general, a maximum thickness and edge thicknesses are specified as a percent of chord at each streamline and then the chord kept to a minimum consistent with mechanical requirements. This resulted in blade solidities which were judged adequate for the aerodynamic loading.

The stream function at the blade leading and trailing edges is shown in Figure I-8 (c). In the figure, various aerodynamic parameters are plotted against stream function. Figure I-8 (d) shows pressure ratio distributions at the fan exit. The upper curve shows the absolute total pressure ratio, the intermediate curve shows the total pressure ratio based on meridional velocity, and the lower curve shows the static pressure ratio. The total pressure ratio curves drop off at the hub and tip because of the higher rotor blade loss coefficients assumed for these areas. The static pressure is somewhat above ambient over the mid-portion of the annulus as a result of the general convergence of the flowpath and the resultant streamline curvatures at the hub and tip, shown in Figure I-6.

Figure I-8 (a) shows respectively the rotor blade D-factor and static pressure rise coefficients. Two forms of the static pressure rise coefficient are used. The first gives the more common form defined as:

$$C_P = \frac{P_{S2} - P_{S1}}{P_{TR} - P_{S1}}$$

and is denoted by the solid line in the figure. The second denoted by the broken line and defined

$$C_P' = \frac{(P_{S2}/P_{S1})^{\frac{\gamma-1}{\gamma}} - 1}{T_{TR}/T_{S1} - 1}$$

may be thought of as a temperature derived pressure rise coefficient and may be a better measure of the blade loading since it accounts for the pumping energy imparted to the flow due to streamline radius changes.

Figure I-8 (e) gives the rotor inlet and exit air angles for design fan operation. Blade leading and trailing edge angles are also shown and indicate the levels of blade incidence and deviation angles included in the design. For these flow angles, the blade inlet Mach numbers are as shown in Figure I-8 (b).

Blade Geometry and Loading

The final geometric parameters for the rotor blading, as derived through the integrated aerodynamic-mechanical design, is presented in Figure I-9. The

blading is based on a constant chord of 3 inches (7.6 cm) and a leading and trailing edge thickness of 0.75 percent of chord. The camber, thickness and stagger distributions meet both the aerodynamic design requirements and the mechanical design criteria.

Figure I-9 also describes the mean camber line curvature distribution in terms of the arc-radius-ratio and the arc-length ratio. These ratios are defined in Figure I-18. The arc radius ratio is unity from the hub to a mean radius of about 15.5 inches (39.4 cm) indicating that this portion of the blade has a single circular arc camber line. From a radius of 15.5 inches (39.4 cm) out to the tip, the arc-radius-ratio is less than unity indicating that the mean camber line radius of curvature is larger for the forward portion of the blade than for the aft portion. The arc-length-ratio was selected for this portion of the blade to keep the juncture point between the forward and aft arcs of the mean camber line just inside the "covered" portion of the blade section.

Leading Edge Modifications

As part of the acoustic testing to be conducted on the fan, the effects of rotor leading edge serrations were to be evaluated. It was felt for both aerodynamic and acoustic reasons that the serrations should be added by extending the leading edge of the aerodynamic profile rather than by cutting into the basic profile. Accordingly, the blades was initially manufactured with 1/4 inch long (0.64 cm) leading edge extension over the full blade span into which the serration geometries may be cut.

The leading edge extension was defined by first locating a 4-to-1 ellipse on a straight line tangent to the mean line leading edge of the basic profile. The leading edge of this ellipse was 1/4 inch (0.64 cm) ahead of the original leading edge and had a thickness of 0.75 percent of the original 3 inch (7.62 cm) chord. This ellipse was then faired smoothly into the basic airfoil with only slight thickening of the shape at the original leading edge location. This resulted in a very smooth blend for the convex side of the profile but somewhat abrupt curvature change on the concave side. This procedure then resulted in serrations which had essentially the same incidence angles as the basic profile. Figure I-9 shows a typical section of the extended leading edge.

Mechanical

The LF336/E rotor is similar to the LF336/A, with changes made only as necessary to accommodate the new set of blades of the LF336/E. The new rotor parts were designed for continuous operation at 6742 revolutions per minute (100 percent speed). All stresses and margins of safety were calculated at a six percent overspeed (7152 rpm) to provide design margin. A cross-section of the LF336/E rotor system is shown in Figure I-10.

The rotor maximum speed is limited by the present carrier assemblies to the LF336/A design speed of 6050 rpm. Future operation to the 100 percent design speed may be possible but would require detailed carrier analysis and a test program for verification. New carriers were not included in the program because of the cost and time required for carrier design and manufacture. This step could be considered if the initial testing of the LF336/E at 6050 rpm is encouraging enough to warrant testing to the design speed.

The following rotor components are new:

Blades
Disk
Blade Retainer Plates
Tip Tang Bolts
Tip Tang Nuts

The following rotor components are unchanged:

Blade Retainer Plate Bolts
Blade Retainer Plate Nuts
Torque Links
Torque Link Bolts
Turbine Bucket Carrier Assemblies
All Sump Hardware
Balance Washers

Two static parts have been added:

Hub Overlay
Turbine Skirt

A removable hub adaptor has been added to the inlet hub to provide the desired inlet flowpath contour. A cylindrical skirt has been added at the exhaust to protect the scroll insulation blankets from turbine exhaust impingement.

Blades

The blade design is similar to the LF336/A design, but includes changes to reflect the new airfoil geometry and to permit operation at the design speed of 6742 rpm. Blade tip tang similarity was maintained to permit the use of existing LF336/A turbine bucket carrier assemblies. Stresses were calculated for three sets of airfoil tip boundary conditions, at the six percent overspeed condition during steady-state (no vibration) and vibration, either in-phase or out-of-phase with the adjacent blade in the same carrier. Changing the tip boundary conditions had little effect on the stress levels. The airfoil stresses at the design tip speed and at the six percent overspeed condition are summarized in Figure I-11 (a). The resultant spanwise stresses were calculated at four locations, the leading and trailing edges and the convex and concave surfaces, and are the algebraic sums of the centrifugal stress,

bending stresses about the major and minor axes, and the resultant spanwise stress due to shear. The principal stresses were calculated at the convex and concave surfaces by combining the resultant spanwise stresses and shear stresses. The Mises Hencky stresses were calculated at the convex and concave surfaces, and are the principal stresses combined according to the Von-Mises Hencky theory of failure. The maximum combined stress is about 85,000 psi (586,000 kN/mm^2) at the six percent overspeed condition. Figure I-11 (b) compares this stress level, including an assumed alternating stress criterion of 20,000 psi (138,000 kN/mm^2), with the allowable properties for Inconel 718, the selected blade material. This comparison shows an alternating stress margin of safety of 0.45, which is adequate for this blade material.

The mechanical analysis of the blade tip tang attachment produced the results summarized in Figure I-12 (a). The maximum calculated stress of 94,200 psi (650,000 kN/mm^2) and an assumed vibratory stress level of 20,000 psi (138,000 kN/mm^2) yield an adequate 0.175 margin of safety for the Inconel 718 blade material at a metal temperature of 600 degrees Fahrenheit (589° K).

Blade and disk dovetail stresses are given in Figure I-12 (b). The maximum stresses, found by combining the tensile and shear stresses at the dovetail fillets, are 90,300 psi (623,000 kN/mm^2) for the blade dovetail and 82,900 psi (572,000 kN/mm^2) for the disk dovetail.

Figure I-13 shows the stress range diagrams for the blade and disk dovetails. Stresses are given for six locations on the cross-section of the dovetail. The alternating stress levels for the dovetail were calculated by scaling the airfoil root loads to the equivalent blade vibratory stress level required for failure. Using this design criterion for dovetail vibratory loads insures that the dovetail vibratory strength exceeds the airfoil vibratory strength. Adequate margins of safety exist in both the airfoil and disk dovetail areas.

Disk

The disk is a solid machined forging made from D6AC (AMS6431), a high strength, low-temperature iron-base alloy. The bore section of the disk is identical to the LF336/A disk to permit the use of existing sump hardware. The disk is thicker than the LF336/A disk to avoid a 4-per-revolution excitation of the 4-wave coupled blade-disk natural frequency in the operating speed range.

Disk stresses are given in Figure I-14. The peak stress is about 60,000 psi (414,000 kN/mm^2) and occurs near the hub. The low disk stresses exist because the disk geometry was established by the coupled blade-disk vibration criterion rather than the absolute stress levels.

Mechanical Vibration

The vibration characteristics of the LF336/E system were evaluated with respect to blade flutter, induced natural blade mode vibrations and induced coupled blade-disk vibrations. Past lift fan experience has shown that fan blades will be flutter-free when the flutter parameter (the inverse Strouhal number) is less than 1.5. The LF336/E flutter parameter at 100 percent design speed is 0.90. This low value is the result of the short stiff blades characteristic of this statorless fan system.

Blade torsional and flexural vibration modes are compared to possible excitation sources in Figure I-15. The blade natural frequencies at all speeds are well above the most probable excitation sources, the two and four cycles per revolution frequencies.

The characteristics of the coupled blade-disk vibrations are also shown in Figure I-15. At the present limiting speed of 6050 revolutions per minute, a sufficient frequency margin exists for the three principal modes shown. At the design tip speed, the margin between the four-wave mode and the four-per-revolution excitation is about 4.7 percent. This level of frequency margin is adequate since past lift fan experience has shown that the front frame four-per-revolution excitation is a weak stimulus for the four-wave mode of vibration.

Estimated Performance

The LF336/E statorless fan system was designed to operate using a J85-5 turbojet as the gas generator supplying the fan tip turbine. The complete turbine and ducting system was the same system designed for the LF336/A lift fan. Performance for the LF336/E lift fan installed in this test set-up was estimated and will be presented in the following discussion.

Fan and Turbine Maps

The turbine used with the LF336/E lift fan system is the same turbine as designed for the LF336/A. A summary of the significant turbine design parameters is given in Table I-III. The turbine design point for the original design was sized for the exhaust gas conditions of the J85-5 engine and designed to match the energy requirements of the LF336/A fan system. For operation with the LF336/E statorless fan system, the energy requirements will be much lower than the original design point.

Operation of the turbine at this off-design condition required a complete turbine map representation for estimation of performance. Figure I-16 presents the map generated for this analysis and identifies the original design point. This map representation was used for performance estimation of the LF336/E statorless lift fan system.

The fan map representation for the LF336/E statorless fan is shown in Figure I-17. The predicted map was generated using analytical-empirical techniques based on test results of previous General Electric fans, with the procedures modified to represent the statorless fan design. The fan design point at a fan pressure ratio of 1.25 and an adiabatic efficiency of 73.7 percent is identified on the map.

Performance

Performance of the LF336/E lift fan system was estimated using the gas discharge of the dry J85-5 turbojet engine. The performance of the engine was calculated using the performance deck provided for the basic J85-5 reheat engine with modification to reflect the configuration used to operate the LF336/E fan system.

Estimated sea level static standard day performance for the LF336/E fan is shown in Figure I-18. Performance is presented for the basic fan without exit louvers. The design speed of 1060 feet per second (923 m/sec) can be achieved at an engine power level equivalent to about 97.5 percent. The limiting speed, as established by the existing LF336 turbine hardware, will require an engine speed of about 94.0 percent. Table I-IV lists the significant fan and engine parameters for operation at the maximum test speed of 950 feet per second (290 m/sec) and the design speed.

FAN AERO-MECHANICAL PERFORMANCE

Tests of the LF336/E fan system were conducted at the facilities of the General Electric Flight Test Center, Edwards Air Force Base, California, and covered the period between October 6, 1972 and January 18, 1973. The test program required about 8 1/2 hours of fan operation. Following completion of the static tests, the fan system was shipped to NASA for continued static testing and cross-flow tests in the 40 by 80 foot windtunnel. The NASA test program also included an investigation of the LF336/E rotor with leading edge serrations.

Test Set-Up

The test propulsion system was composed of the LF336/E statorless fan, the J85-5 engine and interconnecting ducting between the engine discharge and the fan scroll inlet. The propulsion system was installed in a test stand as shown in Figure I-19. This test stand provides for mounting of the fan and engine system with the fan inlet oriented in a vertical plane. A flat plane surface is provided to extend the fan inlet bellmouth and to simulate a wing upper surface. A clean unobstructed fan inlet flowpath was thus provided in this test arrangement. The J85-5 engine, mounted with its inlet facing perpendicular to the fan inlet plane, employs a test bellmouth which is adaptable to installation of an engine inlet sound suppressor. Figure I-20 shows a photograph of the fan inlet and exhaust systems.

The initial test program was conducted in the facilities of the General Electric Flight Test Center, Edwards Air Force Base, California. The test facility is specifically intended for acoustic tests of engine systems and components, and includes an underground control room and test sites which are free of unnecessary obstructions which would influence acoustic measurements. A support frame, including overall thrust measurement capabilities, was provided for mounting the LF336/E test stand. A photograph of the test facility with the LF336/E installed is shown in Figure I-21. The test set-up shown includes the J85 acoustic suppressor which was installed during the acoustic test program.

Test Scope

The purpose of the test program was to determine the aerodynamic and mechanical performance of the LF336/E statorless lift fan. The test set-up consisted of the LF336/E fan with a clean fan inlet. The J85-5 engine was installed without the acoustic inlet suppressor.

Initial plans included three test phases to verify mechanical integrity of the fan, develop a fan operating map, and record acoustic performance of the fan system. During the initial testing, a fan thrust deficiency, associated with low hub base pressures, was observed. Hub base pressure below

ambient pressure were anticipated and included in initial performance estimates, but the base pressure observed during the initial tests of the statorless fan system were much lower than anticipated. Later in the overall program, tests of a scale model were performed to further define the hub base pressure problems. These tests will be described in Part III of this report.

The existence of the low base pressure and its associated low level of fan thrust required a redirection of the initial test effort towards an investigation of methods to improve the level of fan performance. During these initial tests, four basic fan modifications were tested. The results of these tests indicated that large improvements in the hub base pressure levels were not possible through simple modification of the existing lift fan configurations. The testing showed that the low levels of base pressure are inherent in fan exhaust flowfields in the presence of the exit swirl of a statorless fan system. With the realization that the fan performance deficiency due to the low base pressure could not be improved short of a complete fan redesign, the test program was continued to include verification of system mechanical performance and acoustic testing of two fan configurations.

The complete test program is summarized in the test run summary given in Table I-V. Test Runs 1 through 4 were the initial tests of fan mechanical integrity which also identified the fan performance problem. Runs 5 through 12 covered the test interval directed towards the explanatory investigations of possible modifications to improve fan performance. The three most siginifcant modifications investigated during these tests were:

- Venting of the Hub Base and Installation of a Turbine Throttling Ring - The purpose of turbine throttling ring modification was to relieve the low fan tip static pressure allotted to an apparent ejector action between the turbine exhaust flow and the turbine exhaust shroud or skirt. The exhaust shroud is identified in the photograph shown in Figure I-20. The hub base vent was provided to remove swirl from the separated flow in the hub base region and to provide vent air which could relieve the base suction. Figure I-22 shows a photograph of the fan exhaust section with these modifications installed.

- Addition of Fan Turbine Exhaust Stators - A set of existing LF336/A turbine stators was modified and installed on the fan assembly as shown in Figure I-23. The purpose of the turbine stators was to remove the swirl in the turbine exhaust flow which existed because of the light loading levels of the turbine.

- Installation of a Hub Base Fairing - A hub base fairing was designed and installed on the fan system as shown by the photograph in Figure I-24. The hub fairing contour was designed to yield near ambient static pressures across the flowfield in the fan exhaust plane.

At the conclusion of Runs 5 through 12, the test program was revised to include a series of runs to expand the fan operating envelope to the maximum operational speed of 6050 revolutions per minute. This exploratory testing was accomplished during Runs 13 through 15. Testing for definition of the fan operating map was then deleted from the test program at the conclusion

of Run 15. Development of a fan operating map in the presence of the low hub base pressures would not provide any useful performance data applicable to a properly designed statorless lift fan system.

Two comprehensive acoustic tests were performed using the fan configuration as modified only by installation of the turbine stators. During acoustic tests of the fan system, both far field and near field acoustic measurements were taken. Acoustic tests of the fan system with a clean unobstructed inlet were performed during Runs 16 and 17. A massive fan inlet acoustic suppressor was installed for the second acoustic tests conducted during Run 18. A photograph showing the fan system with the fan inlet suppressor installed is shown in Figure I-25.

Test Results

During tests of the unmodified fan, observations of the fan exhaust flow indicated that the turbine exhaust gases were diffusing radially outward at a very high angle. The source of this condition was initially attributed to an ejector action between the turbine exhaust flow and the cylindrical shroud which extended downstream of the turbine exhaust. A turbine throttling ring was installed at the aft edge of the turbine shroud to direct the turbine flow radially inward and to relieve the tip shroud ejector action. Improvements in the hub base pressure were also anticipated based on the expected tip flow improvements. The results of this first fan modification showed little or no improvement in fan overall performance as indicated by thrust measurements and flow surveys of the fan exhaust.

A second modification was added to the fan along with the turbine throttle ring installation. This modification included a hub base vent tube which collected fan exhaust air and recirculated the air into the separated zone behind the hub base. An anti-swirl vane as shown in Figure I-23 was also installed on the vent system for removal of the rotation of the secondary flow entrained in the hub base region.

This configuration was tested both without the fan inlet bellmouth, Run 7, and with the bellmouth installed for measurement of total fan airflow, Run 8. The fan performance obtained during these two test runs is presented in Figure I-26.

The thrust data shown in Figure I-26 compares test results with and without the fan inlet bellmouth installed. The agreement of the two sets of data is important because fan tests with the bellmouth require a thrust correction for inlet momentum forces. The inlet bellmouth, because of its large size and weight, was not mounted on the active portion of the thrust frame; instead, it was secured to the ground and attached to the fan inlet through a rubber slip seal located between the bellmouth and the cylindrical transition section. Figure I-25 shows the location of the transition section. This type of installation causes a thrust error because of the inlet momentum at the plane of the slip seal. A correction for this momentum term was calculated based on the bellmouth wall static pressure and the thrust was increased by the amount of this correction.

The fan inlet airflow, obtained from pressure measurements in the inlet bellmouth, is shown in Figure I-26. The measured data verifies an expected result, in that the fan airflow is above the design level. High fan airflow is anticipated because of the below ambient static pressures throughout most of the fan exhaust stream. The gas horsepower required to achieve a level of fan speed, as shown in the figure, indicates a slightly higher-than-design power level. This change from the unmodified fan power requirements could be caused by a change in fan exit static pressure or a change in turbine operation due to the throttling effect of the turbine ring. Figure I-27 presents typical fan exhaust flow parameters for this test configuration modified by installation of the turbine throttle ring and hub base venting system.

Fan System with Turbine Stators

The fan configuration was modified as shown in Figure I-23 by installation of the LF336/A turbine stators for removal of the turbine exit swirl. The performance of this stator row was expected to be poor because of the high blade incidence angles. The turbine exit swirl for the LF336/E is about 40 to 45 degrees in the direction of fan rotation compared to a stator design angle of 24 degrees. At an incidence of 15 to 20 degrees above design, the performance of the turbine stator would certainly be poor.

The fan configuration with the turbine stators installed was tested during Run 11 and during the acoustic runs to design mechanical speed. The only diffference in the test arrangement was the installation of the inlet bellmouth for Run 11.

Figure I-28 presents the measured overall fan performance for this configuration. Addition of the turbine stators produced a fan airflow reduction from the previous configurations. Throughout the test range, the measured airflow was only slightly above the design value. A sizable improvement in overall fan thrust was also observed. This thrust improvement could have occurred in both the fan and turbine exhaust streams. The major part of the improvement apparently occurred in the turbine exhaust thrust because of the redirection of the exhaust flow into a nearly axial direction.

Figure I-29 shows the fan exhaust flow profiles as measured for this configuration. The exhaust flow survey was taken just downstream of the turbine stator row or about 3.8 inches (9.65 cm) downstream of the rotor blade trailing edges. At this location, the diameter of the flowpath as established by the turbine stators was 37.70 inches (0.958 m). A comparison of these pressure measurements with previous similar data from the other configurations, shows only minor adjustments in the level of the fan exit static pressure. This comparison partially justifies the conclusion that the major thrust improvement was in the turbine exhaust flow.

Fan with Hub Afterbody

A hub afterbody was designed to provide a flowpath in the fan exhaust which would remove the large region of separated flow in the hub base area. The fan was modified by installation of the afterbody without removal of the fan turbine stators as shown in Figure I-24.

Fan overall performance, thrust, airflow and horsepower characteristics are shown in Figure I-30. Comparison of test results before and after installation of the hub afterbody show no significant improvements in fan performance. A small reduction in fan inlet airflow can be observed, and is indicative of some improvement or increase in the static pressure levels in the fan exhaust stream. Figure I-31 presents exit flow data for this configuration. The static pressure profile shows an increase in level over previous configuration data, but is still below ambient throughout the complete flowfield.

Tests of the LF336/E to Design Mechanical Speed

The series of tests conducted to investigate the low hub base pressure and the associated performance deficiency indicated that the LF336/E fan would require a redesign in order to realize any significant improvement in overall thrust performance. Based on the exploratory test results, the fan with only turbine stators installed was selected for the planned acoustic tests. During all of the previous tests, the maximum fan speed was 5300 revolutions per minute. Prior to the acoustic testing, the mechanical integrity of the fan had to be determined to the full speed limit. The configuration used for these tests included the turbine exit stators and the fan inlet bellmouth for measurement of fan total airflow.

Three test runs were required to extend the range of fan operation. During these runs, fan performance data were recorded to compare with and expand the range of performance observed during the previous Test Run 11. The measured overall fan performance is presented in Figure I-32 and compared with similar performance data from tests of Run 11. The extension of the data to about a corrected speed of 6100 revolutions per minute followed the performance trends observed during lower speed operation.

Analysis of Data

The early tests of the LF336/E turbotip fan system identified a performance deficiency associated with excessively low hub base pressures as established by the swirling exhaust flowfield. Numerous tests were conducted, without success, to improve the level of hub base pressure. Even with this performance problem, several significant data analysis procedures were performed which provided valuable fan performance data. This section of the report will present the results of some of the analyses performed using the program test data.

Fan Performance Using Probe Data

The traverse of the fan exhaust flow provided radial distributions of flow angles, total and static pressures and gas total temperature. These profiles served as input for evaluation of overall fan performance through integration of the fan exhaust flow parameters. The integration procedures determined the following fan performance parameters:

- Fan exhaust airflow
- Fan rotor pressure ratio, absolute and axial
- Fan stream total thrust
- Fan stream total energy or power

The integrated fan performance was determined for each of the following test configurations.

- Unmodified fan
- Fan with hub base vent and turbine throttle ring installed
- Fan with hub afterbody and turbine stators installed
- Clean inlet fan with turbine stators installed (acoustic tests)
- Fan with inlet suppressor and turbine stators installed (acoustic tests)

A comparison of fan performance at a fan speed of 5000 revolutions per minute is possible by extrapolation of some of the early test data. The tabulation of the fan performance parameters and cycle performance estimates is given in Table I-VI. Comparison of these measurements and the estimated performance shows almost equal performance for all configurations.

Comparison of Rotor Profiles with Design Predictions

The fan system was tested with a hub afterbody installed to provide design discharge pressure levels in the fan exhaust. The following discussion will compare the results of these tests with similar analytical predicted performance. In addition, comparisons will be made to show the changes in performance due to removal of the hub afterbody.

Before the test results can be compared with analysis, a method is required to correct the data to equivalent operating speeds. Performance of low pressure ratio fan systems has previously been normalized for effects of fan speed using a pressure coefficient defined as follows:

$$H_P = (P-Po)/(\rho_o U_T^2/2)$$

The measured fan exit total and static pressure distributions for tests with the hub afterbody installed were converted into this pressure coefficient. The test results are compared with predicted pressure distributions in Figure I-33. The two sets of data represent performance at the same axial location downstream of the rotor centerline plane, about 3.8 inches (9.7 cm), where the traverse plane was located. The measured flow angles, pitch and yaw, for

the same test point are also shown in Figure I-33. Predicted flow angles are also presented.

Comparison of the test results and the analytical predictions shows the following significant differences in performance:

- The fan exit stream static pressure levels agree with the analytical predictions near the hub afterbody surface. Near the fan tip, the measured pressure levels were below ambient pressure where the analysis assumed an ambient pressure boundary. This below ambient pressure is probably caused by the influence of the blunt base located between the fan and turbine exhaust streams.

- The rotor total pressure rise in the vicinity of the fan tip is considerably lower than predicted pressure rise. This difference is primarily the effect of tip seal leakage interaction with rotor performance.

- The measured pitch flow angles indicate a flow direction which is slightly more axial than the analytical prediction.

- The fan exit swirl angles are less than the predicted angles. The discrepancies are largest at the fan tip and almost vanish near the fan hub. This difference is the direct result of the low tip static pressure levels. Low exit pressures increase the fan airflow with an attendant reduction in the fan exit swirl angles.

In summary, a comparison of test and analytical performance shows some major discrepancies in predicted fan performance, particularly in the vicintiy of the fan tip. These discrepancies appear to occur because of an inadequate representation of tip seal leakage in the design analysis and the inaccuracy of the boundary pressure assumption. The test results indicate that the low base pressure on the blunt base separating the fan and turbine may be a factor in establishing the level of fan exit static pressure.

Figure I-34 compares measured fan flow parameters both with and without the hub afterbody installed. The comparison shows the expected trends in performance; for example:

- The fan exit static pressure is much lower without the hub afterbody installed.

- The pitch flow angles are radially inward throughout the complete flowfield. This radially inward flow is produced by the influence of the low hub base pressures and the turning of the flow to fill the void in the hub area.

- Fan exit swirl angles decrease by about five degrees with the hub afterbody removed. This trend is caused by the high flow conditions associated with the low exit static pressures.

- A small drop in rotor total pressure rise occurred when the afterbody was removed.

The overall operating characteristics of the test fan configuration will be compared with the predicted fan operating map in one of the following sections of this technical discussion.

Integration of Fan Total Thrust

The components of the fan total net thrust include the following:

- Fan Stream Thrust
- Turbine Residual Thrust
- Base Drag of Fan-Turbine Splitter
- Base Drag of Fan Hub

The performance data obtained during the acoustic tests of the clean fan, Runs 16 and 17, were used to determine the breakdown of the total net thrust into each of the components, as shown in Figure I-35.

These components of the fan thrust were obtained by integration of the measurements taken by the two exhaust traverse probes. The fan stream thrust, as previously presented, is the result of an integration of both the momentum and pressure-area terms within the fan exhaust flow. The hub and fan-turbine splitter drags were calculated by integration of the static pressures over the particular base areas. A direct measurement of the turbine residual thrust was not obtained. This thrust component was estimated using the following assumptions and the measured engine gas flow.

- The turbine exit velocity was calculated based on estimated turbine stator performance and fan horsepower requirement.

- The pressure-area drag was estimated using a pressure halfway between the fan-turbine splitter pressure and ambient pressure.

The summation of the thrust components is also shown in the figure. For comparison, the cycle estimated thrust levels of the fan and turbine streams are shown in Figure I-36. A comparison of the measured overall and integrated thrusts shows excellent agreement. The difference in the measured and estimated total thrust, about 550 pounds, (2450N) at design mechanical speed, is primarily due to the low hub base pressure levels.

Comparison of Fan Performance with Estimated Fan Map

Predicted performance of the LF336/E fan was developed using the estimated fan map and an operating line established by a boundary condition of ambient pressure at the exit plane of the fan. Figure I-37 shows the estimated map and the predicted fan operating line.

During tests of the LF336/E fan, performance was measured along only one operating line as established by the actual fan exit static pressure profiles. The measured fan exit static pressure was below ambient throughout the exit plane, with the hub pressure much below ambient. The presence of a below ambient pressure boundary condition will establish the fan operating line at a higher than predicted flow. The test operating line, as established by measurements taken during Runs 16 and 17, is shown on Figure I-37. Appropriate fan speeds used in the map presentation are identified by the data points. Comparison of the test operating line and the map shows excellent agreement up to the maximum corrected test speed of 90 percent. At the 90 percent speed point, the fan may be operating slightly below objectives as indicated by the small displacement of the data point from the predicted speed line. The difference in the predicted and test operating line can be attributed to the low exit pressures.

This comparison is the only verification of fan operation achieved during these tests because of the elimination of the planned tests intended to explore the extremes of the fan map. Based on this comparison, there is no reason to believe that there were any gross performance deficiencies in the fan aerodynamic design.

ACOUSTIC TESTS

Following the aero-mechanical tests of the LF336/E fan, an acoustic test program was performed using the final fan configuration as modified by installation of the turbine exit stator row. The propulsion system included the statorless fan, the J85 engine, and interconnect ducting as shown in Figure I-19. The initial acoustic tests were conducted at the outdoor test facility at the General Electric Flight Test Center (EFTC). After testing at General Electric, the fan was delivered to NASA and additional tests were performed at the outdoor test site at the Ames Research Center.

Acoustic Test Hardware

The test vehicle used during the acoustic test was the LF336/E system with a NASA-furnished suppressor installed on the inlet of the J85 engine. The inlet suppressor is identified in the photograph, Figure I-25, showing the acoustic test set-up.

During the testing at EFTC a massive fan inlet suppressor was installed to suppress fan inlet radiated noise and to allow determination of exhaust radiated statorless lift fan noise. Details of the design of the massive fan inlet suppressor are given in Reference 2. The fan inlet suppressor is also shown in Figure I-25. In addition to suppressing the inlet radiated fan noise, the massive inlet suppressor provided a 90 degree directivity shift to further reduce the levels at the microphone locations. Note that the inlet duct was wrapped with a lead-vinyl blanket to reduce any structure-born transmission of noise.

Test Sites

Edwards Flight Test Center

The test program was conducted at an outdoor test facility designed and constructed for testing full scale lift fans and engines. The site shown in Figure I-38 is located at the General Electric Edwards Flight Test Center at Edwards Air Force Base, California and is in an area free of buildings and obstructions. The area surrounding the acoustic test site consists of desert sand and brush. Figure I-38 is a photograph taken across the top of the control room which extends only thirty inches (76.2 cm) above the ground. The photograph shows the large bellmouth positioned in front of the LF336/E fan and the J85 with its inlet suppressor removed.

The test stand is attached to four concrete columns which protruded above the asphalt apron and the fan was mounted in the stand ten feet (3.05 m) above the ground with the fan flow parallel to the ground. No portion of the test stand was forward of the lift fan upper wing simulation surface which prevented any turbulence being generated by test stand structures.

A sketch of the microphone locations at EFTC is shown in Figure I-39. There were seventeen microphones located at 10 degree increments from 0 to 160 degrees relative to the fan inlet on a 150 foot (45.7 m) arc. Seven near field microphones were located on a 20 foot (6.1 m) arc at angles of 90, 110, 130, 150, 210, 230, and 250 degrees relative to the fan inlet. The near field mikes can be seen in Figure I-38. All microphones were in a horizontal plane through the fan centerline.

NASA Ames Outdoor Test Site

Additional LF336/E fan testing was conducted at an outdoor test site located at NASA, Ames Research Center. An aerial view of the test site is presented in Figure I-40. As the photograph shows, the acoustic path to a given microphone was in some places asphalt and concrete and in others short grass and asphalt. The microphone layout is sketched in Figure I-41. Far field microphones were on a 150 foot (45.7 m) arc in ten degree increments from 0 to 160 degrees. Two arrangements of near field microphones were used, both on a 20 foot (6.1 m) arc. The first, used for Runs 1 and 2, had the microphones located at 20 degree increments from 30 to 150 degrees. The second arrangement, for Run 3 and all successive runs, had the seven microphones located at 90, 110, 130, 150, 210, 230, and 250 degrees. This latter arrangement duplicated the near field microphone locations used at Edwards Flight Test Center, and in the NASA 40 by 80 foot (12.2 m x 24.4 m) wind tunnel.

Engine and fan centerline height at NASA Ames was 9 feet 8 inches (2.95 m) and all microphones were located in a horizontal plane through the fan centerline.

Sound Data Acquisition and Processing

Data Acquisition, Edwards Flight Test Center

All data acquisition for the near and far sound fields was made using Bruel-Kjaer model 4133 microphone systems in conjunction with an AR200 tape recorder operating at 60 inches per second (152 cm per second). Figure I-42 includes a schematic of the data acquisition system at EFTC, and a photograph of some of the equipment.

All far field microphones were oriented to point at the test vehicle and had Bruel-Kjaer UA0237 windscreens installed on the microphone heads. The near field microphones were oriented to point in the same direction as the J85 inlet and used Bruel-Kjaer model UA0052 nose cones.

The free field frequency response of each microphone head is derived from a pressure response curve recorded automatically by the electro-static actuator method traceable to the Bureau of Standards. The free field characteristics for various angles of incidence for microphones with protecting grid, nose cones, and windscreens are given by the microphone manufacturer. Individual microphone head sensitivities are determined by the insertion of a Bruel-Kjaer

pistonphone on the cartridge mounted to a standard microphone system. Both the pistonphone and standard microphone system are traceable to the Bureau of Standards.

Prior to initiation of testing, a frequency response of each data channel (minus microphone head) was made by the insertion of a Hewlett-Packard Pseudo-Random Pink Noise Generator into each cathode follower and recorded on magnetic tape.

Prior to and subsequent to each day's testing, an absolute calibration was made by the insertion of a pistonphone on each microphone and recorded on tape. Since the test site is 2300 feet (701 m) above sea level, a barometric correction was made to the pistonphone output as provided by manufacturer's specifications. Any microphone whose voltage output with the pistonphone applied was found to deviate more than $\pm$ 1.5 dB from the laboratory calibration was replaced.

Data Acquisition, NASA Ames

Data acquisition at NASA Ames was similar to that at EFTC as the sketch in Figure I-43 shows, except that the tape recorder was a Honeywell Model 7600 operated at 30 inches per second (76 cm per second). The step amplifier, tape recorder, monitor scope, and monitor voltmeter were all located in the General Electric Mobile Sound Evaluation Unit. During test operations at both test sites, sound was recorded continuously for a minimum of two minutes to allow enough sample length for data processing.

Data Processing, 1/3 Octave Bands

All 1/3 octave band data processing was performed at the General Electric Edwards Flight Test Center facilities using a General Radio real time analyzer in conjunction with a Honeywell 316 and SDS930 computer. Thirty-two second averaging time was used for data processing with data for each angle sampled from the same period of time for each data point.

Before data processing could be initiated, the total data acquisition and reduction system frequency response characteristics had to be determined and made available in the computer for final data processing. The first step in this process was to analyze the pink noise calibration tapes for each data channel, and determine the response characteristics for the total system as referenced to 250 Hz (frequency of the pistonphone) at each 1/3 octave band. Final one-third octave data processing was made by determining absolute sound pressure levels for the 150 foot (45.7 m) arc and 200, 500 foot (61 m, 151 m) sidelines corrected to standard day (59° F (15° C), 70% relative humidity) conditions as per Reference 6, and for ground attenuation effects as per Reference 7.

Data Processing, 20 Hz Narrowbands

All narrowband analyses were made at the General Electric Company facilities using a Federal Scientific Ubiquitous Spectrum Analyzer and a 139B Digital Averager. All data were processed using a 20 Hz bandwidth filter and an averaging time of 12.8 seconds. No corrections for humidity or acquisition/processing responses were included in the narrowband plots.

Results And Comparisons

The test programs conducted at both General Electric and NASA provided acoustic data for numerous configurations of the LF336/E statorless lift fan. Typical fan modifications that were tested included:

- Massive fan inlet suppression
- Treated exit louvers
- Serrated blade leading edges

These acoustic data, coupled with previous tests of conventional rotor-stator LF336 fan configurations, provides the basis for evaluating the merits of a rotor-only fan system. All succeeding 1/3 octave band SPL and PNL comparisons are made on a 200 foot (61 m) sideline while all 20 Hz narrowband SPL's are compared at a 150 foot (45.7 m) arc.

Fan Noise Comparisons

In this section, acoustic levels of the LF336/E statorless fan from NASA Ames Research Center testing are compared to LF336/A, LF336/B, LF336/C-1 and LF336/C-11 fans (Reference 1). Table I-VII lists the design parameters of these fans of the LF336 family.

Comparisons of statorless and conventional quieted fan configurations has shown that equal fan thrust can be achieved through proper selection of fan pressure ratio. For equal thrust, the statorless fan will require a larger fan diameter, at a lower pressure ratio, with minor increases in overall installation diameter in exchange for the reduced thickness of the fan relative to the more conventional design. This trade-off of fan diameter for thickness is one of the merits of the statorless fan concept.

Comparisons will be made at equal tip speeds and equal absolute pressure ratios. Comparisons of noise generation at equal tip speed is equivalent to comparing fans having equal thrust but different pressure ratios. Comparison at equal absolute pressure ratio implies similar fan loading characteristics and equal thrust for the same diameter. Pressure ratio has been used as a correlating parameter of aft radiated fan noise or rotor-stator noise while equal tip speed comparisons have been associated with inlet radiated or rotor alone noise. Comparisons will be made both ways; but in applications, the statorless fan would be designed to operate at a lower pressure ratio than conventional fans.

Figure I-44 compares statorless fan 1/3 octave band BPF directivity patterns to the LF336/B and LF336/C-11 fans at three fan speeds (no C-11 data available at 6000 RPM). Since all three fans are the same diameter, equal fan speed is equal tip speed. At the forward angles, the statorless fan is lower than the other two fans. In the aft quadrant, the statorless fan BPF levels are consistently lower than the LF336/B and at least as quiet as the LF336/C-11 at the critical angles of 110° to 130°. These angles are the most critical for sideline noise measurements with lift fans. Narrowband BPF directivity patterns for the statorless and LF336/B fans are compared in Figure I-45 at 6000 RPM ans show similar trends as Figure I-44.

PNL directivity patterns are presented in Figure I-46 and show that the statorless fan forward quadrant PNLs are quieter than the LF336/B and equal to or slightly lower than the LF336/C-11. In the aft quadrant, statorless fan levels are the same or lower than LF336/B but 1 to 3 PNdB higher than LF336/C-11. Since the statorless fan is not significantly quieter than conventional rotor-stator lift fans, this implies that the maximum effect of spacing has been reached at two chords. This is shown more clearly in Figure I-47 where the reduction of perceived noise level with increased spacing is shown at the 110 degree aft quadrant. For spacings approaching two chords, only small noise reductions occur with increased spacing. The noise level at the two-chord spacing can be considered to be rotor alone noise, which is in excellent agreement with the measured LF336/E noise levels.

The previous comparison of measured acoustic performance of statorless fans and conventional rotor-stator configurations was based on equal fan speeds at equal fan tip diameters. A difference in thrust levels exist by virtue of the differences in design pressure ratio and the thrust loss due to residual swirl in the exhaust of the statorless fan. Correction for this thrust difference based on 10 log (F/F) presents a noise level adder of 2 dB to the statorless fan levels.

Figure I-48 compares the fan pressure ratio of the LF336/A (which was assumed for the LF336/B and C) with the absolute pressure ratios developed by the LF336/E statorless fan. The absolute pressure of the LF336/E fan is based on the average total pressure at the fan exit measured in the direction of the swirling flow.

Directivity patterns of the 1/3 octave band which contains the BPF are compared in Figure I-49 at equal absolute pressure ratios. In the forward quadrant, the trends are the same as in the previous section with statorless fan levels generally lower than LF336/B but equal to LF336/C-11. In the critical aft angles between 110 and 130 degrees, the statorless fan is generally the same as the LF336/C-11 and lower than the LF336/B at the lower two pressure ratios. At the higher pressure ratio, the statorless fan is 1 to 3 dB above the LF336/C-11. On a PNL directivity comparison, as shown in Figure I-50, the statorless fan is the same as the LF336/B at forward angles and 1 to 2 PNdB higher in the aft quadrant. Figure I-51 compares the three LF336 lift fans as a function of absolute pressure ratio at four acoustic angles. At 40 and 60 degrees, the LF336/E is consistently lower than LF336/B at all pressure ratios but about 2 PNdB higher than the treated LF336/C-11 configuration. At 110 and 120 degrees, the LF336/B and LF336/E are almost identical at all pressure ratios and both are 2 to 3 PNdB above the LF336/C-11 levels.

On either basis - equal tip speed or equal pressure ratio - the statorless fan has noise levels comparable to the quietest conventional fan modified for minimum noise. Therefore, the statorless fan would seem to be a viable candidate, from the acoustic point of view, for quiet lift fan applications.

Fan Exhaust Directivity Patterns

Knowledge of the split between inlet radiated noise and exhaust radiated noise levels aids in analyzing the strength and directivity of the various fan noise sources. To determine this split, an existing massive fan inlet suppressor was installed on the statorless fan. In addition to suppressing fan inlet radiated noise, the suppressor, shown in Figure I-25, provided a 90 degree directivity shift to any fan inlet radiated noise. During previous tests, Reference 2, the massive fan inlet suppressor effectively suppressed fan inlet radiated noise and permitted measurement of exhaust radiated noise.

Fan PNL directivities are presented in Figure I-52 with and without the fan inlet suppressor at 6000, 5400, and 4800 revolutions per minute. The exhaust radiated levels in the forward quadrant are 5 to 8 PNdB below the unsuppressed levels. In Figure I-53, the 40 and 60 degree microphone PNL's are compared as a function of fan speed. At 40 degrees, the exhaust radiated noise levels are 6 to 10 PNdB lower than the unsuppressed levels at 6000 to 3000 revolutions per minute. At 60 degrees, there is 5 to 6 PNdB difference over the speed range.

Looking at Figure I-52, installing the inlet suppressor appeared to slightly increase the PNL levels in the aft quadrant. Figure I-53 shows the 110 and 120 degree PNL's as a function of physical fan speed. At 110 degrees, the inlet suppressor has no effect; however, at 120 degrees there is an incease of 2 PNdB near 4700 revolutions per minute and very little effect at other speeds. These slight changes are probably due to increased turbulence from the massive fan inlet suppressor or velocity changes in the fan tip region when the inlet duct was installed in the inlet plane of the fan.

Figure I-54 compares the directivity patterns of the 1/3 octave band which contains the BPF at three fan speeds with and without the inlet suppressor. At the 40 degree microphone the fan exhaust radiated levels are 6 to 10 dB below the unsuppressed levels. In the aft quadrant at 5400 and 4800 revolutions per minute. the exhaust radiated SPL's are higher than the total or unsuppressed levels. However, Figure I-55 compares the 20 Hz narrowband BPF directivity patterns with and without the inlet suppressor and indicates that inlet radiated BPF noise has been eliminated to 120 degrees at 6000 revolutions per minute. At lower speeds, Figure I-56 indicates that the 90 degree exhaust radiated BPF SPL's are 1 to 3 dB higher at 5400 and 4800 revolutions per minute and these are lower than the unsuppressed levels. At 110 degrees the exhaust radiated levels are lower at all speeds; however, at 120 degrees the exhaust radiated BPF levels have increased 4 to 7 dB over the unsuppressed levels at speeds from 4000 to 5400 revolutions per minute.

1/3 octave band spectra are compared in Figure I-57 at the 40 degree microphone. At this microphone, fan inlet radiated noise is evident down to 500 Hz at all speeds. The 20 Hz narrowband spectra in Figure I-58 show that

fan broadband suppression is about the same at all frequencies. At the 60 degree microphone in Figure I-59, the 1/3 octave band spectra again indicate fan inlet radiated noise is present down to 500 Hz. 20 Hz narrowbands in Figure I-60 indicate that the fan broadband suppression is not as much as at the 40 degree microphone. Looking at the 20 Hz BPF directivity as a function of fan speed, Figure I-61 indicates that the fan exhaust radiated BPF SPL is 16 to 9 dB below the unsuppressed fan levels at the 40 degree microphone. At the 60 degree microphone the exhaust radiated BPF SPL is 12 to 8 dB down except for 3800 revolutions per minute. Why this particular speed does not agree trendwise with the other speeds is unknown.

The split between exhaust radiated and inlet radiated noise levels can be easily determined. To calculate inlet radiated levels, one only has to logarithmically subtract the exhaust radiated levels from the unsuppressed levels. This provides the capability of evaluating different exhaust and inlet suppression requirements and determining the effect on the overall noise levels.

Treated Exit Louver Suppression

Acoustically treated exit louvers were installed and tested on the statorless fan during tests at NASA. The louver cascade is shown in Figure I-62 and was previously used in the LF336/C test program (Reference 1). It consisted of eight airfoils, each 0.58 inch (1.48 cm) thick with 7.9 inch (20.1 cm) chord. The airfoils were treated on both sides with two degree-of-freedom resonators and had acoustic design parameters $L/H \doteq 1.3$ and $H/\lambda \doteq 1.4$. They were located about 8 inches (20.3 cm) downstream of the rotor trailing edge. Reference 1 determined that little appreciable acoustic energy was radiated from the open ends of the louver cascade.

A comparison of the PNL directivity patterns with and without the treated exit louvers is shown in Figure I-63 at 6000, 5400, and 4800 revolutions per minutes. Suppression of 2 to 4 PNdB was achieved at angles of 80 to 110 degrees. Figure I-64 presents the directivity patterns of the 1/3 octave band which contains the BPF. Again, suppression is evident from 80 to 110 degrees at all speeds. 1/3 octave band spectra at the 110 degree microphone are compared in Figure I-65. Fan BPF and fan broadband suppression is evident for frequencies at and above the BPF; however, there is an increase in noise in the 630 Hz to 2500 Hz bands and a decrease at frequencies below 250 Hz. Narrowbands of 110 degree microphone spectra at 6000 and 5400 revolutions per minute are shown in Figure I-66 and show broadband humps of noise near 1200 and 2100 Hz at 600 revolutions per minute. This increase in the midfrequency range is due to wake scrubbing and interaction noise over the louvers. The flow out of the statorless fan has swirl which would tend to increase this scrubbing noise.

In Reference 1, it was shown that for the LF336/C fan at 95 percent fan speed (5750 RPM), there was no suppression from the louvers; however, at 80 percent fan speed (4800 RPM), 1 to 2 PNdB suppression was realized. At that time, it was observed at high power settings the Mach number of the flow over the louvers was of the order of 0.7. High Mach numbers are known to reduce the effectiveness of resonator treatment. At lower fan speeds, the Mach number was lower; threfore, the treatment was more effective. At the highest fan speed of the statorless fan (6000 RPM), the Mach number based on the above calculations

is about 0.5 at which the treatment should be more effective.

Inlet Radiated Power Level Predictions

A theoretical analysis of the noise generated by inlet turbulence-rotor interaction was conducted and a mathematical model developed to predict the inlet radiated sound power levels.

No inlet turbulence measurements have been made for the LF336/E statorless fan. Thus it was necessary to estimate levels by scaling turbulence measurements taken during testing of a fan with radius ratio and axial Mach number that were similar to the LF336/E; however, this fan was an axial inflow design while the LF336/E is a radial inflow design.

SPL levels were calculated at several radial locations from hub to tip and integrated over the annulus area to obtain sound power level. A comparison of the measured and predicted inlet radiated sound power levels is shown in Figure I-103. The measured inlet sound power levels were obtained by integrating measured far field SPL's from 0 to 90 degrees. In Figure I-67, the measured inlet power levels were obtained by integrating the measured far field SPL's from 0 to 90 degrees. In Figure I-67, the measured and predicted level of the 1/3 octave band which contains the blade passing frequency are in good agreement, but the location of the BPF is not consistently predicted by the theoretical analysis. In an attempt to better place the BPF in the 1/3 octave band, the eddy size was systematically varied at various radial locations. In Figure I-68, the assumed eddy sizes were increased by a factor of ten at all radial locations, at the outer two radial locations, and at the outer radial location. It appears that increasing the eddy size at the outer one of two radial locations causes the BPF to fall in the correct 1/3 octave band. The effect of increasing the eddy size by factors of 5, 10, and 15 at the two outer radial locations is shown in Figure I-69. The best fit is provided with a factor of 15 increase; however, the signal to broadband ratio obviously does not match the measured levels. In Figure I-70, the outer radial location eddy size was increased by a factor of 5, 10, 15. Again, the best fit of the BPF occurs with the factor of 15 increase and the broadband levels do not agree.

The theoretical model used in these few comparisons give encouraging results. There is a distinct need, however, for actual turbulence measurements on the LF336/E fan to verify the results and to confirm or deny the assumptions in the theoretical model. The model does seem sensitive to inlet turbulence eddy sizes when placing the BPF in the correct 1/3 octave band.

PART II - SERRATED LEADING EDGE DEVELOPMENT

Investigations and studies by NASA and General Electric have identified that significant noise reductions can be achieved through the use of serrated leading edges of turbomachinery airfoils. As part of the statorless fan program, a sub-program, was included to develop and test serrated leading edges on this fan configuration. The development of the serration configuration was accomplished by a series of cascade tests of various serrated airfoils derived from the statorless fan blade geometry. The selected optimum serration geometry was then incorporated into the statorless fan system and a series of acoustic tests were performed for comparison of fan noise characteristics both with and without serrations. This part of the report describes the cascade development program and presents the results of the fan acoustic tests.

SERRATED LEADING EDGE DEVELOPMENT

A two-dimensional cascade test program studied the effects of serrations on the acoustic and aerodynamic performance of blade contours representative of those employed in the LF336/E statorless lift fan. The test airfoils had a two inch (5.08 cm) chord and blade shapes equivalent to the meanline plane of the actual rotor blading. Two unserrated and six serrated blade configurations were tested. The serration geometry covered a range of serration lengths between four and eight percent of the airfoil chord. Serration tooth spacing ranged between 1.3 and 2.0 times the serration length. The test program included a range of blade inlet Mach numbers and inlet air angles which encompassed the blade design flow conditions of .85 Mach number 57 degrees air angle. During the test program, aerodynamic performance was obtained through measurements of the cascade exit flow field. Acoustic performance was obtained by measurement of the exhaust turbulence levels and through measurement of the overall sound levels in the semi-reverberant exhaust section of the test facility. Details of this test program are presented in Reference 7.

Test Cascades and Serrations

The purpose of the program was to develop a leading edge serration for the LF336/E statorless fan. Accordingly, the airfoil section was scaled from the LF336/E fan blade section and is shown in Figure II-1. The airfoil chord selected for the cascades was 2.0 inches (5.08 cm) and thus the blade aspect ratio was set at 2.0 based on the four inch (10.16 cm) wide test section. Figure II-1 also shows a sketch of the design procedure employed in development of the leading edge extension. A summary of the airfoil geometry selected for the cascade test program is given in Table II-I.

The test serration configurations were selected to cover a range of serration heights and spacings. Table II-II gives the significant dimensions of the six serration configurations which were tested. Two unserrated cascades

were also tested to establish baseline conditions and performance. One unserrated configuration was a blade contour equivalent to the as-designed airfoil and had a blade chord of 1.848 inches (4.696 cm). The second unserrated configuration had a chord of 1.962 inches (4.983 cm) and thus was representative of airfoils modified by the leading edge extension but prior to serrating the leading edges.

Each cascade configuration consisted of 15 blades installed in parallel plexiglass walls. The airfoil leading edge was located one chord downstream of the leading edge of the cascade walls.

Experimental Results

The total program included testing over a range of inlet flow conditions, velocity and air angle, for a total of six serrated and two unserrated cascade configurations. The range of flow Mach numbers was from about 0.75 to 0.97 and the range of inlet air angles was varied between 51 and 60 degrees. The aerodynamic design inlet flow condition for the blade section at the 50 percent flow streamline is summarized in Table II-III. Other significant performance parameters are listed, such as blade loading and exit deviation angles. The estimated inlet flow condition at the aerodynamic design speed is an inlet Mach number of 0.97 at an airflow angle of 57 degrees. This flow condition corresponds to operation at the design speed or thrust levels. A second operating condition which is of interest for fan systems employed in V/STOL aircraft is the "Noise Rating" or "Nominal Rated" operating point. This operating point is defined as 80 percent of design thrust, with the remaining 20 percent thrust increment reserved for aircraft maneuvering control forces. The noise generation characteristics of lift fan systems are usually evaluated at this partial thrust level.

The inlet airflow condition at the "Noise Rating" point was estimated using off-design cycle calculations and is an inlet Mach number of 0.85 at the design air angle of 57 degrees. Since this operating condition is of prime interest for noise generation where the noise estimates are performed, the major portion of the test program was directed towards an investigation of performance at these flow conditions. Only selected configurations were employed in extended tests covering a wider range of flow velocities and inlet air angles.

Aerodynamic Performance

The effects of serration geometry on blade aerodynamic performance were evaluated based on test measurements taken at an inlet Mach number equivalent to the "Noise Rating" point. At these inlet air conditions, aerodynamic performance was obtained through measurement of the total pressure loss and exit deviation angles. The effects of the serration geometry on these two performance parameters are shown in Figure II-2. The serration geometry is presented using the parameters of serration height, H, serration spacing, S, and blade chord, C.

These data show reductions in total pressure losses for all serration configurations. In addition, the minimum losses occur at serration heights of five to eight percent of the blade chord. The losses also appear to decrease as the serration spacing, S, approaches the serration height, H. Lower blade deviation angles were measured for all serration geometries, with no apparent influence due to serration height-to-spacing ratio.

During the program, blade off-design performance was obtained for a range of inlet Mach numbers and inlet air angles. Aerodynamic performance at these off-design conditions for both serrated and unserrated configurations is shown in Figure II-3. Serrated leading edges improved performance for both increased inlet Mach numbers and flow angles less than or greater than the design inlet flow angle of 57 degrees. This trend of improved off-design performance is a significant test result. It appears that serrated leading edges exhibit the desired performance characteristics of a very sharp leading edge airfoil without the associated poor performance at off-design air angles. The desired sharp leading edge characteristic is indicated as a very small increase in fan total pressure loss coefficient with increasing inlet Mach number. The good off-design performance is shown as a broader tolerance for inlet air angle excursions without large increases in total pressure loss or exit air deviation angles. In a compressor or fan design, this type of performance improvement would appear as increases in off-design efficiency coupled with increases in stall margin. For comparable performance, the improvements due to serrations could be utilized to achieve increases in fan blade loading as manifested by lower tip speeds or reduced blade areas.

Wake Turbulence Levels

In the previous discussion, the effects of serrations on aerodynamic performance were evaluated using two serration dimensional parameters, (H/C) and (H/S). A similar comparison of the measured exit turbulence levels is presented in Figure II-4. Turbulence levels, both axial and normal, decrease as the serration height (H) is increased. Serration heights of greater than six percent of the blade chord yield the lowest turbulence levels. Effects of serration spacing (H/S) are not as clearly identified as in the case of a similar comparison of the aerodynamic performance.

The effects of serrations on blade off-design wake turbulence levels are shown in Figure II-5. Addition of serrations shows a reduction in turbulence levels both with increasing Mach numbers and at incidence angles above and below the design level. At low Mach numbers and at an inlet air angle equivalent to zero degrees incidence (54 degrees), the effects of serrations on blade turbulence levels appear to be negligible.

Acoustic Performance

Acoustic performance of the cascades was determined by noise measurements in the discharge plenum chamber. Figure II-6 shows the noise with and without serrations as a function of Mach number. All serration geometries yield noise reductions throughout the Mach number range.

An analysis of noise generated by a cascade and its relationship to the wake turbulence was presented in Reference 8. The analysis predicted a noise change proportional to 20 log u/U. Figure II-7 shows a comparison of this theoretical reduction with results obtained during the cascade tests. Reasonable agreement is obtained except for configurations SR1 at 60 degrees and SR5 at 57 degrees. Apparently, the measured noise change is due to reduced turbulence in the blade wake, thus better blade performance is indicative of lower noise.

The effect of serration geometry on noise was consistent with results presented previously for aerodynamic performance. Figure II-8 is a plot of noise versus H/C at constant values of H/S, which is comparable to Figure II-4. At constant serration height (H/C), larger spacing, and constant geometry (H/S), the larger tooth height and spacing produce less noise. The conclusion from Figures II-4 and II-8 is that serrations improve performance and lower losses which results in lower noise.

SERRATED ROTOR ACOUSTIC TESTS

The cascade tests, as defined previously, led to the selection of serration configuration SR6, as defined in Table II-II. This serration configuration was incorporated in the rotor blading of the LF336/E for acoustic tests to determine noise reductions compared to a clean unserrated rotor. The tests of the fan were conducted at the NASA Ames Research Center test site, and included configurations with and without a circular inlet vane installed. During the following discussion, the effects of serrated leading edges on fan noise generation will be based on acoustic data obtained for the fan without the circular vane installed.

Serrations reduced the perceived noise level (PNL) by 2 to 4 PNdB primarily from 80 to 100 degrees (relative to the fan inlet on a 200 foot (61 m) sideline) as shown in Figure II-9 at 6000, 5300 and 4800 revolutions per minute. At forward angles, however, the use of PNL is somewhat deceiving since it weights the 1/3 octave band which contains the BPF most heavily and in the forward angles the BPF-not fan broadband noise-controls the spectra. Figure II-10 presents a comparison of serrated and unserrated sound power levels (re 10^{-13} watts) at three fan speeds. Serrations clearly reduced fan broadband power levels from 630 Hz to the BPF by 1 to 2 dB. Above the band containing the BPF, there was little or no reduction due to serrations. The region of the spectrum around 315 Hz is influenced by the ground null; however, lower frequencies down to 100 Hz show lower sound power levels with the serrated rotor. There are two possible reasons for the reduction at these low frequencies. One is that the fan is performing differently with the serrated rotor and jet velocities are reduced thus lowering these low frequency levels. The second possibility is that these low frequencies observed in the forward quadrant, which are usually associated with jet noise, are in fact fan broadband noise which has been reduced by serrations. Figure II-11 indicates that the second possibility is correct. Here the serrated and unserrated 160 Hz sound pressure levels (SPLs) at three fan speeds are compared at acoustic angles on a 200 foot (61 m) sideline. The SPLs from 30 to 100 degrees have been reduced

2 to 5 dB by serrations. However, aft angles show little change with serrations. Apparently, the low frequency noise observed in the forward quadrant is caused by fan rather than jet noise turbulence. Furthermore, serrations reduce this low frequency noise.

At higher fan broadband levels, e.g., at 1600 Hz in Figure II-12, the effect of serrations can be seen at angles of 30 degrees rearward at 4800, 5300, and 6000 revolutions per minute. For some reason, which is not clear at this time, the 110 degree level was not reduced by serrations. The reductions range from 2 to 4 dB. Similar results are observed for the 2500 Hz SPL's in Figure II-13. Again the 110 degree SPL's with serrations are the same as the unserrated levels.

Serrated and unserrated SPL's of the 1/3 octave bands which contain the BPF for 6000, 5300, and 4800 revolutions per minute are compared in Figure II-14. At forward angles up to 80 degrees the SPL's at the two lower fan speeds show no effect due to serrations and the 6000 rpm SPL's only show about a 1 dB drop due to serrations. The forward SPL's which contain the BPF are controlled by the BPF and the BPF is not affected by serrations or are slightly increased as the narrowband SPL's in Figure II-15 indicate. Note that Figure II-19 compares both 1/3 octave band BPF and 20 Hz narrowband BPF on a 150 foot (45.7 m) arc. Typical 120 Hz narrowband spectra are shown in Figure II-20 for 60 degrees and 120 degrees. The aft spectra BPF is only 4 dB above the broadband noise which accounts for the difference between the aft quadrant 1/3 octave band BPF and 20 Hz BPF levels in Figure II-16.

At frequencies above the BPF, serrations do not achieve a reduction except at 80, 90, and 100 degrees. Figure II-17 is a typical frequency, 8000 Hz, at three fan speeds.

These comparisons verify that serrating the leading edge of the rotor produced fan broadband noise reductions of 2 to 5 dB. The appearance of these reductions at low frequencies indicates that the fan broadband noise may extend to frequencies as low as 100 Hz.

PART III - PERFORMANCE IMPROVEMENT

HUB BASE PRESSURE INVESTIGATIONS

During tests of the LF336/E statorless fan, a large thrust deficiency was observed. Through measurements of the fan exit flow and pressure profiles, the low thrust was traced to excessively low fan exit static pressures, particularily in the hub base area. The original estimates of base pressure, as included in the fan design and performance estimates, were based on experience derived during tests of fans with axial exhaust flow. With swirling flow, as in a statorless fan, this experience was no longer applicable and a new method of estimating hub base pressures was required. A program was initated to develop the required background through a combined theoretical and experimental investigation of base pressures for cases with and without swirling flow. This section of the report summarizes the significant results of this study, including a statorless fan aerodynamic redesign based on the experimental results. Details of this investigation may be found in Reference 9.

Theoretical Analysis

When flow exits from an annular nozzle with a blunt centerbody the pressure over the aft face of the centerbody may be considerably different from the ambient pressure into which the jet is exhausting. This base pressure may have a significant effect on the flow and thrust coefficients of the nozzle. If the jet exits axially without swirl, base pressure coefficients based on average jet velocity head are on the order of -.10 to -.15. However, if the jet has radial or circumferential velocity components it is found that the base pressure coefficients may vary widely from these values. This analysis was undertaken to develop an analytical model which could be used to predict base pressure, thrust, and flow coefficients for annular nozzles with non-axial flow. The analysis also considers the effects of radial distribution of swirl, nozzle radius ratio and nozzle pressure ratio.

Conceptually, the reduction of the base pressure below ambient pressure can be thought of as being the result of three separate factors. First, in a jet with axial exit velocity, the shear forces between the high velocity main stream flow and the relatively stagnant air mass composing the centerbody wake must be balanced by an equal and opposite force acting across the base area. This component of base pressure is a true drag force and results in a thrust loss.

Second, there is a component of base pressure due to the meridonal curvature of the flow streamlines in the vicinity of the nozzle exit. This streamline curvature causes a radial static pressure gradient in the flow and thus causes the base pressure to differ from ambient pressure. If the flow exits axially the streamline curvatures are small but if the flow is angled radially inward or outward the streamline curvatures are much larger and the effect on the base pressure may be significant. This component of the base pressure has no effect on the nozzle velocity coefficient since it is essentially a potential flow phenomonen.

Third, if the jet has a swirl velocity component, a radial pressure gradient must exist in the flow stream to support the centrifugal forces generated by the swirl. This then results in a base pressure lower than the ambient pressure. Furthermore, the swirling jet induces a rotational motion to the centerbody wake which in turn causes a radial pressure gradient across the base area and a further reduction in average base pressure. This component of base pressure can cause a large loss in nozzle thrust coefficient and represents the energy lost in the swirl velocity component.

It is evident that the above three effects are closely interrelated so that they cannot be treated independently in a mathematical analysis of the problem, however it is conceptually enlightening to recognize the separate factors affecting the base pressure.

Assumption and Boundary Conditions

Figure III-1 shows the general scheme of the flow model assumed in this analysis. The flow downstream of the nozzle exit is divided into two distinct regions, the main stream flow and the centerbody wake. The dividing line between these two regions is the hub streamline of the main flow. It is recognized that there is actually flow interchange across this boundary but it can be taken as the line across which the time averaged flow is zero. Thus the total time averaged mass of air within the wake region is constant. It is assumed that static pressures in the two regions are equal along this streamline and that shear forces between the two regions may exist along this line.

The outer streamline of the main flow is assumed to be an isobaric surface where the static pressure equals the ambient pressure into which the jet is exhausting. Shear stresses and mixing along this outer boundary are assumed to have negligible effect on the base pressure of the centerbody.

At Station 1, the upstream boundary of the main flow, it is assumed that the radial distributions of total pressure, total temperature, and angular momentum can be specified. At Station 2, the downstream boundary of the main flow, it is assumed that the slope and curvature of all streamlines are zero. Total temperature and swirl angle distributions at this station are derived from the upstream values assuming that energy and angular momentum are conserved along each streamline. The total pressure distribution at Station 2 is derived from the upstream total pressure and the assumption that the loss due to the shear stress between the main flow and wake is distributed uniformly across the main stream.

Other assumptions are that the flow is steady, axisymmetric and has the properties of an ideal gas. At the inlet station, it is assumed that the radial distributions of angular momentum can be sufficiently well represented as a linear relationship to the stream function. Details of the flowfield calculations are given in Reference 9.

Experimental Program

The experimental phase of the hub base pressure study was intended to verify the theoretical analysis through test of scale annular jet models with and without swirling flow. These scale model tests were conducted to evaluate several empirical parameters required in the theoretical analysis, and to provide a method of flow observations of the jet wake zone downstream of the hub base.

A total of 11 models were tested with different hub radius ratios and radial flow angles. Table III-I contains data defining the exit geometry of each model. The test configuration is identified by the model number plus a prefix of either A or S to identify axial or swirling flow, respectively.

Test Results

The results of the hub base pressure test may be separated into two major categories:

- Tests with axial flow, simulating a rotor stator fan exit
- Tests with swirling flow, simulating a statorless fan exit

In addition, several miscellaneous tests were performed to investigate effects of variable pressure ratio, blockage for simulation of exit louvers and skewed swirl distributions.

Flow surveys were taken for each model at several downstream locations. Figure III-2 presents typical pressure and angle distributions for test model 6 that had a radius ratio of 0.55 with zero degrees of radial flow angle. Flow profiles are presented for the plane directly downstream of the nozzle exit and for the most downstream test location. The profiles for the axial case, as shown in Figure III-2, are typical of flow in the wake of the base. Close to the exit plane, the base pressure is slightly below ambient pressure and the static pressures in the main flow average to a level near ambient pressure. At the far downstream location, the flow has filled the base wake, with stream static pressures at or slightly above the ambient levels.

The flow surveys for the model with swirling flow are also shown in Figure III-2. For this condition, the static pressure profiles exhibit large pressure gradients. Immediately downstream of the exit plane, the pressure level decreases steadily from tip to hub, achieving pressure coefficients of about -0.8 near the hub. The swirl distribution in the main flow is nearly a constant 35 degrees as established by the swirl vanes. In the wake of the hub, the flow is purely tangential as indicated by the 90 degree swirl angle. As the flow proceeds downstream, the pressure gradients smooth out with reverse flow in the wake region. The reverse flow is indicated by swirl angles that approach 180 degrees at the wake centerline.

Based on the flow surveys at several downstream locations behind each model, the locations of the flow streamlines were determined. Figure III-3

shows the flow field with axial flow and with swirl. Without swirling flow, the base closes on itself some distance downstream of the exit plane. For the case with swirl, the hub wake does not appear to converge but approaches some limiting size. This test result agrees with the wake mixing assumptions included in the theroetical model. The mixing region of the jet outer boundary is also indentified for each model test. This zone represents the boundaries of the outer flow of the jet and the location of the streamline entraining the measured total model flow. Figure III-4 and III-5 present graphically the level of flow entrained in this mixing region as a function of position downstream of the exit plane. With swirl, the level of flow entrainment is about 30 to 50 percent greater than for axial flow.

The integrated mass flow weighted total pressure was determined from the profile data, and in turn used to define the total pressure (mixing) loss coefficients. These data are shown in Figure III-6 and III-7, and again show higher losses for the case with swirling flow. These higher rates of loss and flow entrainment can be expected for a swirling jet when the absolute total pressure levels of both cases are equal. With swirl, the axial velocity components are lower, and thus the mixing process would occur in a shorter axial distance.

The flow profiles, as measured at the model exit plane, were used as the basis for determining overall performance for each configuration. The measure flow data were used to determine overall thrust coefficient, flow coefficient and average hub base pressure variation with model geometry and swirl levels. These overall performance parameters are shown in Figures III-8 and III-9.

A comparison of the theoretical predictions and the test data is shown in Figures III-10 through III-12 and shows good agreement. Similar comparisons of the axial flow conditions were equally as encouraging. Details of the procedures used in evaluation of the constants and comparisons with additional test results are given in Reference 9.

STATORLESS FAN AERODYNAMIC REDESIGN

An analytical model has been developed to describe the flow field of annular jets with blunt bases. Application of this theory for the case with swirling flow is representative of the exit of a statorless fan rotor system. The empirical constants for the analytical model were derived during model tests both with and without swirling flow using turning vanes to inject swirl in the exhaust flow. This arrangement was equivalent to exit from a stator blade row where the level of swirl is a fixed parameter independent of the levels of stream total pressure. For a rotor case, as occurs in a statorless fan, the levels of swirl are related to the rotor pressure ratio and the rotational tip speed. For this reason, one of the constants, C_2, must include corrections to reflect these variations of swirl levels. For the test models, the constant C_2 was determined to be 0.48 when the level of hub swirl was 60 percent of the meridinal velocity at a 0.5 radius ratio. Using this test

point as a base and estimated variations with swirl level, the characteristics shown in Figure III-13 were selected for analysis of statorless fan systems. The remaining empirical constants, FF, C_{PL} and C_9, were assumed to be the same for either a rotor or a stator configuration. The friction factor, FF, was assumed to be 0.04. The values of C_{PL} and C_9 are also given in Figure III-13.

Application of Base Pressure Analysis to Designs

A parametric study of the performance of statorless fans was accomplished using the mathematic model of the exhaust flow. The significant fan design parameters considered during the study were fan pressure ratio, exit hub radius ratio and rotor radial pressure rise distributions. Throughtout the studies, the fan tip speed was set at 1125 ft/sec (343m/sec) which is typical for an advanced technology rotor design. High tip speeds are desirable for statorless fans since they require lower swirl levels at a given rotor pressure rise. This relationship of fan exit swirl and pressure ratio for the design tip speed condition is shown in Figure III-13.

Fan performance figures of merit are thrust, flow and power conversion efficiency. The variation of these figures of merit with fan design conditions are shown in Figures III-14 through III-16. Each performance parameter shows improvements as the hub radius ratio is decreased, with rotor exit swirl or loading distributions producing only minor changes in performance. A typical minimum hub exit radius ratio would be 0.4 as established by the mechanical design ability of inserting the blades in the hub disk. Selecting designs yielding maximum thrust/area at a 0.4 radius ratio, the effect of exit swirl distributions on performance is as shown in Figure III-17. The fan pressure ratio variation with swirl distribution is shown for the rotor tip and for the average of the complete rotor. The effect of increased skewness of the swirl distribution is to increase the difference between the tip and stage average pressure levels. For minimum skewness, consistent with maximum performance, a design condition was selected for a 30 percent distribution where the average pressure ratio is 1.275.

Comparison of LF336/E and Selected Design

The original LF336/E statorless fan was optimized and designed without considering the low hub base pressures as observed during the demonstration testing. Application of conventional rotor design techniques forced the LF336/E rotor design to employ relatively high rotor hub radius ratios for acceptable hub loading. This large hub size, coupled with the low hub base pressures, showed thrust deficiencies of about 20 to 25 percent of design levels. When the low hub base pressures are considered during fan design, the hub loading criteria is no longer the design limit. Mechanical design considerations become the dominant criteria in establishing the fan radius ratio.

The theory developed during this analysis was used to estimate fan performance for the original LF336/E statorless fan design and the proposed modified design utilizing a low hub radius ratio. Figure III-18 compares the flowpath of the two fan designs and points out the large reduction in hub radius. A comparison of estimated performance for the original and redesigned statorless fan configurations is given in Table III-II. In addition, fan performance as determined during the LF336/E demonstration tests is also tabulated. The first column of tabulated data presents performance as estimated during the original LF336/E fan design effort. This performance reflects estimates using base pressure levels consistent with previous lift fan experience and, therefore, does not include the effects of the low hub base pressures and therefore represent the objectives established during the initial design studies.

The mathematical model was used to estimate performance of the original statorless fan configuration. A comparison of the results shows the ability of this theory to estimate statorless fan performance. The theory predicts fan thrust and flow levels about 9 percent above the actual test data. This difference may be due to effects of seal leakage, not included in the theoretical treatment, and a deficiency in fan blading performance because the test fan rotor was not designed for operation with the extremely low exit pressures and attendent high hub flow conditions.

The estimated performance for the modified fan shows significant improvements over both the objective and measured performance of the LF336/E fan. This large improvement is achieved primarily through reductions of the hub radius that are possible because of the low hub base pressures. An evaluation of the blade loading for the proposed fan design shows low blade D-Factors and pressure rise coefficients throughout the inner flowpath. Figure III-19 presents the spanwise variation of blade loading for a configuration with a tip solidity of 1.3 and a hub solidity of 2.3. These data show that the hub loading is indeed very low, in fact, negative, with tip loadings that may be slightly high for an acceptable design. An Increase of blade tip solidity or speed would reduce the loadings to acceptable levels.

A comparison of the new statorless fan design with the LF336/A, a built and tested fan, identifies the aerodynamic trades required for removal of the exit stator row. The proposed statorless fan design utilizes a higher tip speed than the LF336/A fan. Statorless fans desire higher tip speeds while the LF336/A speed was established through optimization of the turbine using a J85 gas generator. This difference in the tip speed accounts for the increased exit radius ratio of the conventional fan.

The thrust per unit area and the power conversion parameters are the two prime figures of merit of a fan system. The thrust per unit area for the revised statorless design approaches the levels for a conventional design. This high thrust is produced by the high flow per unit area. The thrust efficiency of a statorless fan design is inherently low because of the thrust loss in the residual swirl. This loss appears as the 20 percent deficiency of the statorless fan design.

CONCLUSIONS

A 36 inch (0.914 m) diameter statorless fan was designed and fabricated to obtain aerodynamic and acoustic performance of a rotor only single stage turbotip fan. Early tests of the fan system indicated a large performance deficiency associated with lower-than-anticipated hub base pressures. Performance and acoustic tests were conducted for the unmodified fan configuration at both General Electric and NASA Ames Research Center. Acoustic performance was obtained both with and without leading edge rotor serrations.

The program was extended to include a detailed investigation, theoretical and experimental, of the identified low hub base pressure of statorless fans. The results of this study were utilized in the definition of a redesigned statorless fan configuration.

The conclusions that were derived from these programs are as follows:

1) Statorless turbotip lift fans develop low base pressures that can produce large thrust deficiencies if not adequately considered during the aerodynamic design of the fan. Through proper application of design techniques that do consider the low hub base pressure, it is possible to design an attractive statorless fan system. For the statorless fan, hub aerodynamic loading is not a limiting criteria as is the normal condition for turbotip fan configurations. Instead, the hub of a statorless fan is established only by mechanical considerations.

2) Comparison of acoustic performance of statorless and conventional rotor-stator fan configurations were made on both equivalent tip speed and absolute pressure ratio basic. On either basis, the statorless fan has noise levels comparable to the quietest conventional fan modified for minimum noise, including rotor stator spacing and treatment similar to the LF336/C11 fan configuration.

3) Cascade tests of serrated blading indicated that:

   - Serration of the leading edges of a typical rotor airfoil design produced improvements in aerodynamic performance, reductions in wake turbulence levels and reductions in downstream noise levels.

   - The performance improvements, associated with the serrated leading edges, were largest during off-design operation of the airfoils and at high inlet Mach numbers approaching sonic speeds. Only small gains were observed when the inlet flow angle established zero incidence at flow Mach numbers below about 0.80. In a fan or compressor this type of performance improvement would appear as an increase in off-design efficiency coupled with increased stall margin.

4) Comparison of statorless fan acoustic characteristics with and without rotor leading edge serrations indicated that:

- Serrations lowered fan broadband noise primarily at 80, 90, and 100 degrees at all speeds.
- Pure tone reductions were not obtained with serrations.
- Reduction in fan broadband noise and not tones is consistent with the rotor-alone analysis which indicated that serrations primarily effect fluctuating pressure on the rotor and thus broadband noise generation.
- Low frequency SPL's down to 100 Hz were reduced with serrations which may indicate that fan broadband noise occurs at these frequencies.

6) The analytical and experimental investigation of hub base pressures, in the presence of swirling flow, developed a method for reasonable prediction of hub base pressures and overall flow parameters. The accuracy of the theoretical model was limited by the range of test variables used in evaluating the empirical constants.

7. Application of the theory developed for prediction of base pressures to the exhaust conditions of statorless fans verified the experimental results obtained during the LF336/E fan tests. Application of this theory to redesigned fan systems identified an encouraging configuration with performance levels higher than previous statorless fan objectives that also approach those of a conventional rotor-stator fan system.

NOMENCLATURE

Symbol	Definition	Units
A	Area	ft^2 (m^2)
BPF	Blade passing frequency	HZ (HZ)
C	Blade chord	in (cm)
CPS	Static pressure coefficient, $(P_S - P_0)/(P_{T1} - P_0)$	
CPT	Total pressure coefficient, $(P_T - P_0)/(P_{T1} - P_0)$	
C_F	Nozzle flow coefficient, W/W_i	
C_P	Specific heat at constant pressure	BTU/lb °R (joule/g °K)
C_P	Static pressure rise coefficient, $(P_{S2} - P_{S1})/(P_{TR} - P_{S1})$	
C_P'	Static pressure rise coefficient, $[(P_{S2}/P_{S1})^{Y-1} - 1]/(T_{TR}/T_{S1} - 1)$	
C_{PL}	Empirical constant used in base pressure analyses	
C_{P1}	Hub base pressure coefficient at outer radius, $(P_{B1} - P_0)/(P_{T1} - P_0)$	
C_{P2}	Average hub base pressure coefficient, $(P_B - P_0)/(P_{T1} - P_0)$	
C_T	Nozzle overall thrust coefficient, $(C_F)(C_V)$	
C_V	Nozzle velocity coefficient, V/V_i	
C_u	Tangential velocity	ft/sec (m/sec)
C_2	Empirical constant used in base pressure analysis	
C_9	Empirical constant used in base pressure analysis	

Symbol	Definition	Units
D_{FT}	Fan tip diameter	in (meters)
D-F	Blade loading diffusion factor	
F	Fan thrust	lb (kN)
FPk	Fan total pressure ratio	
g	Gravitational constant	ft/sec^2 (m/sec^2)
h	Enthalpy	BTU/sec (joule/sec)
Δh	Rotor enthalpy rise, $h_2 - h_1$	BTU/sec (joule/sec)
H	Serration tooth height	in (cm)
H_P	Pressure coefficient $(P - P_0)/(\rho_0 U_T^2/2)$	
J	Mechanical equivalent of heat	ft lb/BTU (Nm/joule)
J_0	Fan rotor polar moment of inertia	$lb\text{-}ft\text{-}sec^2$ ($kg\text{-}m\text{-}sec^2$)
K	Ratio of turbine locked rotor to design point torque	
L	Serration teeth spacing	in (cm)
M	Mach number	
N	Rotational speed	RPM (RPM)
N	Rotor pressure rise profile factor	
N_{DP}	Fan design speed	RPM (RPM)
N_E	Engine speed, 100 N/18,650	pct (pct)
N_F	Fan speed, 100 N/6742	pct (pct)
P	Fan rotor power	HP (kw)
P_B	Area average hub base pressure	lb/in^2 (kN/m^2)
P_{B1}	Pressure at outer radius of hub base	lb/in^2 (kN/m^2)

Symbol	Definition	Units
P_S	Static pressure	lb/in^2 (kN/m^2)
P_{STD}	Standard pressure, 14.696 lb/in^2 (101.32 kN/m^2)	lb/in^2 (kN/m^2)
P_T	Total pressure	lb/in^2 (kN/m^2)
R	Radius	in (cm)
$\overline{R}$	Fan hub radius ratio	
S	Serration root spacing	in (cm)
SPL	Sound pressure level, re: 0.0002 $dynes/cm^2$	dB (dB)
T_{DP}	Turbine design point torque	lb-ft (kN-m)
T_e	Blade edge thickness	in (cm)
T_m	Blade maximum thickness	in (cm)
T_{STD}	Standard day temperature, 518.69°R (288.2°K)	°R (°K)
$T_{5.4}$	Fan turbine inlet temperature	°R (°K)
u'/U	Axial RMS turbulence intensity ratio	
U	Rotor tangential speed	ft/sec (m/sec)
v'/U	Normal RMS turbulence intensity ratio	
V	Effective velocity	ft/sec (m/sec)
V_i	Ideal velocity based on P_{T1} and P_0	
W	Airflow	lb/sec (kg/sec)
W_T	Nozzle exit total airflow based on measuring section	lb/sec (kg/sec)
W_i	Ideal flow based on P_{T1} and P_0	lb/sec (kg/sec)
W_{10}	Fan inlet airflow	lb/sec (kg/sec)
Z	Axial distance from nozzle exit plane	in (cm)

Symbol	Description	Units
β	Radial flow angle of nozzle exit flowpath	deg (deg)
β_1	Cascade inlet air angle	deg (deg)
β_{1C}	Rotor inlet air angle	deg (deg)
β^*_{1C}	Rotor leading edge blade angle	deg (deg)
β_{2C}	Rotor exit air angle	deg (deg)
β^*_{2C}	Rotor trailing edge blade angle	deg (deg)
η_T	Turbine efficiency	
γ	Ratio of specific heats	
δ	Pressure correction, P/P_{STD}	
δ	Deviation angle, $\beta^*_{2C} - \beta_{2C}$	
η	Fan adiabatic efficiency	
θ	Temperature correction, T/T_{STD}	
ρ	Density	lb sec^2 ft^4 (kg sec^2 m^4)
τ	Fan speed time constant	sec (sec)
$\overline{\omega}$	Loss coefficient, $(P_2 - P_1)/(P_{T1} - P_{S1})$	

Subscripts

0	Ambient
1	Upstream
2	Downstream
H	Hub
R	Relative to rotor system
T	Tip

REFERENCES

1. Kazin, S.B.; Volk, L.J.: "LF336 Lift Fan Modification and Acoustic Test Program," General Electric Company, NASA CR-1934, December, 1971.

2. Stimpert, D.L.; and Uhl, W.R.; "Aero-Acoustic Design and Test of a Multiple Splitter Exhaust Noise Suppressor for a 0.914 m Diameter Lift Fan," General Electric, NASA CR-121108, January, 1973.

3. Przedpelski, A.J.; "Lift Fan Technology Studies," General Electric Company, NASA CR-761, April, 1967.

4. Smith, E.G.; and Sowers, H.D.; "Cascade Tests of Serrated Leading Edge Blading at High Subsonic Speeds," General Electric Company, NASA CR-2472, June, 1973.

5. Katsanis, T.; "Use of Quasi-Orthogonals for Calculating Flow Distributions in the Meridional Plane of a Turbomachine," National Aeronautics and Space Administration Report TND-2546, December, 1964.

6. "Standard Values of Atmospheric Absorption as a Function of Temperature and Humidity for Use in Evaluating Aircraft Flyover Noise," S.A.E. ARP 866, August, 1964.

7. "Method of Calculating the Attenuation of Aircraft Ground to Ground Noise Propagation during Takeoff and Landing," Society of Automotive Engineers, Inc., Aerospace Information Report 923, August, 1966.

8. Benzakein, M.J. et al; "Fan Compressor Noise Research," General Electric Company Report No. FAA-RD-71-85 I, March, 1972.

9. Simonson, M.R.; Smith, E.G.; Uhl, W.R.; "Analytical and Experimental Investigation of Flow Fields of Annular Jets With and Without Swirling Flow," General Electric Company, NASA CR-137536, June, 1974.

Table I-I. Turbine Inlet Gas Conditions For Preliminary Studies.

Turbine Inlet Airflow, lb/sec (kg/sec)	49.7 (22.5)
Turbine Inlet Total Pressure, psia (kN/m^2)	54.56 (376)
Turbine Inlet Total Pressure, °R (°K)	2060 (1144)
Inlet Fuel/Air Ratio	0.0227

Table I-II. Aerodynamic Design Point Parameters.

Total Pressure Ratio, P_{T2}/P_{T1}	1.25
Static Pressure Ratio, P_{S2}/P_0	1.032
Corrected Air Flow, lb/sec (kg/sec)	174.8 (79.2)
Efficiency, percent	73.7
Corrected Tip Speed, ft/sec (m/sec)	1060 (323)
Radius Ratio	0.554
Specific Flow, lb/sec ft^2 (kg/sec m^2)	35.2 (172)
Rotor Tip Relative Mach Number	1.134
Hub Work Coefficient, $2\Delta h/U_2^2$	1.11
Number of Blades	42
Aspect Ratio of Blade	2.4
Rotor Tip Solidity	1.127
Corrected RPM	6742
Average Exit Swirl Angle, Deg.	27.0
Corrected Fan Stream Only Lift, lb (N)	3750 (16,680)

Table I-III. LF336/A Turbine Design Parameters.

Inlet Total Temperature, °R (°K)	1711 (950)
Inlet Total Pressure, psia (kN/m^2)	31.84 (219.5)
Inlet Gas Flow, lb/sec	44.12 (20.01)
Total to Static Pressure Ratio	2.34
Total to Total Pressure Ratio	1.92
Turbine Exit Static Pressure, psia (kN/m^2)	13.62 (93.9)
Turbine Exit Total Pressure, psia (kN/m^2)	17.38 (119.8)
Speed, RPM	6048
Design Power, HP (kw)	3563 (2711)
Exit Axial Mach Number	0.551
Turbine Efficiency	0.818
Pitch Wheel Speed, ft/sec (m/sec)	1076 (328)
Stage Velocity Ratio	0.584
Stage Work Function	0.645
Turbine Tip Diameter, in. (m)	42.93 (1.090)
Turbine Hub Diameter, in. (m)	38.63 (0.981)
Bucket Length, in. (cm)	2.15 (5.46)
Annulus Area, $in.^2$ (m^2)	275 (25.55)
Admission Arc, Degrees	360
Turbine Exit Flow, lb/sec (kg/sec)	43.75 (19.84)
Diffuser Exit Total Temperature, °R (°K)	1480 (822)
Diffuser Exit Total Pressure, psia (kN/m^2)	17.00 (117.2)

Table I-IV. Estimated LF336/E Performance.

	Design Point	Mech Limit Speed
Fan Speed, percent	100	89.6
Fan Tip Speed, ft/sec (m/sec)	1060 (323.1)	950 (289.6)
Engine Speed, percent	97.5	94.0
Fan Net Thrust, lbs (N)	4050 (18,010)	3220 (14,320)
Fan Inlet Airflow, lb/sec (kg/sec)	172 (78.0)	153 (69.4)
Fan Pressure Ratio	1.25	1.196
Engine Discharge Airflow, lb/sec (kg/sec)	42.64 (19.34)	39.30 (17.83)
Engine Discharge Pressure, psia (kN/m^2)	32.69 (225.4)	28.9 (199.3)
Engine Discharge Temperature, °R (°K)	1637 (909)	1506 (837)

Table I-V. LF336/E Run Summary.

Run	Date	Duration	Max Fan RPM	Configuration
1	10-6-72	:11	2875	Unmodified
2	10-7-72	:17	4069	Unmodified
3	10-7-72	:15	4720	Unmodified
4	10-7-72	:18	5300	Unmodified, Aborted Because of Scroll Blanket Loosening
5	10-11-72	:18	5201	Turbine Throttling Ring
6	10-12-72	:23	5213	Turbine Throttling Ring, Ambient Base Vent
7	10-13-72	:24	5225	Turbine Throttling Ring, Fan Discharge Base Vent
8	10-14-72	:16	5200	Turbine Throttling Ring, Fan Discharge Base Vent, Fan Inlet Bellmouth
9	11-17-72	:08		Turbine Shroud and Throttling Ring Removed, Fan Inlet Bellmouth, Aborted Due to Loss of Stress Readout
10	11-18-72	:38	4220	Same as 9
11	12-11-72	:32	4866	Turbine Stream Stators, Fan Inlet Bellmouth
12	12-16-72	:25	4800	Turbine Stream Stators, Hub Afterbody, Fan Inlet Bellmouth
13	1-9-73	:39	4803	Turbine Stream Stators, Fan Inlet Bellmouth, Engine Inlet Suppressor
14	1-9-73	:23	5416	Same as 13
15	1-10-73	:30	6008	Same as 13
16	1-11-73	:53	6034	Turbine Stream Stators, No Fan Inlet Bellmouth, Aborted Because of Icing and Heavy Fog
17	1-11-73	:43	6019	Same as 16
18	1-18-73	1:22	6045	Turbine Stream Stators, Fan Inlet Bellmouth and Fan Inlet Suppressor

Total Fan Time = 8:35

Table I-VI. Fan Performance Based on Exhaust Traverse Data.
(At a Corrected Fan Speed of 5000 RPM)

Configuration	Fan Exhaust Airflow (lb/sec)	Fan Exhaust Airflow (kg/sec)	Fan Absolute Pressure Ratio	Fan Axial Pressure Ratio	Fan Stream Thrust (lbs)	Fan Stream Thrust (N)	Fan Rotor Power (HP)	Fan Rotor Power (kw)
Unmodified Fan	131	59.4	1.153	1.115	1800	8006	1050	799
Hub Vent and Turbine Throttling Ring Installed	126	57.2	1.157	1.122	1770	7873	1020	776
Hub Afterbody and Turbine Stators Installed	129	58.5	1.145	1.110	1830	8140	980	746
Turbine Stators Installed with Inlet Bellmouth	136	61.7	1.141	1.110	1850	8229	980	746
Clean Fan with Turbine Stators Installed	138	62.6	1.142	1.112	1830	8140	980	746
Fan with Inlet Suppressor and Turbine Stators Installed	138	62.6	1.147	1.117	1890	8407	980	746
Fan Design Estimates	125	56.7	Not Calculated	1.121	1780	7917	1010	769

Table I-VII. LF336 Lift Fan Configurations.

Fan	Test Number	Date	Vanes	Spacing Chords	Acoustic Splitter	Acoustic Treatment	Test Location
LF336/A	1	1-69	45	.15	No	No	EFTC
LF336/B	1	2-69	45	2	No	No	EFTC
LF336/C	1	12-69	45	1	No	No	EFTC
LF336/C	11	6-70	90/Leaned	2	Yes	Yes	EFTC
LF336/E	16,17	1-73	0	∞	No	No	EFTC
LF336/E	1	3-73	0	∞	No	No	NASA (Ames)

Table II-I. Significant Parameters For Serrated Cascade Test Airfoils.

Chord	2.0 inches* (5.08 cm)
Aspect Ratio	2.0
Solidity	1.439
Blade Leading Edge Angle	54.9°
Blade Trailing Edge Angle	36.7°
Design Incidence Angle	+2.1°
Design Deviation Angle	4.2°
Blade Maximum Thickness	5.5%
Blade Leading Edge Radius	0.75%

*Includes 0.152 inch (0.386 cm) leading edge extension for serrations

Table II-II. Summary of Serration Geometry.

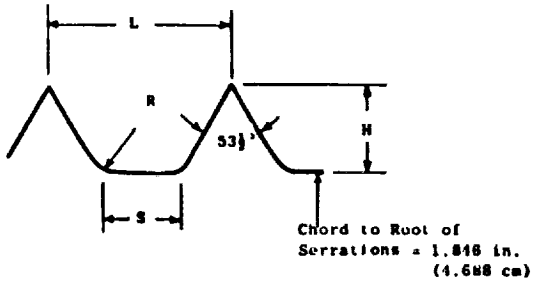

	H		H/C	S		L		R			
Serration	(in)	(cm)	(in)	(in)	(cm)	(in)	(cm)	(in)	(cm)	H/S	L/H
BL1	0.116	0.295	-	-	-	-	-	-	-	-	-
SR1	0.116	0.295	0.063	0.036	0.091	0.153	0.389	0.024	0.061	3.2	1.32
SR2	0.077	0.196	0.042	0.024	0.061	0.102	0.259	0.016	0.041	3.2	1.32
SR3	0.116	0.295	0.063	0.076	0.193	0.193	0.490	0.024	0.061	1.5	1.66
SR4	0.152	0.386	0.083	0.100	0.254	0.253	0.643	0.031	0.079	1.5	1.66
SR5	0.077	0.196	0.042	0.072	0.183	0.150	0.381	0.016	0.041	1.1	1.95
SR6	0.116	0.295	0.063	0.076	0.193	0.193	0.490	0.061	0.155	1.5	1.66
BL2	-	-	-	-	-	-	-	-	-	-	-

Table II-III. Estimated Aerodynamic Design Point Operating Conditions For Serrated Airfoil Sections.

Inlet Mach Number	0.97
Inlet Air Angle	57°
Diffusion Factor	0.36
Static Pressure Rise Coefficient	0.33
Total Pressure Loss Coefficient	0.045
Blade Incidence Angle	+2.1°
Blade Deviation Angle	4.2°

Table III-I. Base Pressure Model Descriptions.

Model	Radius Ratio	Flow* Angle	Outer Flowpath Exit Diameter In. (cm)		Inner Flowpath Exit Diameter In. (cm)	
1	0.4	10	3.116	7.915	1.246	3.165
2	0.4	0	3.116	7.915	1.246	3.165
3	0.4	-10	3.116	7.915	1.246	3.165
4	0.4	-20	3.116	7.915	1.206	3.165
5	0.55	10	3.420	8.687	1.879	4.773
6	0.55	0	3.420	8.687	1.880	4.773
7	0.55	-10	3.420	8.687	1.878	4.773
8	0.55	-20	3.420	8.687	1.879	4.773
9	0.70	10	4.000	10.160	2.795	7.099
10	0.70	0	4.000	10.160	2.803	7.099
E**	0.638		3.710	8.052	2.366	6.010

*Radially out Designated Positive Angle
**Scaled From LF336/E Lift Fan

Table III-II. Comparison of Statorless Fan Designs.

	Original LF336/E Estimates	LF336/E Tests	Revised LF336/E Estimates	New Fan Design	LF336/A Fan
Pressure Ratio	1.30	1.28	1.28	1.275	1.30
Tip Speed, ft/sec (m/sec)	1060	1060	1060	1125	950
Exit Radius Ratio	0.64	0.64	0.64	0.40	0.55
Flow/Exit Tip Area, lb/sec ft^2 (kg/sec m^2)	25.7	24.2*	26.6	40.8	33.86
Thrust/Exit Tip Area, lb/ft^2 (kN/m^2)	473	340*	372	670	687
Thrust/Power, lb/HP (kN/kw)	1.15	---	0.93	1.03	1.21
Inlet Flow/Area, lb/sec ft^2 (kg/sec^2 m^2)	35.2	33.1	36.4	35.3	40.0

*Based on Test Measurements Corrected to Design Speed.

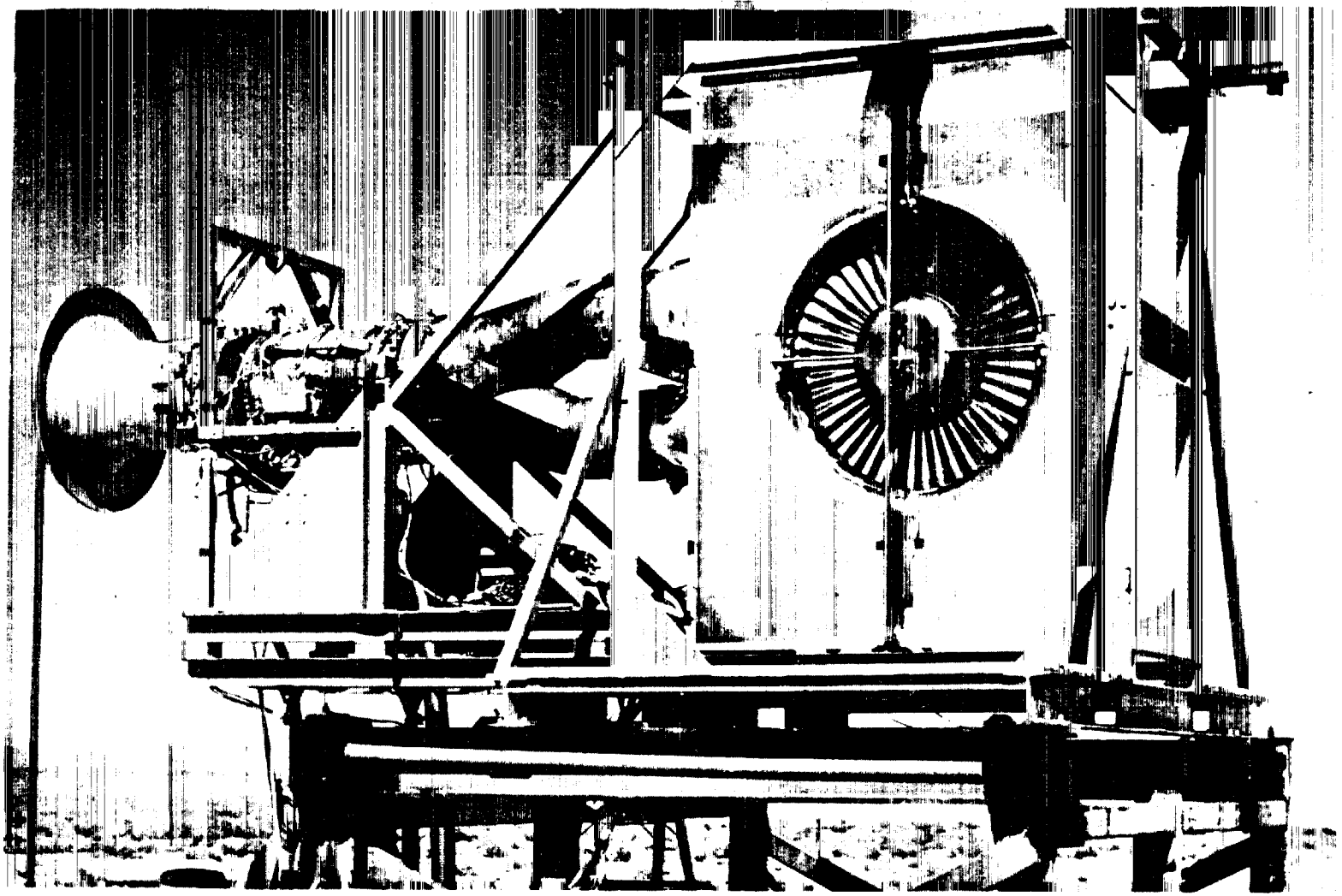

Figure I-1 LF336/A Fan Installed in Test Stand

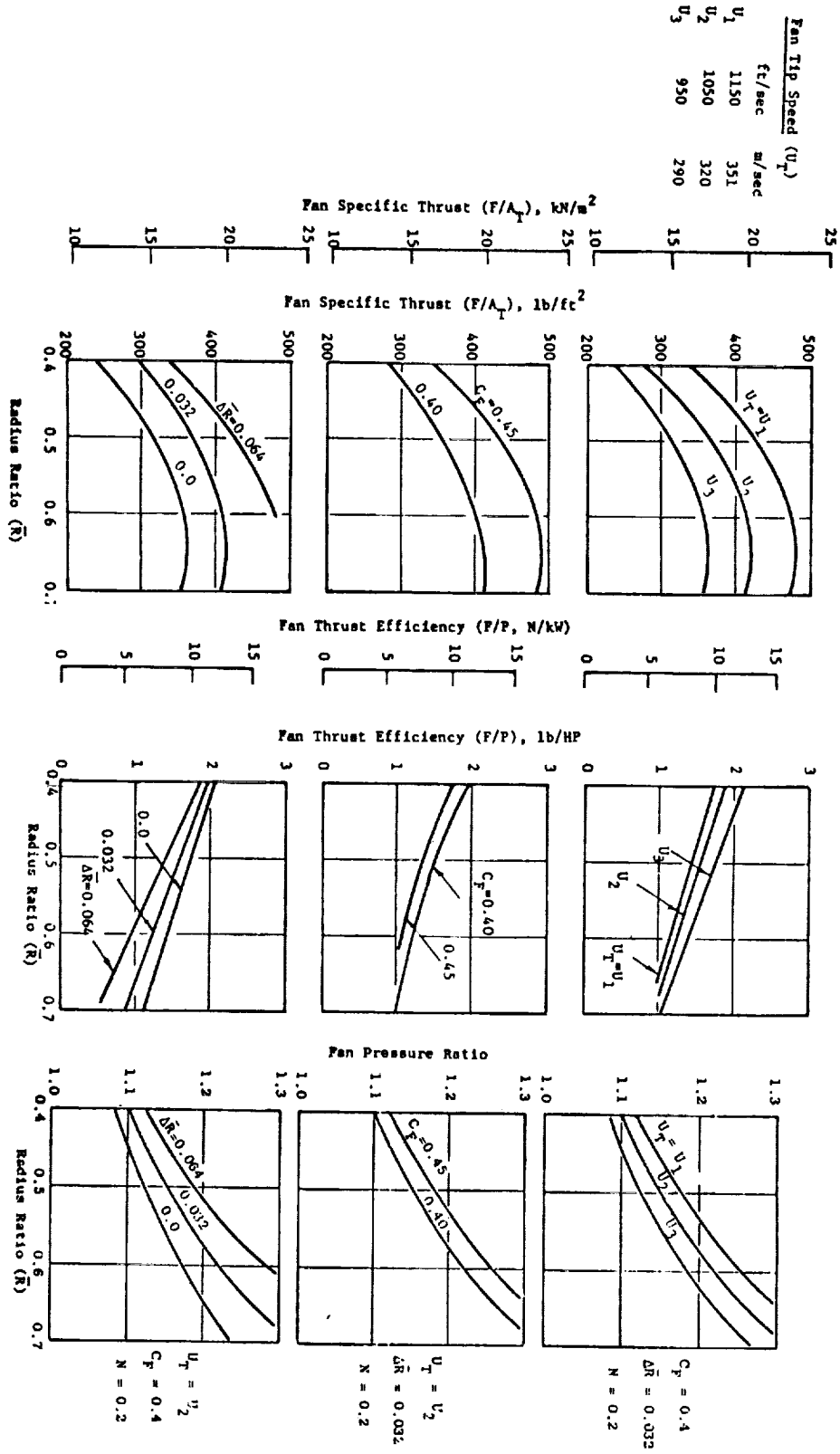

Figure I-2 Statorless Fan Parametric Data

Fan Tip Speed (U_T)	ft/sec	m/sec
U_1	1150	351
U_2	1050	320
U_3	950	290

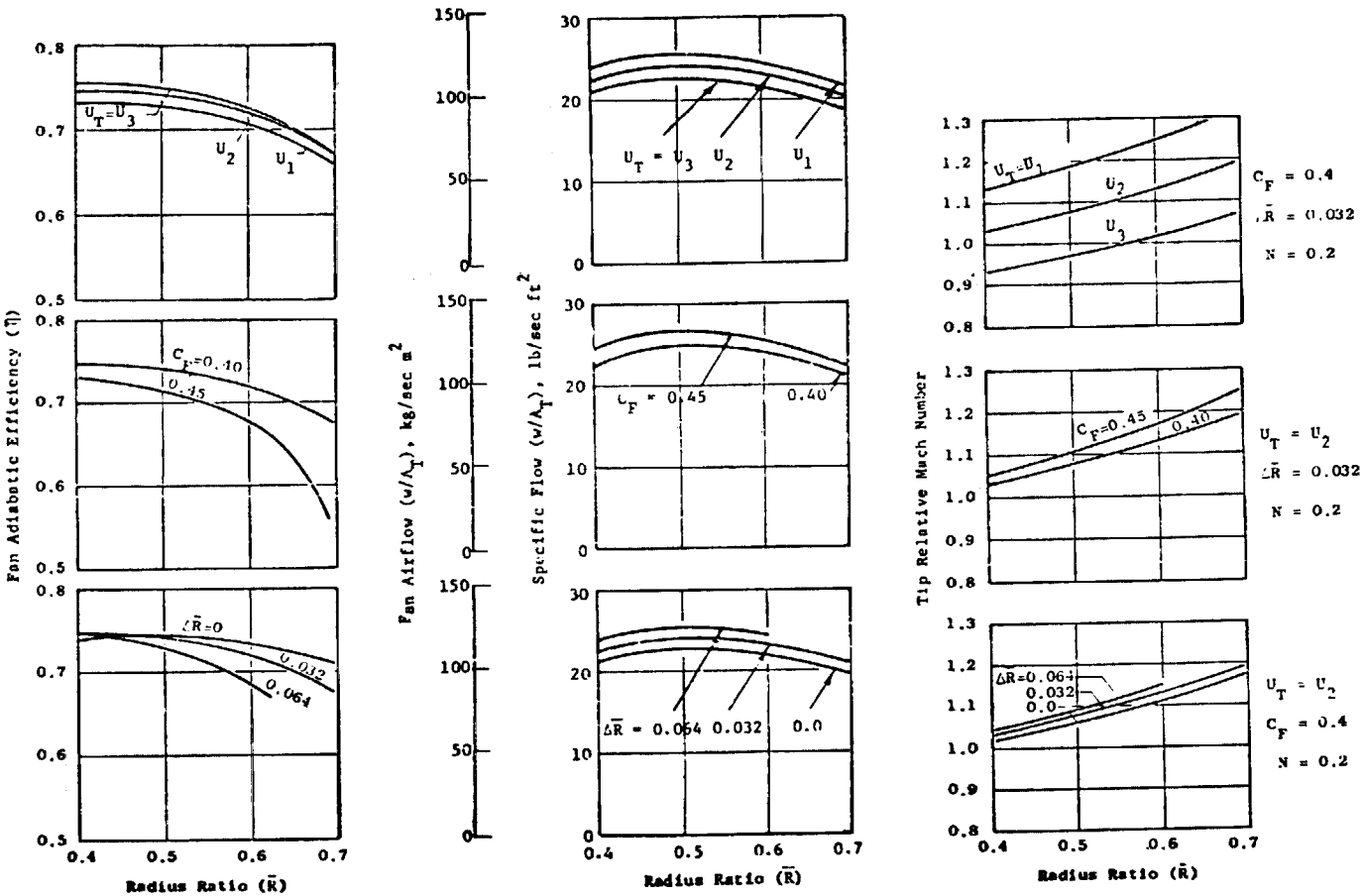

Figure I-2 Statorless Fan Parametric Data (Continued)

Fan Tip Speed (U_T)	ft/sec	m/sec
U_1	1150	351
U_2	1050	320
U_3	950	290

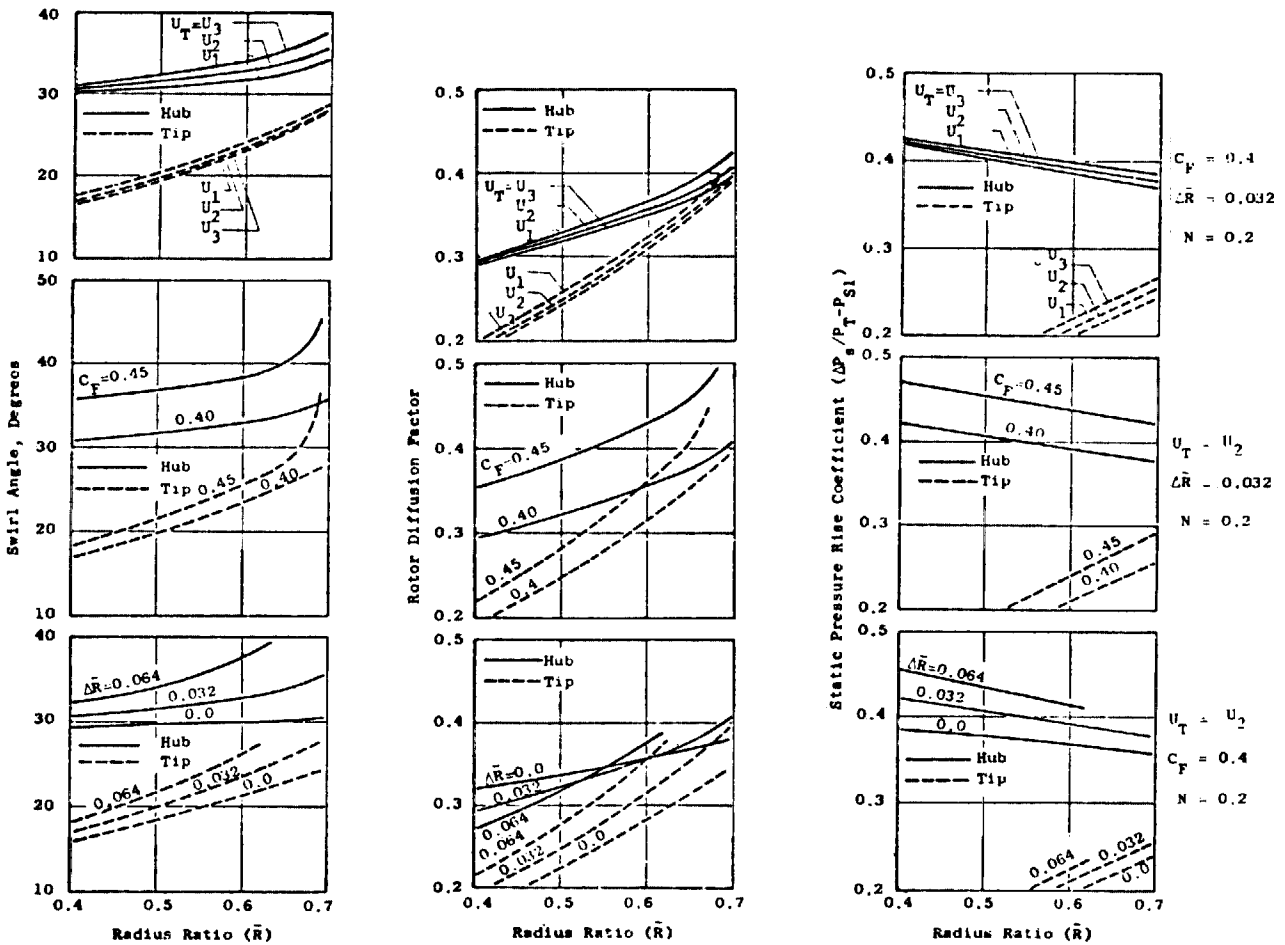

Figure I-2 Statorless Fan Parametric Data (Concluded)

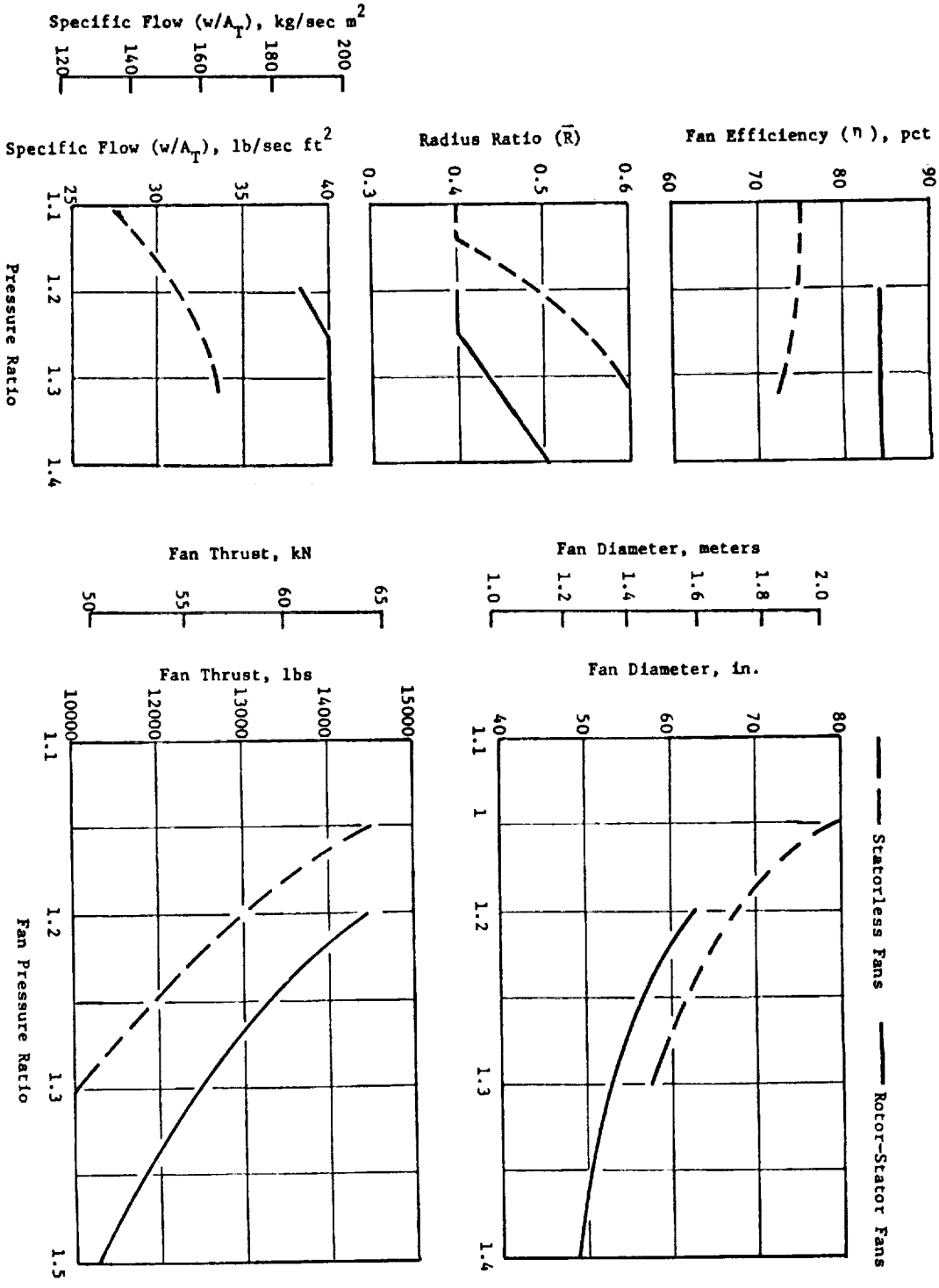

Figure I-3 Statorless Fan Design Data

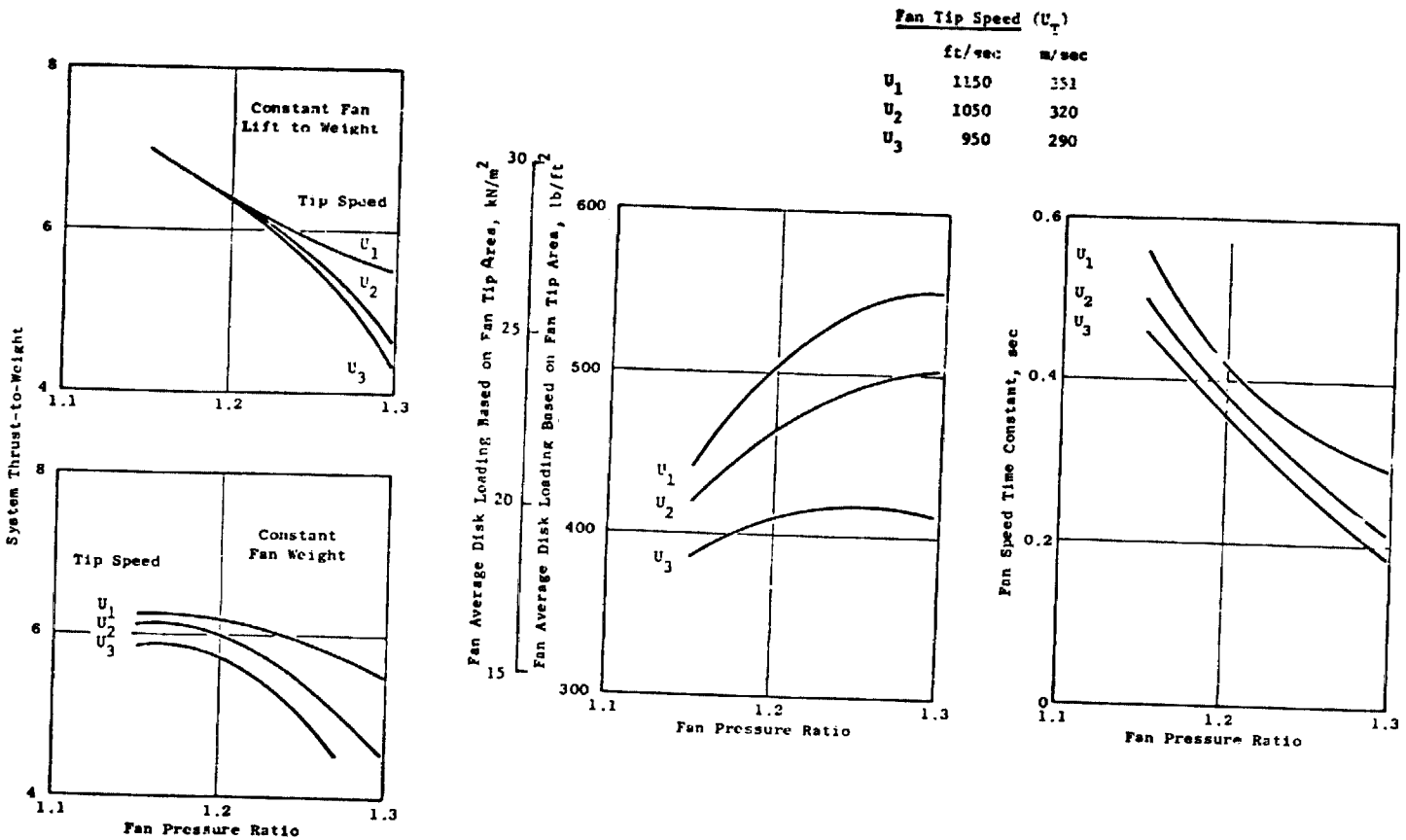

Figure I-4 Statorless Fan Optimization Parameters

	Fan Tip Speed	
	ft/sec	m/sec
U_1	1150	351
U_2	1050	320
U_3	950	290

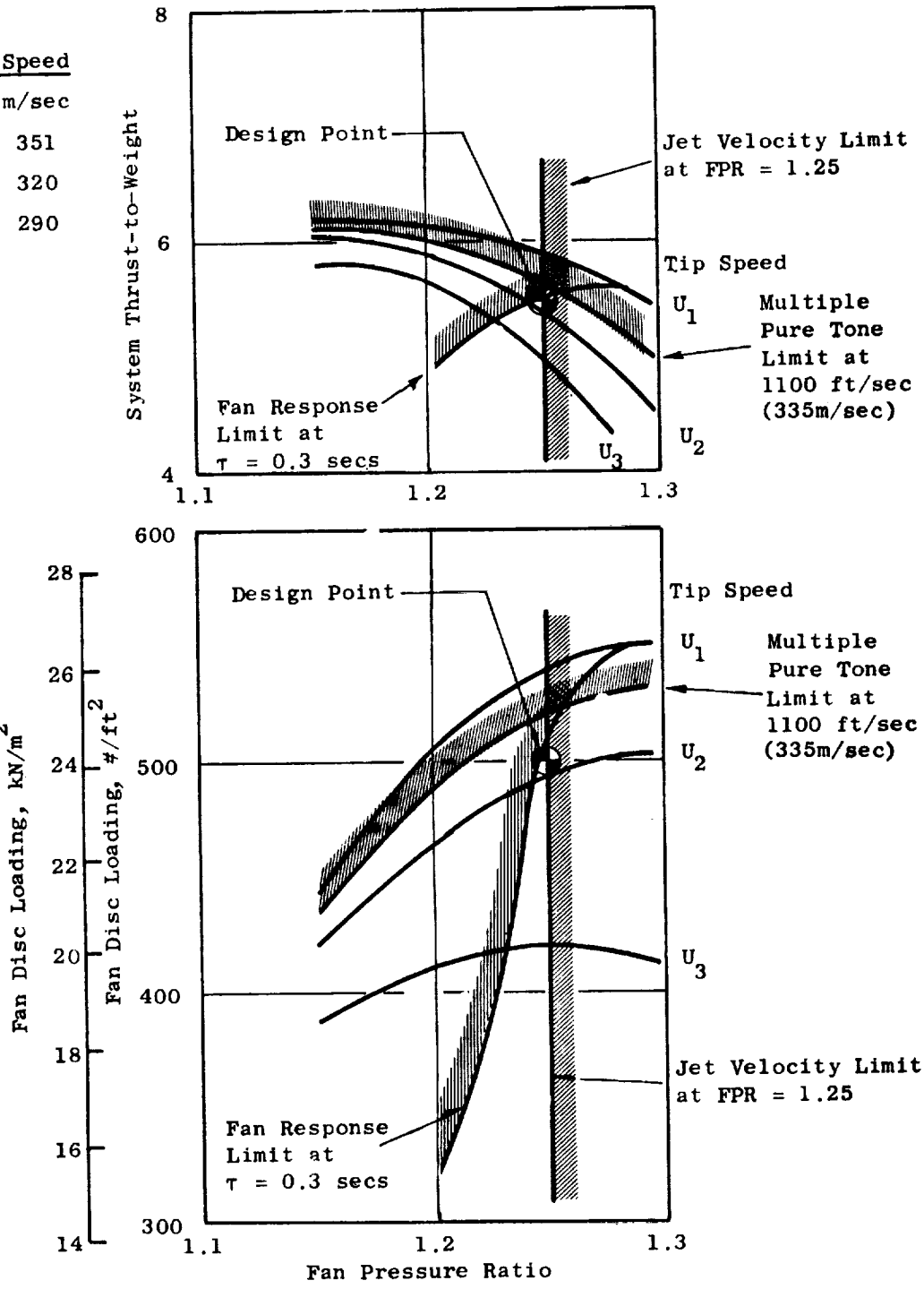

Figure I-5 Boundaries Established by Design Criteria

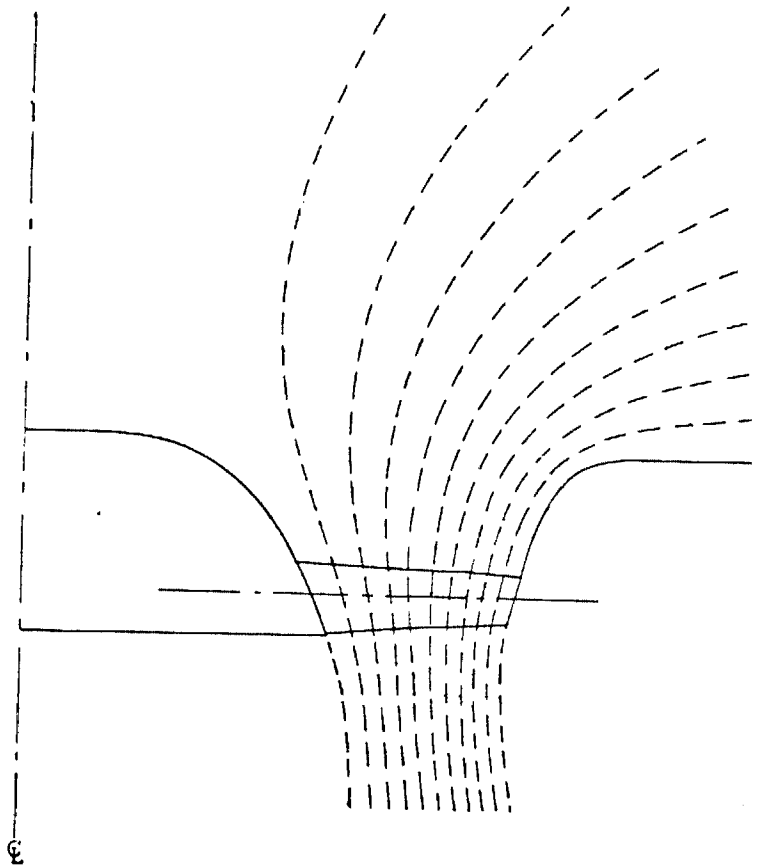

Figure I-6 Flowpath and Computed Streamlines

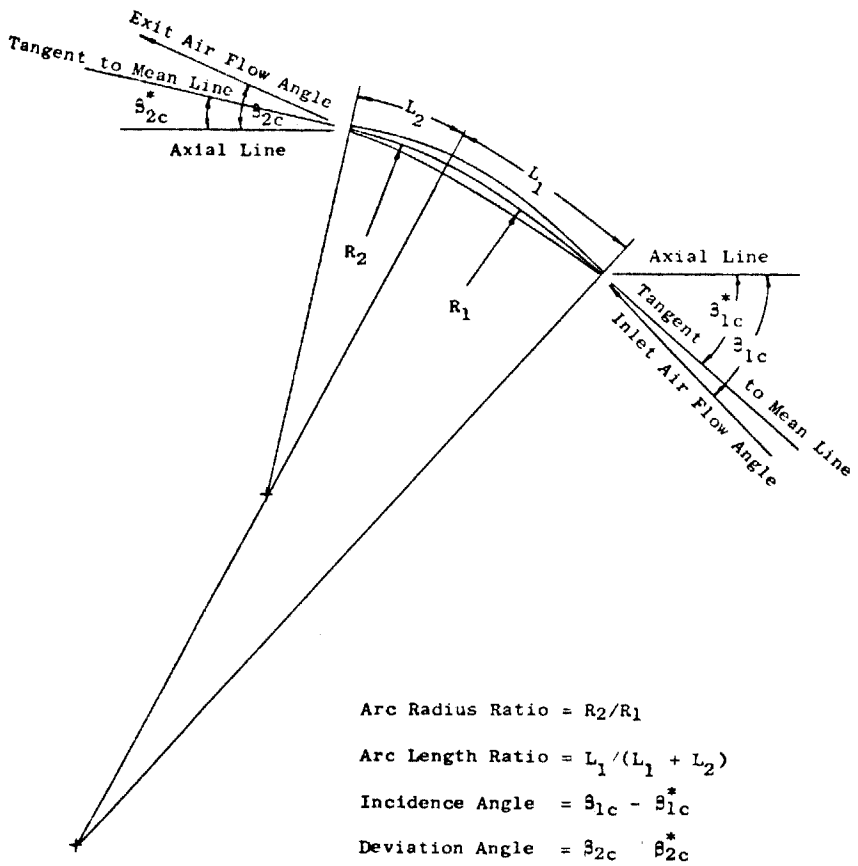

Figure I-7 Airfoil Definition

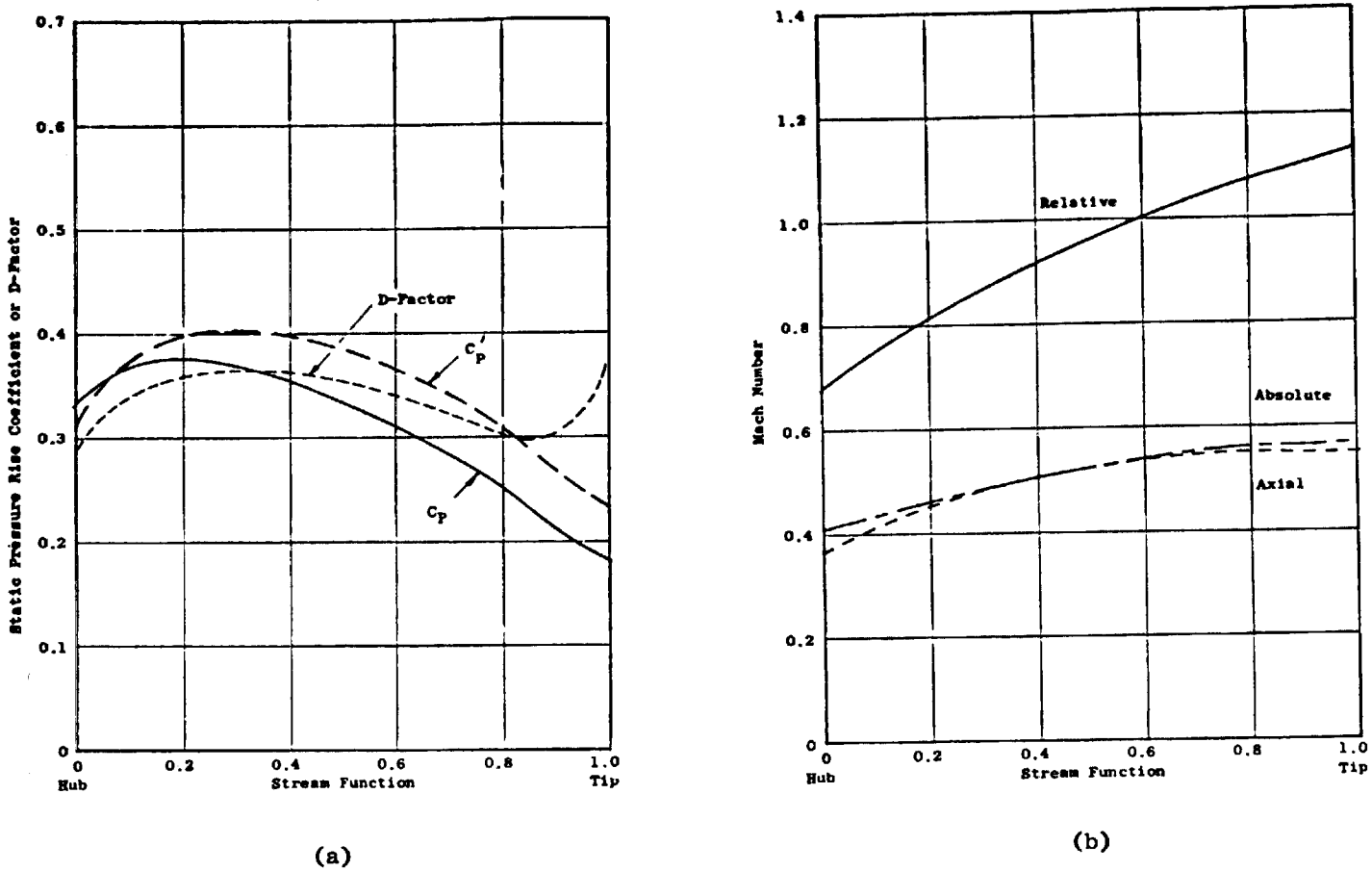

Figure I-8 Statorless Fan Aerodynamic Design Parameters

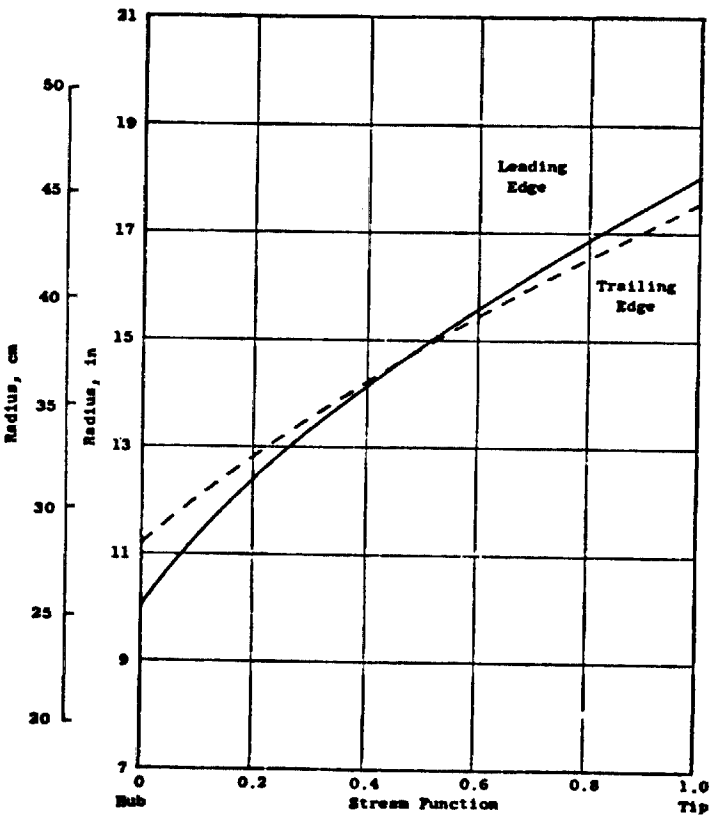

(c)

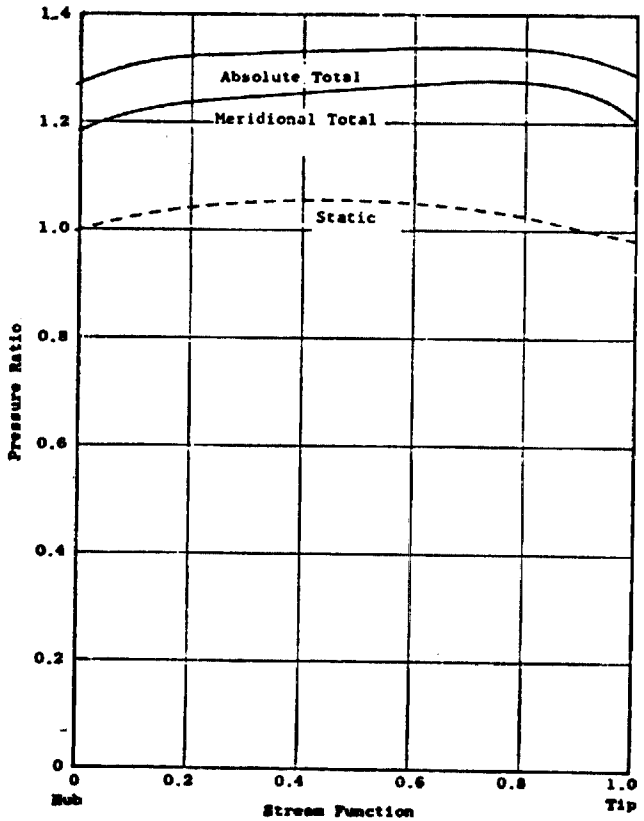

(d)

Figure I-8 Statorless Fan Aerodynamic Design Parameters (Continued)

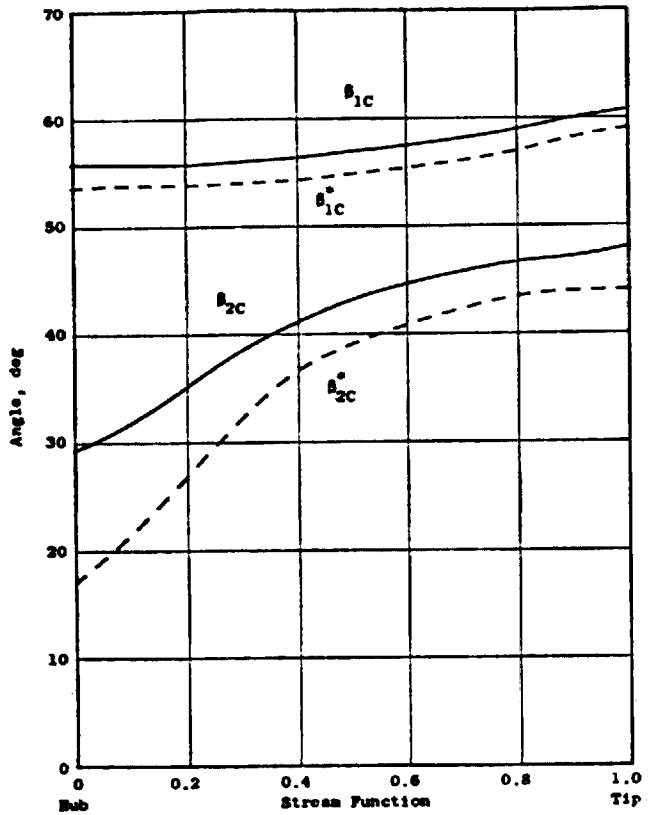

(e)

Figure I-8 Statorless Fan Aerodynamic Design Parameters (Concluded)

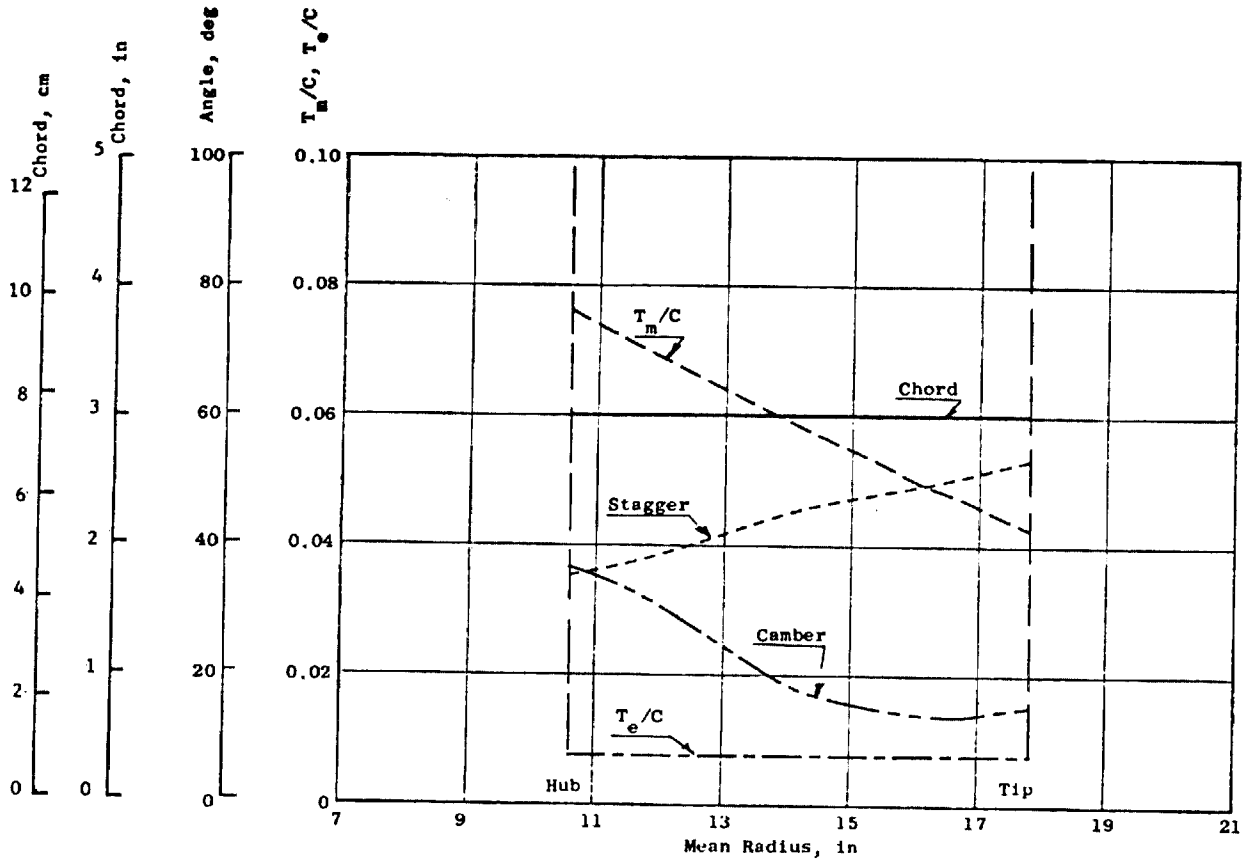

Figure I-9 Blade Geometric Parameters

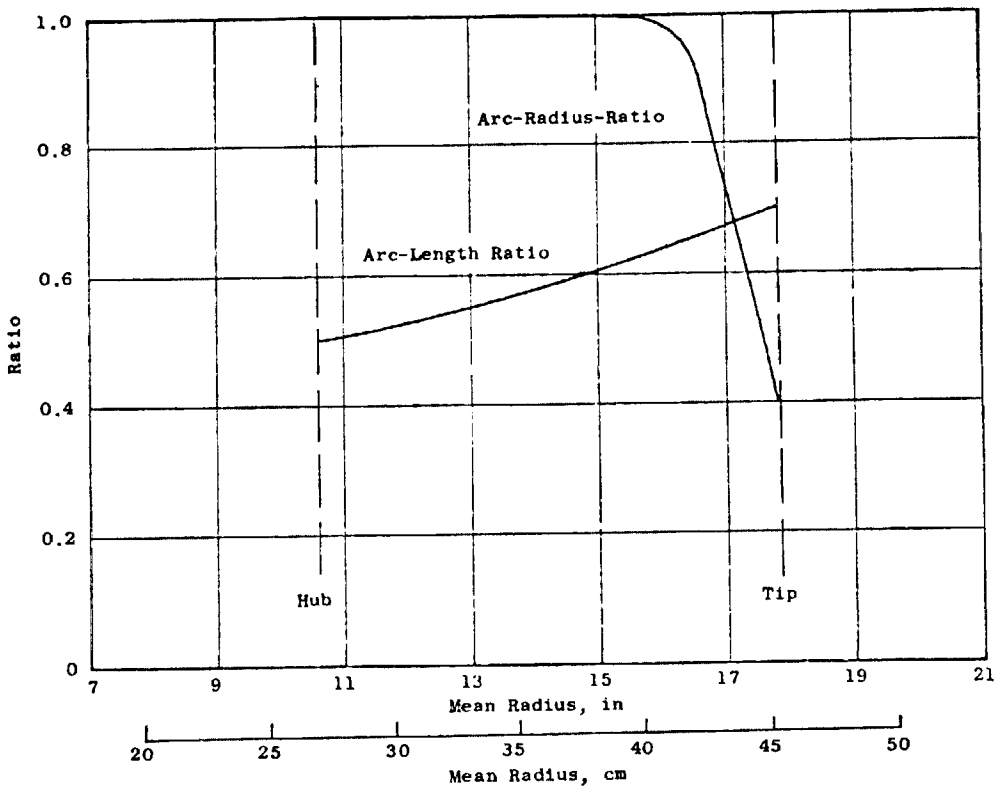

Figure I-9 Blade Geometric Parameters (Continued)

Figure I-9 Blade Geometric Parameters (Concluded)

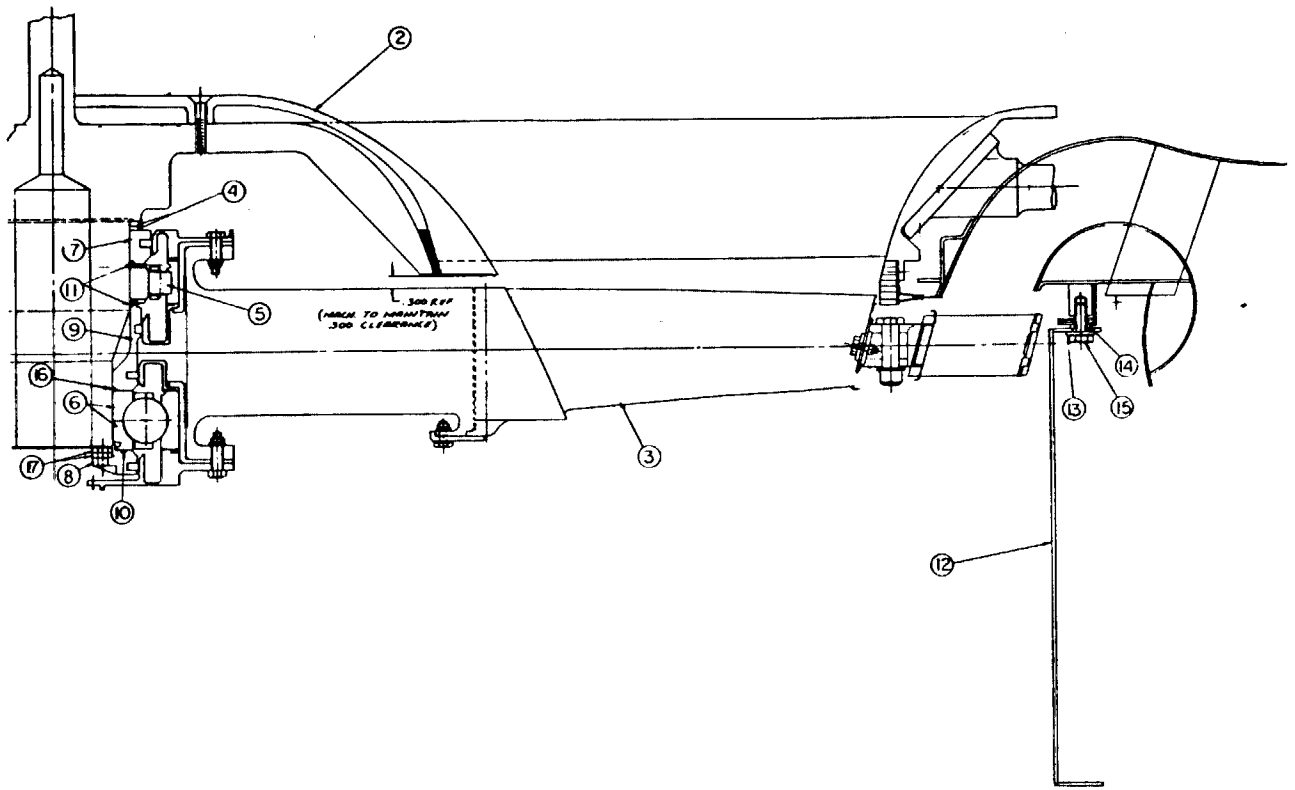

Figure I-10 LF336/E Fan Assembly Drawing

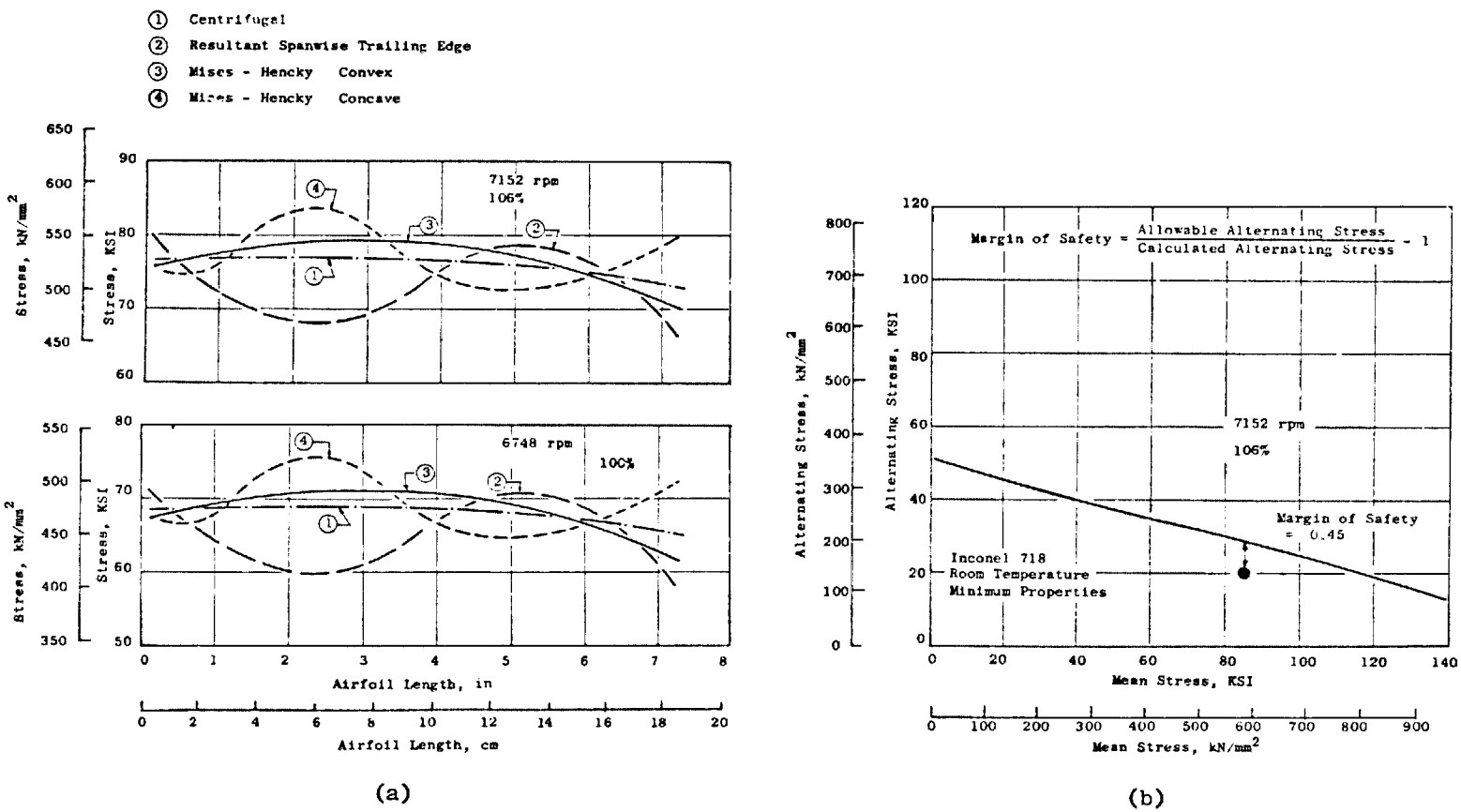

Figure I-11 Airfoil Stresses

7152 RPM (106%)

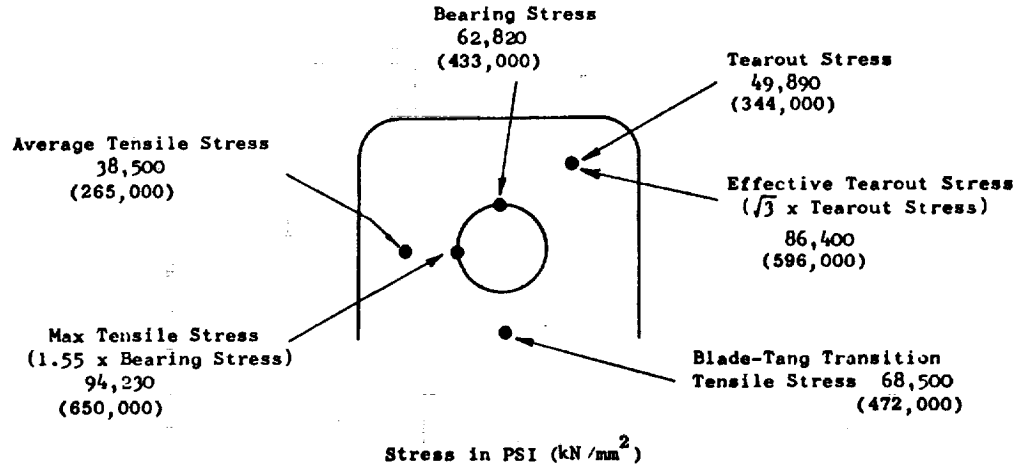

(a)

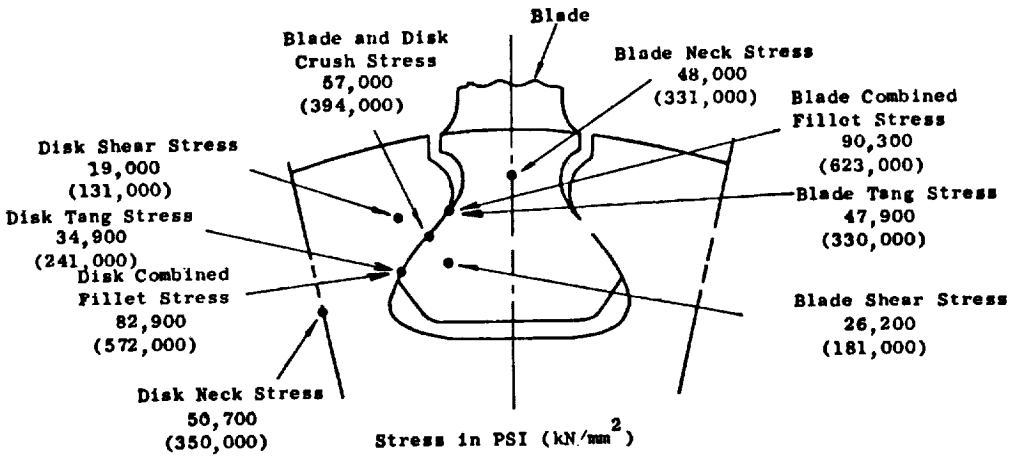

(b)

Figure I-12 Tip Tang and Dovetail Stresses

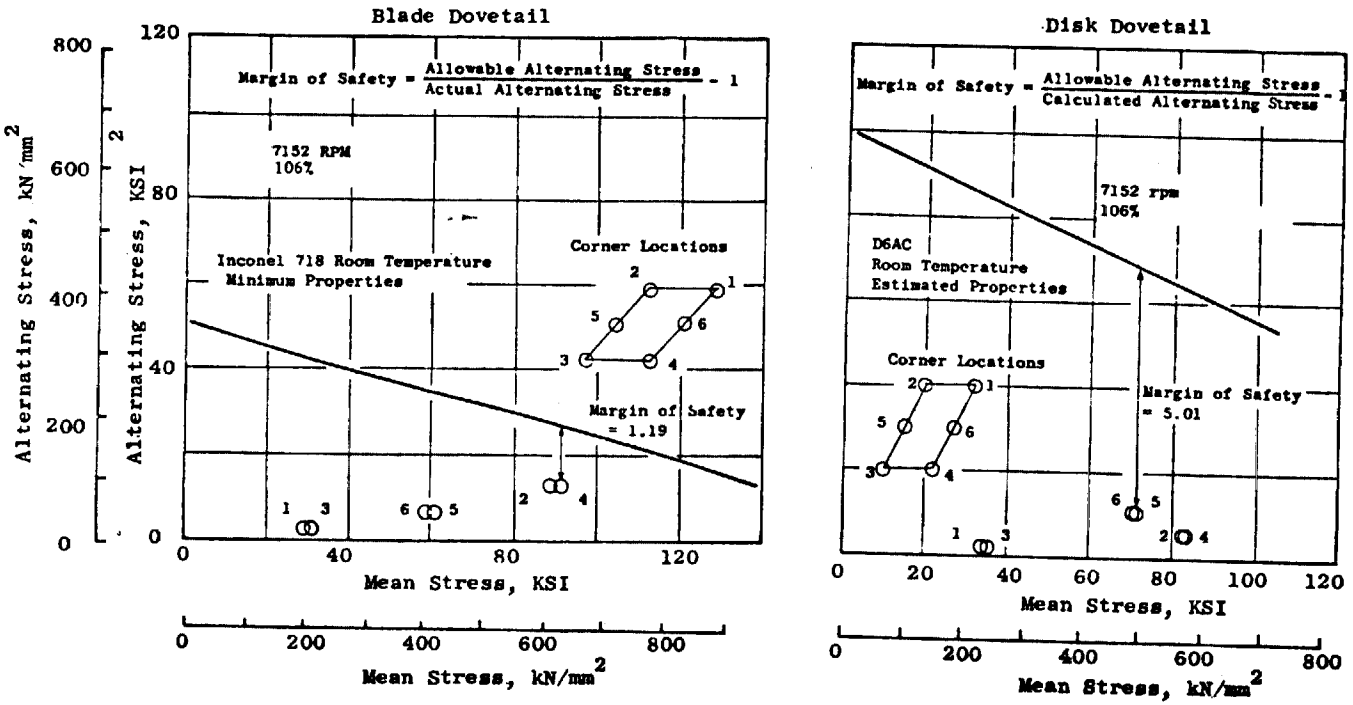

Figure I-13 Dovetail Stress Range Diagram

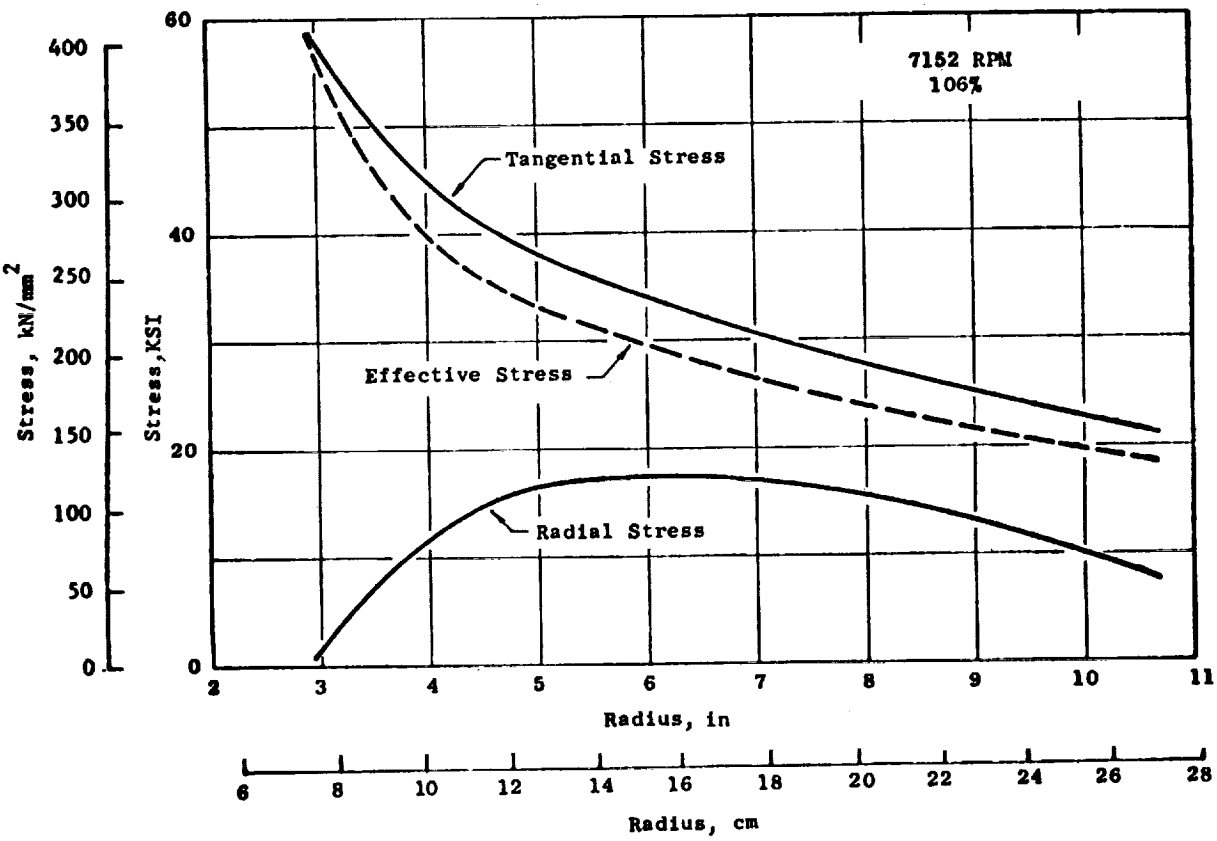

Figure I-14 Disk Stresses

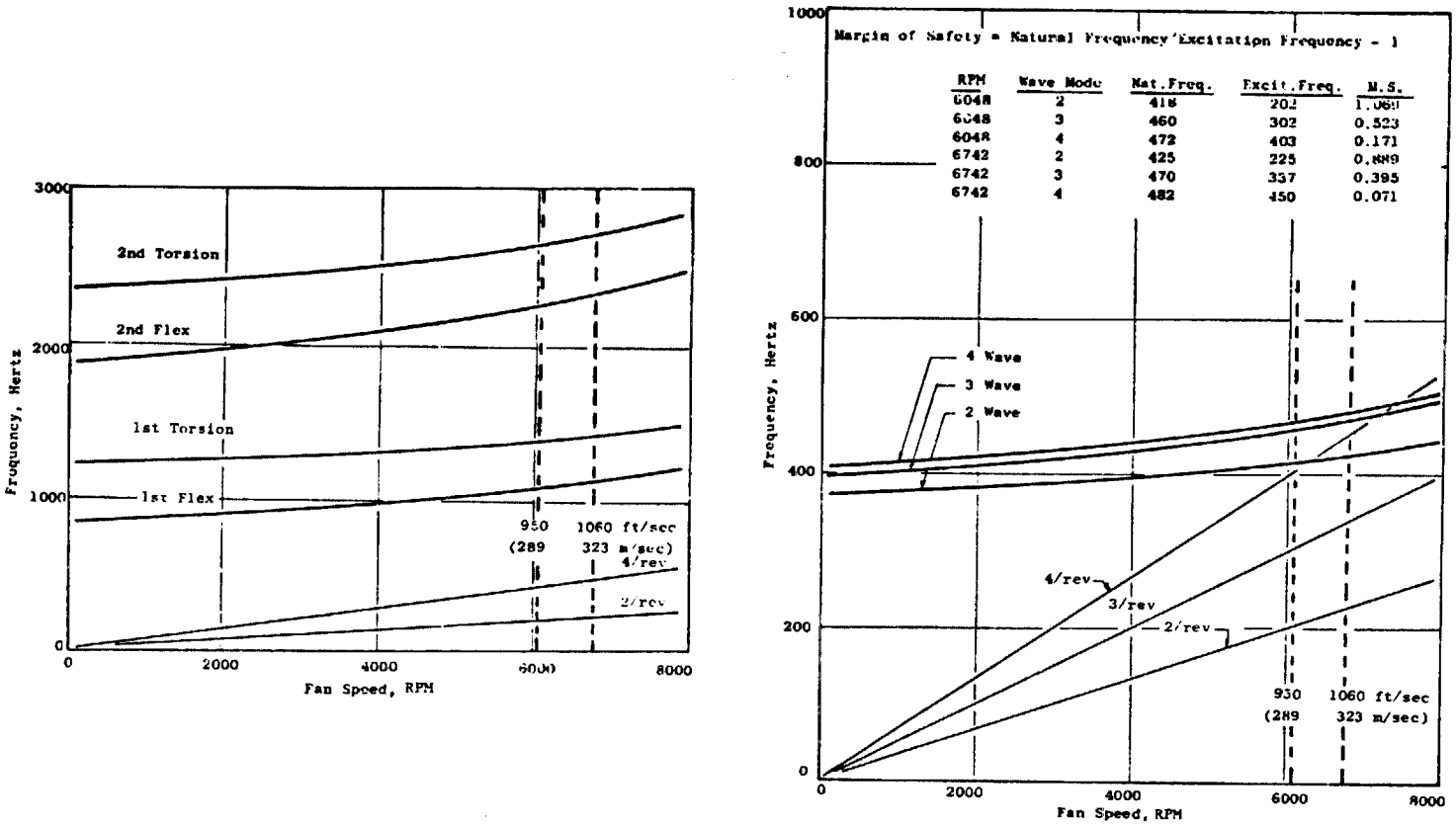

Figure I-15 Rotor Frequencies

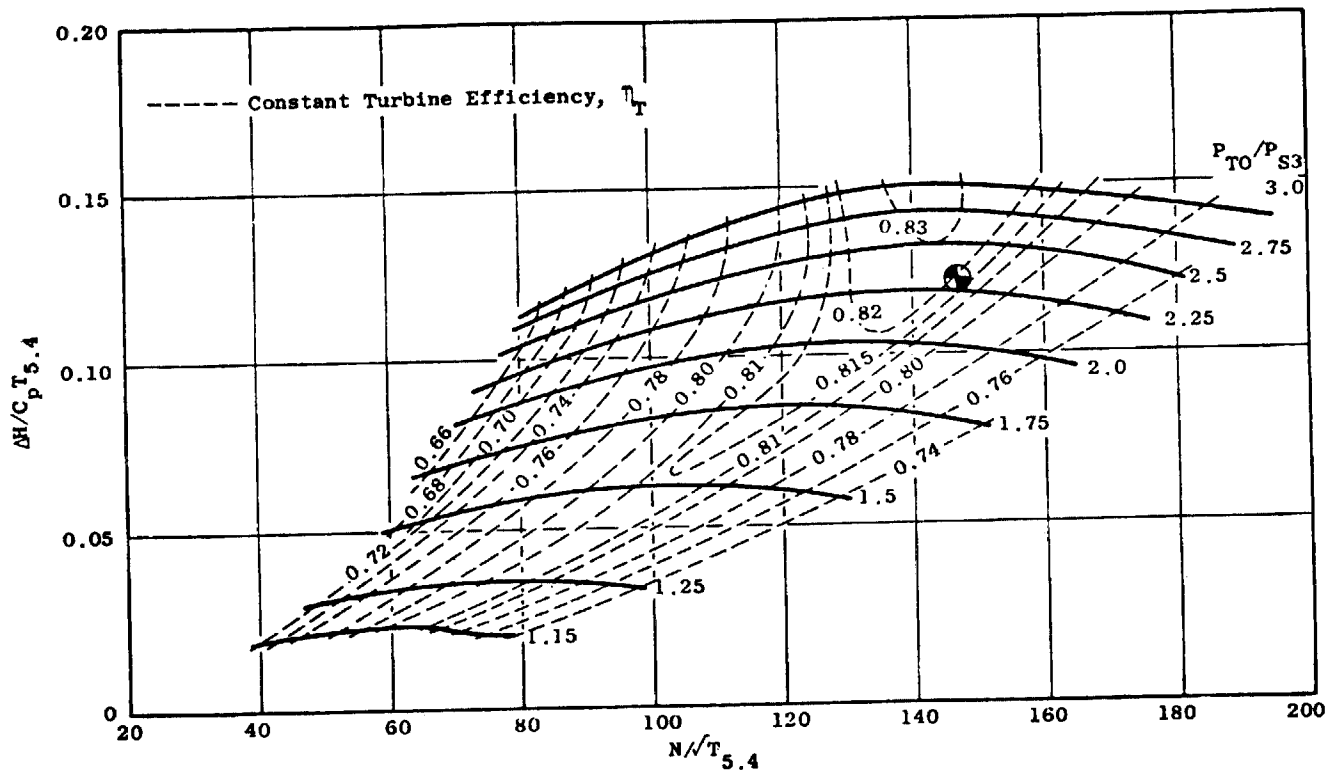

Figure I-16 Estimated Turbine Map

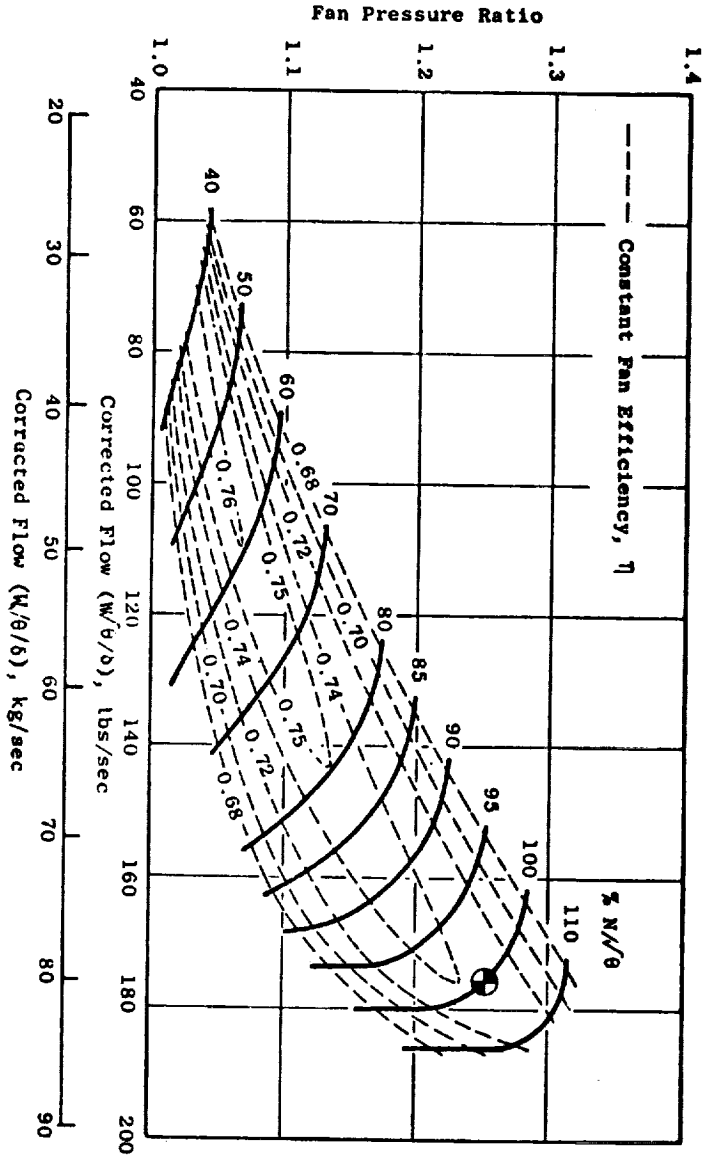

Figure I-17 Estimated Fan Map

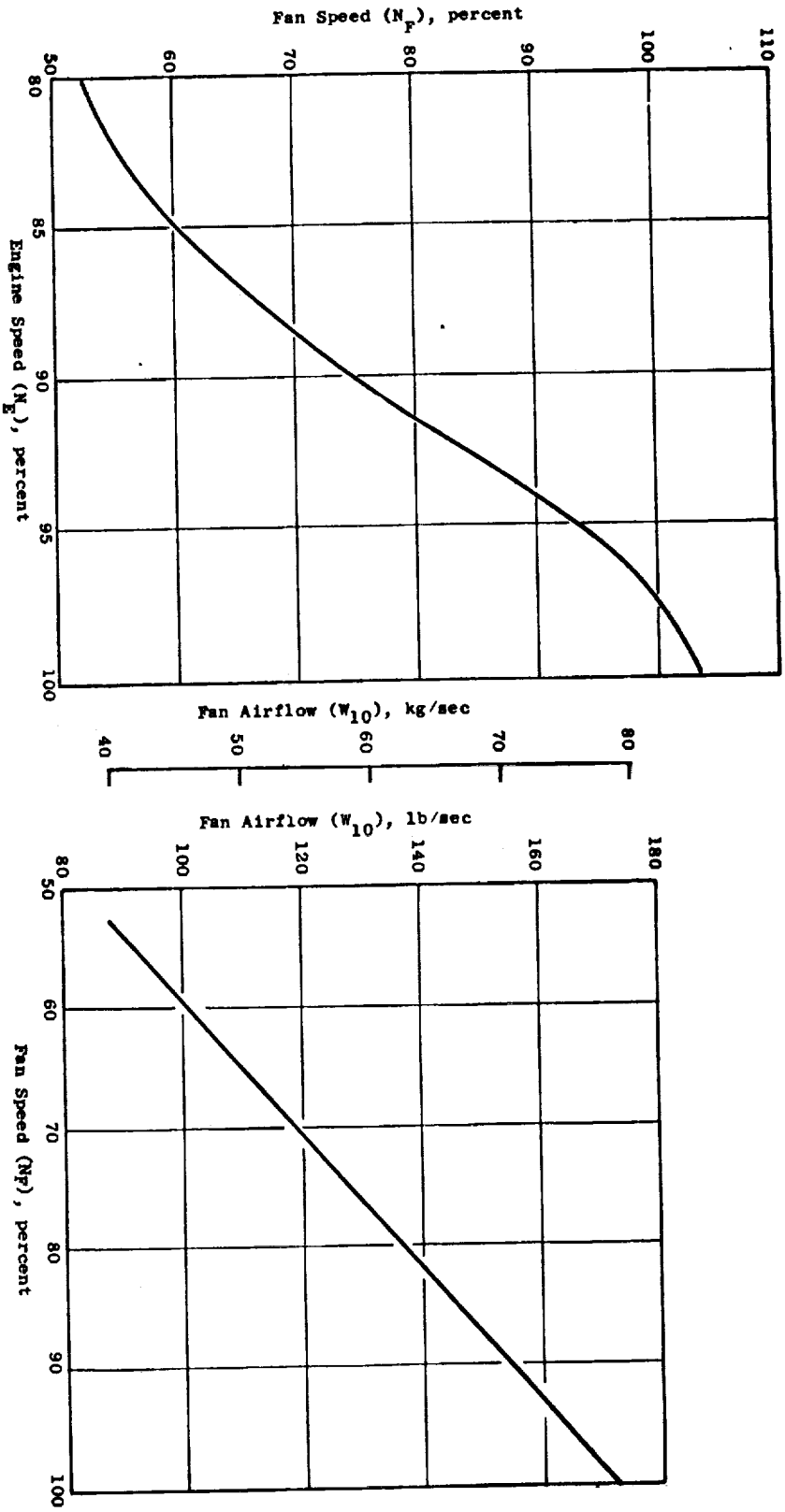

Figure I-18 Estimated LF336/E Performance, Sea Level, Static, Standard Day

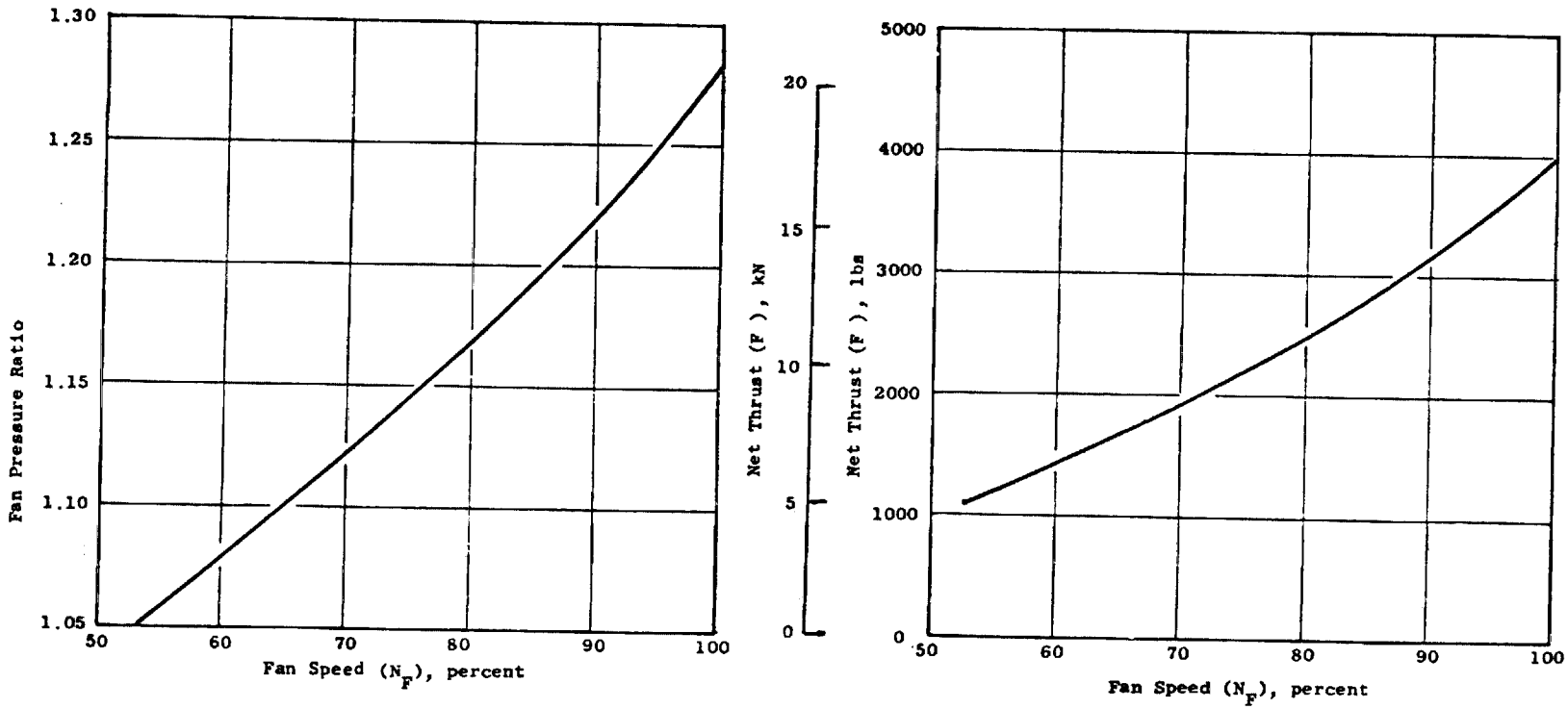

Figure I-18 Estimated LF336/E Performance, Sea Level, Static, Standard Day (Continued)

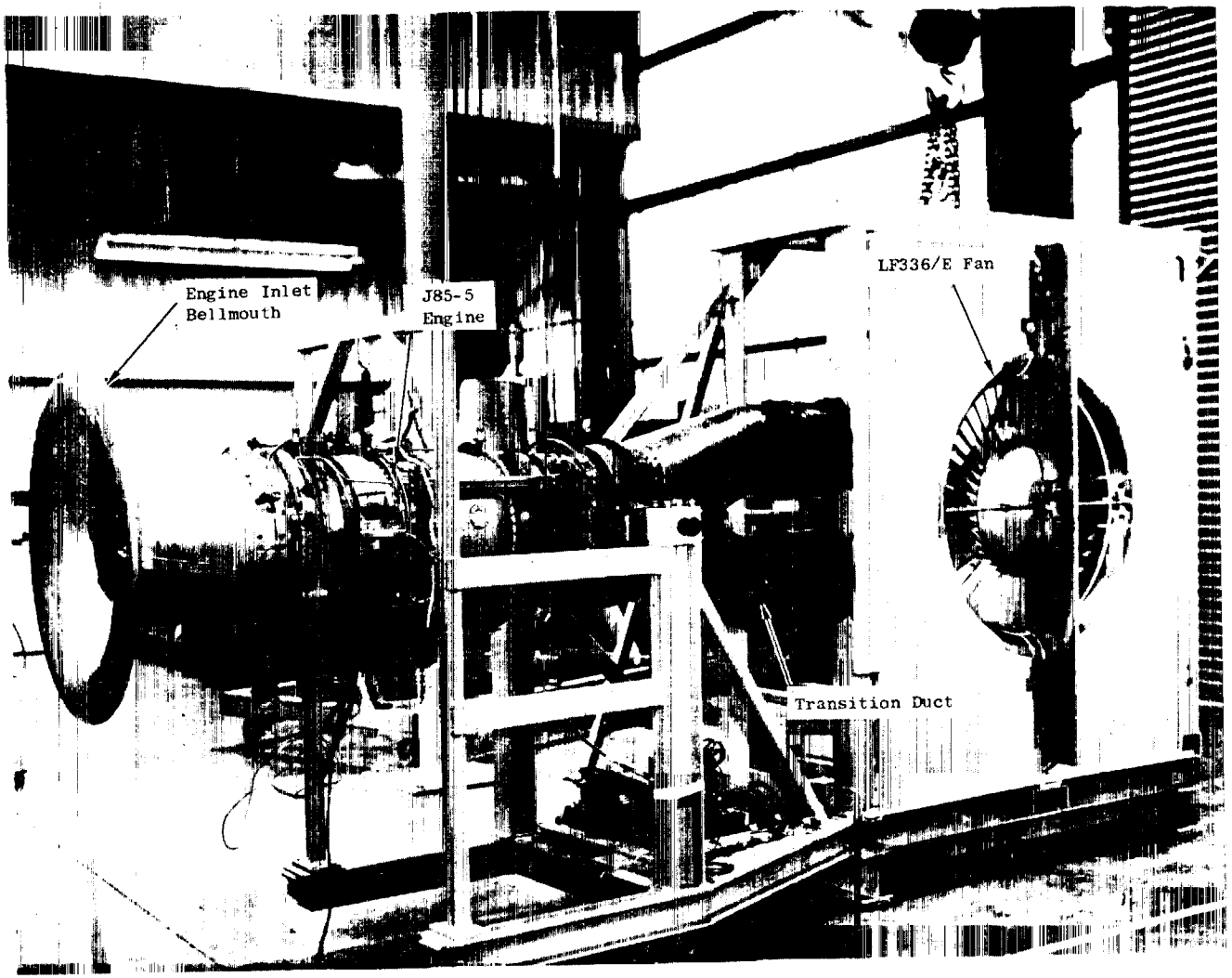

Figure I-19 LF336/E Statorless Fan Installed in Test Stand

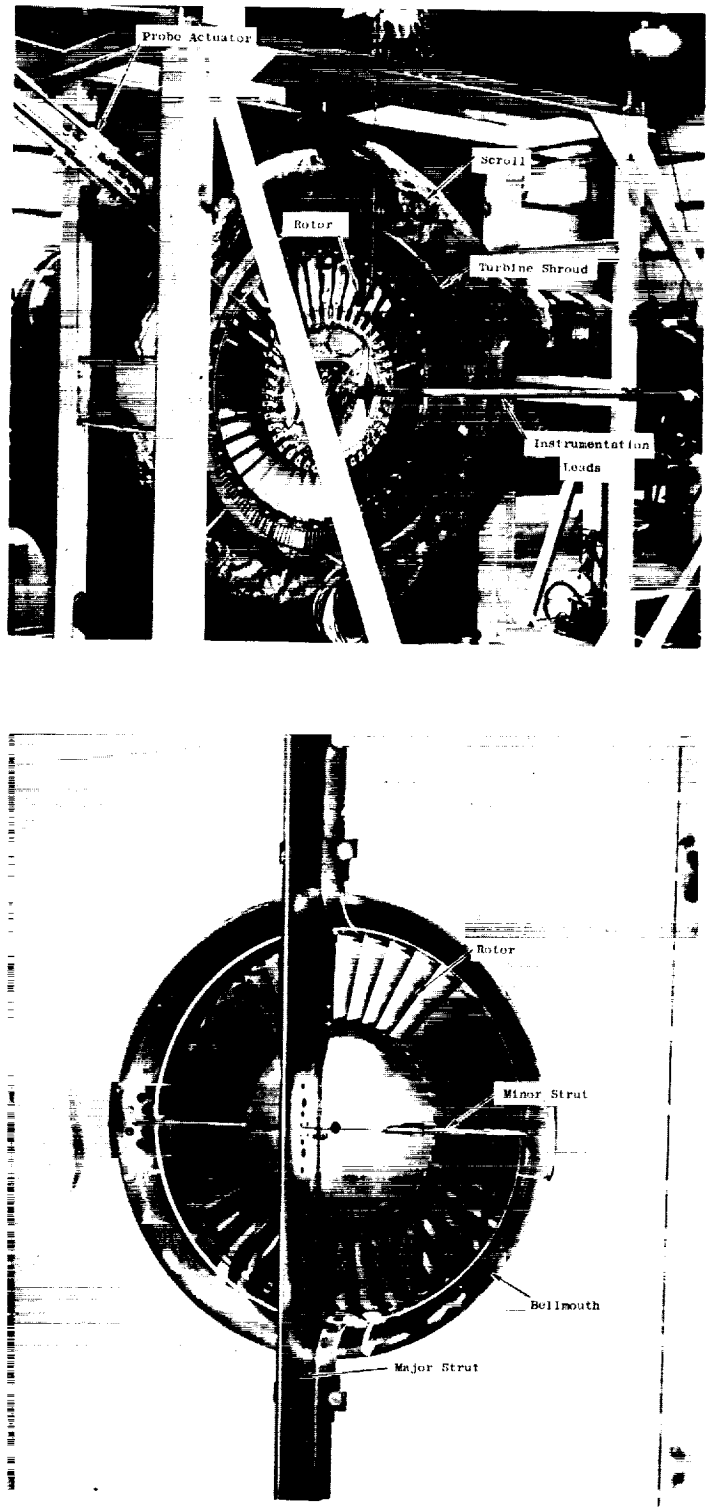

Figure I-20 LF336/E Showing Inlet and Exhaust Geometry

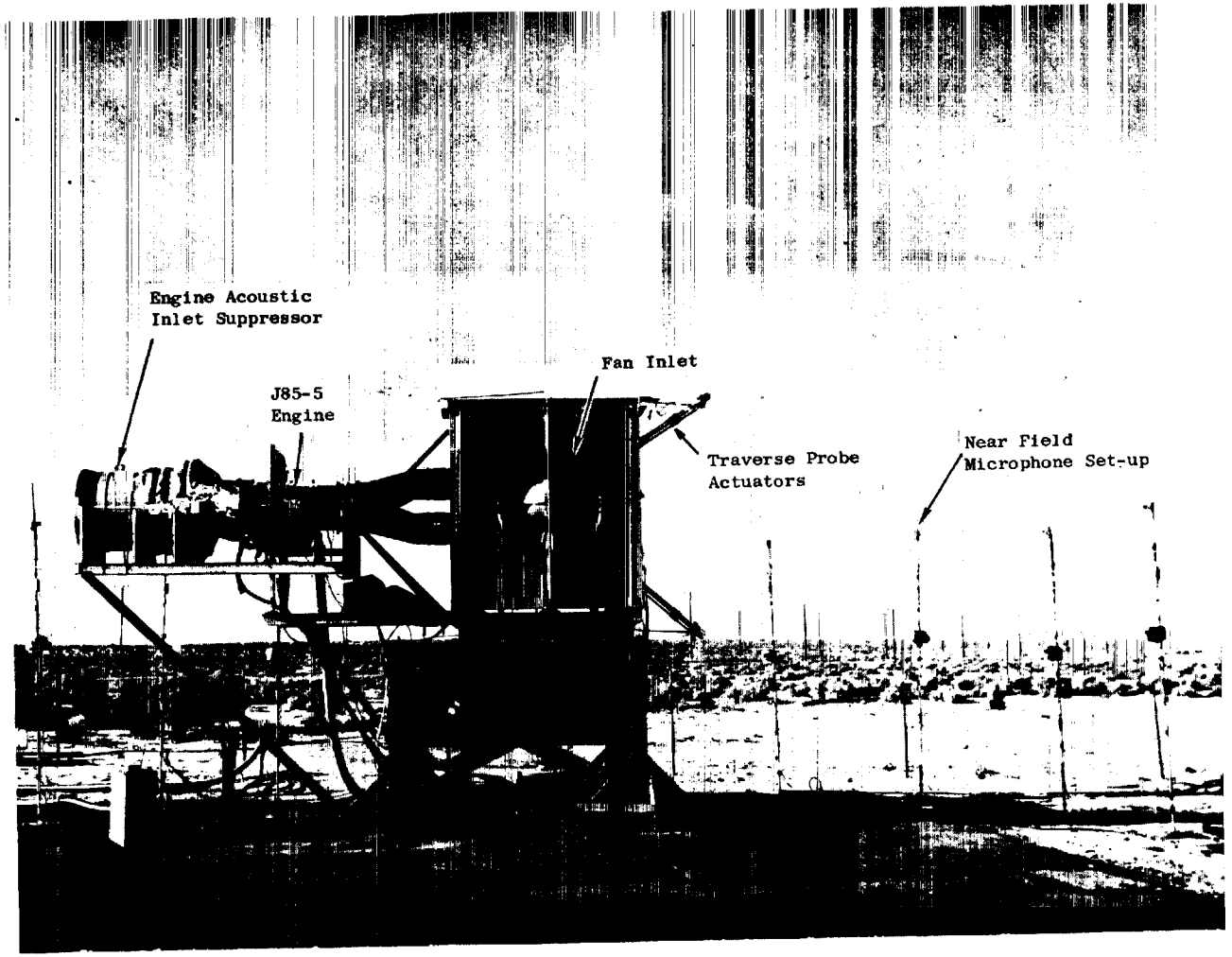

Figure I-21 LF336/E Installed on the Thrust Stand at the Test Site

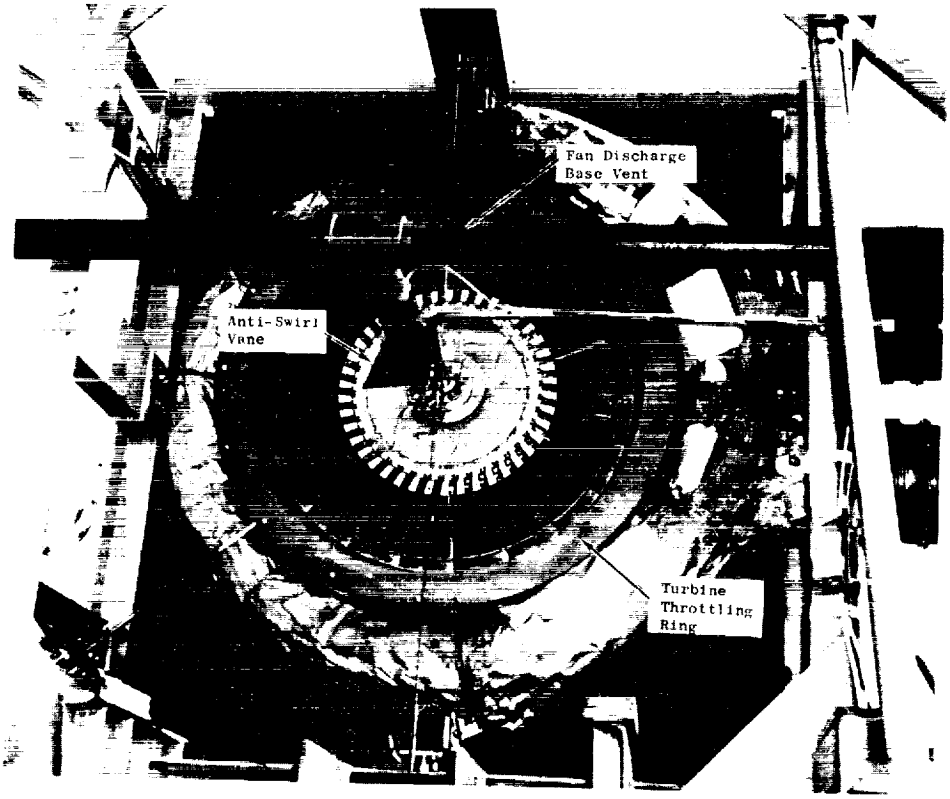

Figure I-22 Fan Exhaust Showing Installation of Base Vent and Turbine Throttling Ring

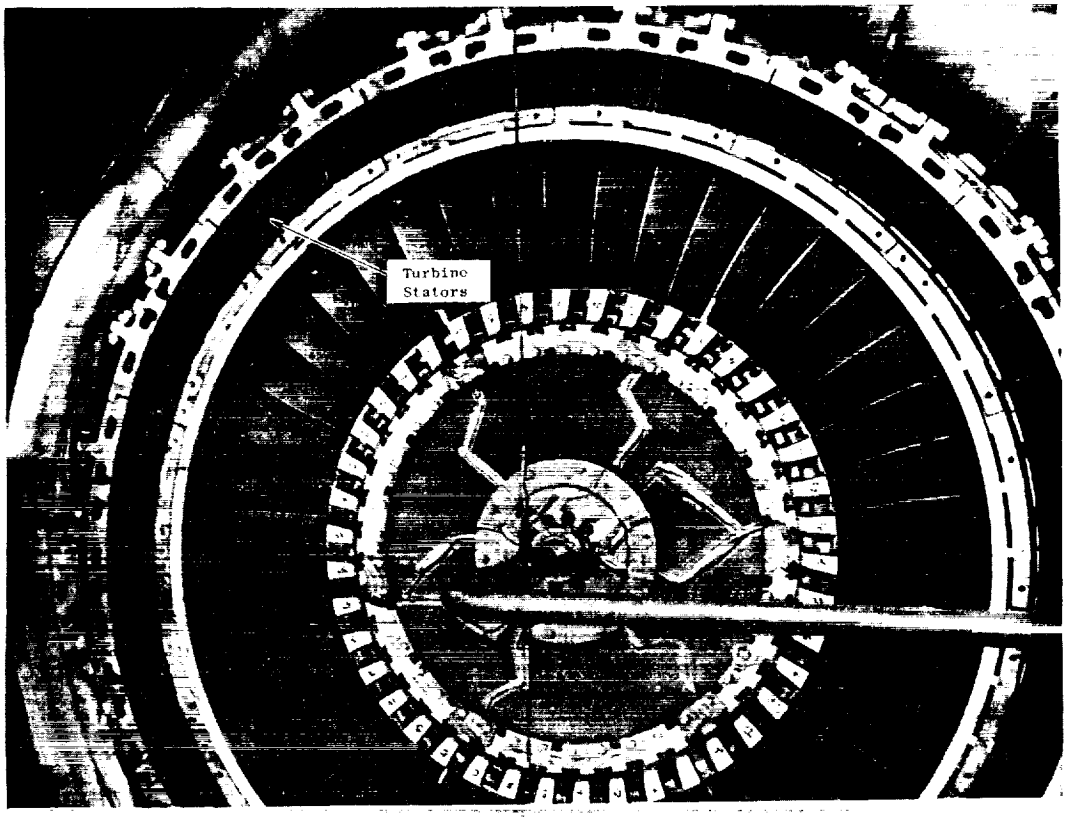

Figure I-23 Turbine Stator Modification to the Fan Exhaust

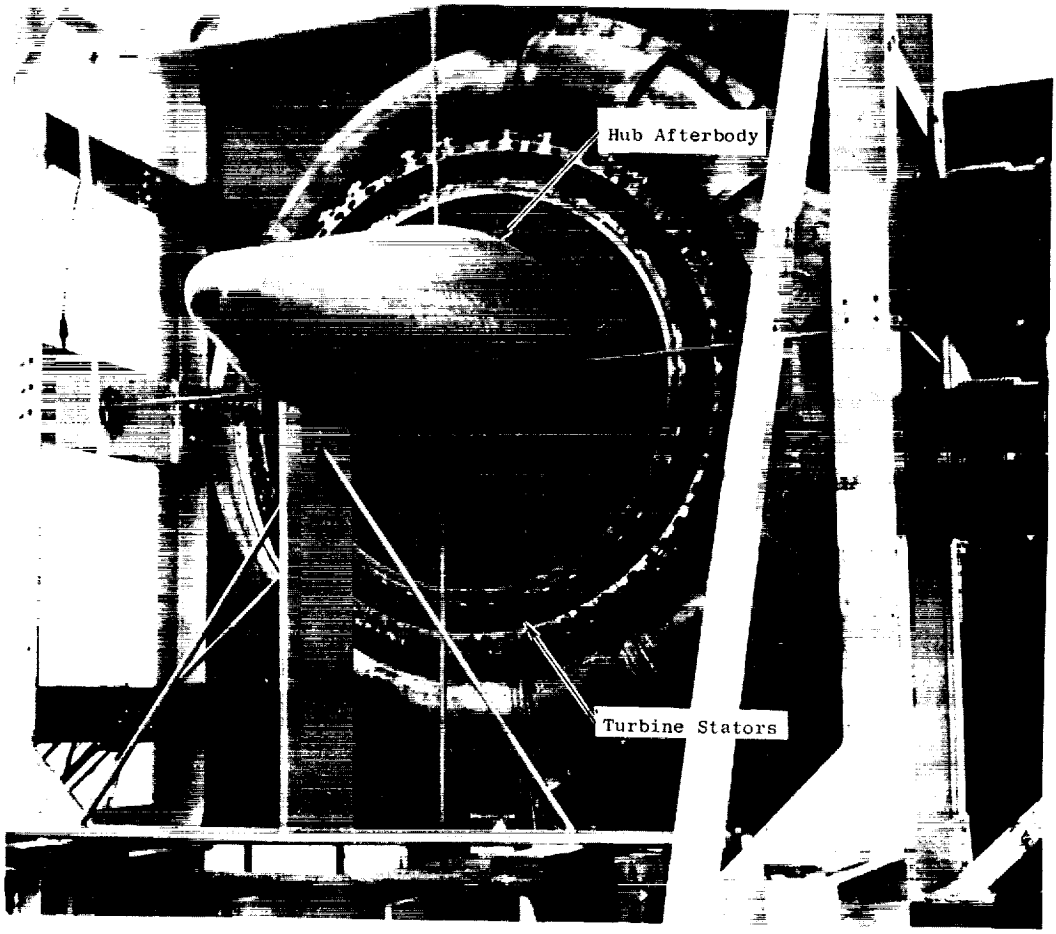

Figure I-24 Fan Modification Showing the Hub Afterbody and Turbine Stator Installation

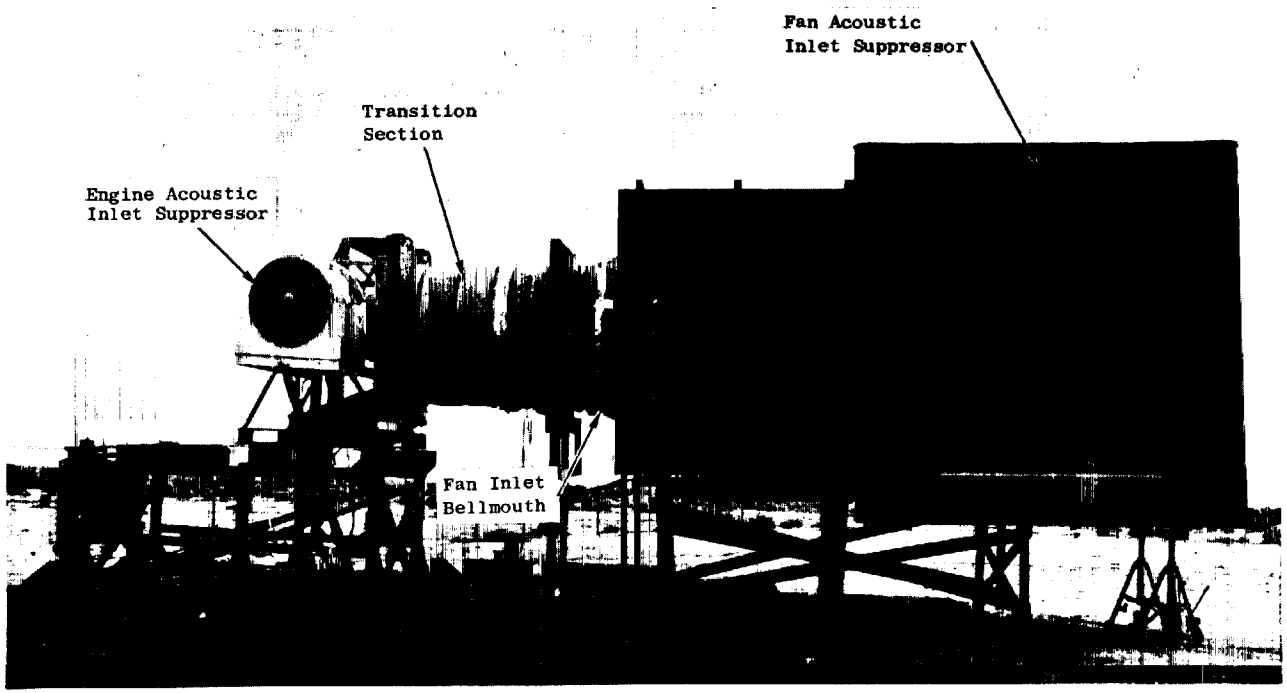

Figure I-25 Fan Assembly with Fan Inlet Suppressor Installed

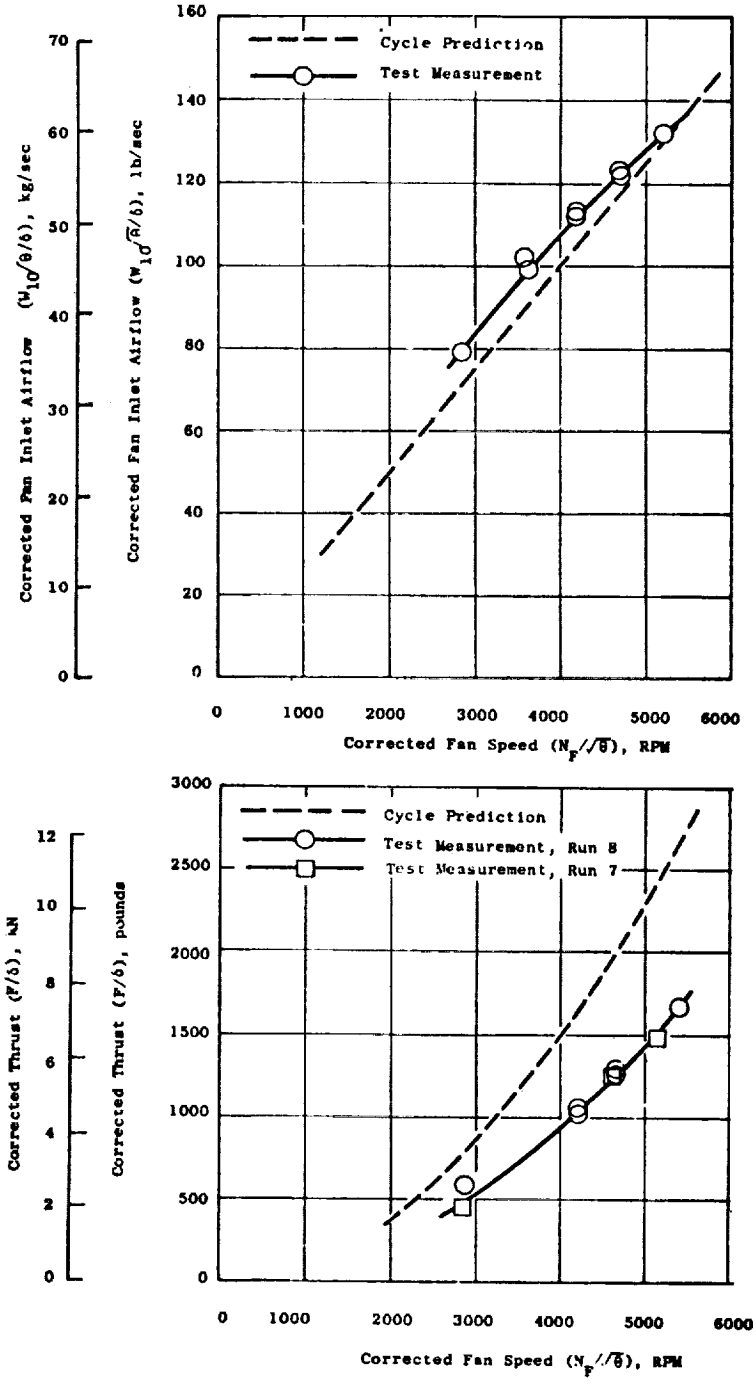

Figure I-26 Performance with Hub Base Vent and Throttle Ring Installed

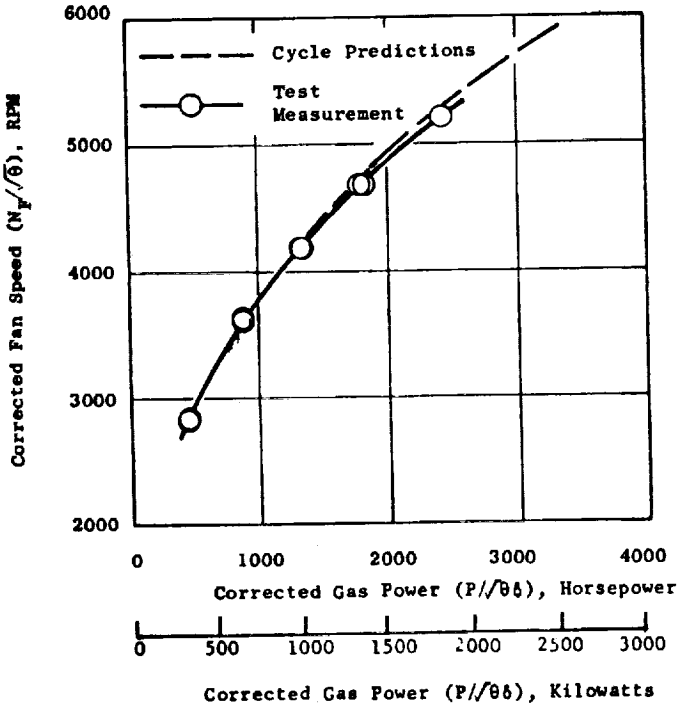

Figure I-26 Performance with Hub Base Vent and Throttle Ring Installed (Concluded)

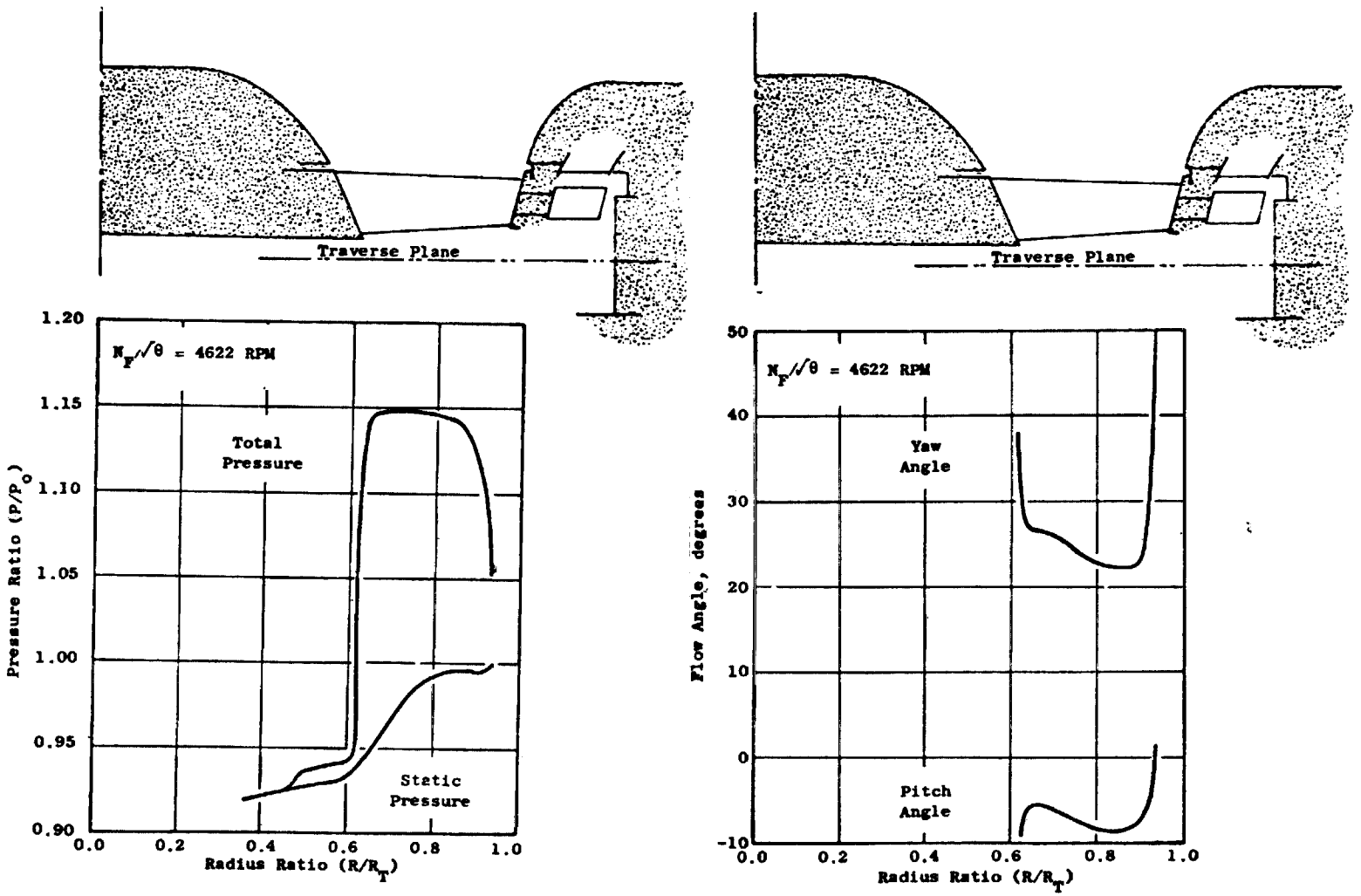

Figure I-27 Rotor Exit Flow Surveys with Hub Base Vent and Turbine Throttle Ring Installed

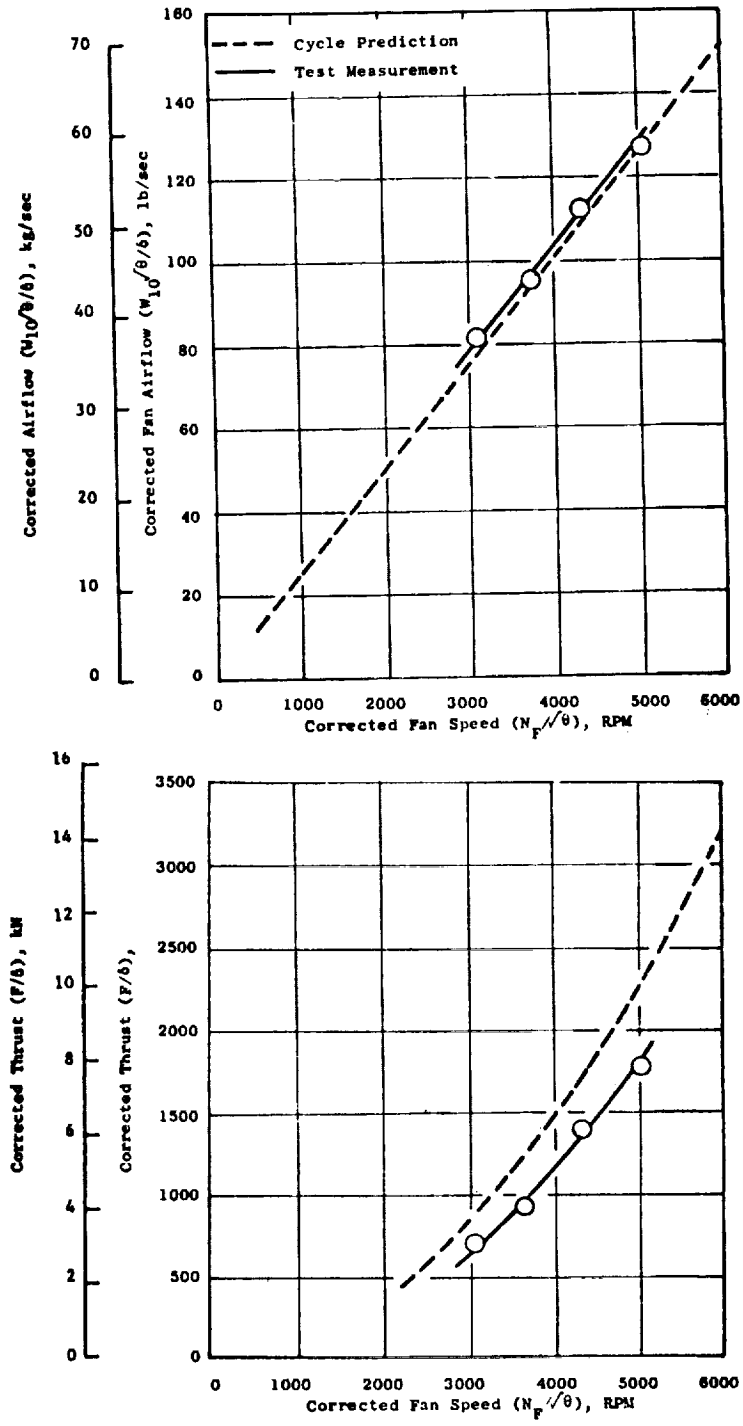

Figure I-28 Performance with Turbine Stators Installed

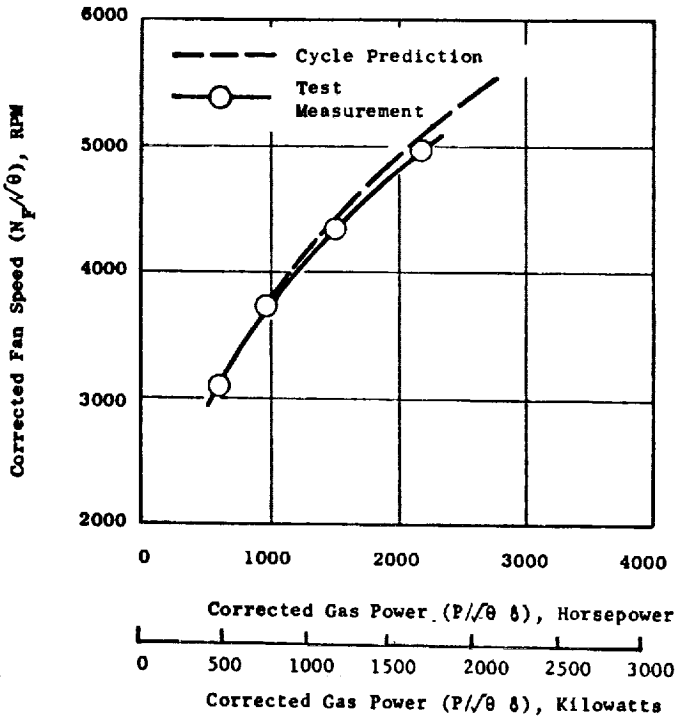

Figure I-28 Performance with Turbine Stators Installed (Concluded)

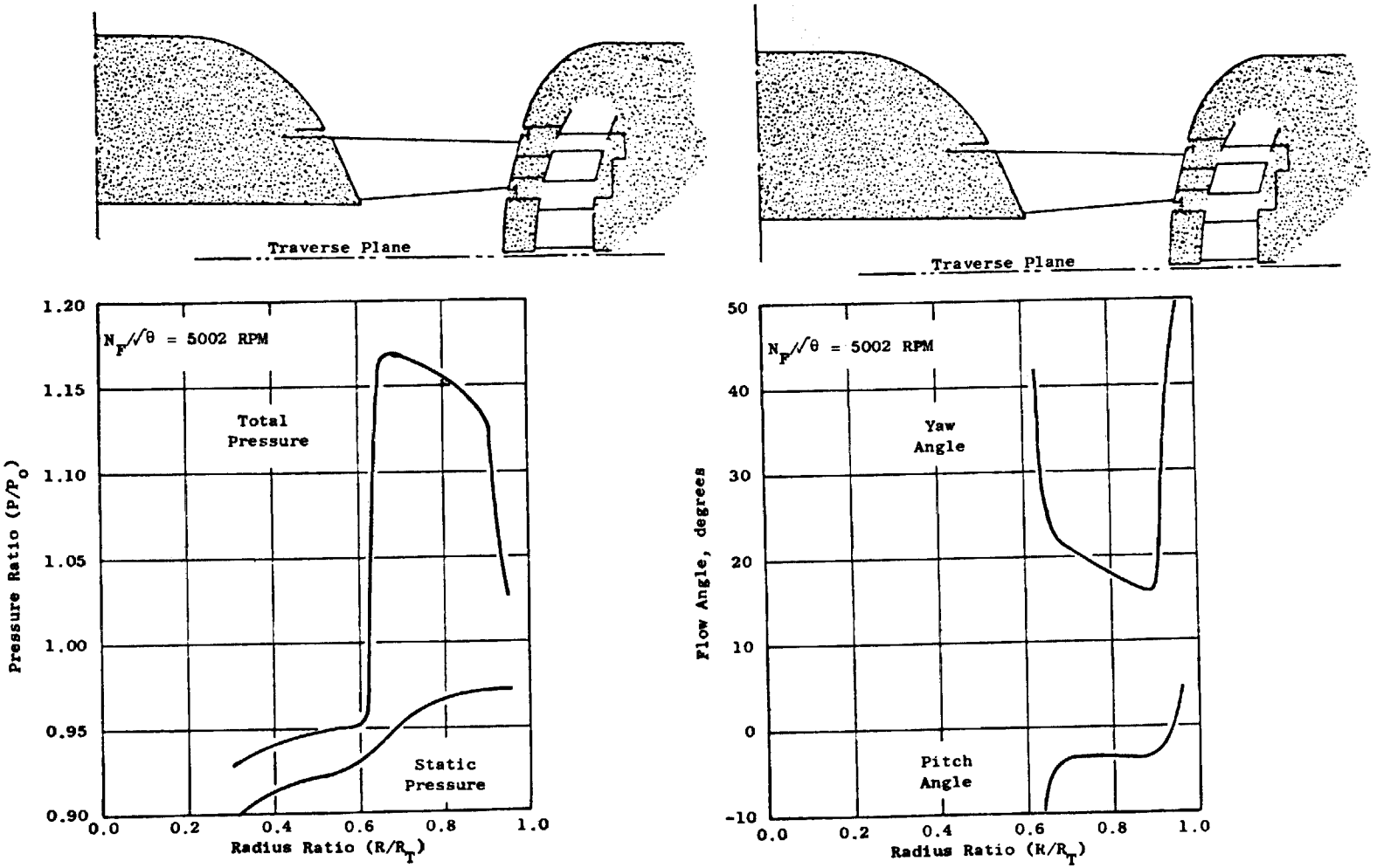

Figure I-29 Rotor Exit Flow Surveys with Turbine Stators Installed

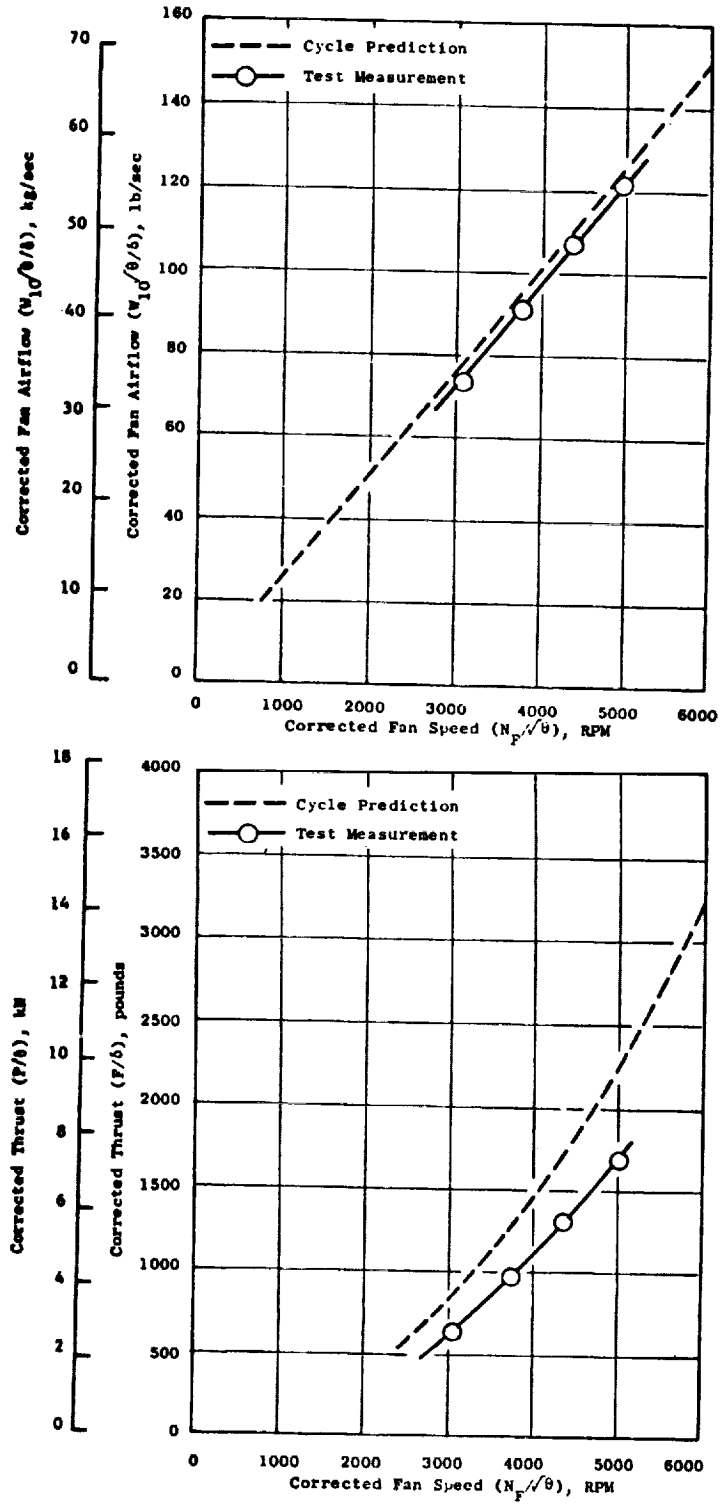

Figure I-30 Performance with Hub Afterbody Installed

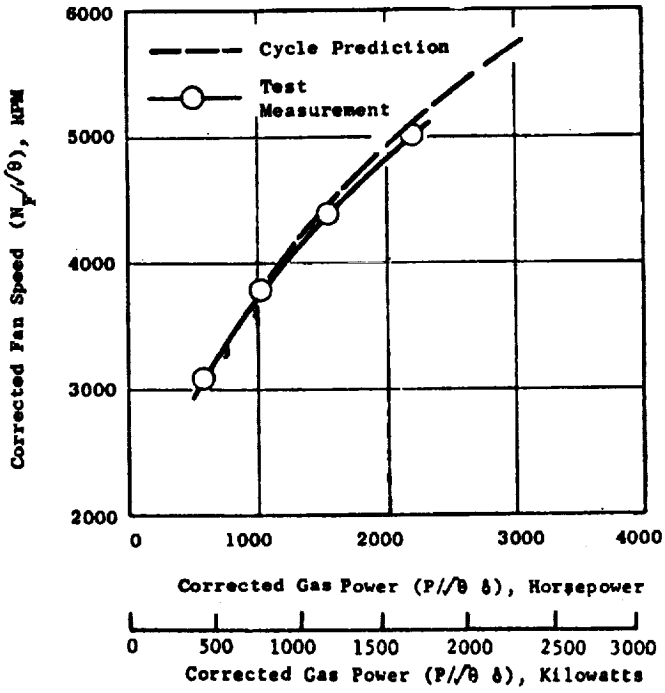

Figure I-30 Performance with Hub Afterbody Installed (Concluded)

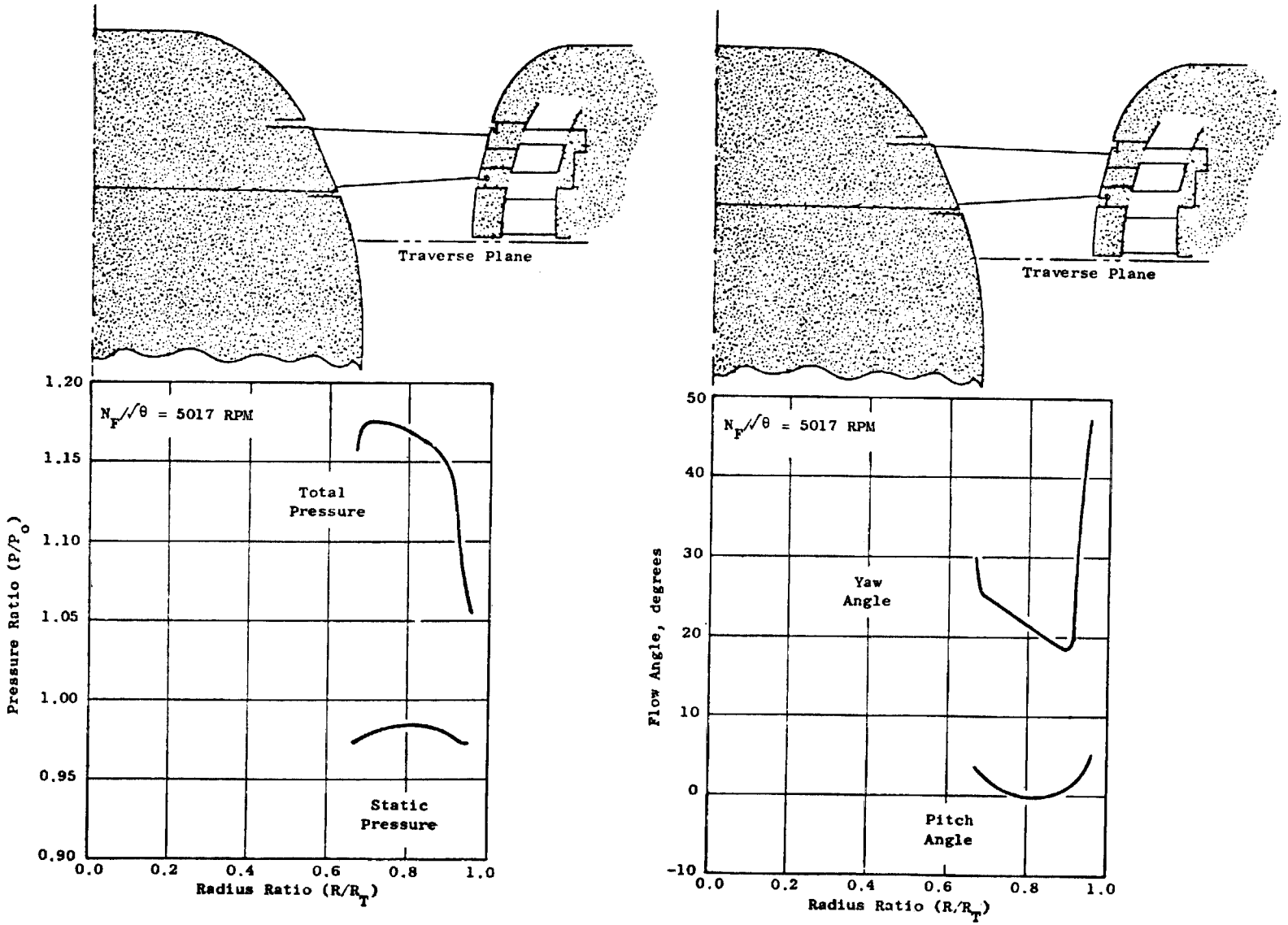

Figure I-31 Rotor Exit Flow Surveys with Hub Afterbody Installed

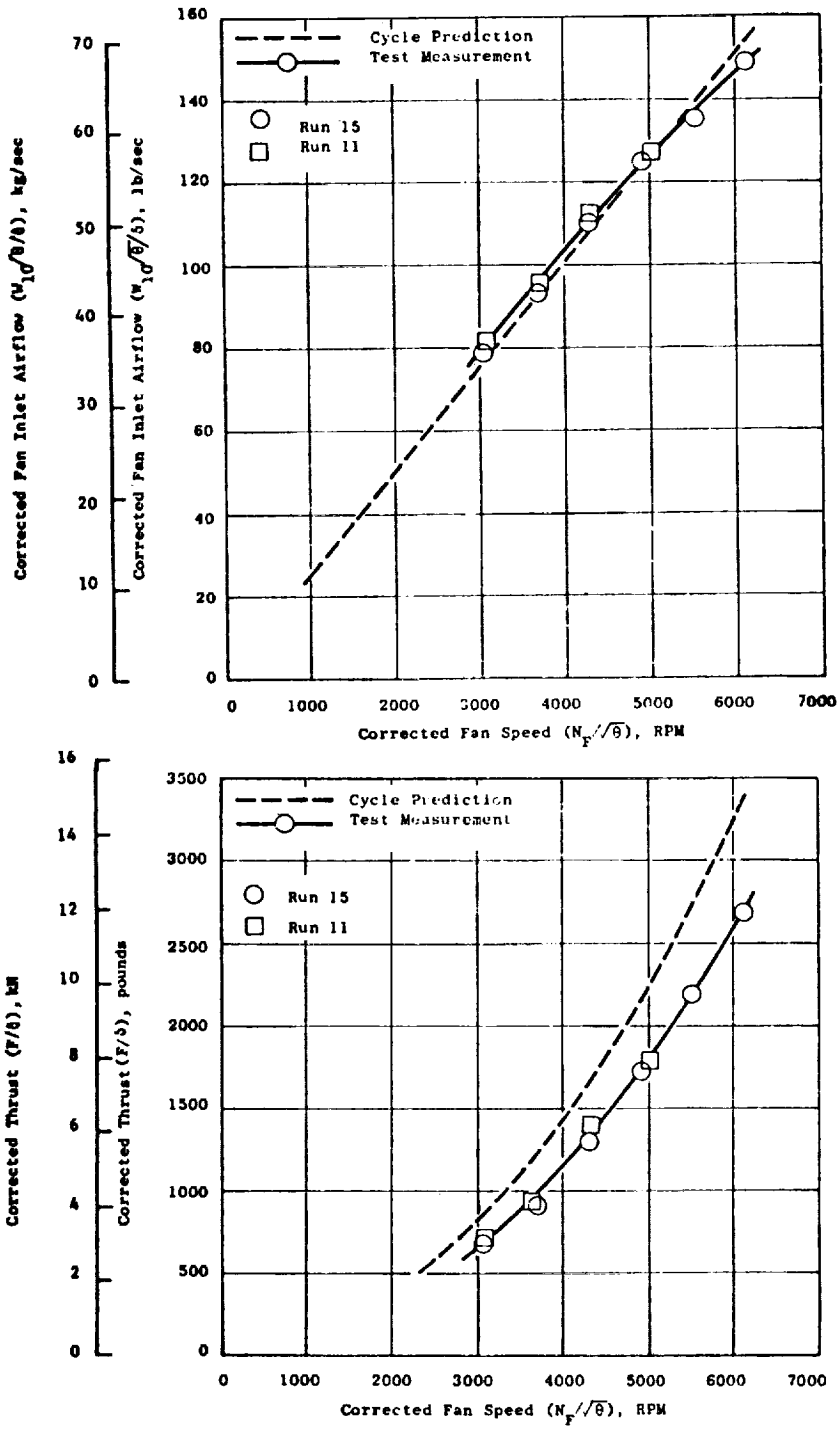

Figure I-32 Fan Performance for Acoustic Test Configuration

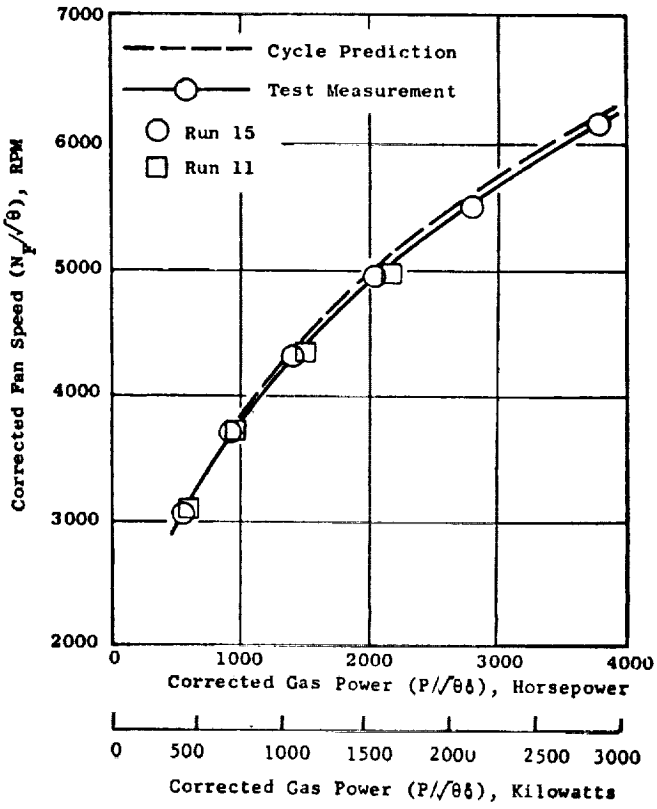

Figure I-32 Fan Performance for Acoustic Test Configuration (Concluded)

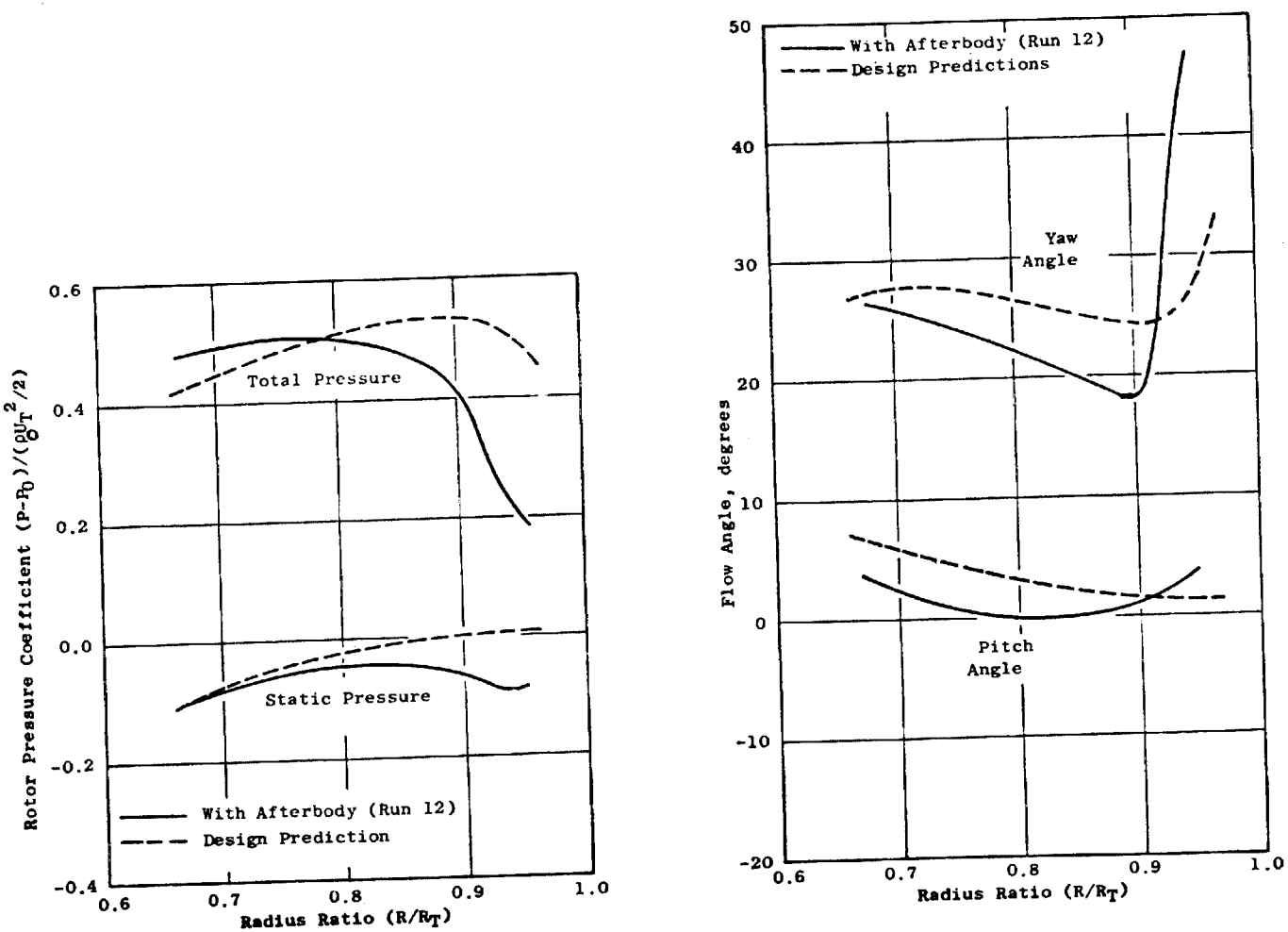

Figure I-33 Comparison of Measured and Predicted Fan Exit Flow Profiles

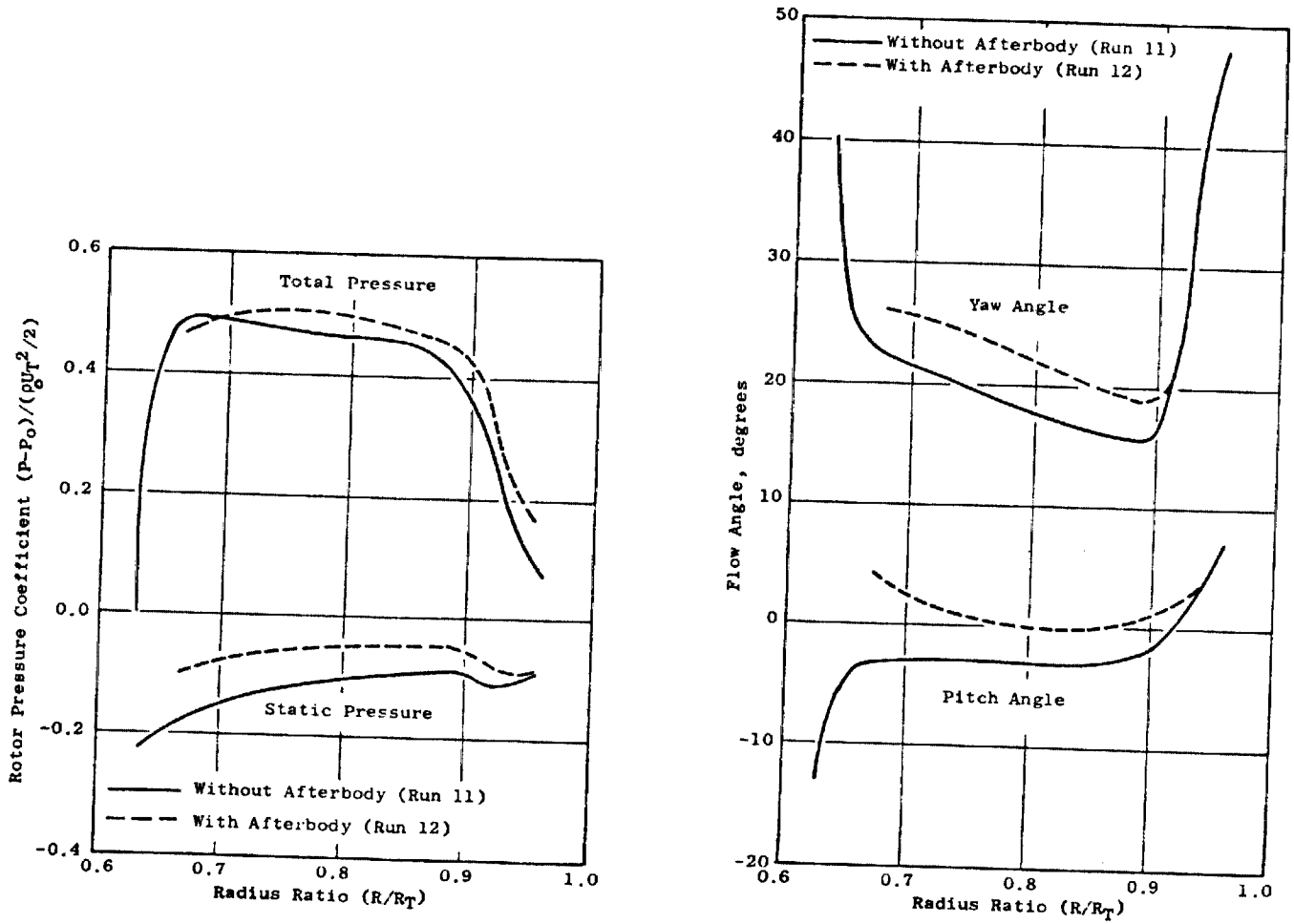

Figure I-34 Effects of Hub Afterbody on Fan Exhaust Profiles

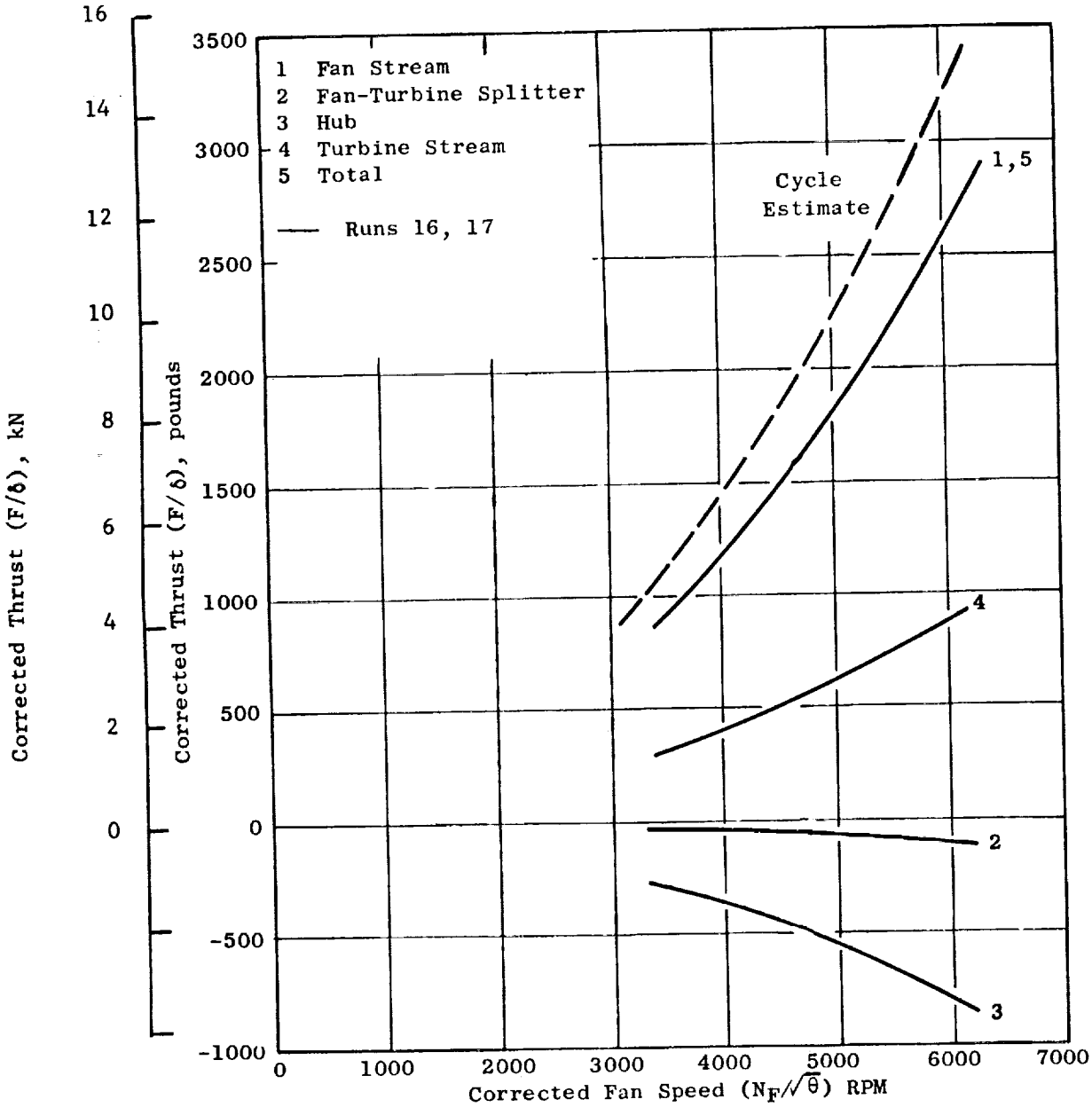

Figure I-35 Breakdown of Thrust Components Based on Exhaust Flow Traverses

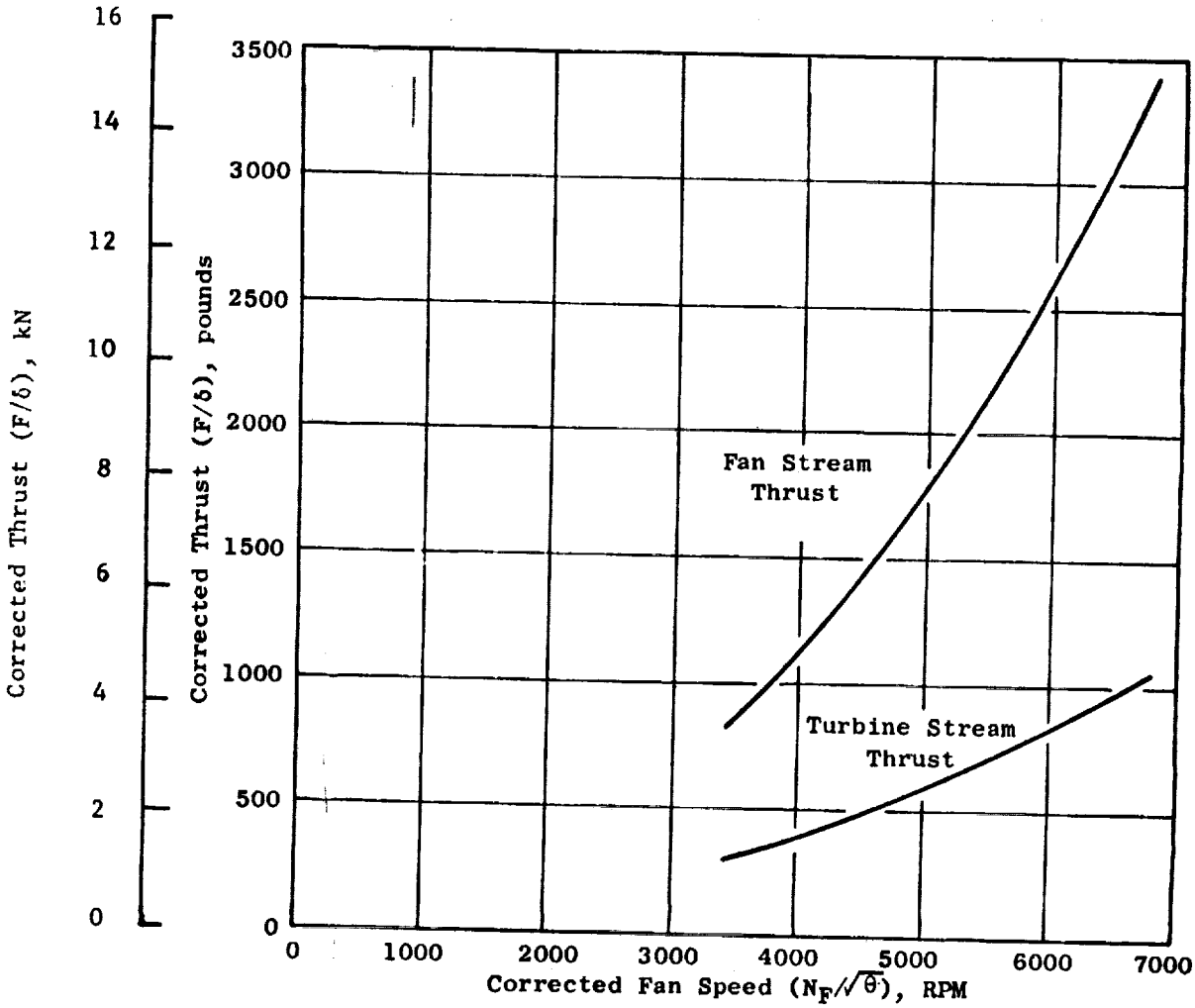

Figure I-36 Cycle Estimates of Fan and Turbine Stream Thrusts

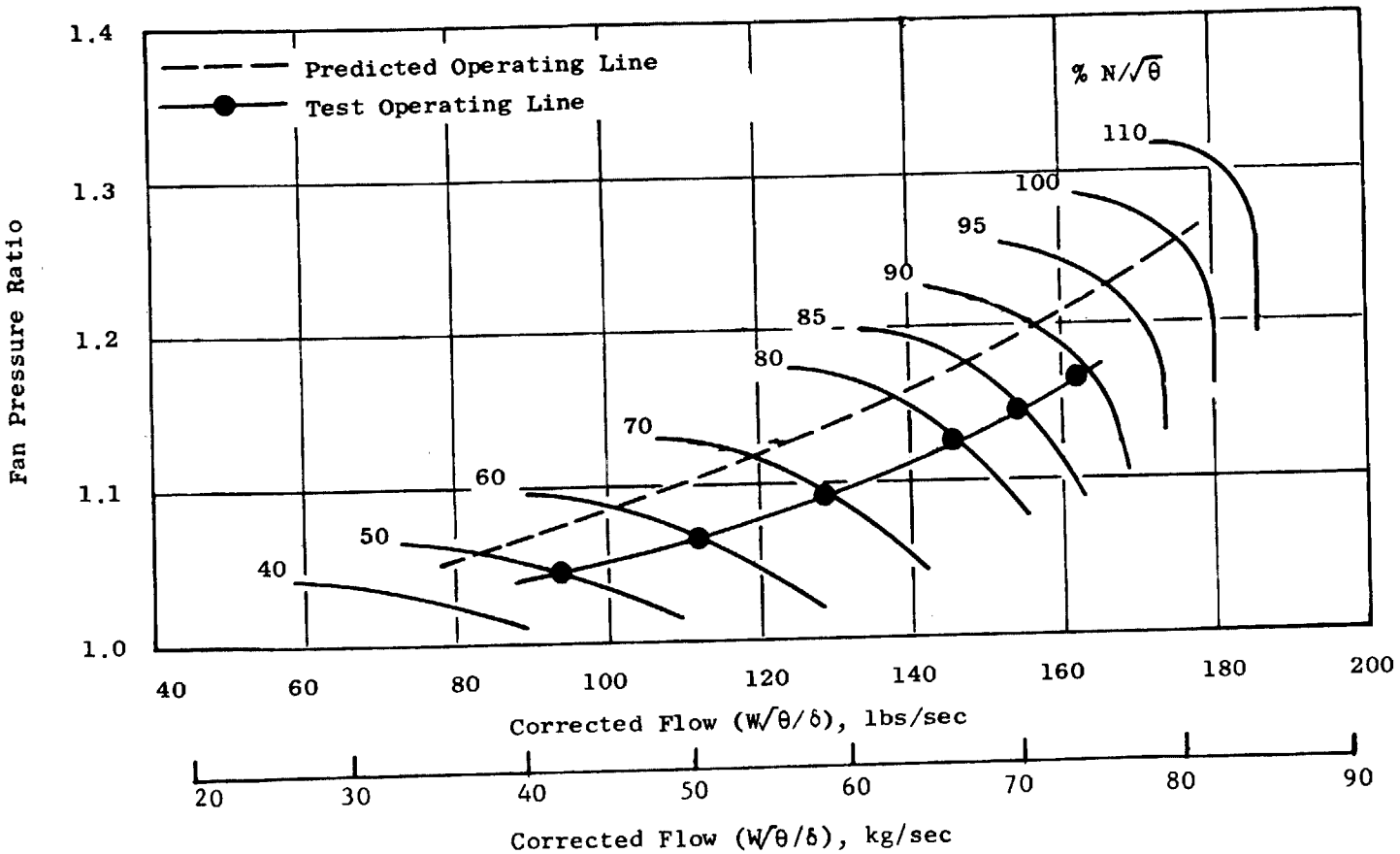

Figure I-37 Comparison of Predicted and Test Operating Lines on LF336/E Fan Map

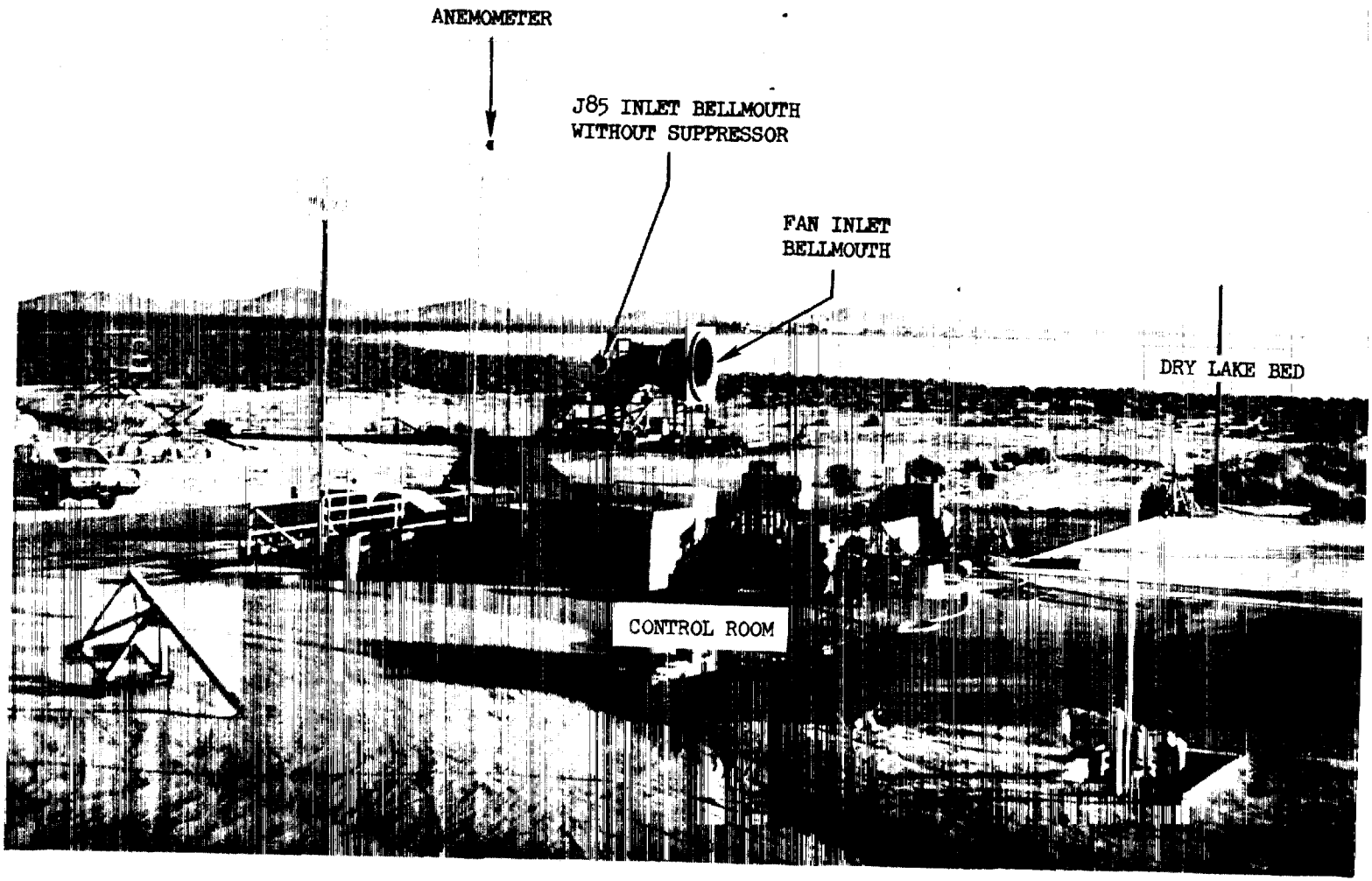

Figure I-38 General Electric Edwards Flight Test Center Acoustic Test Facility

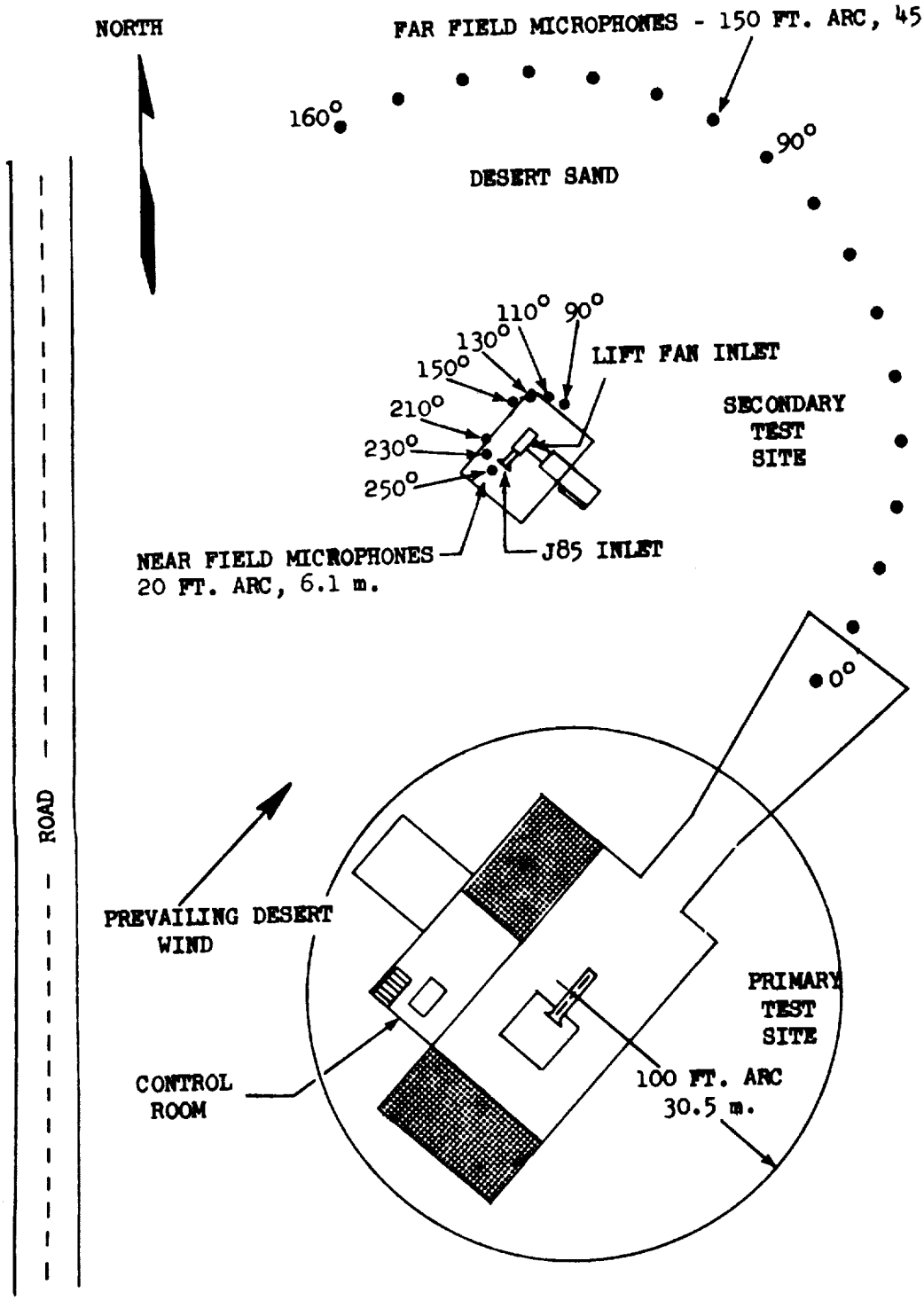

Figure I-39 Sketch of Microphone Orientation at Edwards Flight Test Center

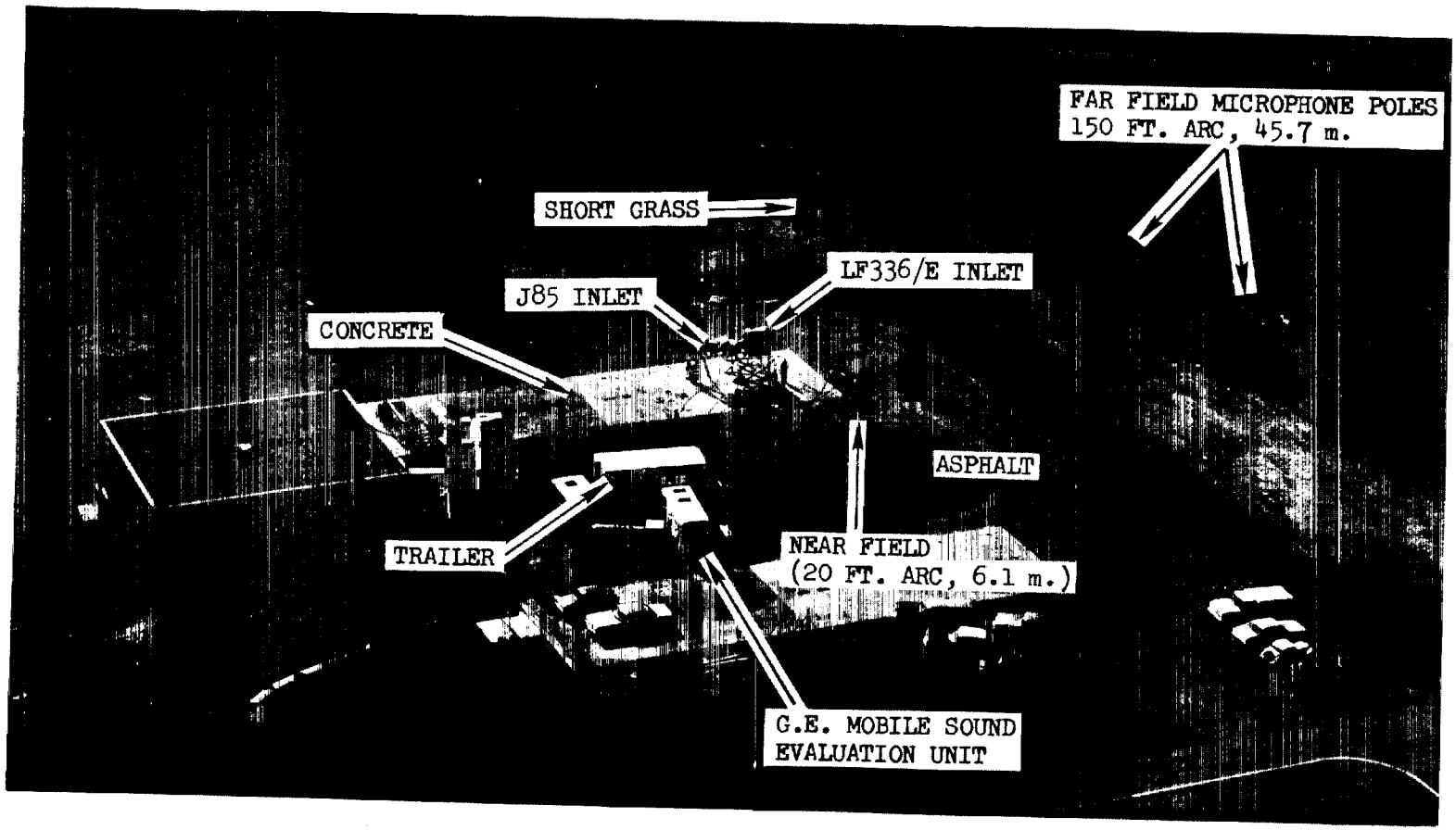

Figure I-40 NASA Ames Research Center - Acoustic Test Facility

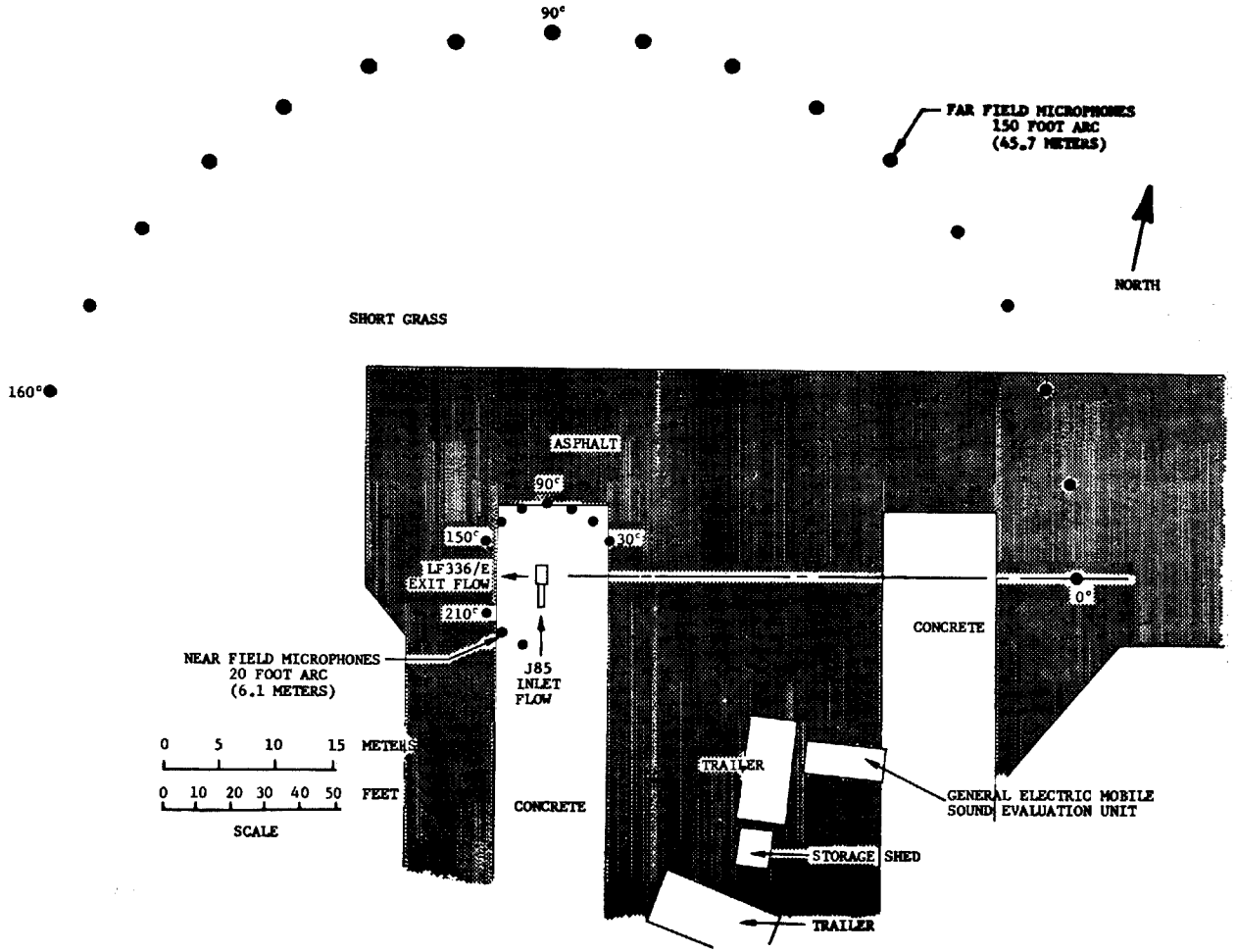

Figure I-41 Microphone Orientation at NASA Ames Outdoor Test Site

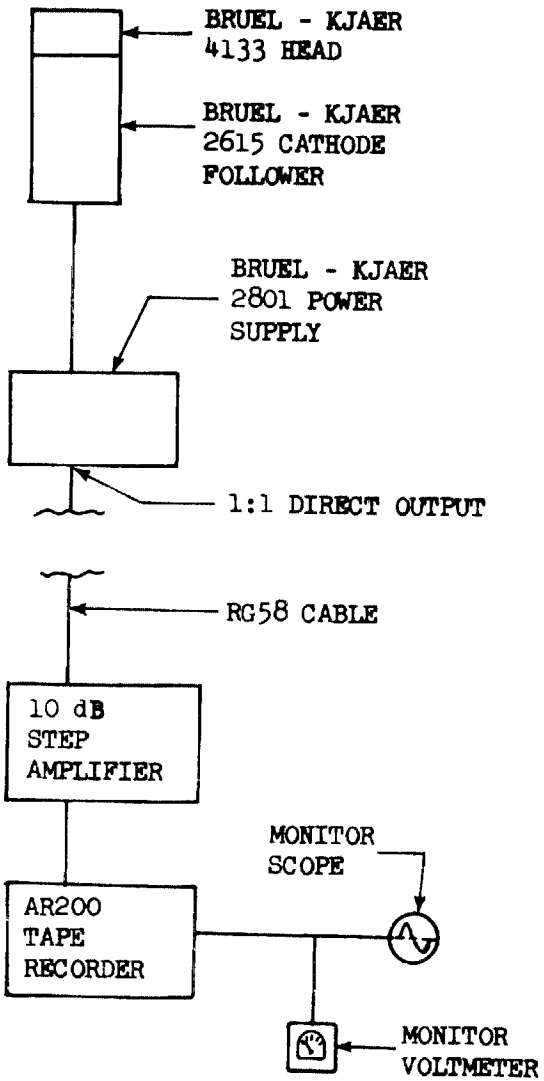

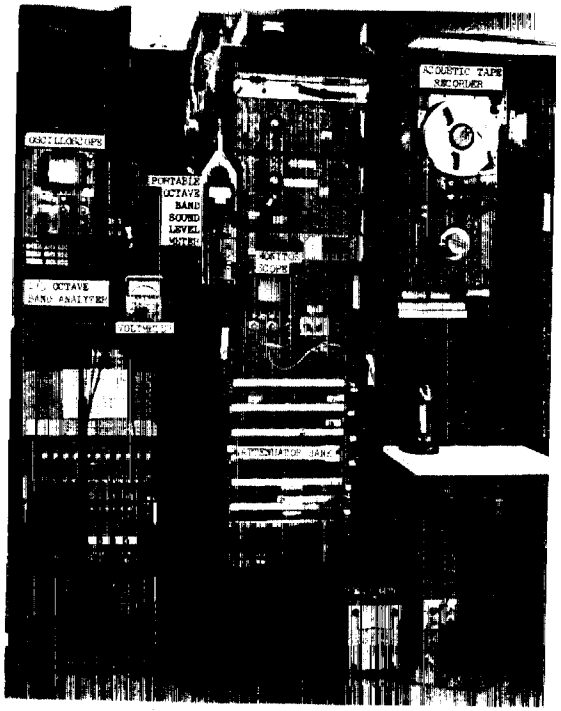

Figure I-42 Acoustic Data System - General Electric Flight Test Center

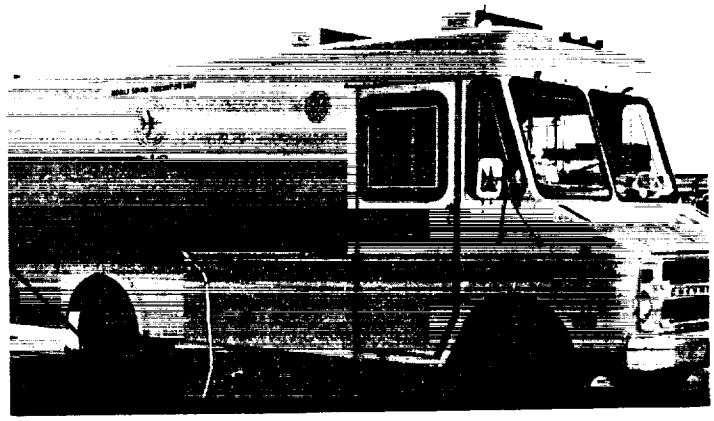

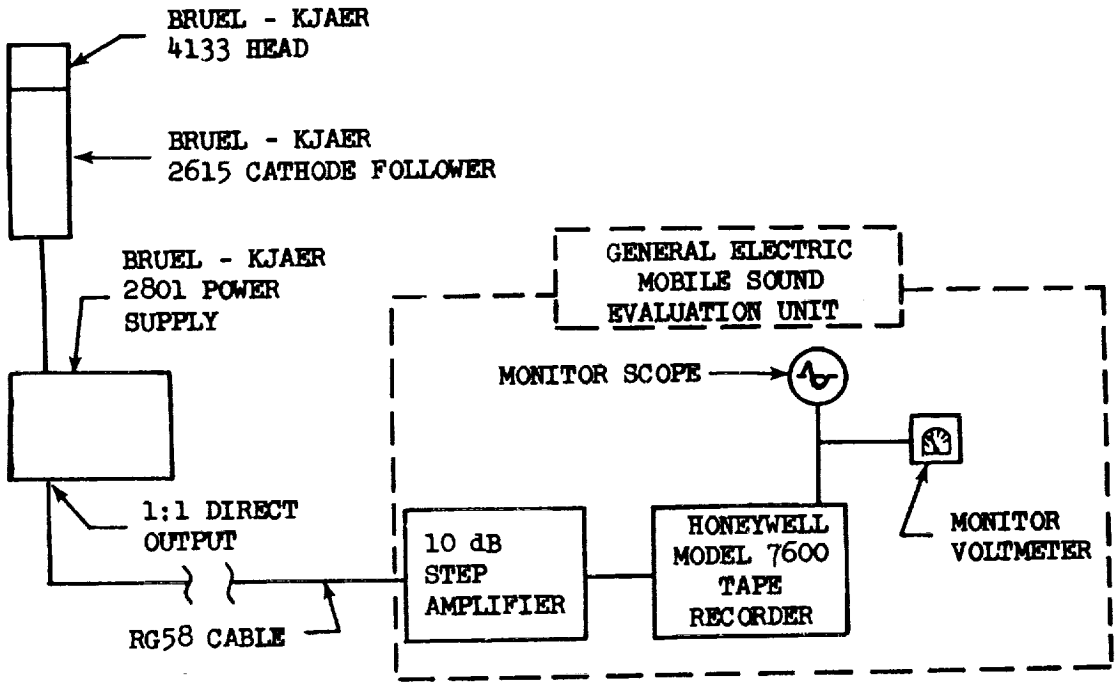

Figure I-43 Acoustic Data System - NASA Ames Research Center

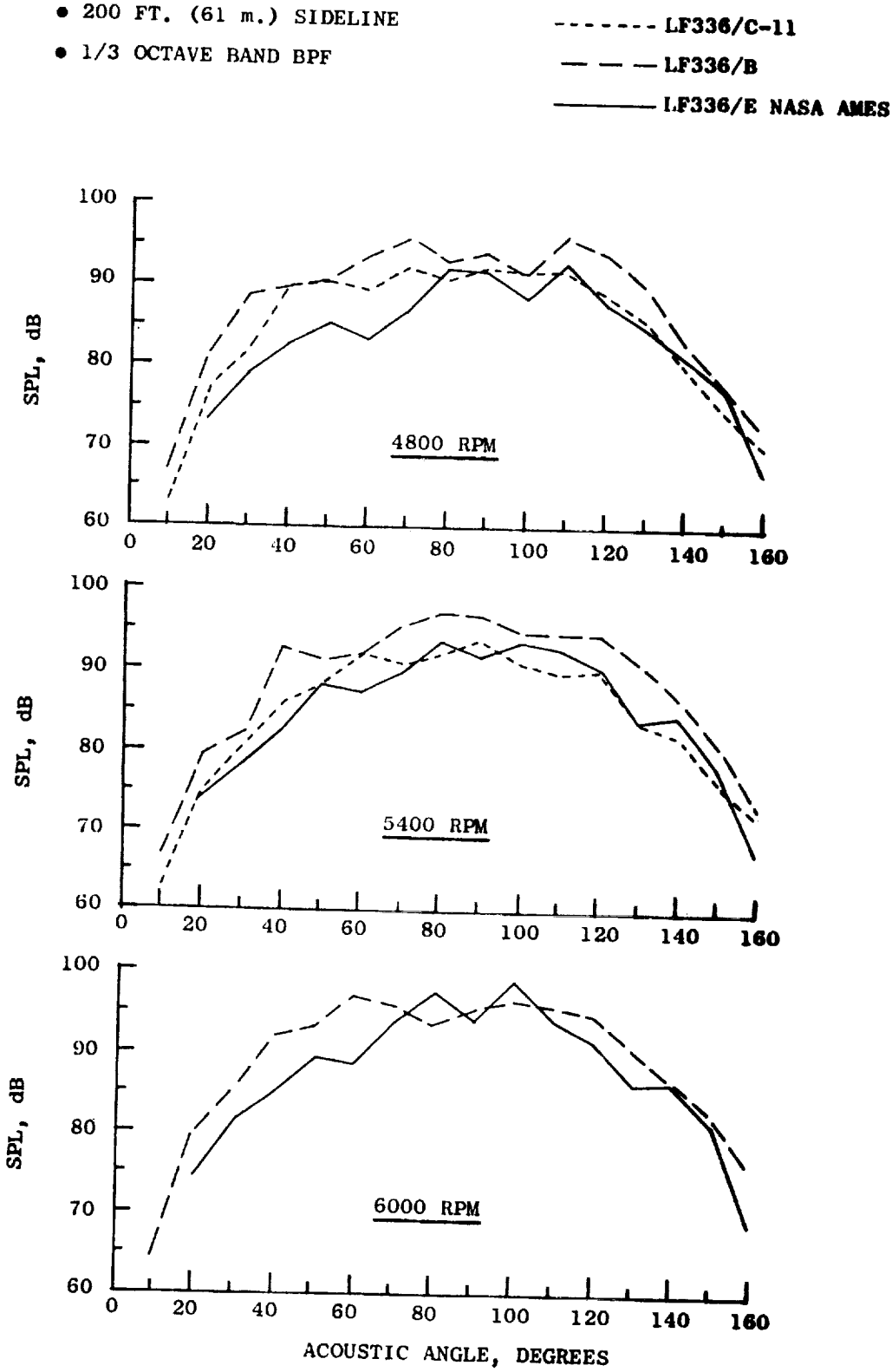

Figure I-44 LF336/C-11, LF336/B and LF336/E 1/3 Octave Band BPF Directivity Patterns at Constant Tip Speed

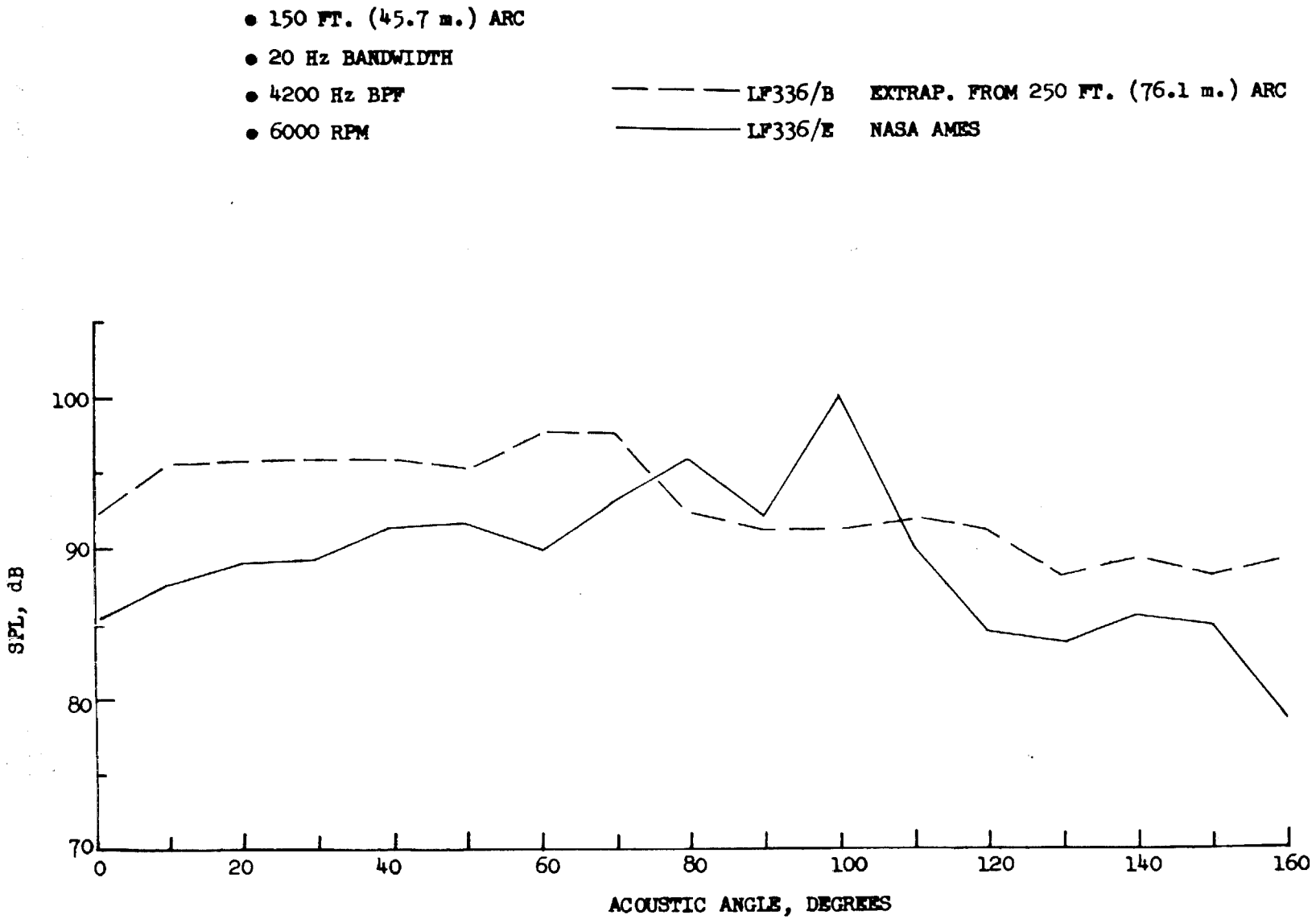

Figure I-45 LF336/B and LF336/E Narrowband BPF Directivity Patterns at Constant Tip Speed

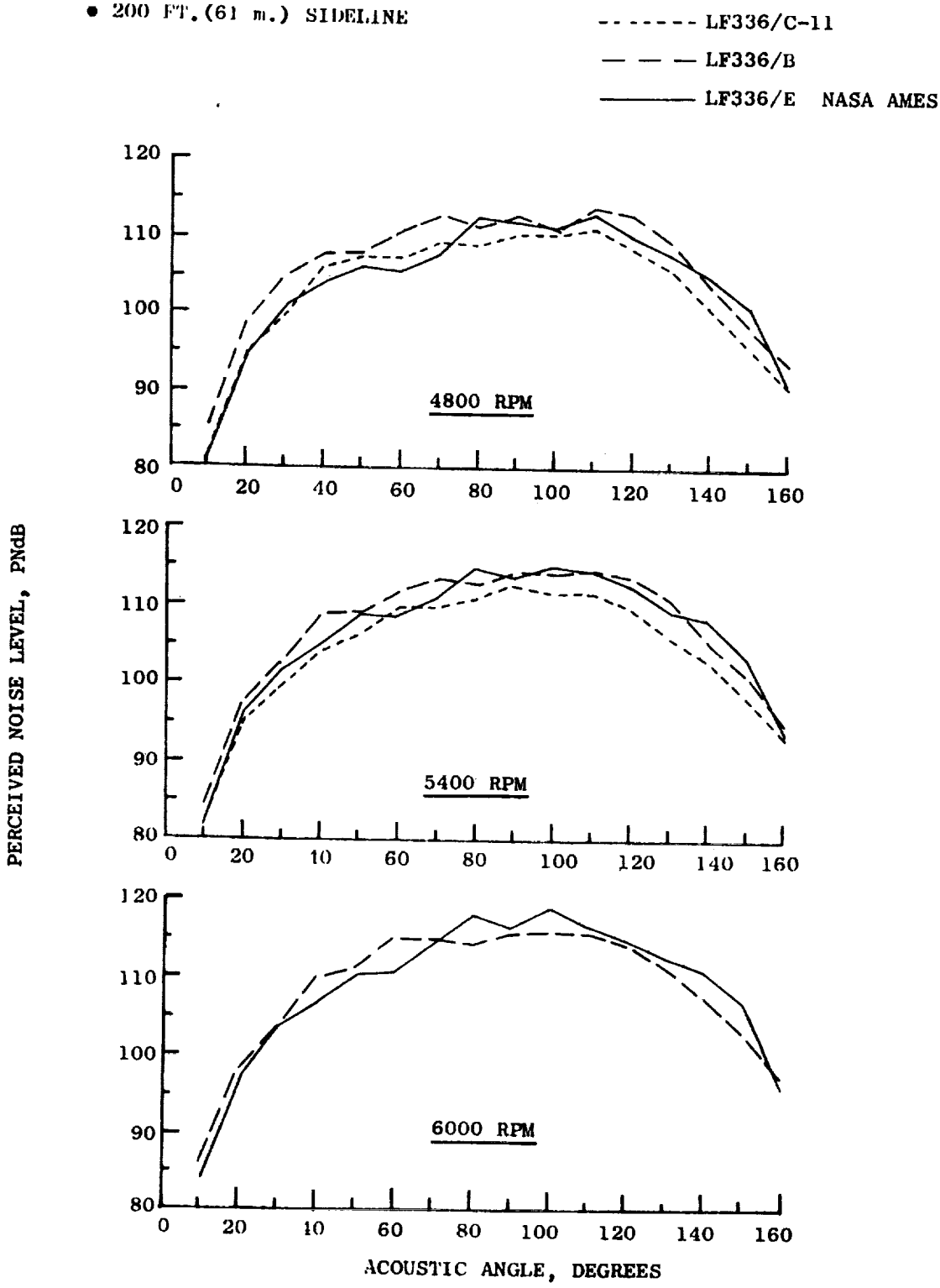

Figure I-46 LF336/C-11, LF336/B and LF336/E PNL Directivity Patterns at Constant Tip Speed

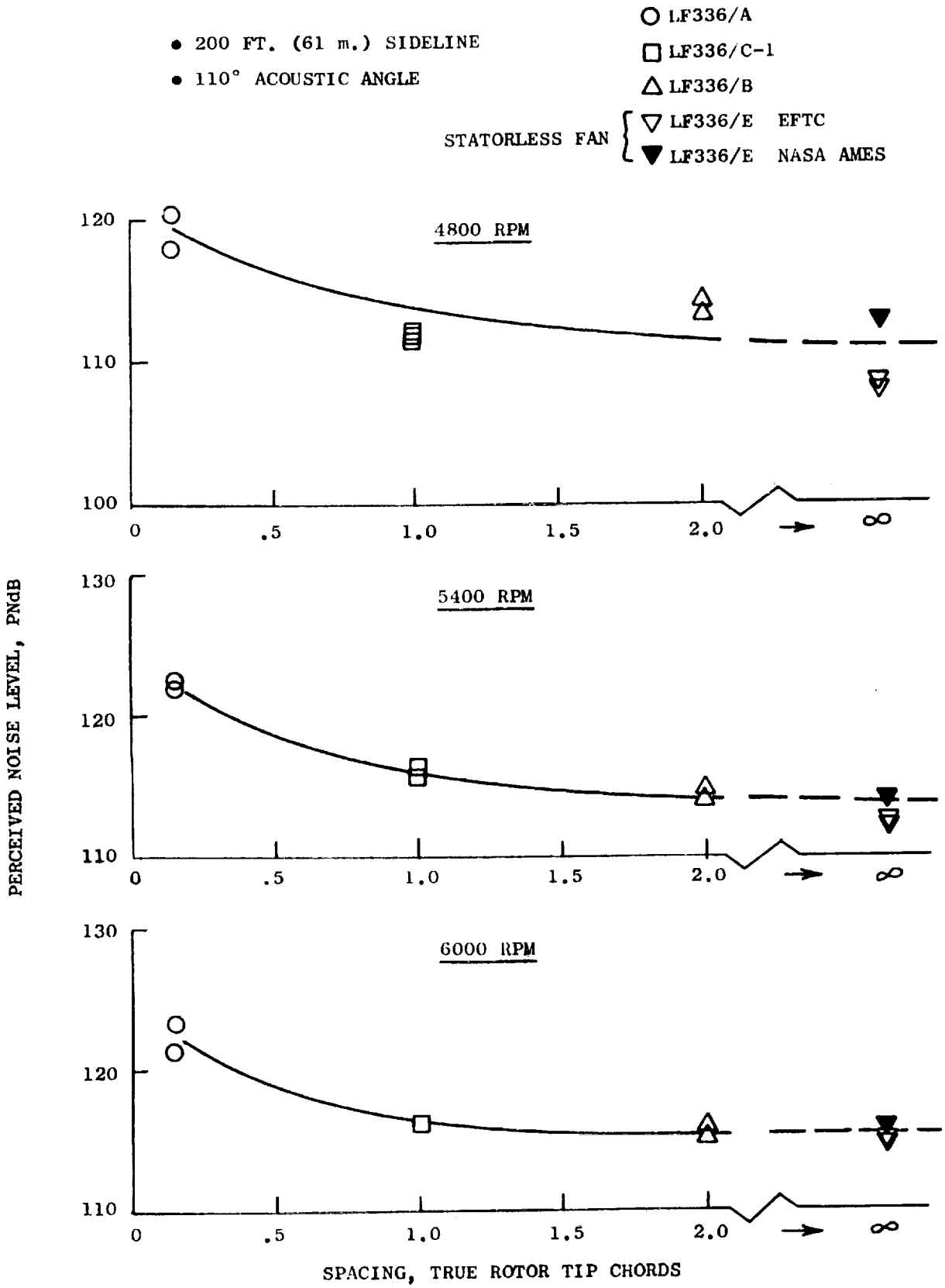

Figure I-47 Effect of Rotor - Stator Spacing on PNL

• EFTC TEST SITE

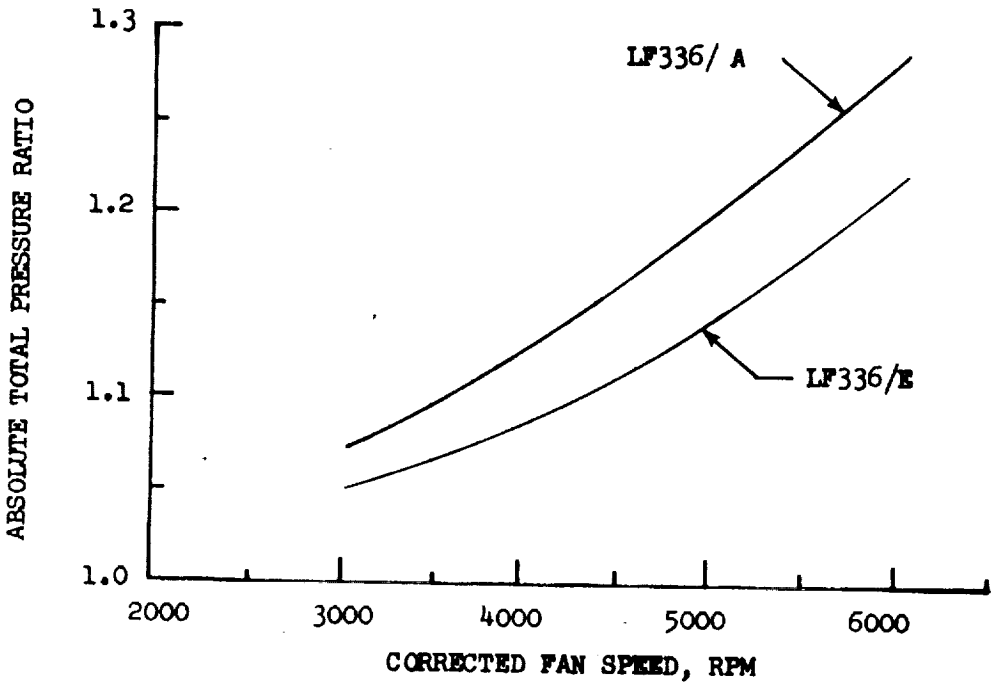

Figure I-48 LF336/A and LF336/E Absolute Total Pressure Ratios as a Function of Fan Speed

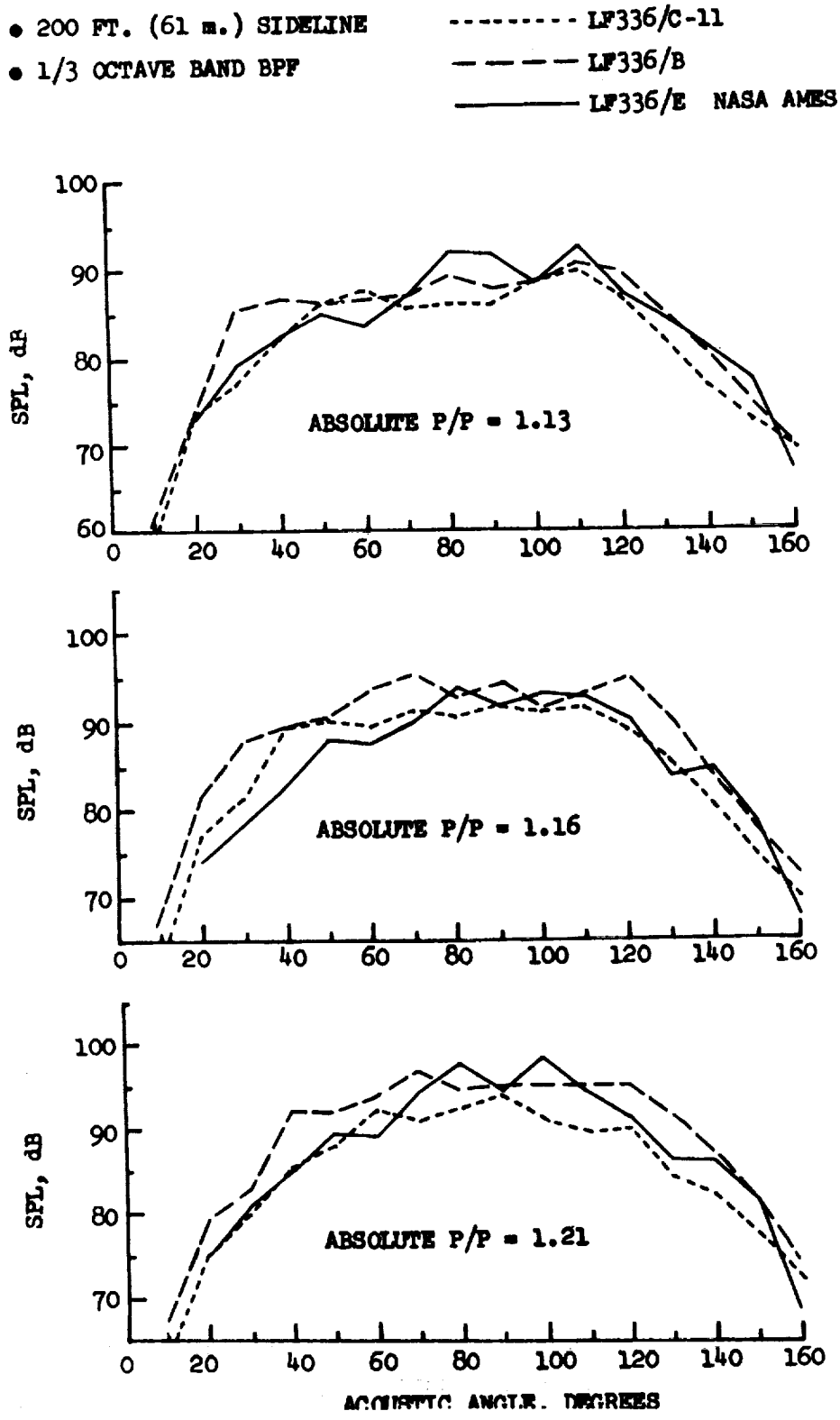

Figure I-49 LF336/C-11, LF336/B and LF336/E 1/3 Octave Band BPF Directivity Patterns at Constant Absolute Pressure Ratios

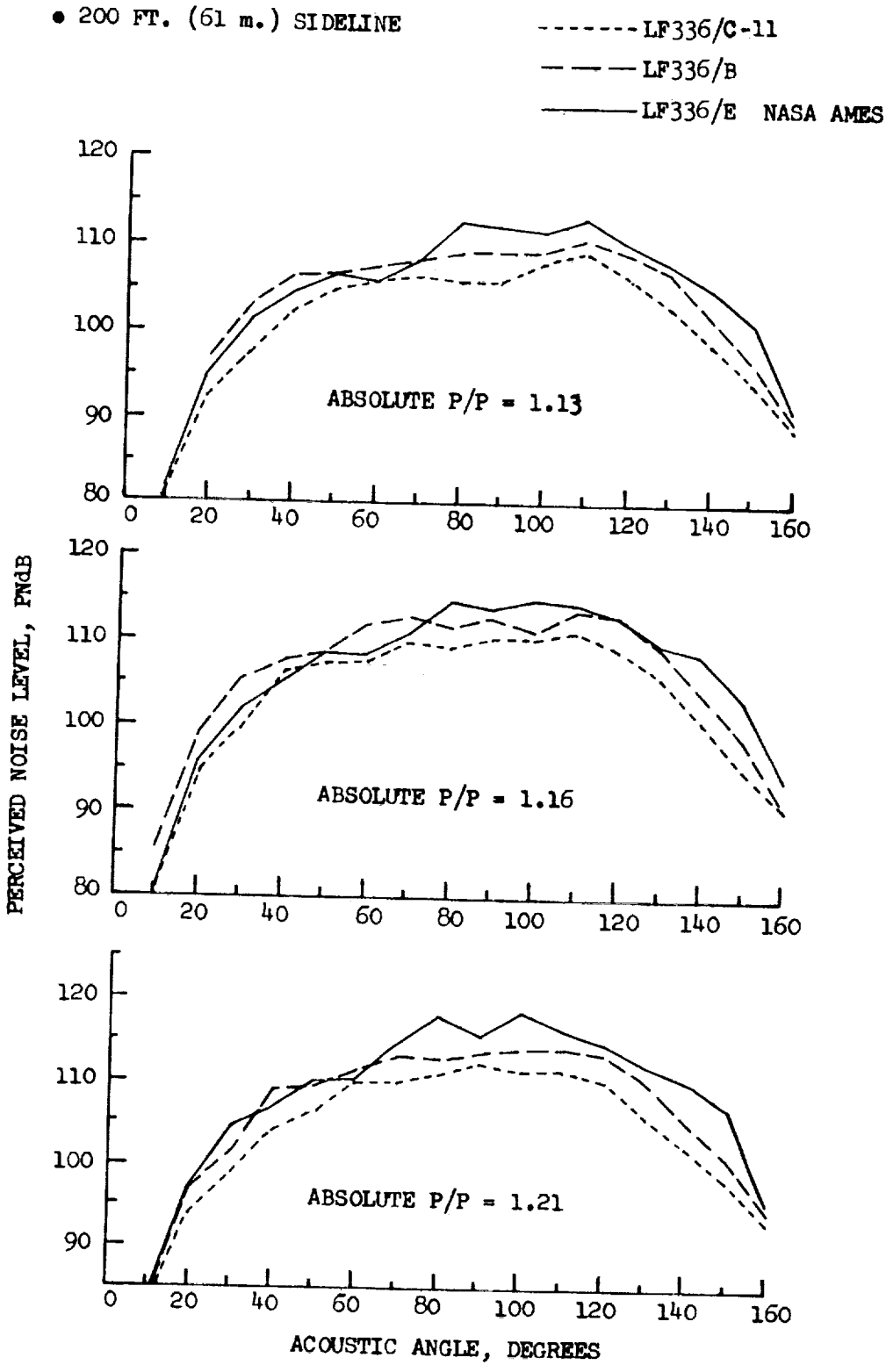

Figure I-50 LF336/C-11, LF336/B and LF336/E PNL Directivity Patterns at Constant Absolute Pressure Ratios

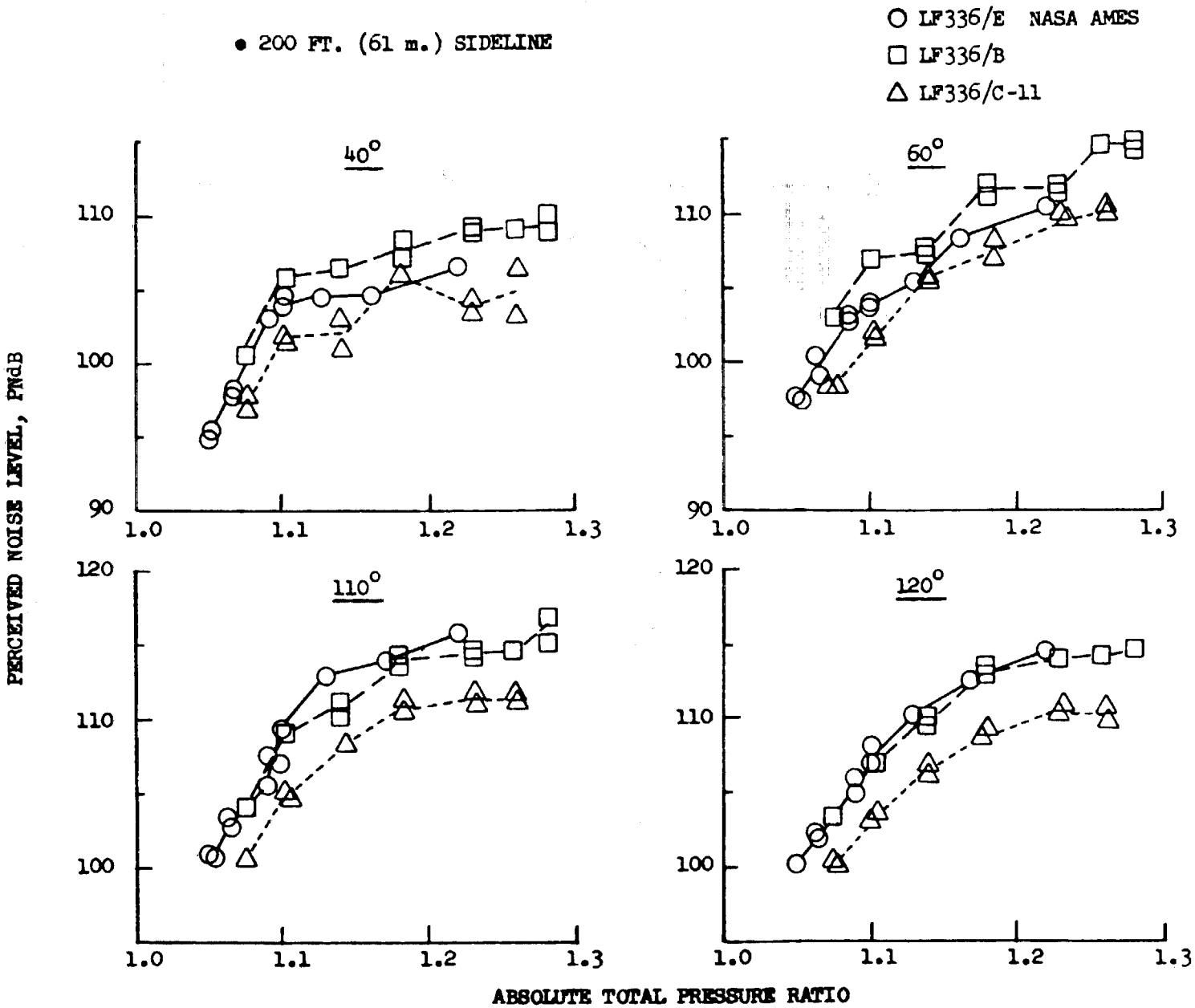

Figure I-51 LF336/C-11, LF336/B and LF336/E PNLs as a Function of Absolute Pressure Ratios at 40°, 60°, 110° and 120°

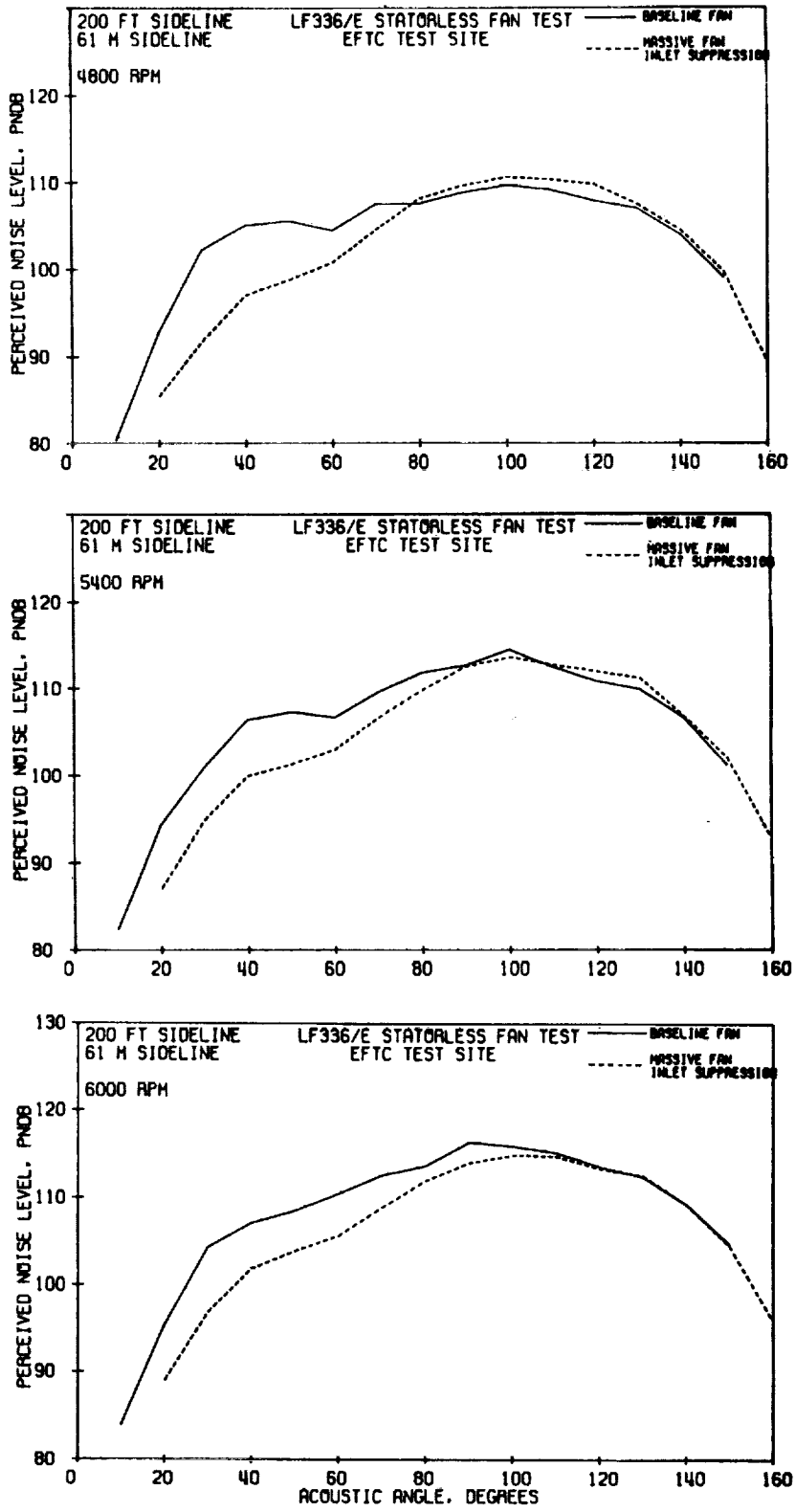

Figure I-52 Effects of Massive Inlet Suppression on PNL Directivity Patterns

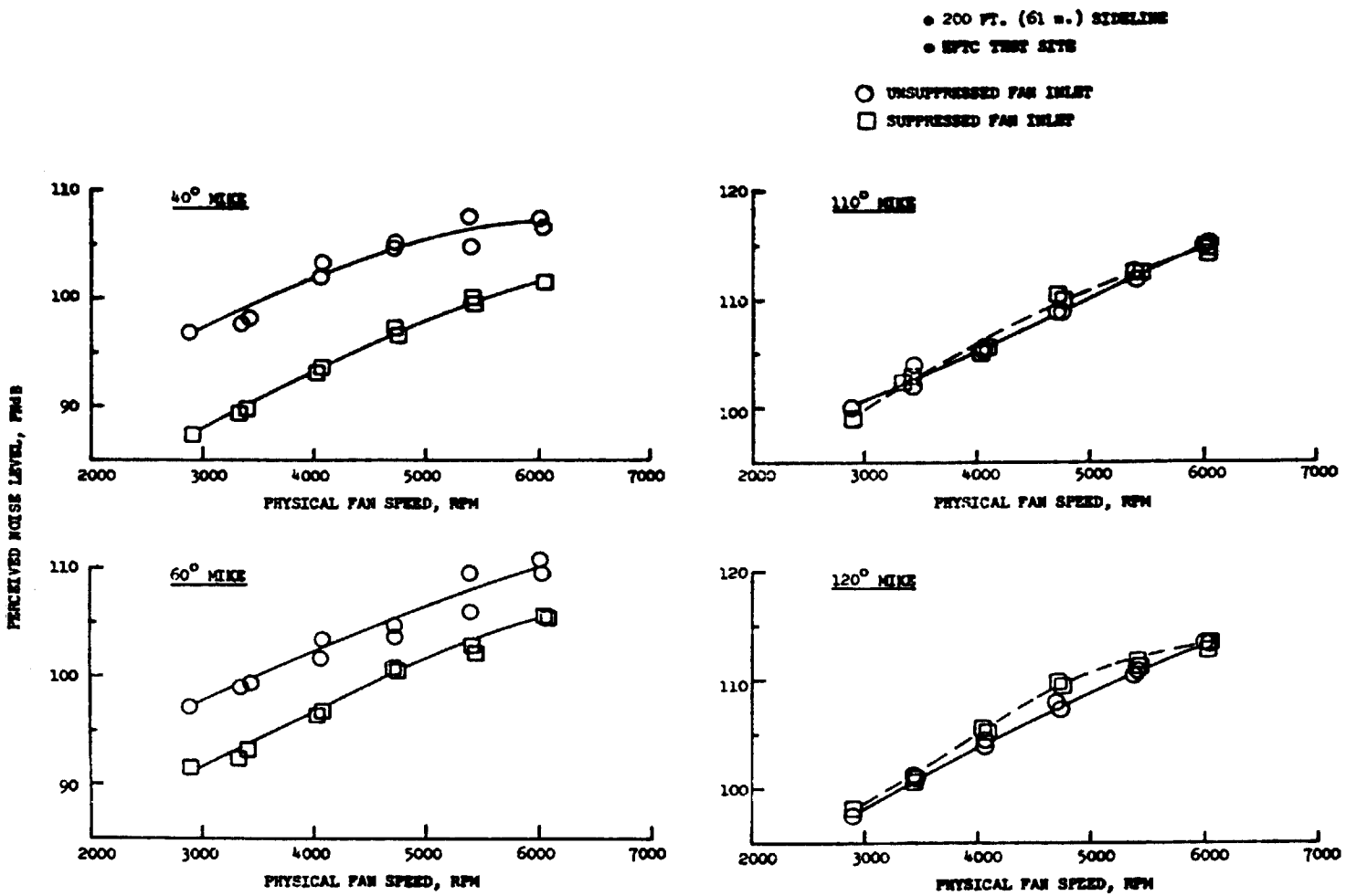

Figure I-53 Effects of Massive Fan Inlet Suppression on Perceived Noise Levels

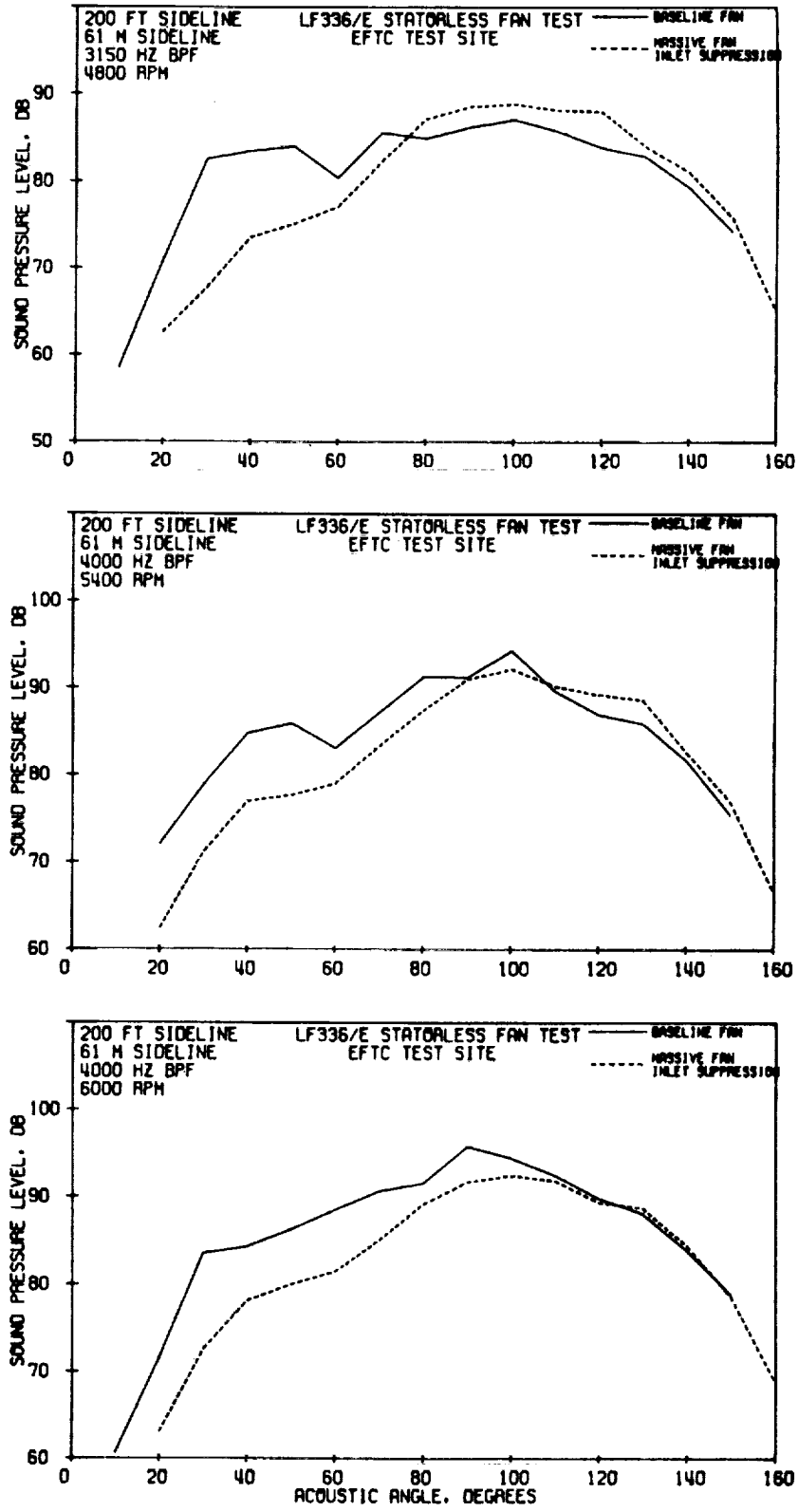

Figure I-54 Effect of Massive Fan Inlet Suppression on 1/3 Octave Band BPF Directivity Patterns at 4800, 5400 and 6000 RPM

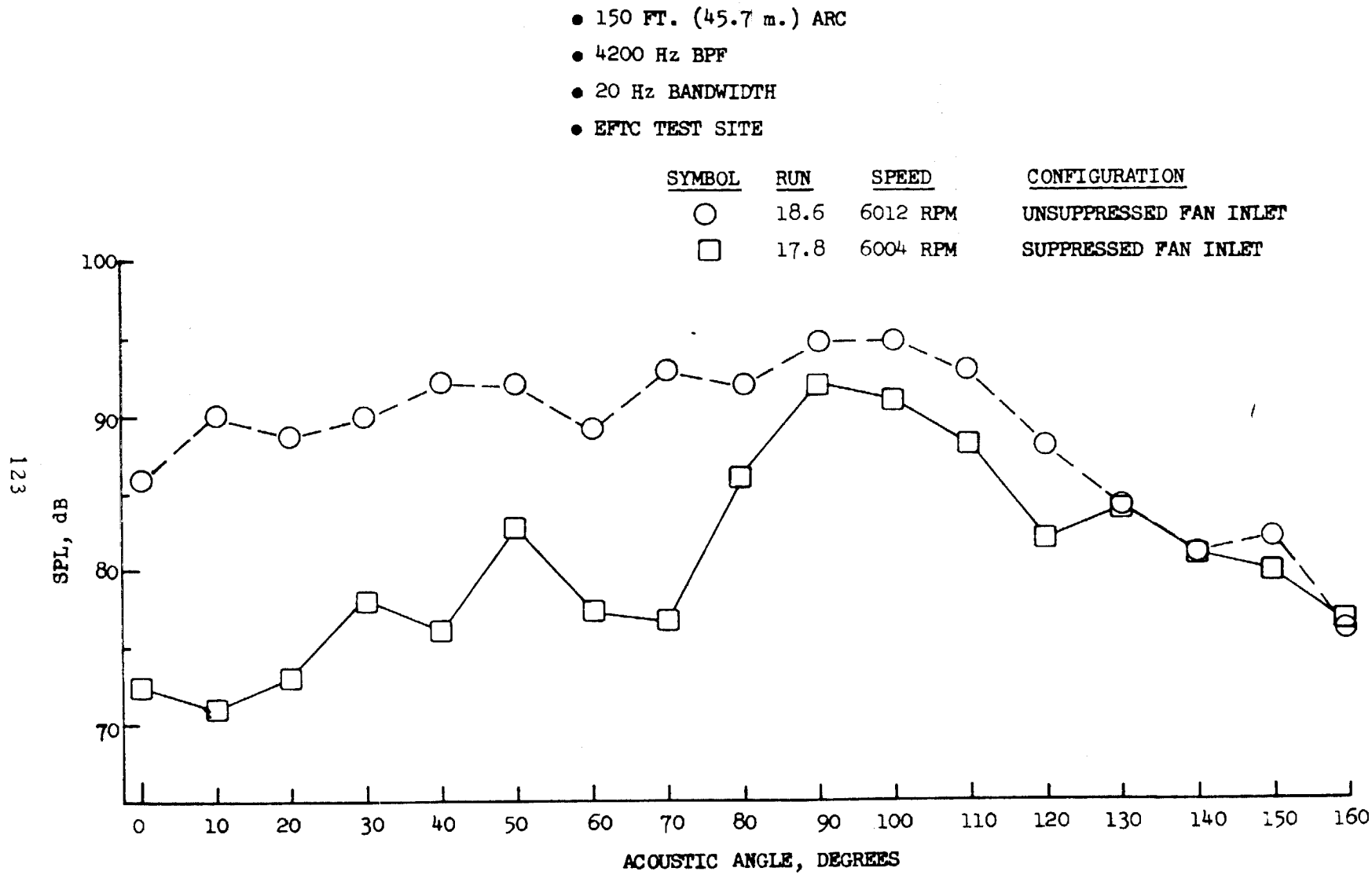

Figure I-55 Effect of Massive Fan Inlet Suppression on Narrowband BPF Directivity Pattern at 6000 RPM

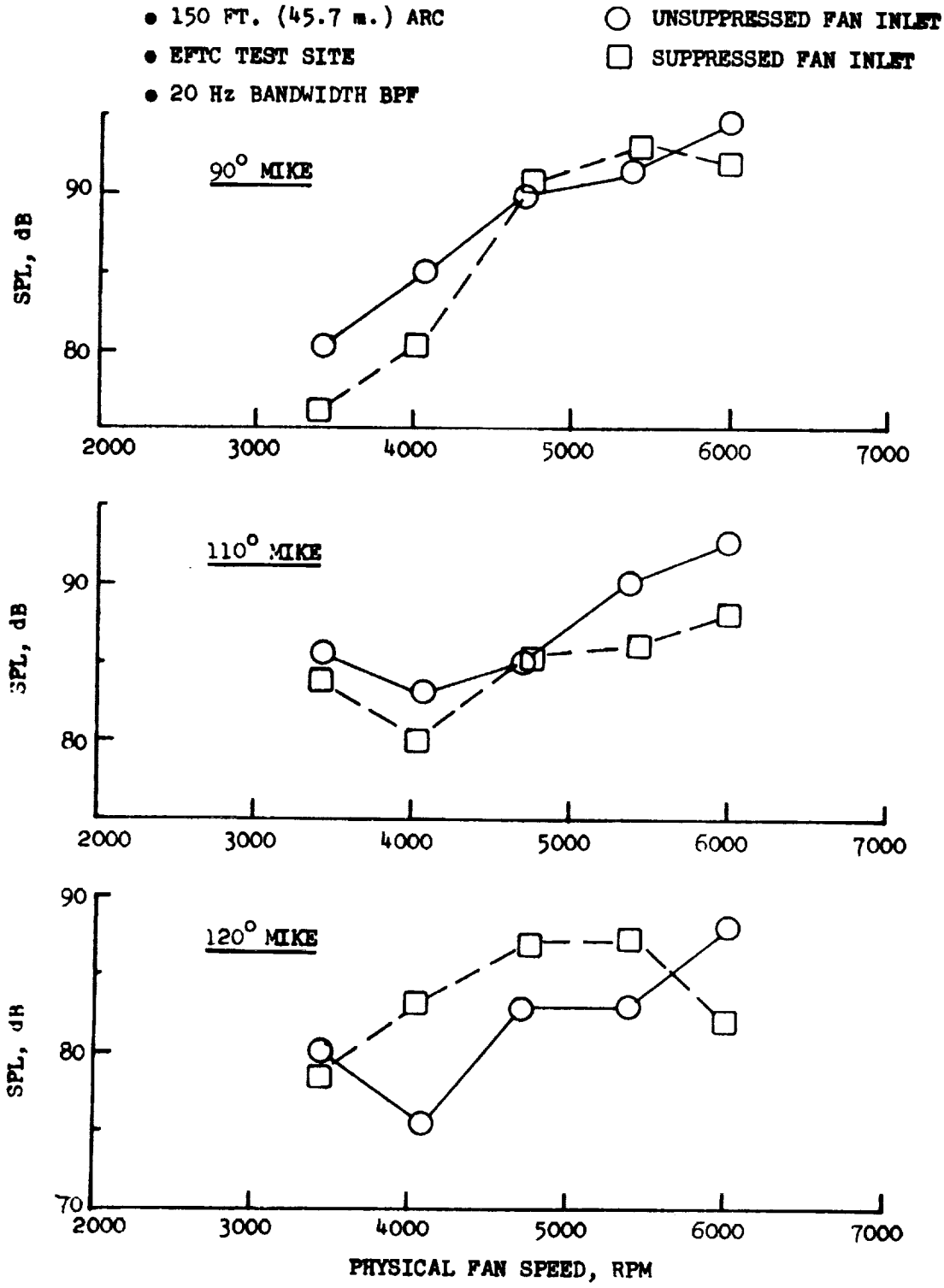

Figure I-56 Effect of Massive Fan Inlet Suppression on Narrowband BPF at 90°, 110° and 120° as a Function of Fan Speed

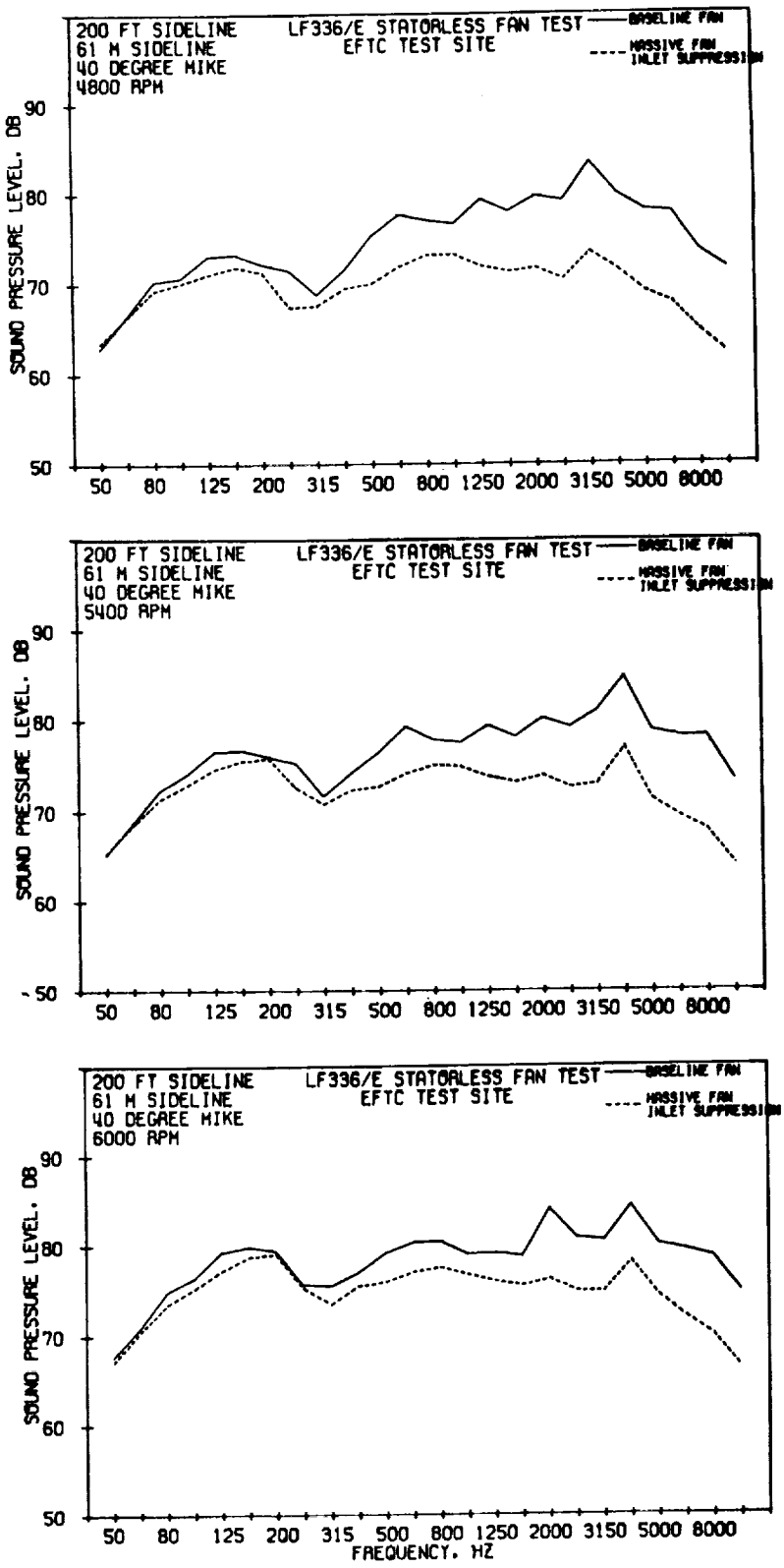

Figure I-57 Effect of Massive Fan Inlet Suppression on 40° 1/3 Octave Band Spectra at 4800, 5400 and 6000 RPM

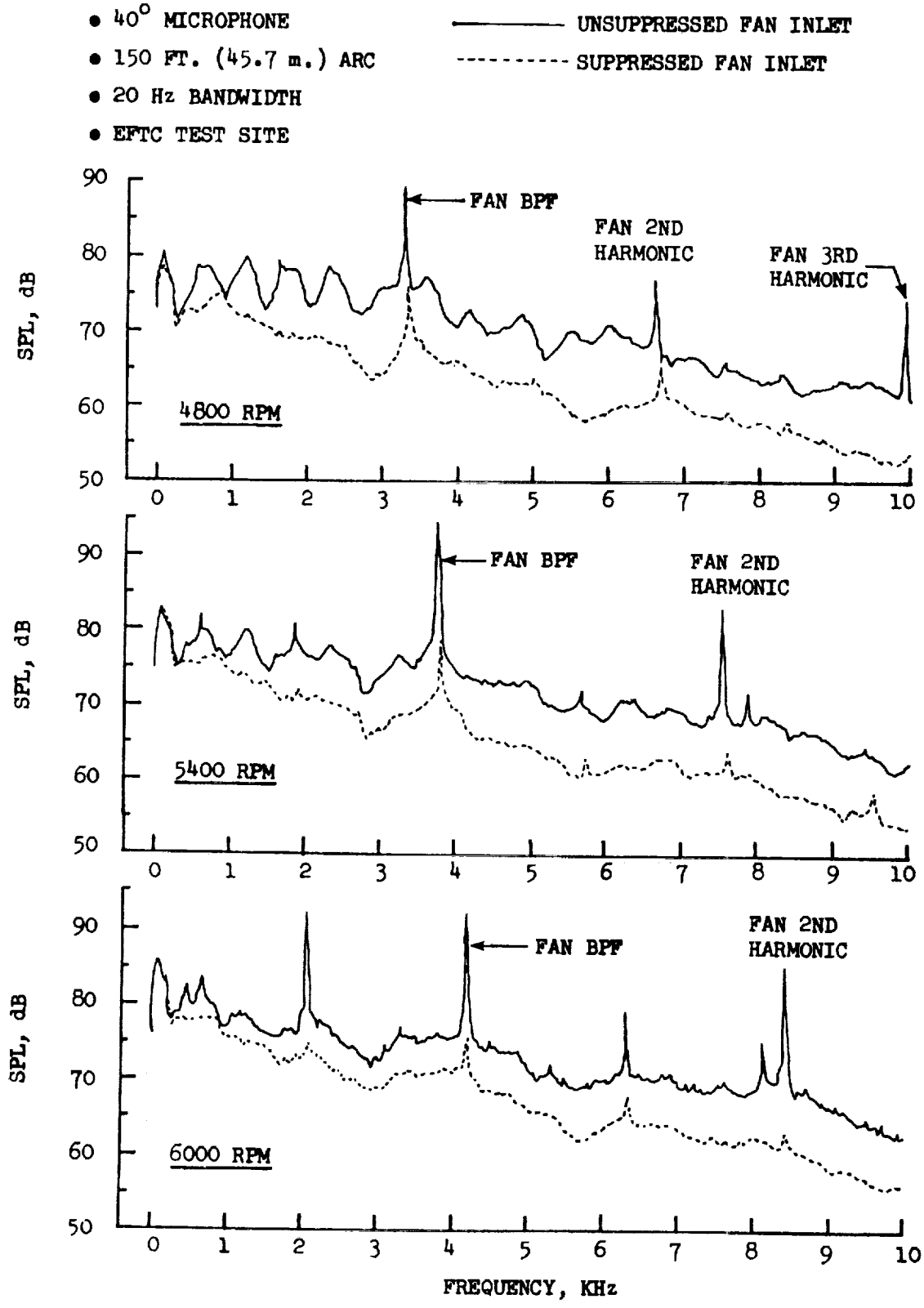

Figure I-58 Effect of Massive Fan Inlet Suppression on 40° Narrowband Spectra at 4800, 5400 and 6000 RPM

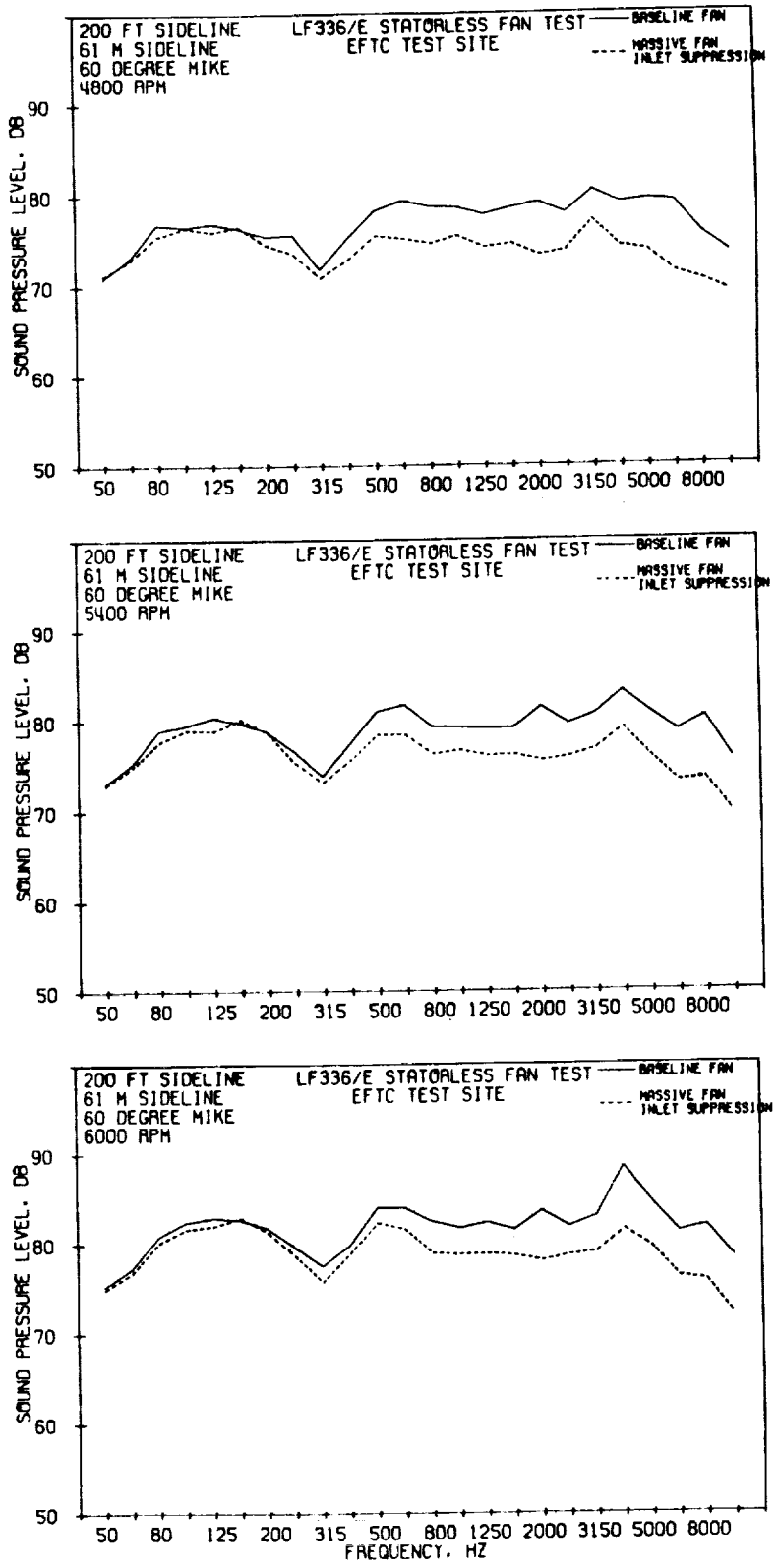

Figure I-59 Effect of Massive Fan Inlet Suppression on 60° 1/3 Octave Band Spectra at 4800, 5400 and 6000 RPM

- 60° MICROPHONE
- 150 FT. (45.7 m.) ARC
- 20 Hz BANDWIDTH
- EFTC TEST SITE

——— UNSUPPRESSED FAN INLET

- - - - - - - - - SUPPRESSED FAN INLET

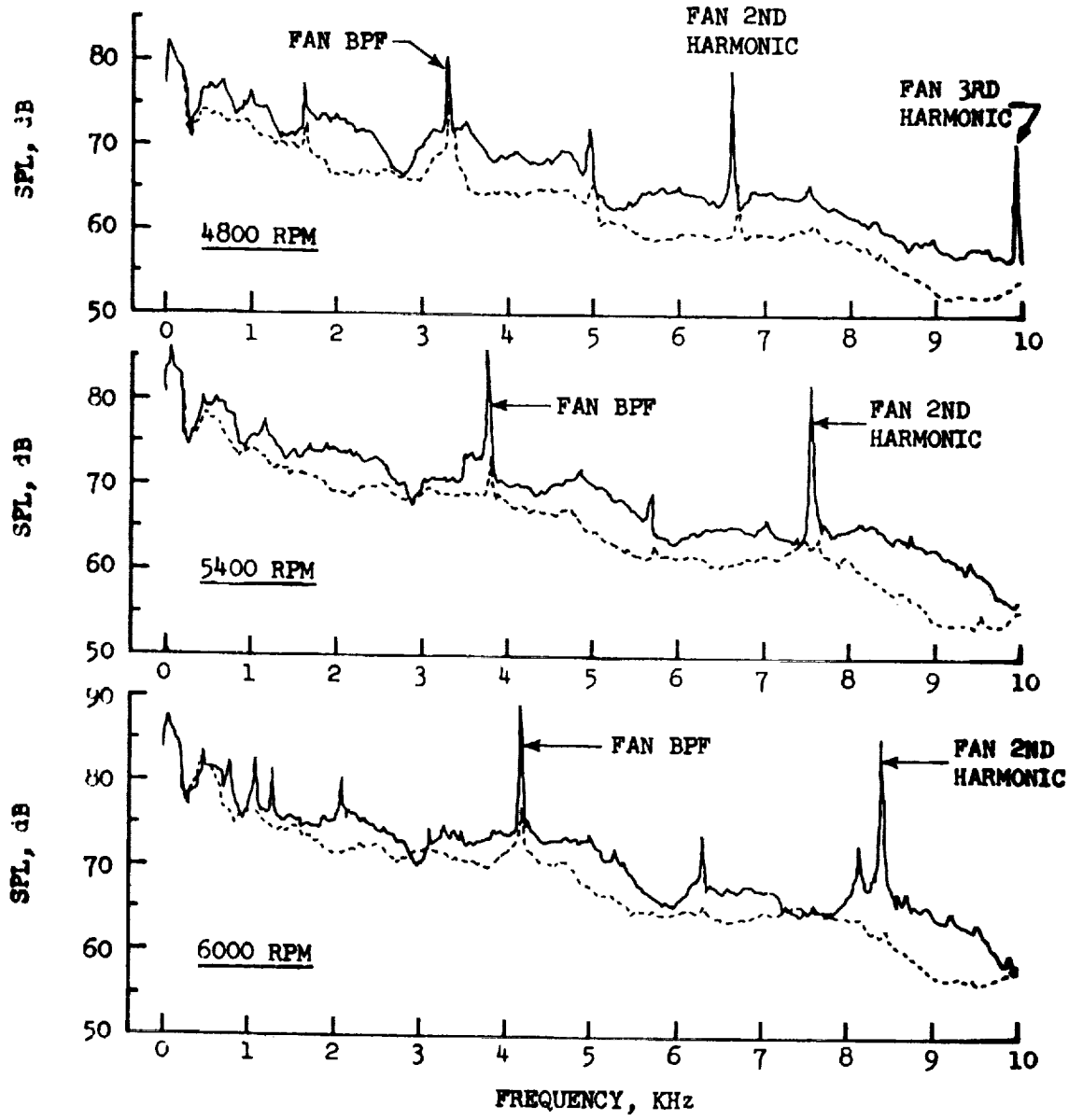

Figure I-60 Effect of Massive Fan Inlet Suppression on 60° Narrowband Spectra at 4800, 5400 and 6000 RPM

- 150 FT. (45.7 m.) ARC
- EFTC TEST SITE
- 20 Hz BANDWIDTH BPF

○ UNSUPPRESSED FAN INLET
□ SUPPRESSED FAN INLET

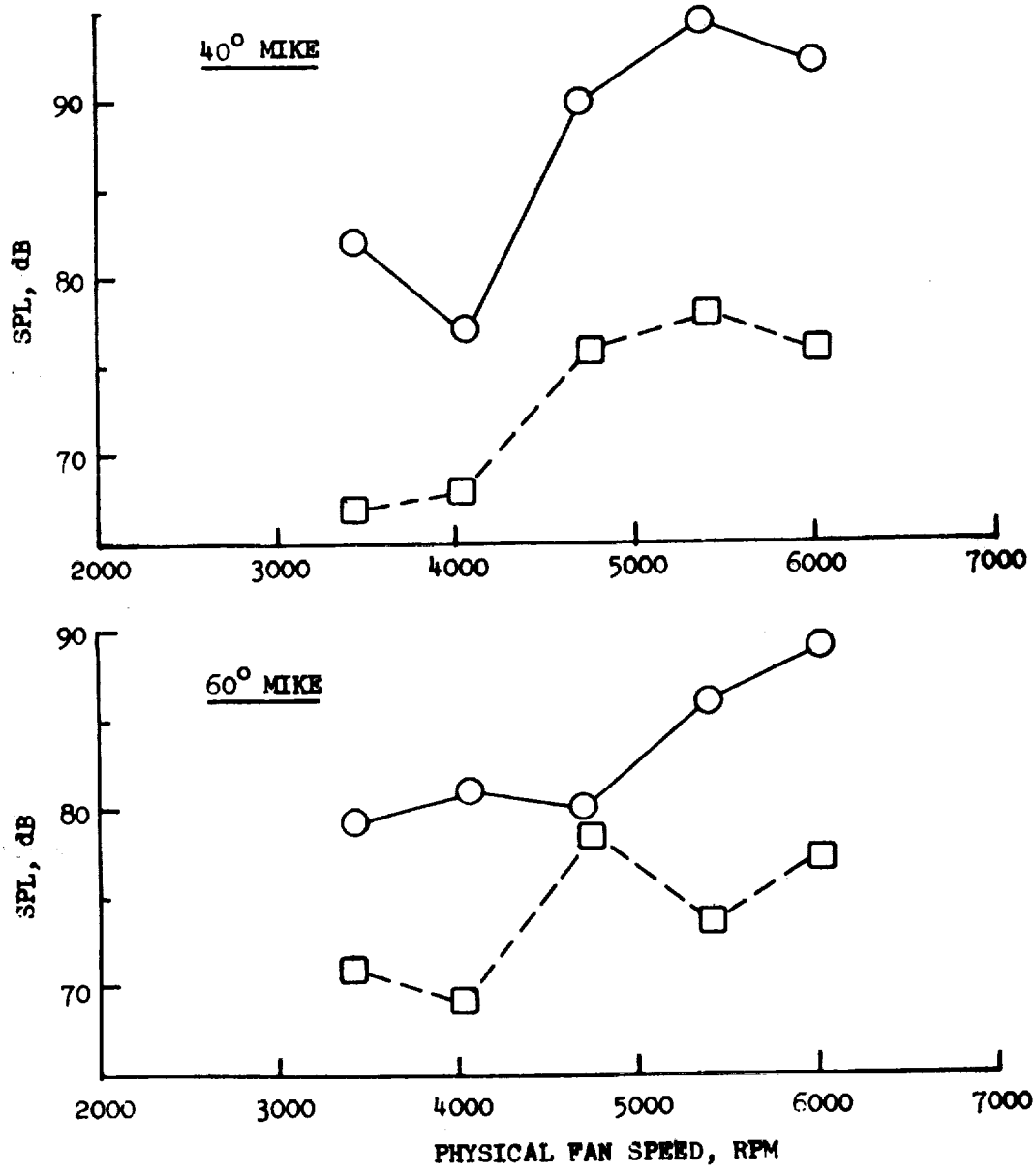

Figure I-61 Effect of Massive Fan Inlet Suppression on 40° and 60° Narrowband BPF as a Function of Fan Speed

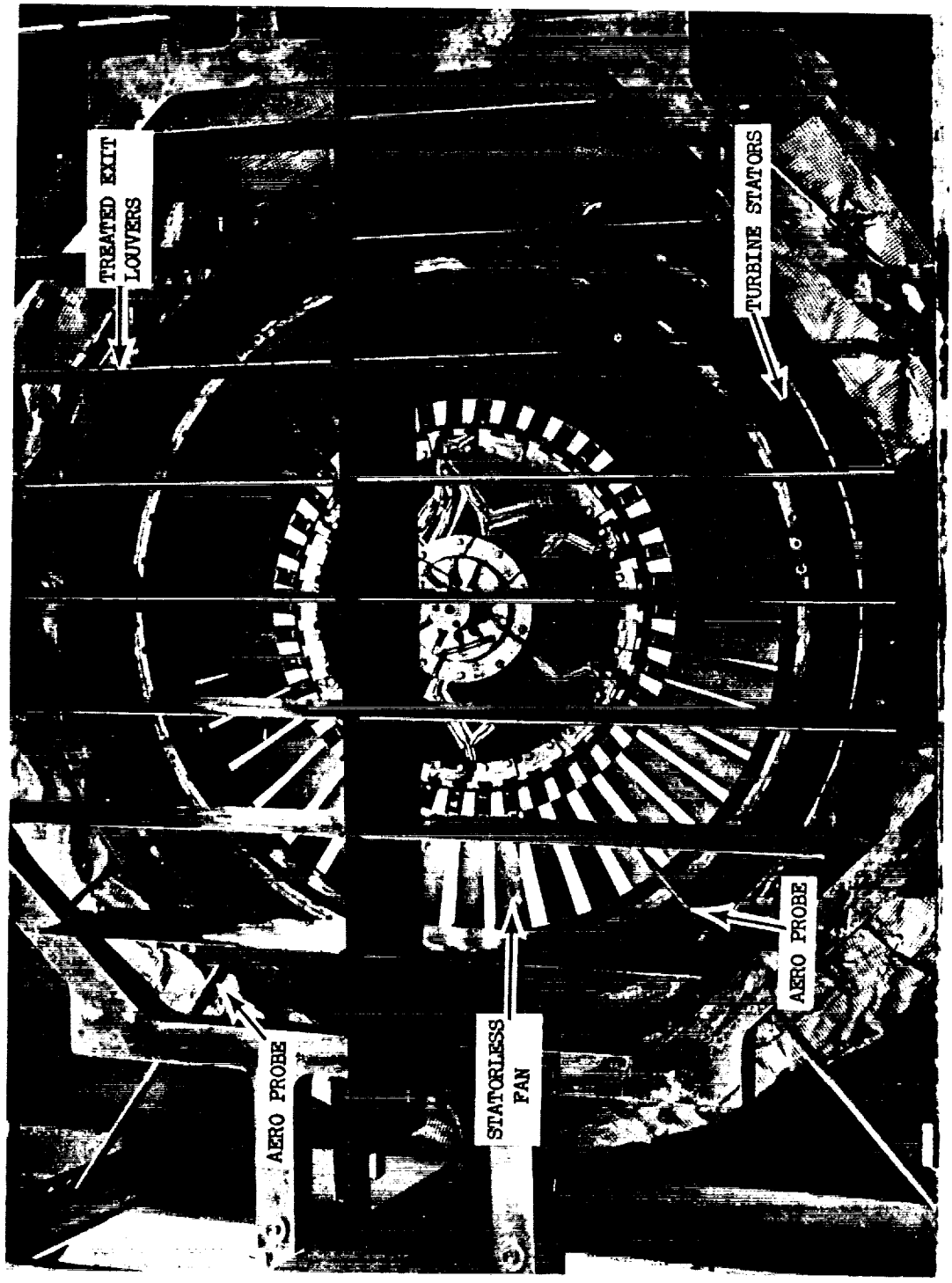

Figure I-62 Treated Exit Louver System

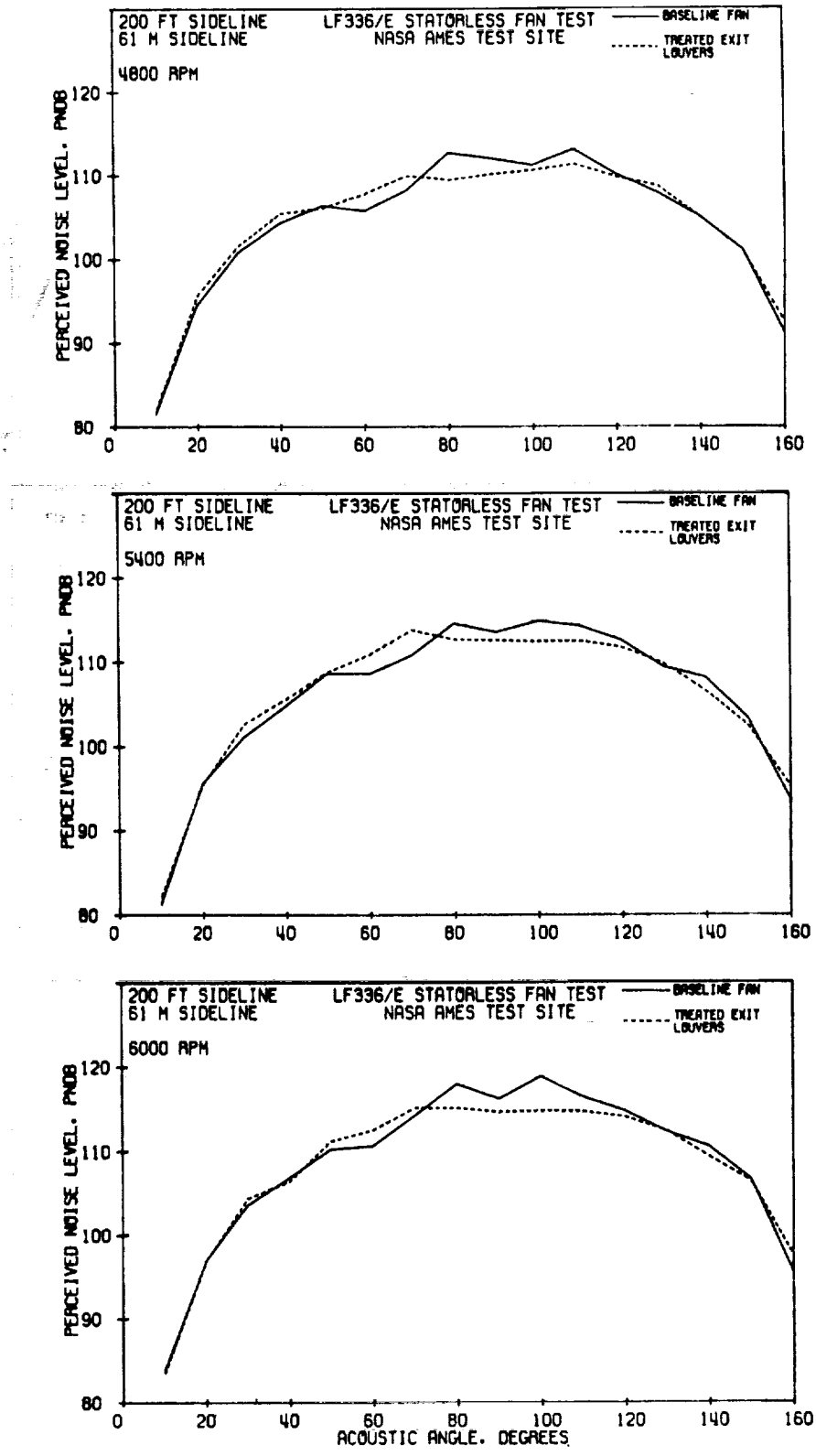

Figure I-63 Effects of Treated Exit Louvers on PNL Directivity Patterns

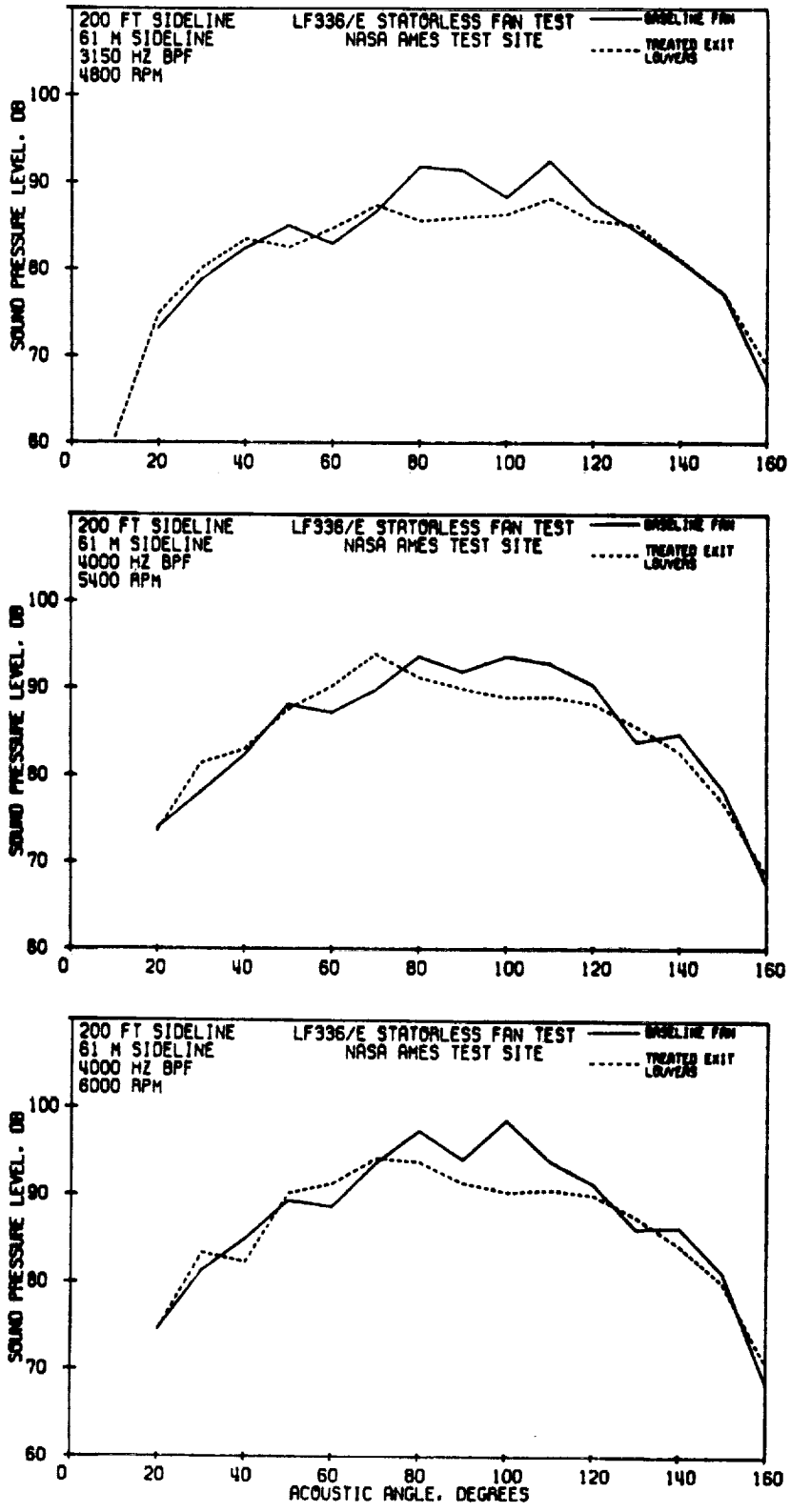

Figure I-64 Effects of Treated Exit Louvers on 1/3 Octave Band BPF Directivity Patterns

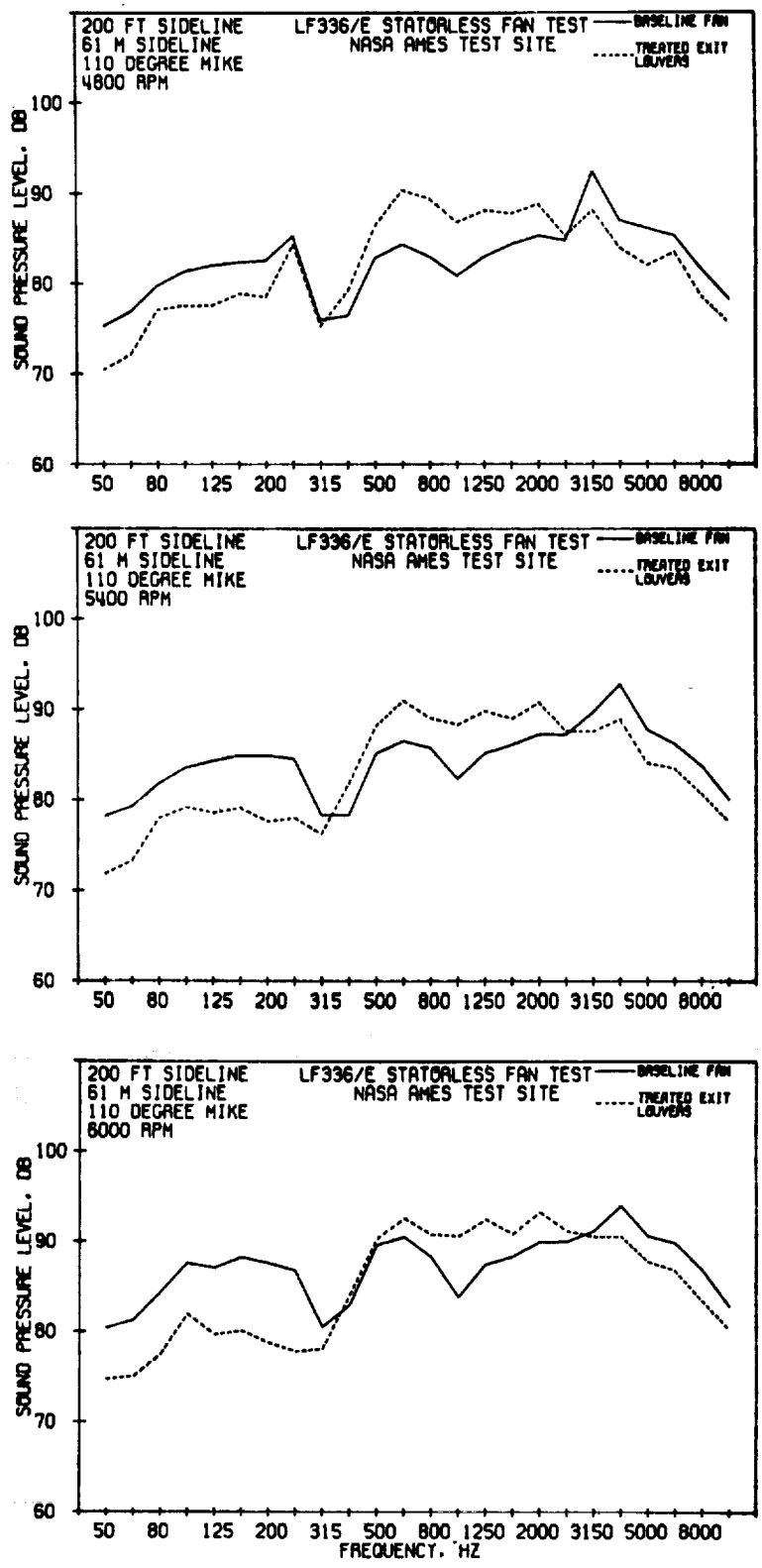

Figure I-65 Effects of Treated Exit Louvers on 110° 1/3 Octave Spectra

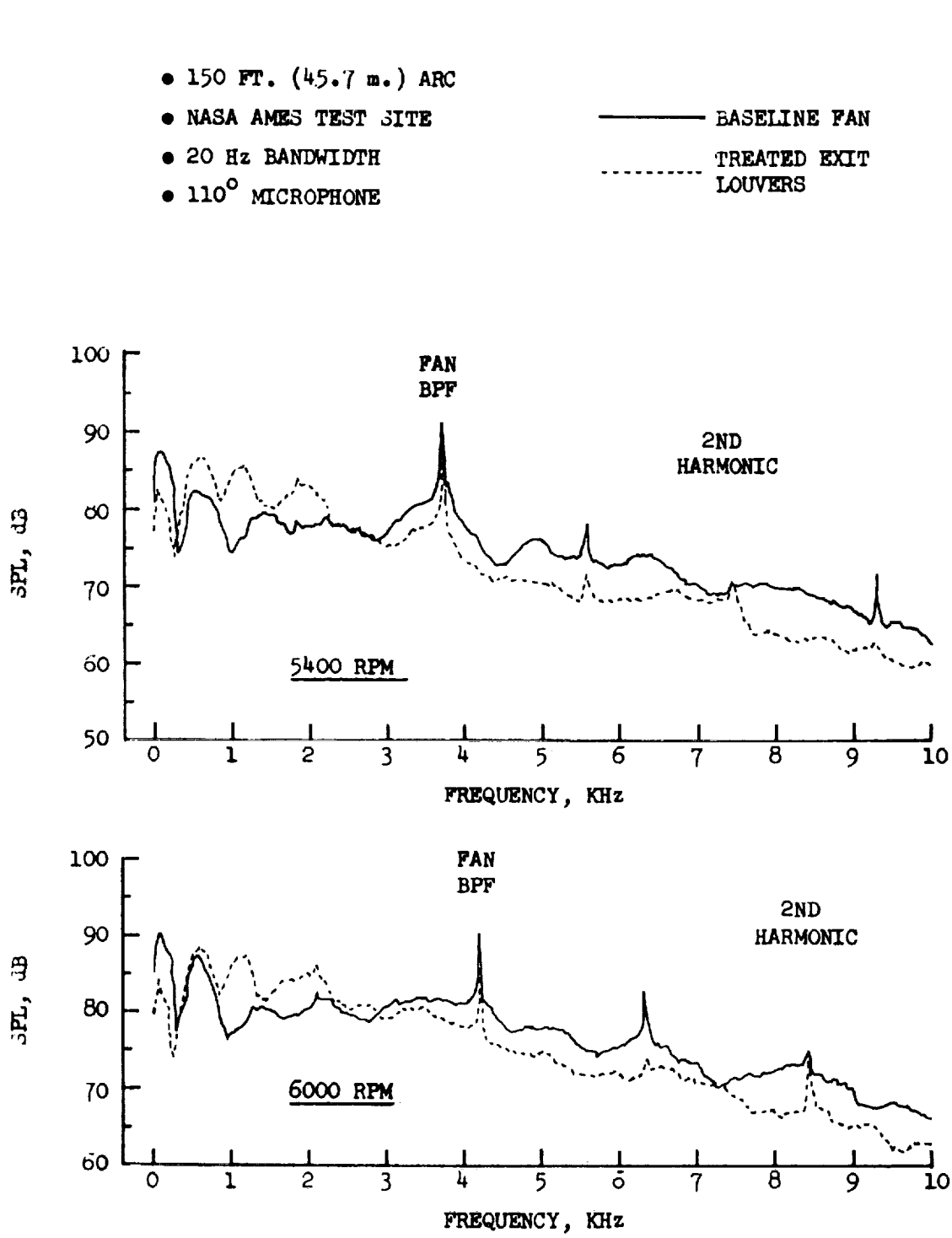

Figure I-66 Effect of Treated Exit Louvers on 110° Narrowband Spectra at 5400 and 6000 RPM

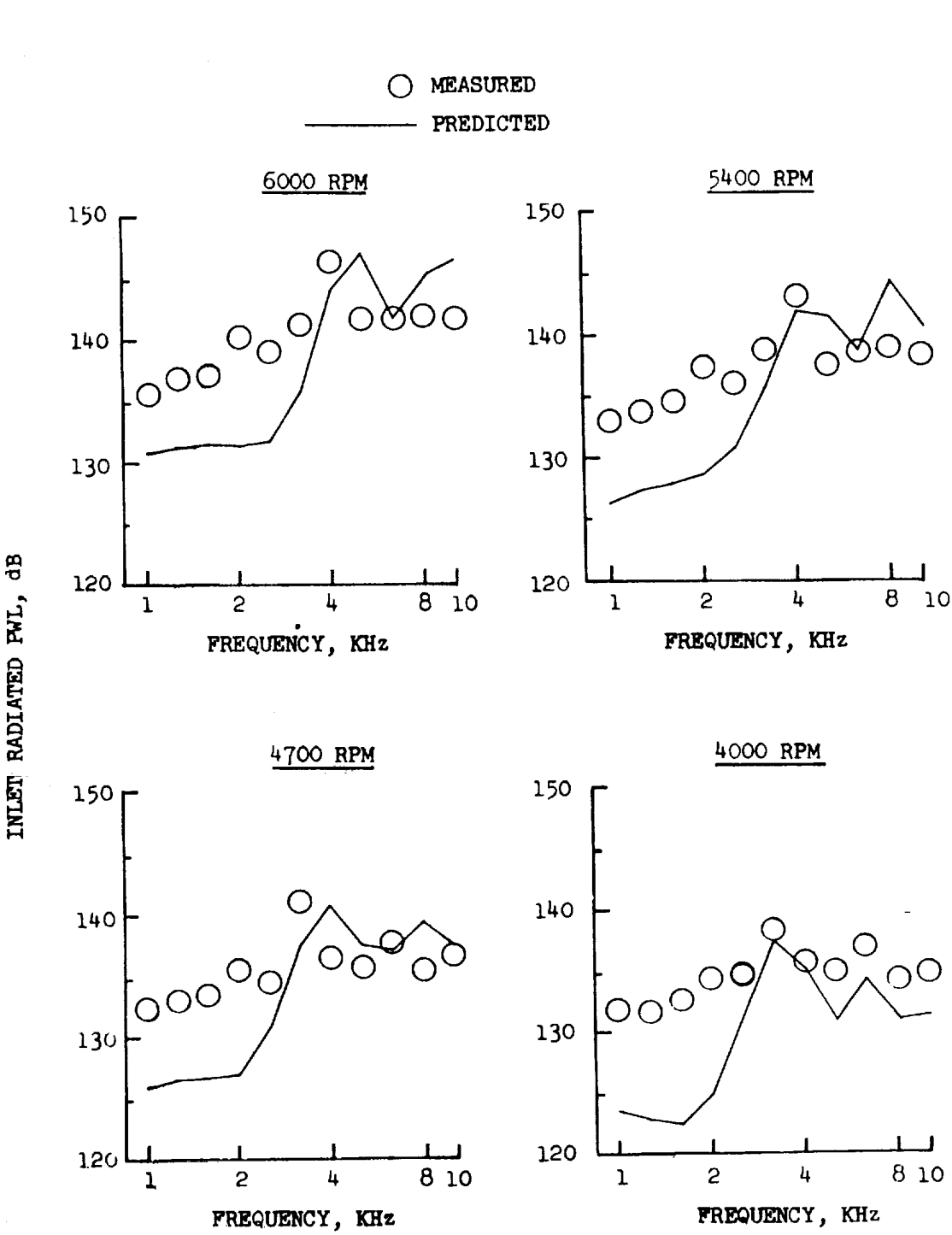

Figure I-67 Comparison of Measured and Predicted Inlet Radiated Sound Power Levels

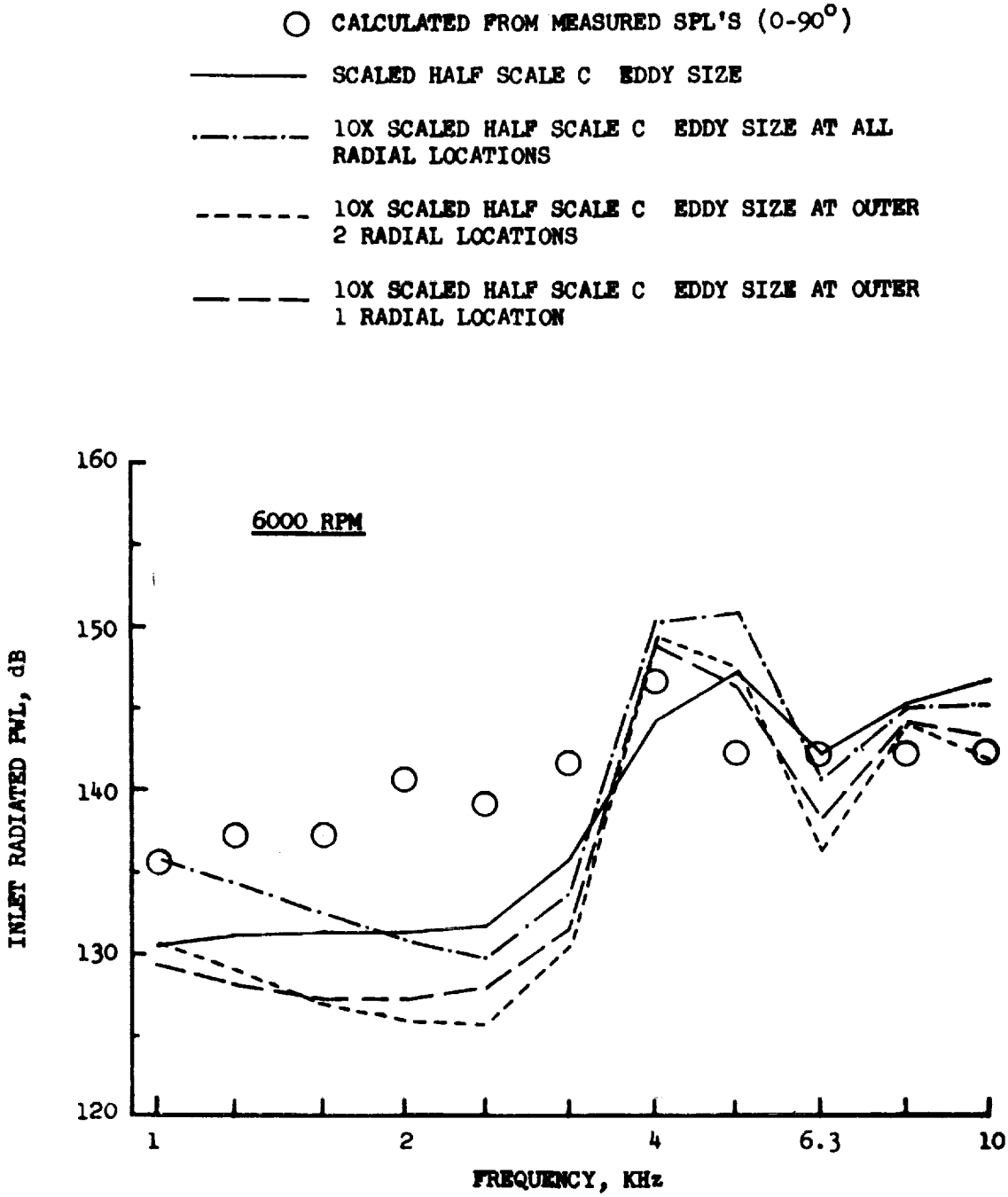

Figure I-68 Comparison of Measured and Predicted Inlet Radiated Sound Power Levels Varying Eddy Size at Radial Locations

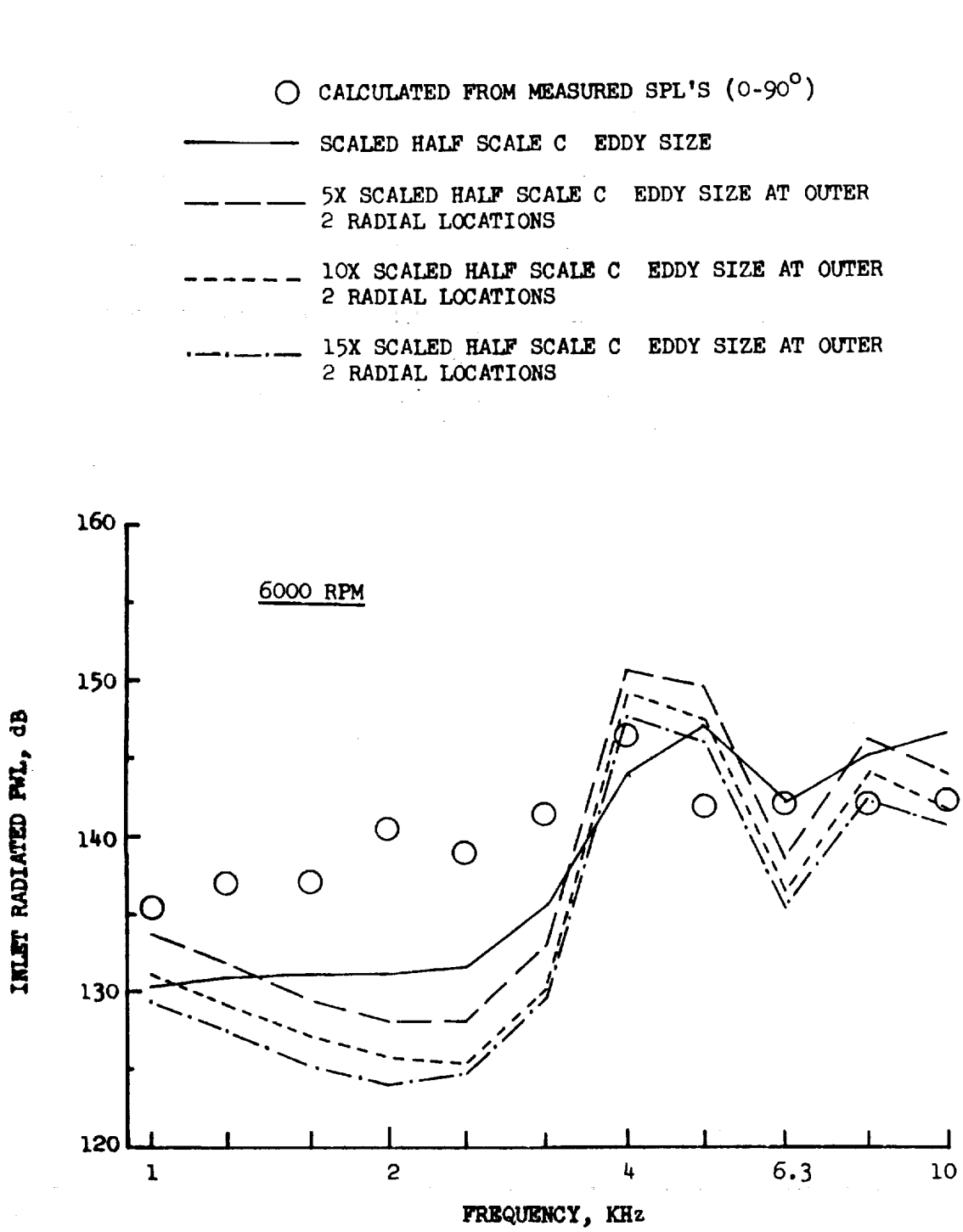

Figure I-69 Comparison of Measured and Predicted Inlet Radiated Sound Power Levels Varying Eddy Size at Outer Two Radial Locations

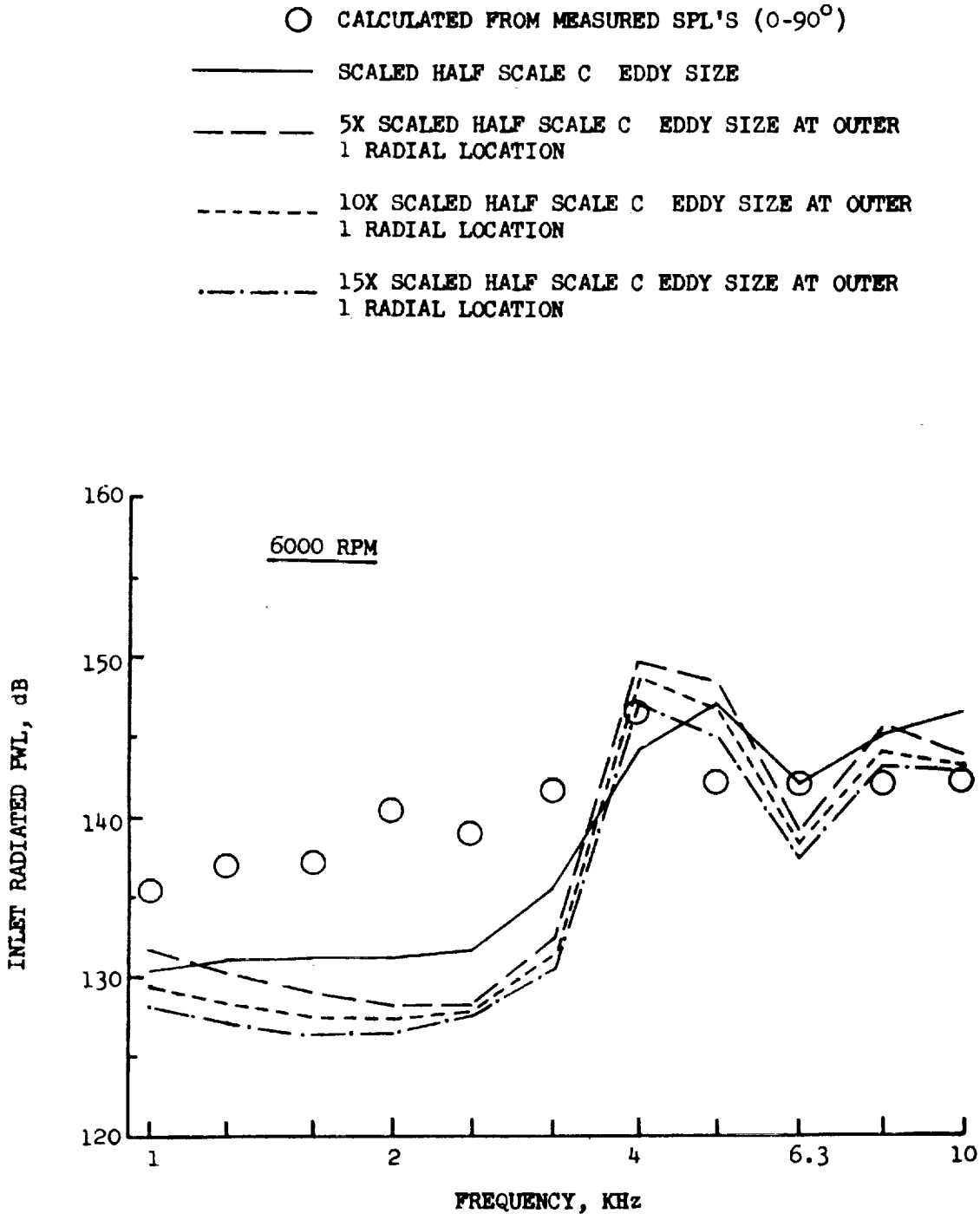

Figure I-70 Comparison of Measured and Predicted Inlet Radiated Sound Power Levels Varying Eddy Size at Outermost Radial Location

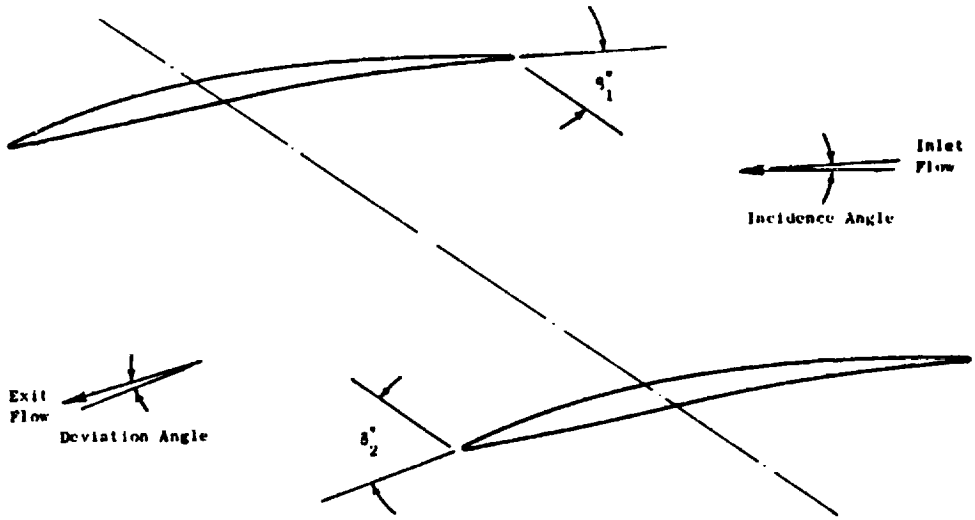

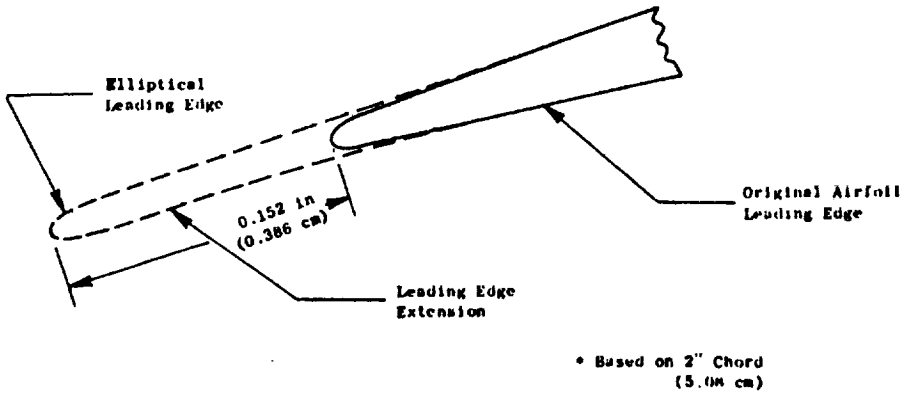

Figure II-1 Cascade Airfoil Geometry

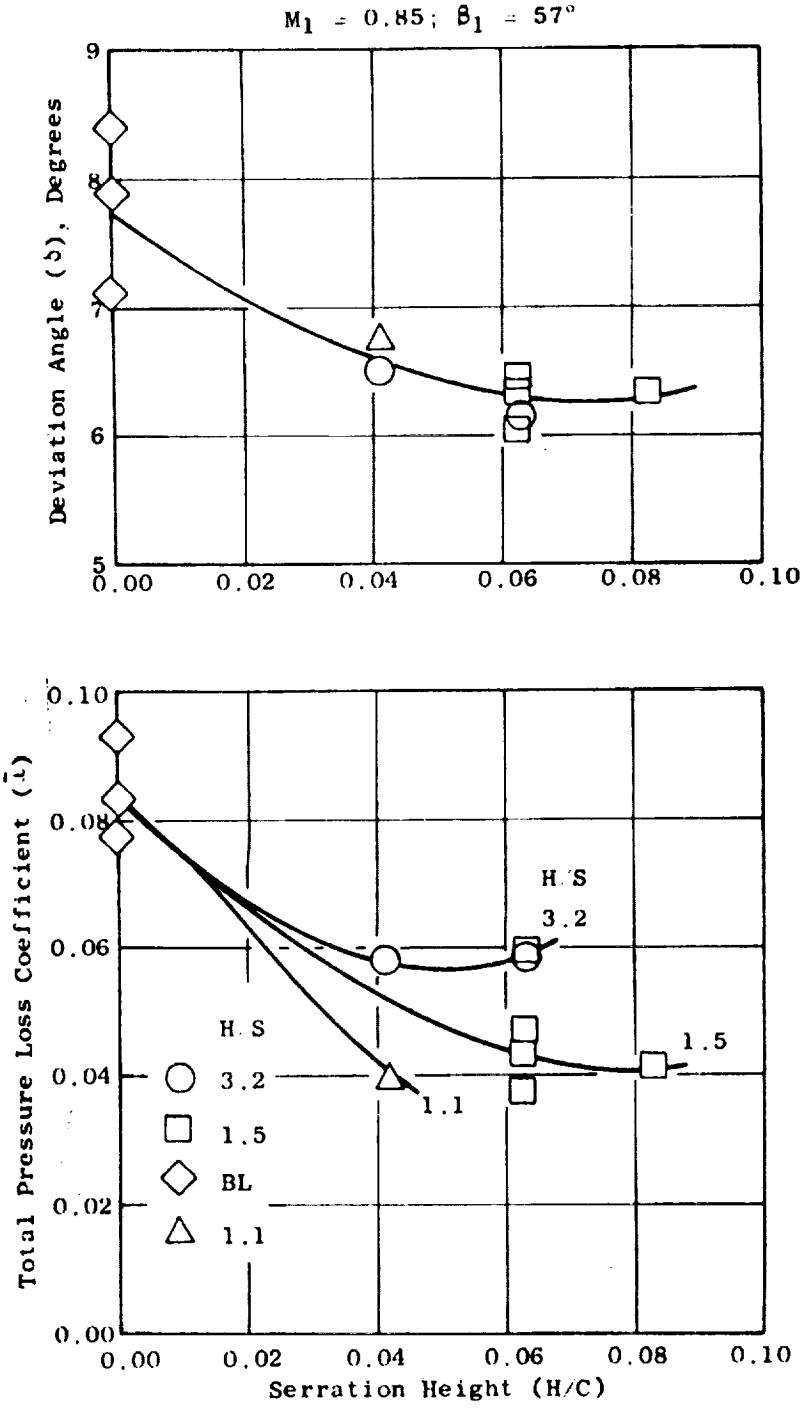

Figure II-2 Effects of Serration Geometry on Blade Aerodynamic Performance

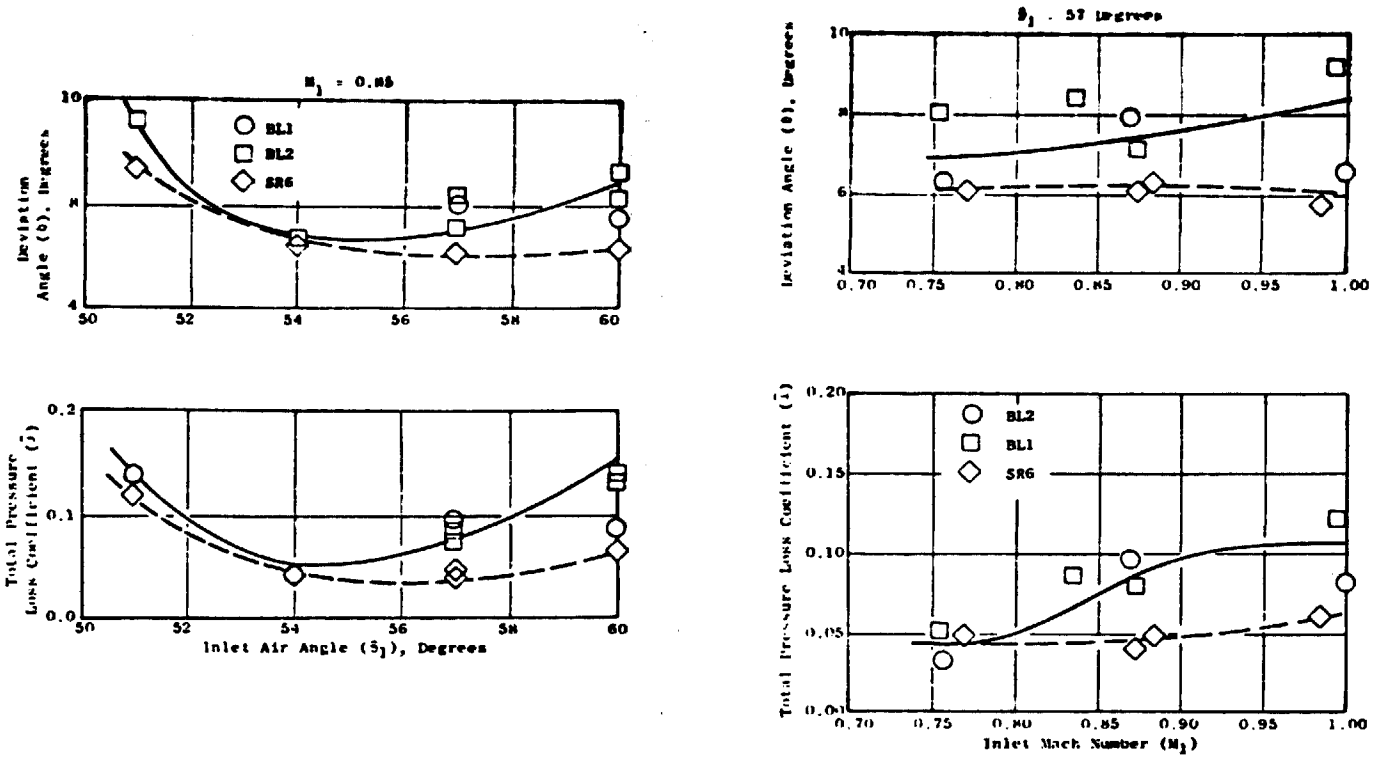

Figure II-3 Effects of Serrations on Off-Design Aerodynamic Performance

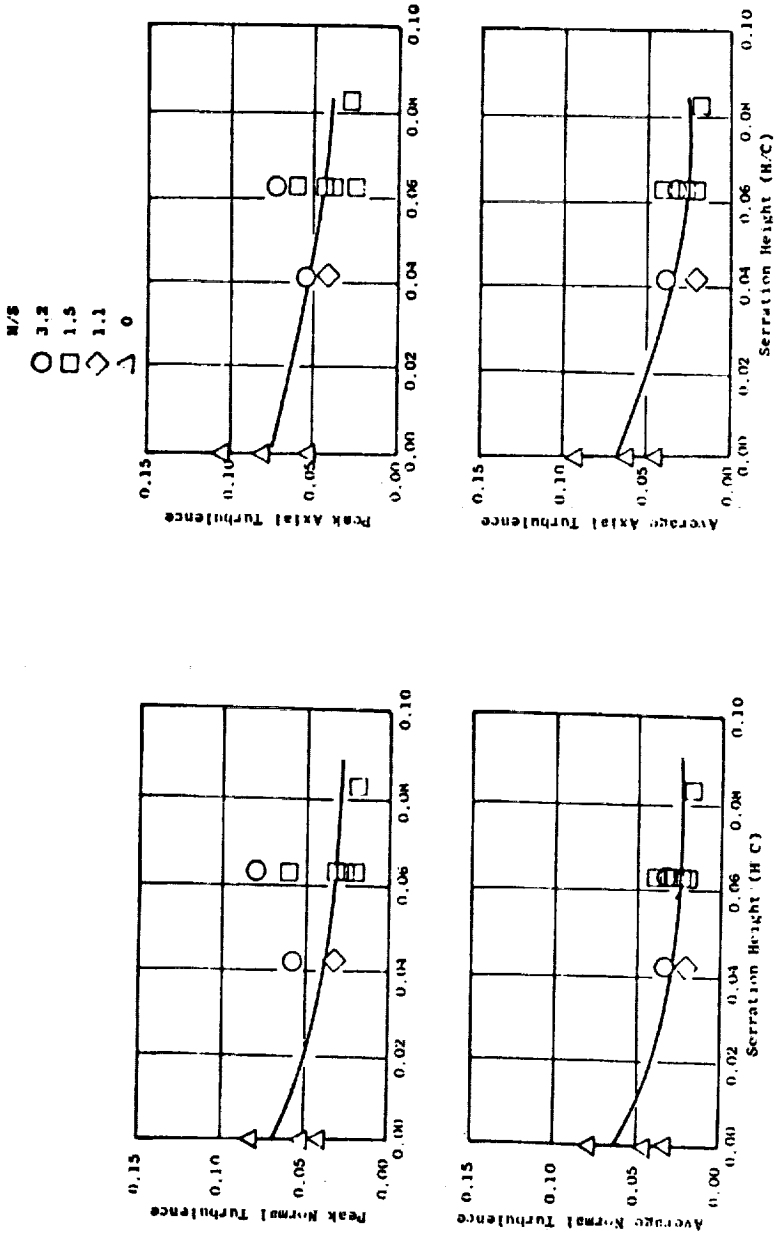

Figure II-4 Effects of Serration Geometry on Exit Turbulence Levels

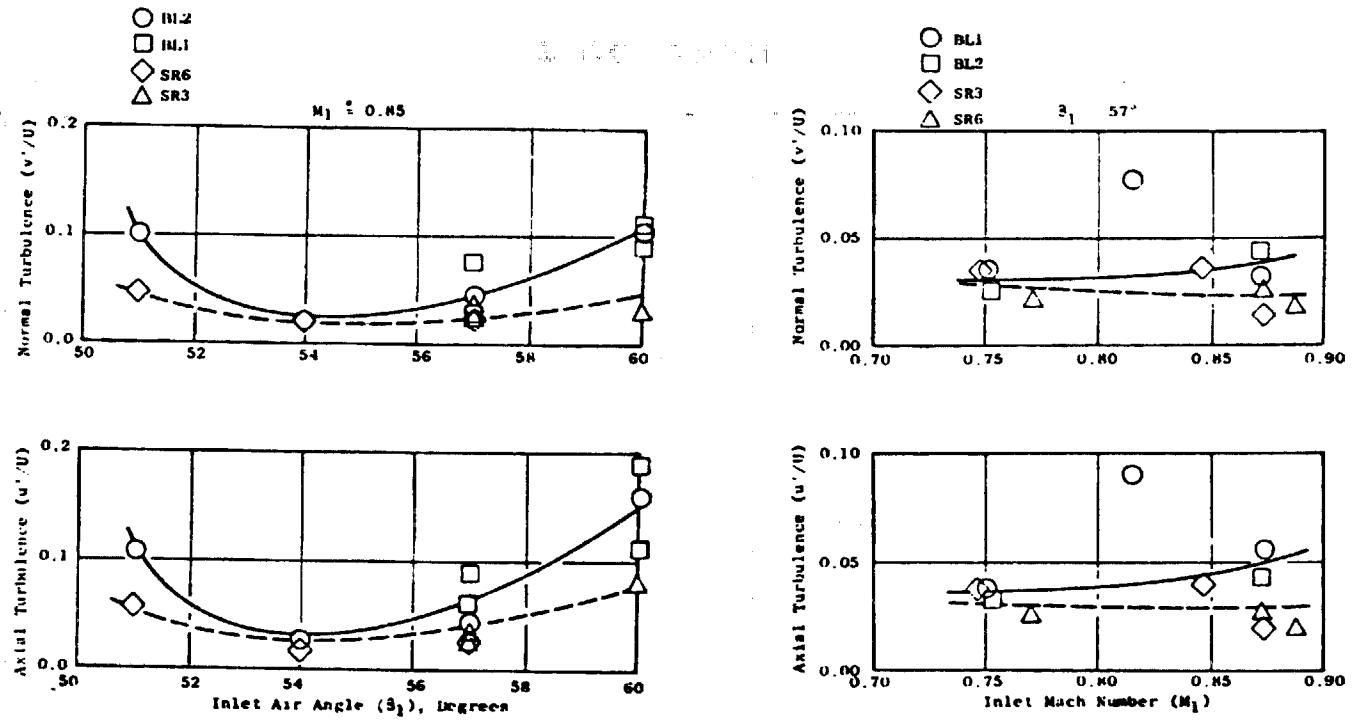

Figure II-5 Effects of Serrations on Turbulence Levels During Off-Design Operation

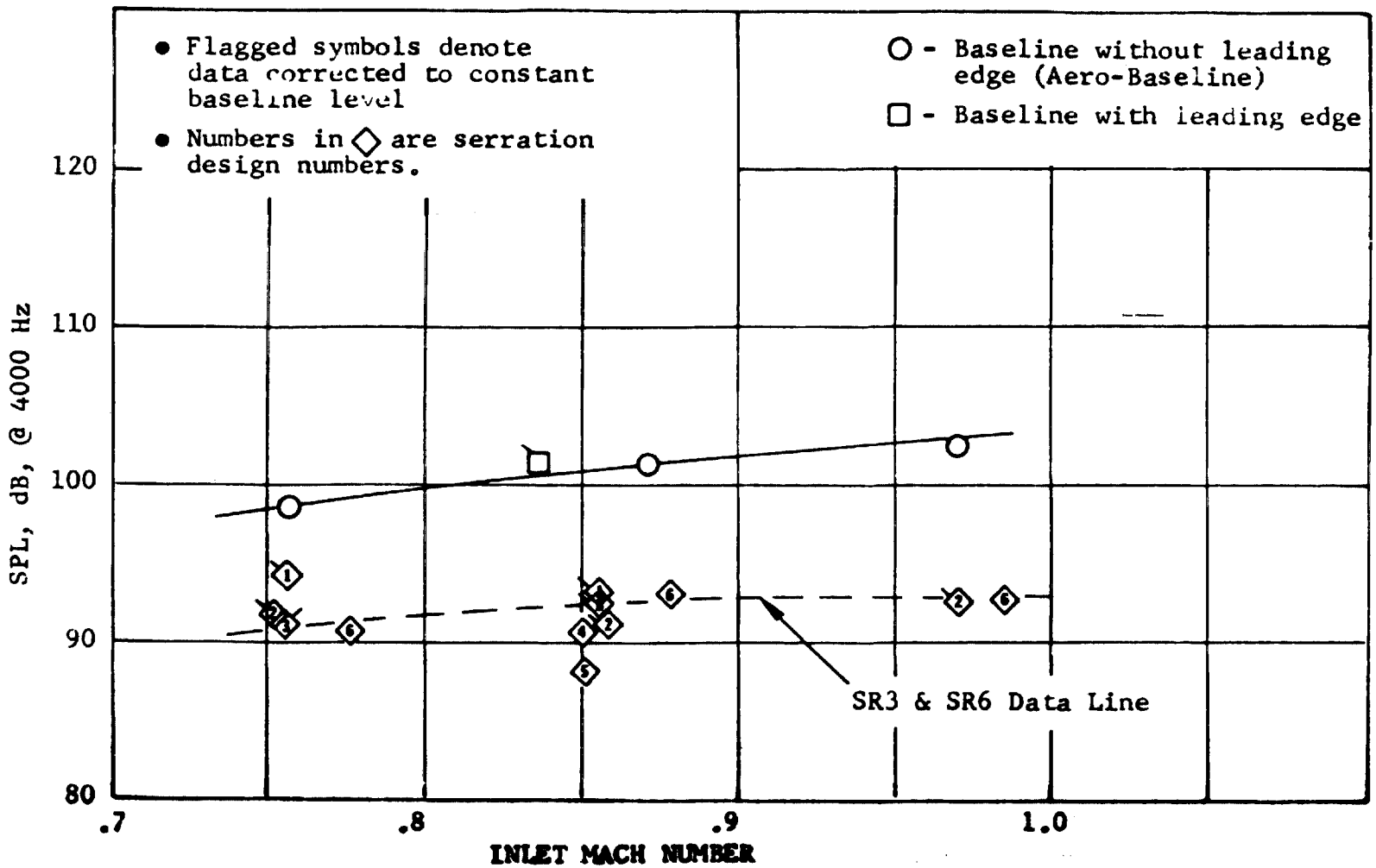

Figure II-6 Unserrated and Serrated Blades Measured Noise at 4000 Hertz

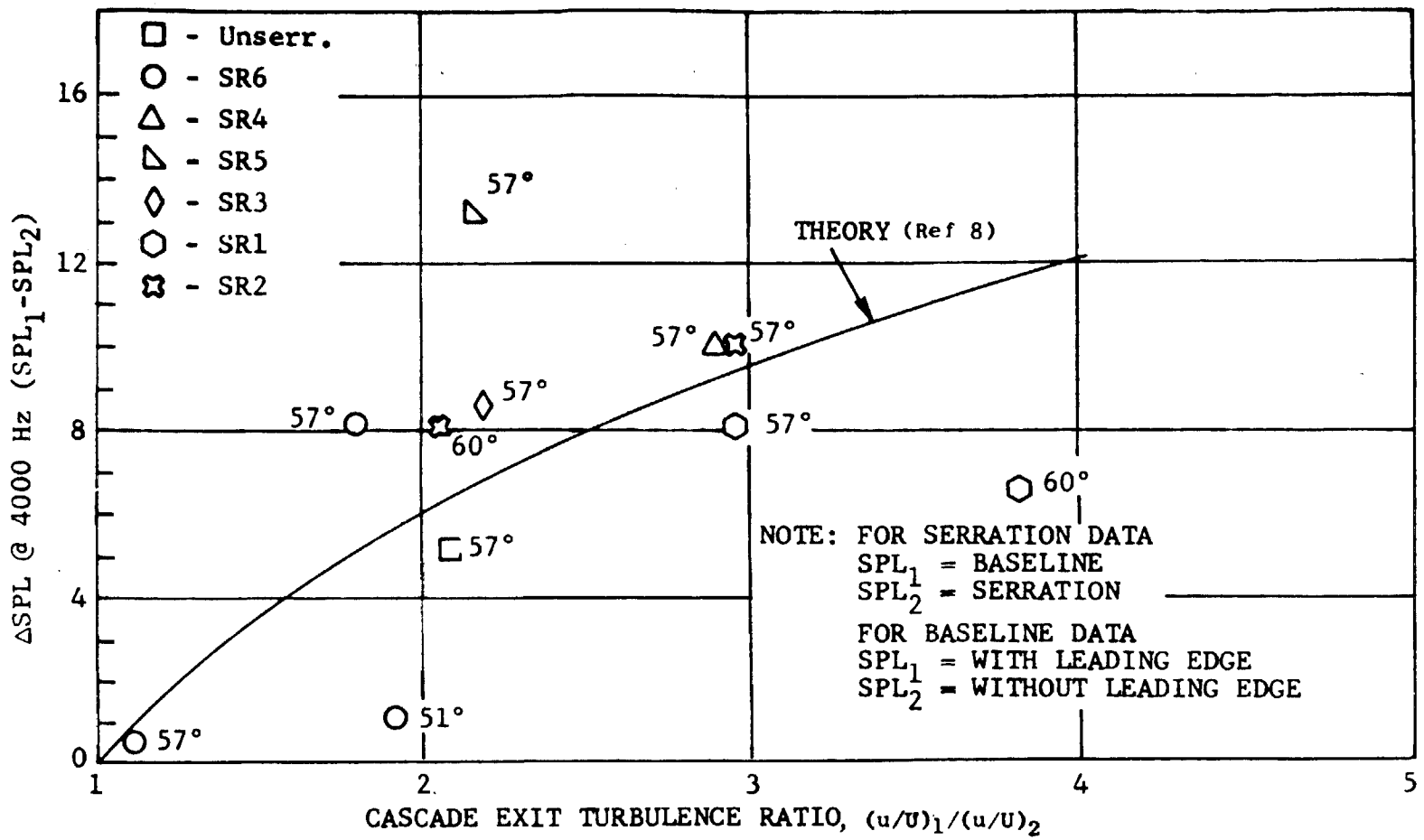

Figure II-7 Comparison of Measured Noise Reduction and Theoretical Prediction, Mach = 0.85

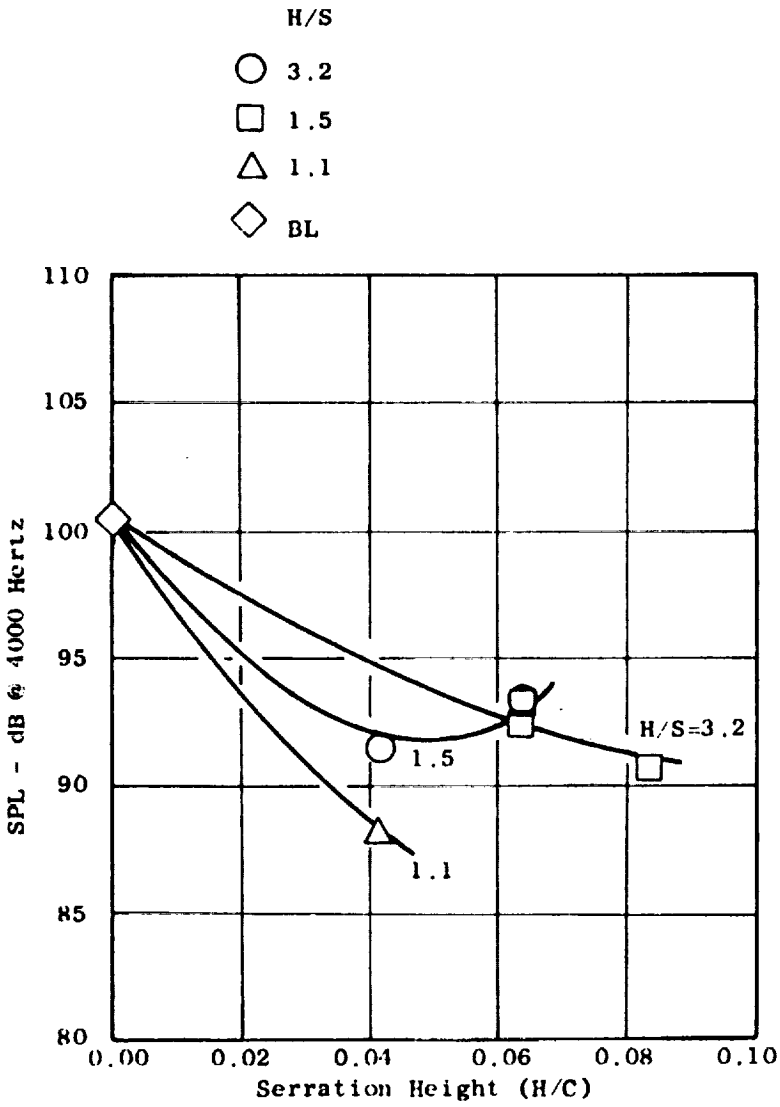

Figure II-8 Effects of Serration Geometry on Acoustic Performance

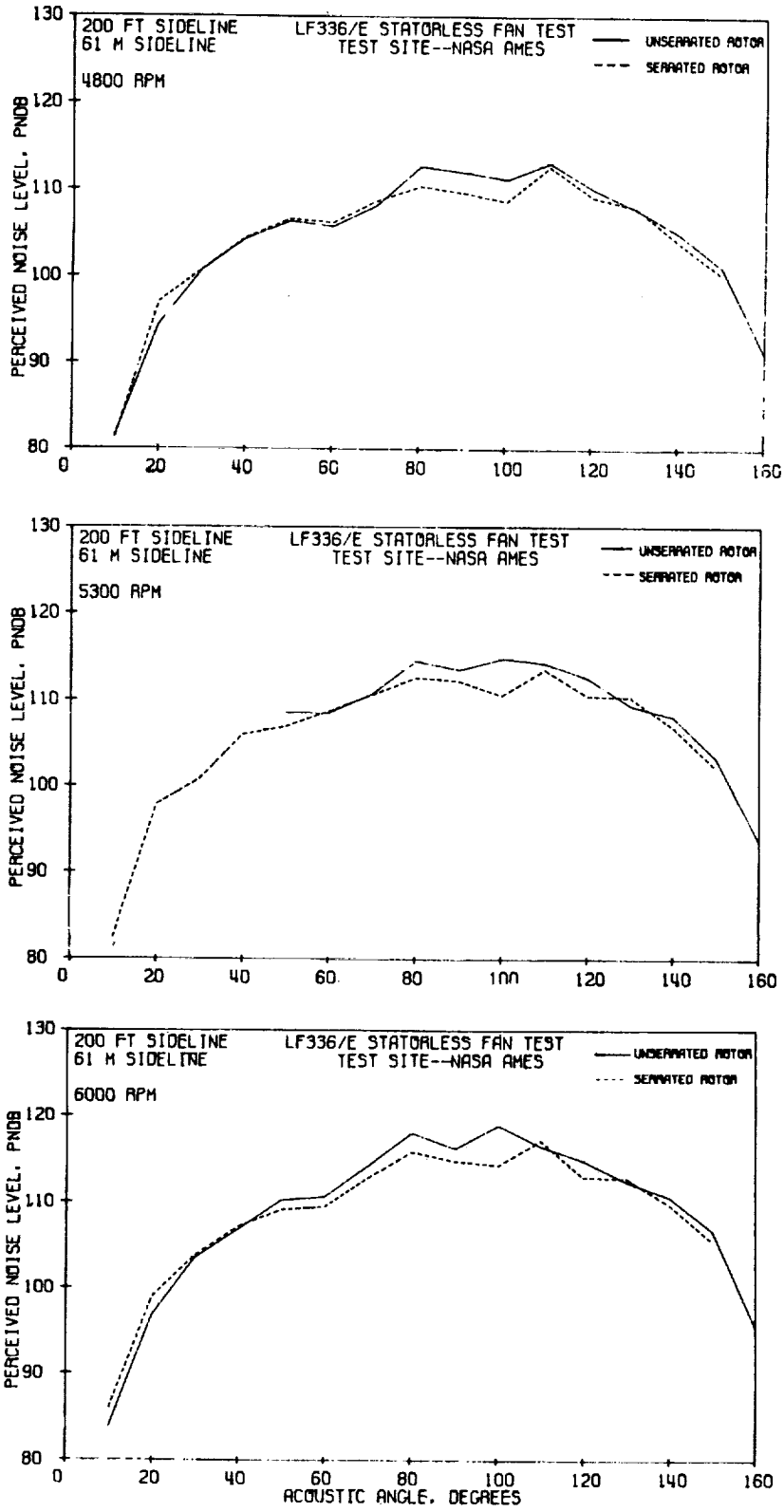

Figure II-9 Serrated and Unserrated LF336/E PNL Directivity Patterns

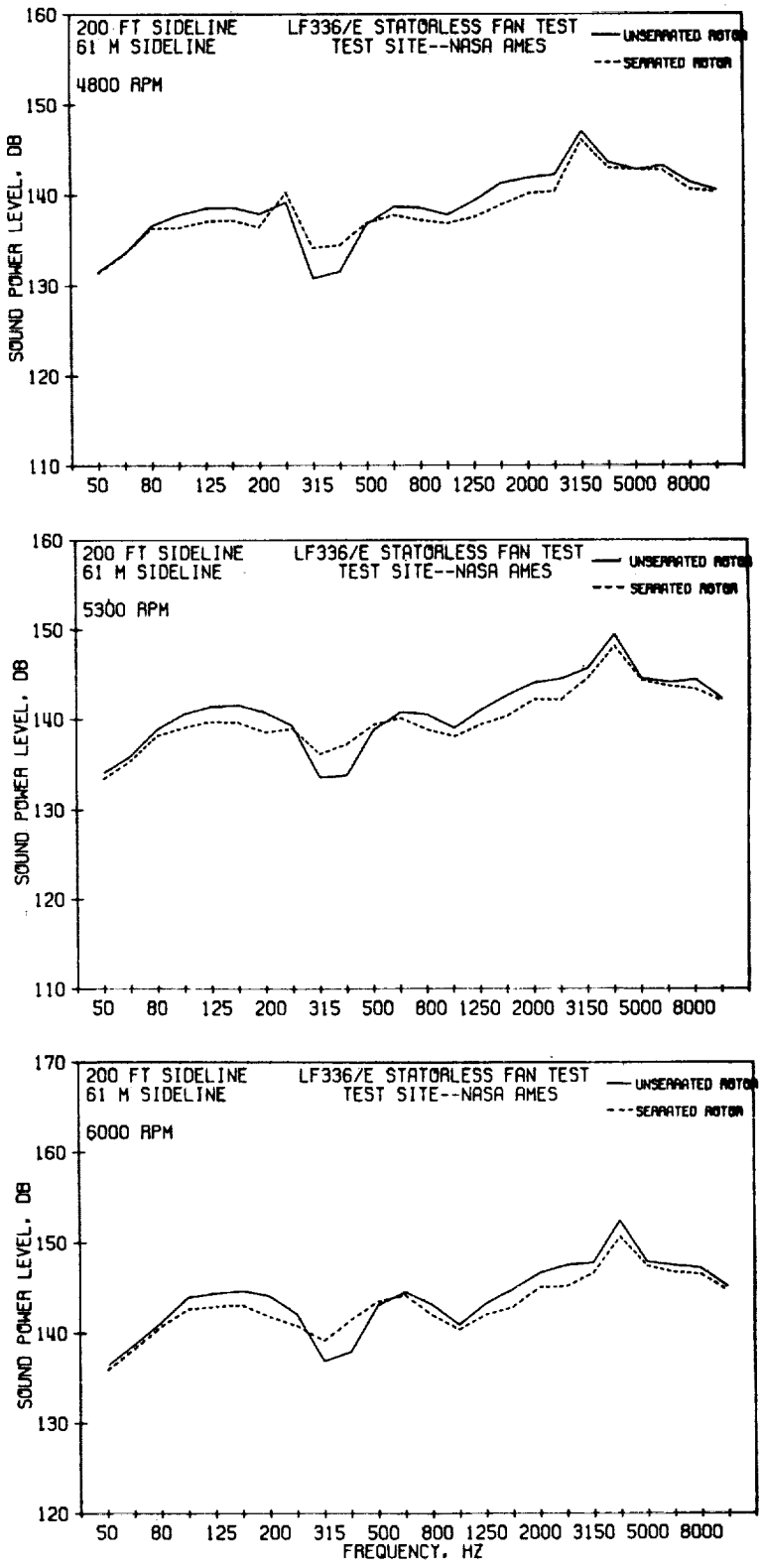

Figure II-10 Serrated and Unserrated LF336/E PWL Spectra

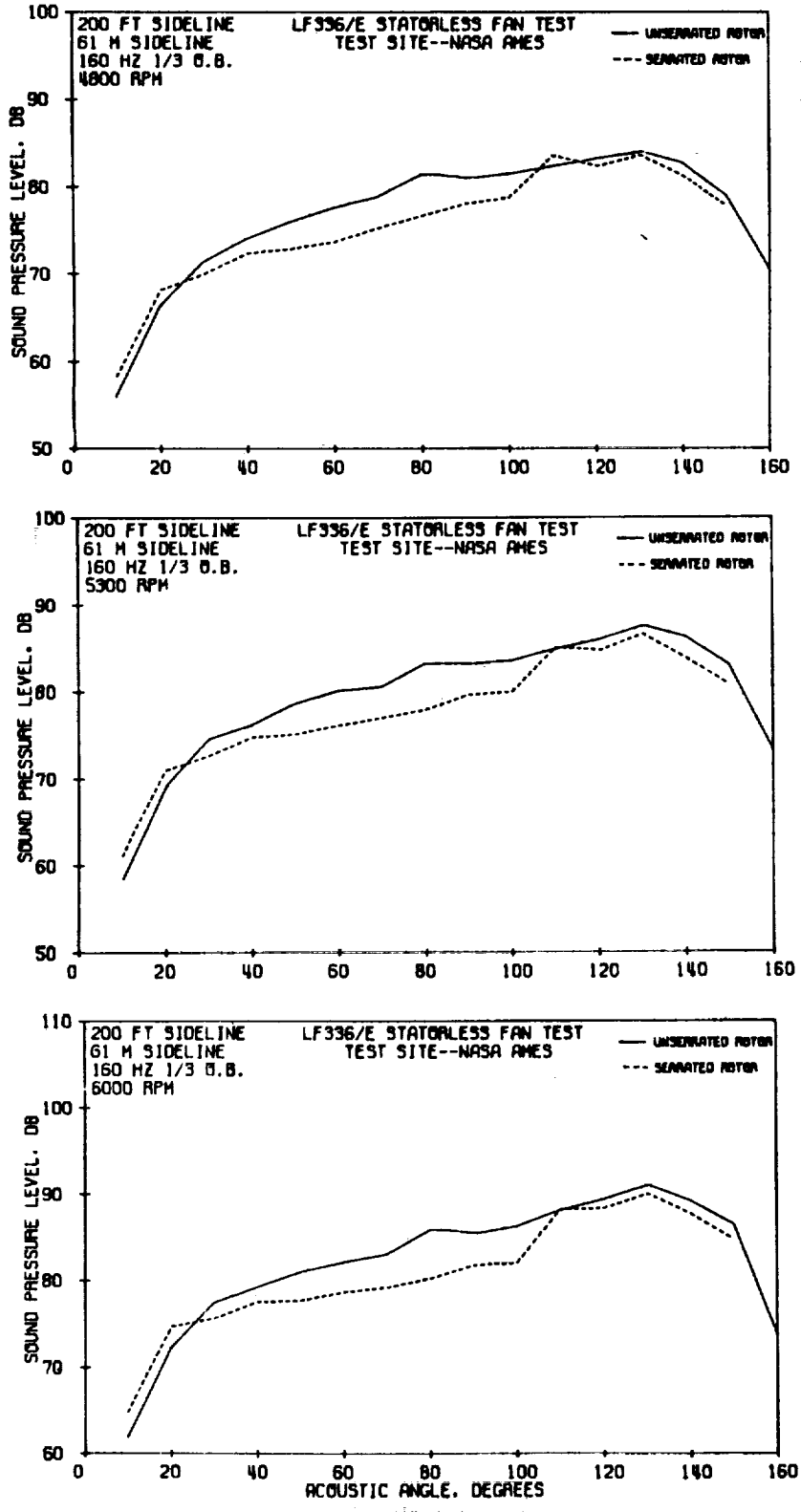

Figure II-11 Serrated and Unserrated LF336/E 160 Hertz 1/3 Octave Band SPL Directivity Patterns

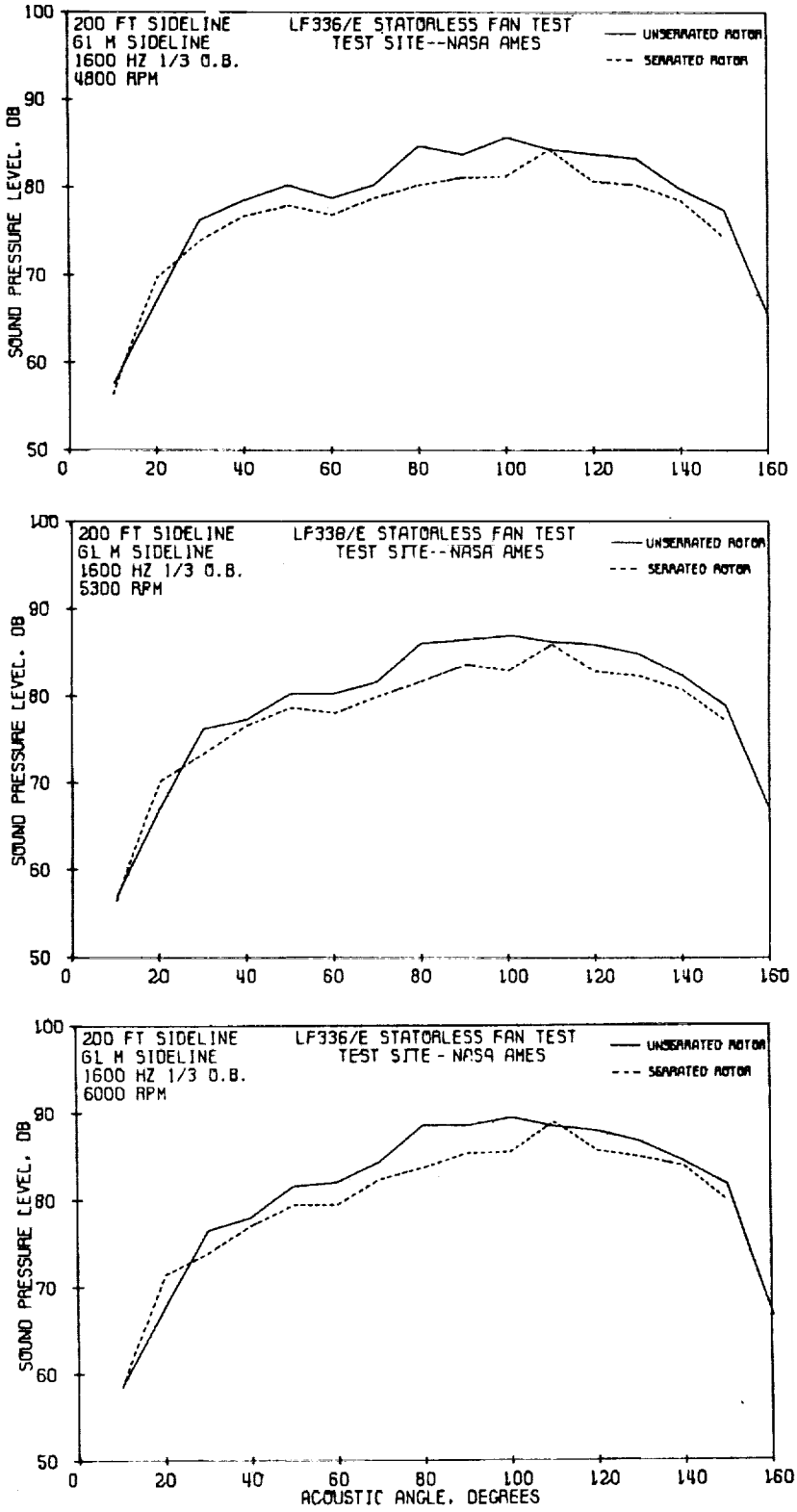

Figure II-12 Serrated and Unserrated LF336/E 1600 Hertz 1/3 Octave Band SPL Directivity Patterns

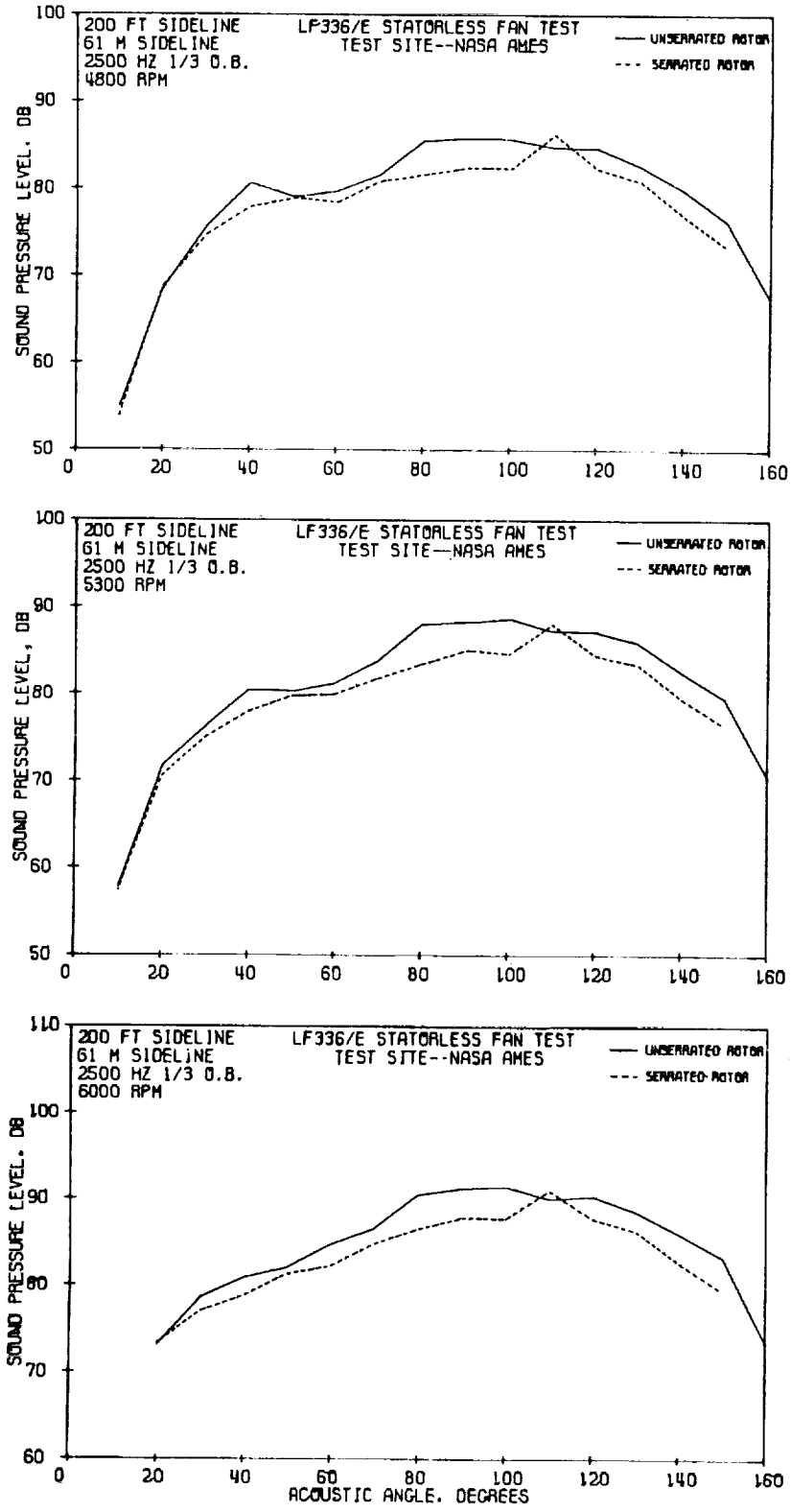

Figure II-13 Serrated and Unserrated LF336/E 2500 Hertz 1/3 Octave Band SPL Directivity Patterns

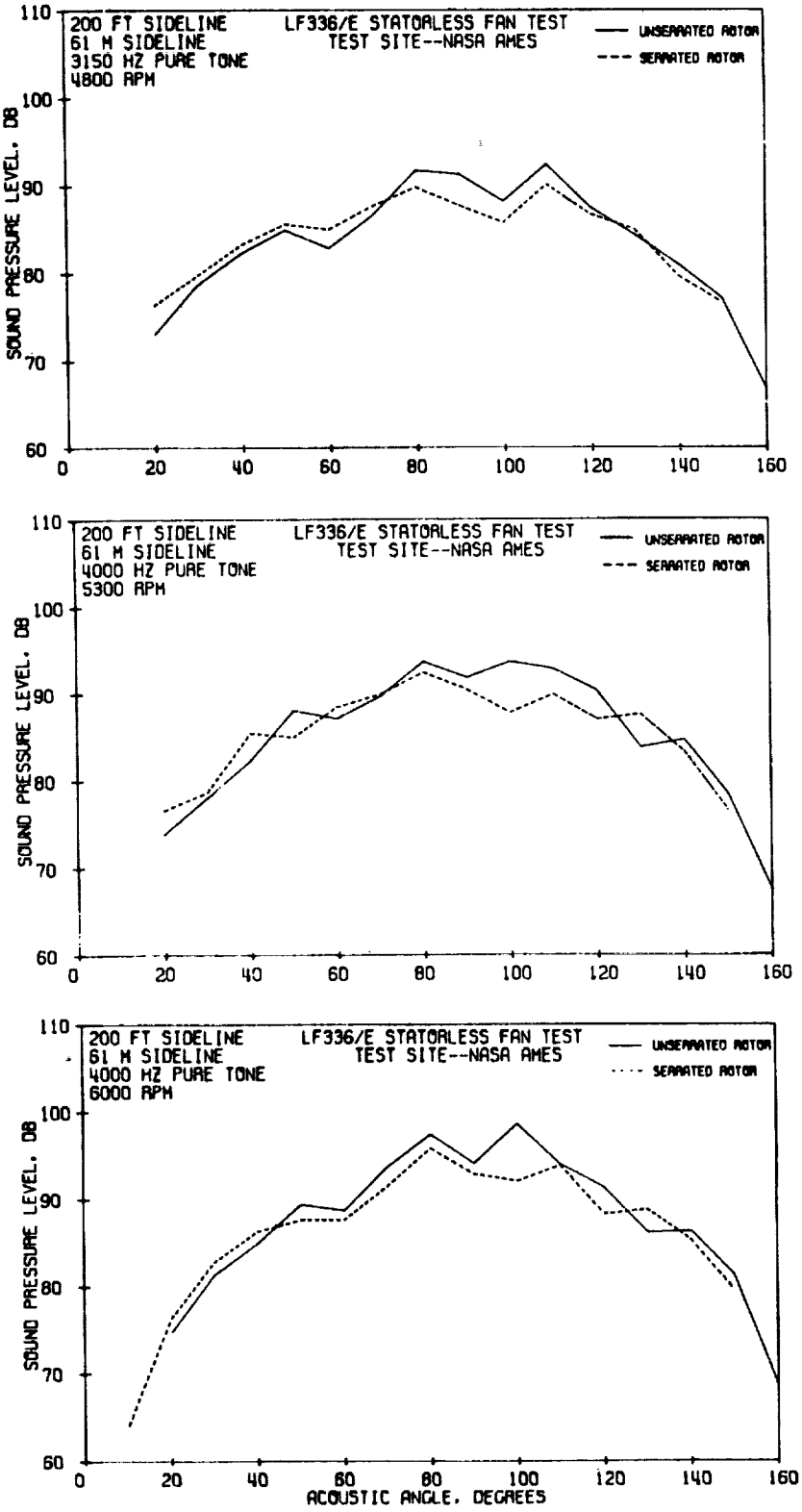

Figure II-14 Serrated and Unserrated LF336/E BPF 1/3 Octave Band SPL Directivity Patterns

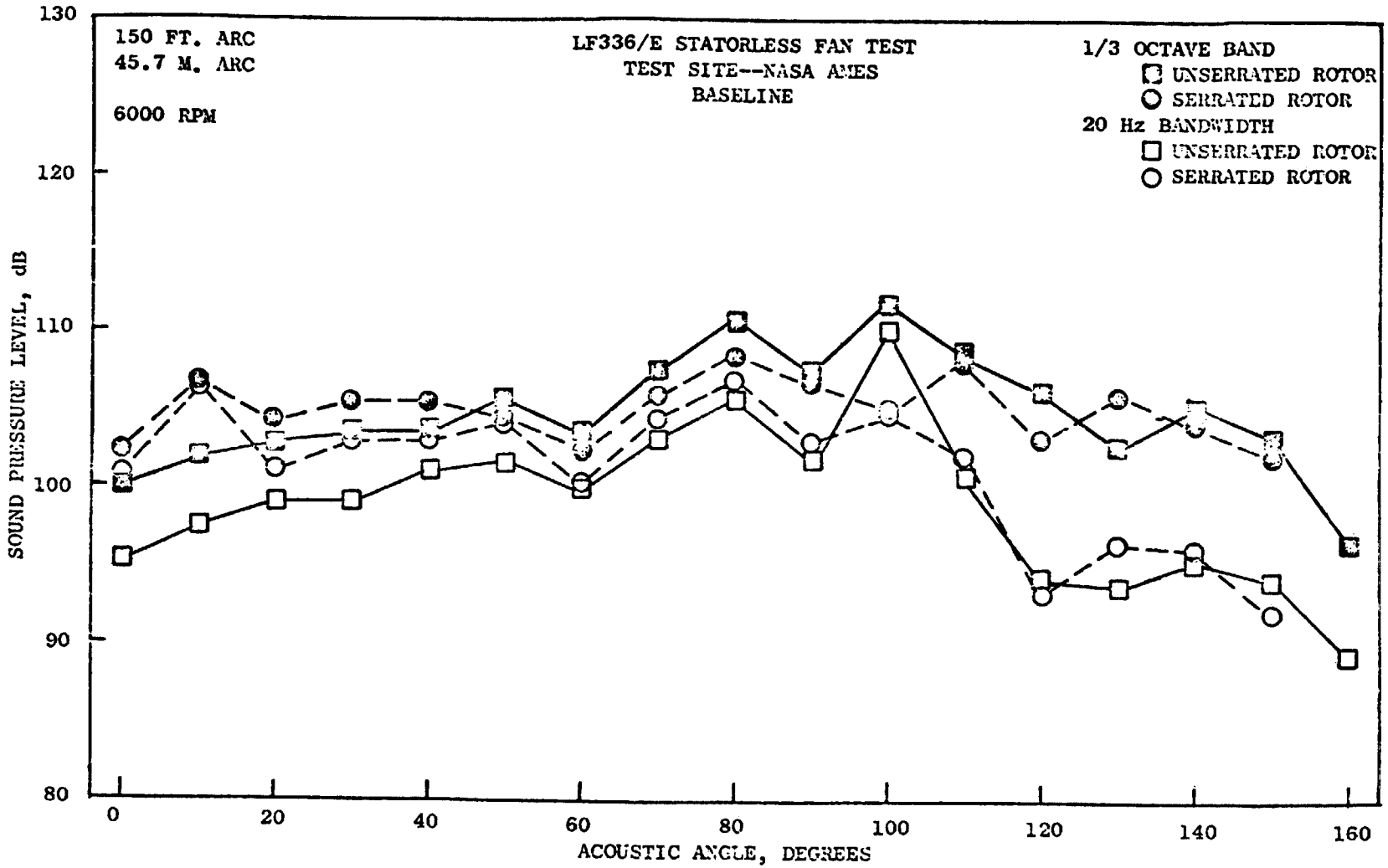

Figure II-15 Serrated and Unserrated LF336/E BPF (1/3 Octave Band and 20 Hertz Narrowband) SPL Directivity Patterns on a 150 foot (45.7 M) Arc

150 FT. ARC
45.7 M. ARC
20 Hz BANDWIDTH
6000 RPM

LF336/E STATORLESS FAN TEST
TEST SITE--NASA AMES

——— UNSERRATED ROTOR
– – – SERRATED ROTOR

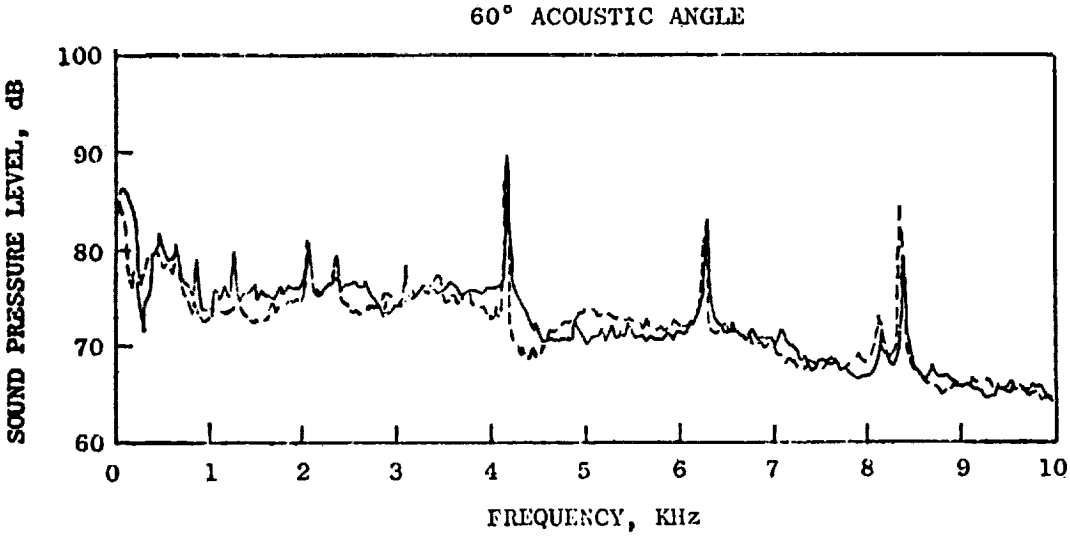

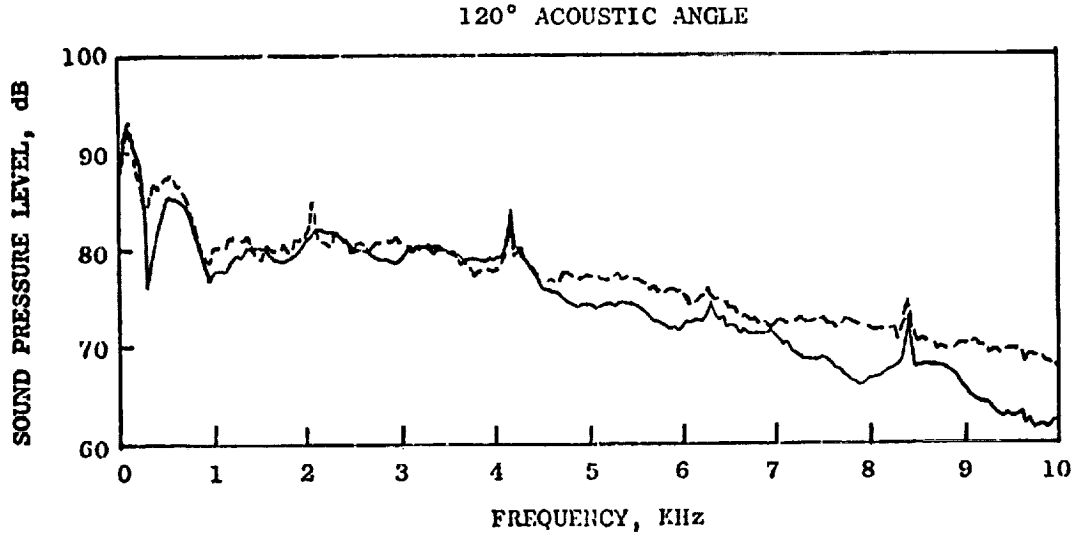

Figure II-16 Serrated and Unserrated LF336/E 20 Hertz Narrowband Spectra at 60 Degrees

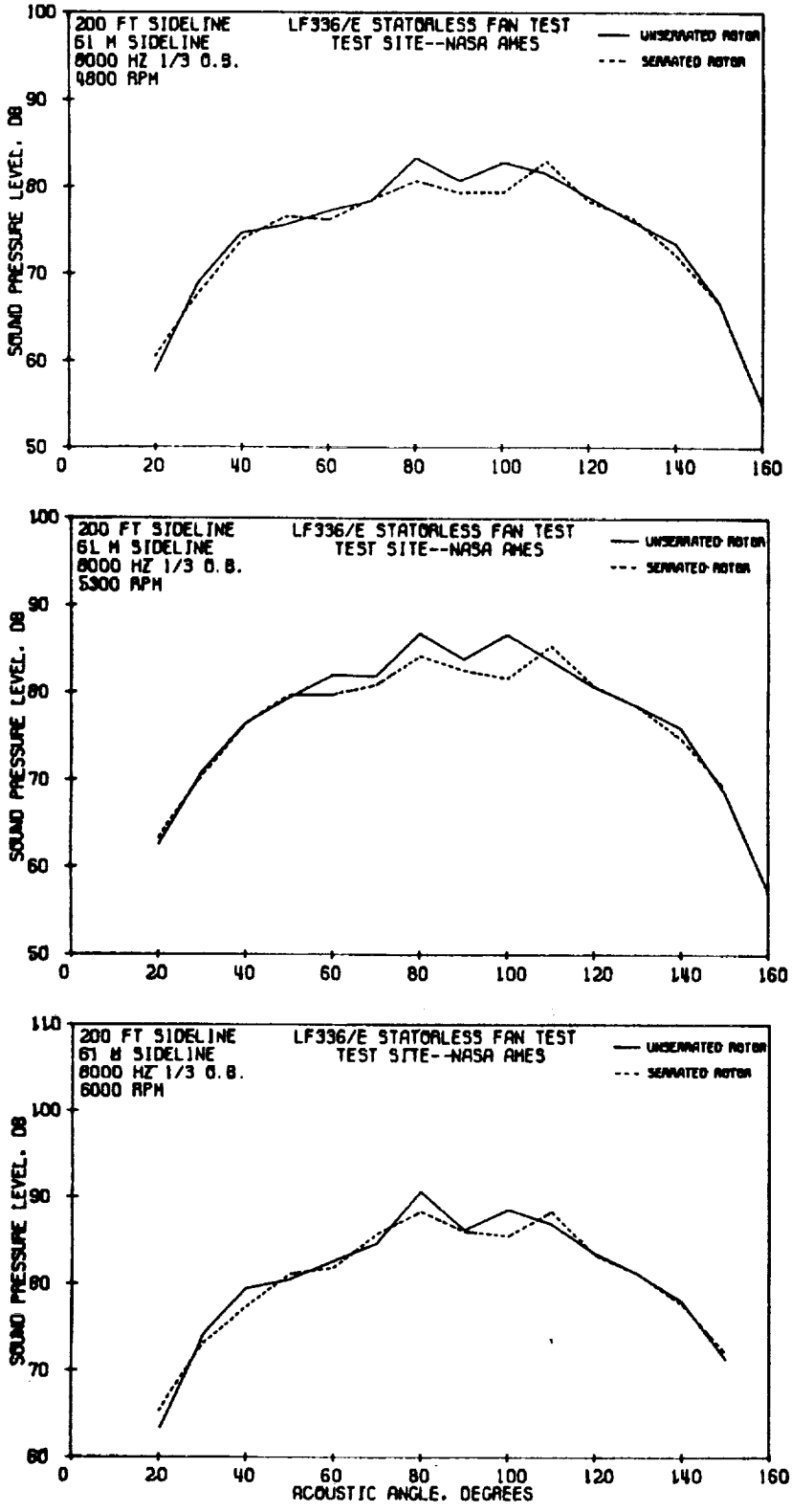

Figure II-17 Serrated and Unserrated LF336/E 8000 Hertz 1/3 Octave Band SPL Directivity Patterns

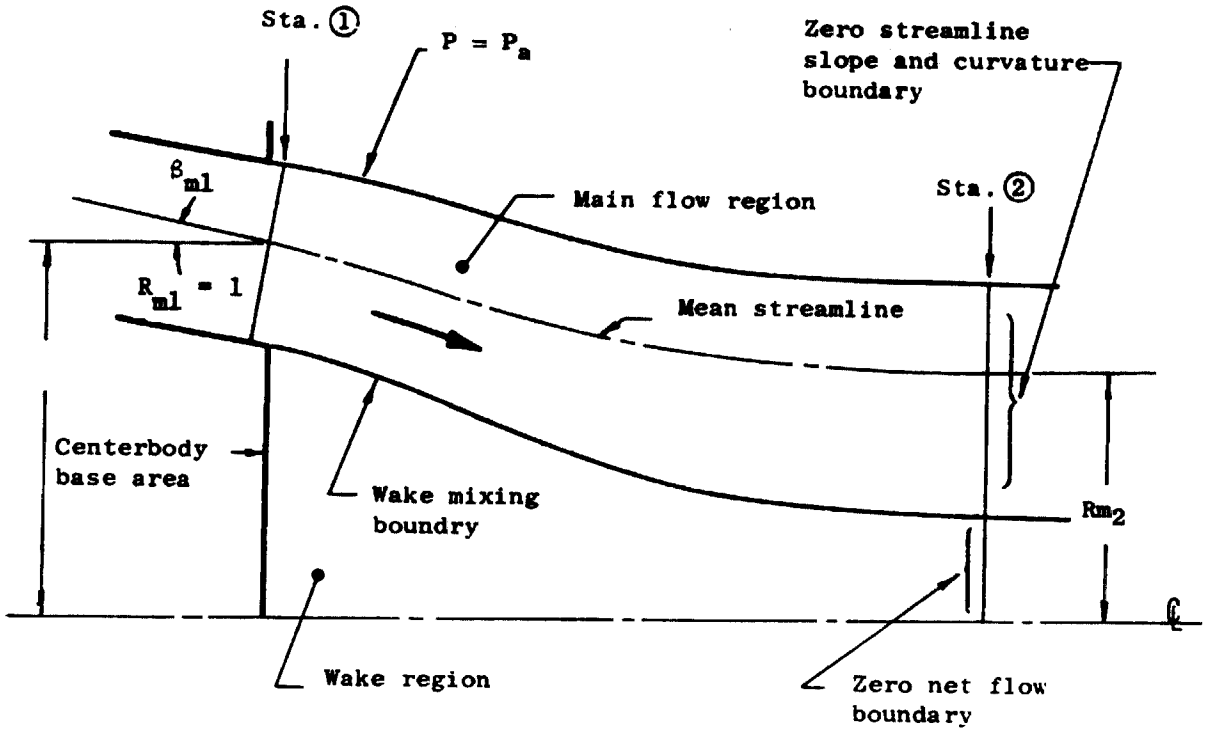

Figure III-1 Analytical Model

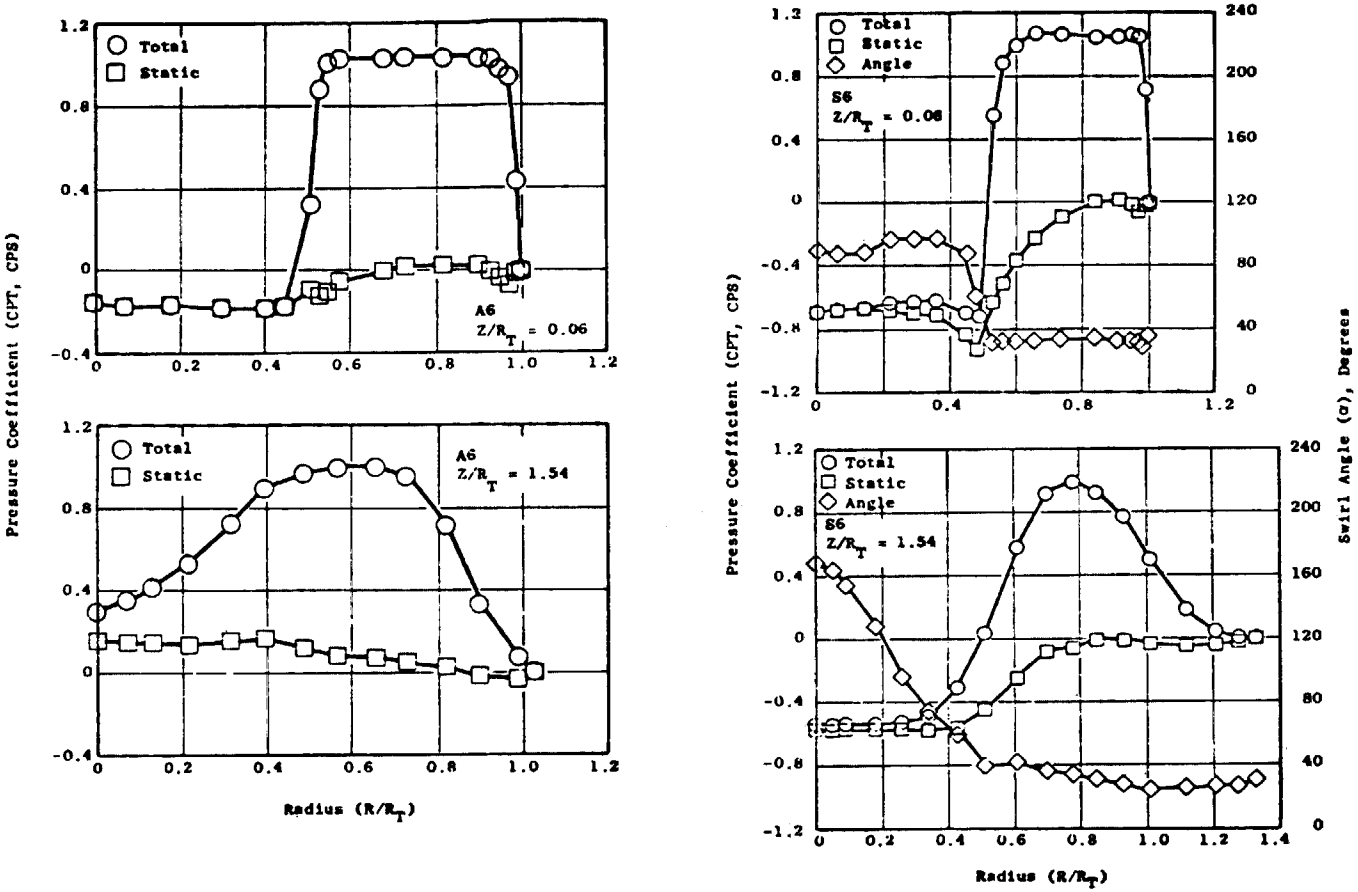

Figure III-2 Flow Profiles for Jet Model 6 (Typical)

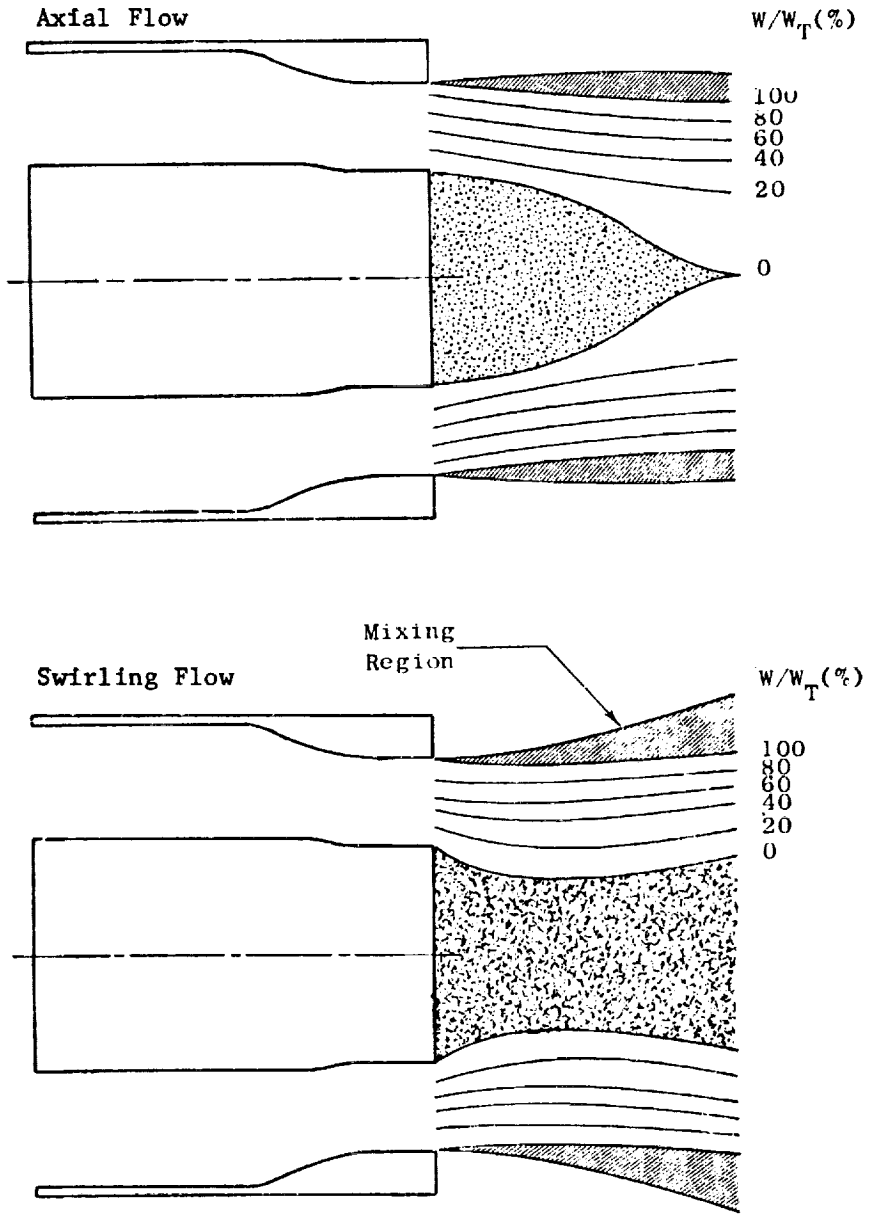

Figure III-3 Graphical Representation of the Flowfield with Axial and Swirling Flows

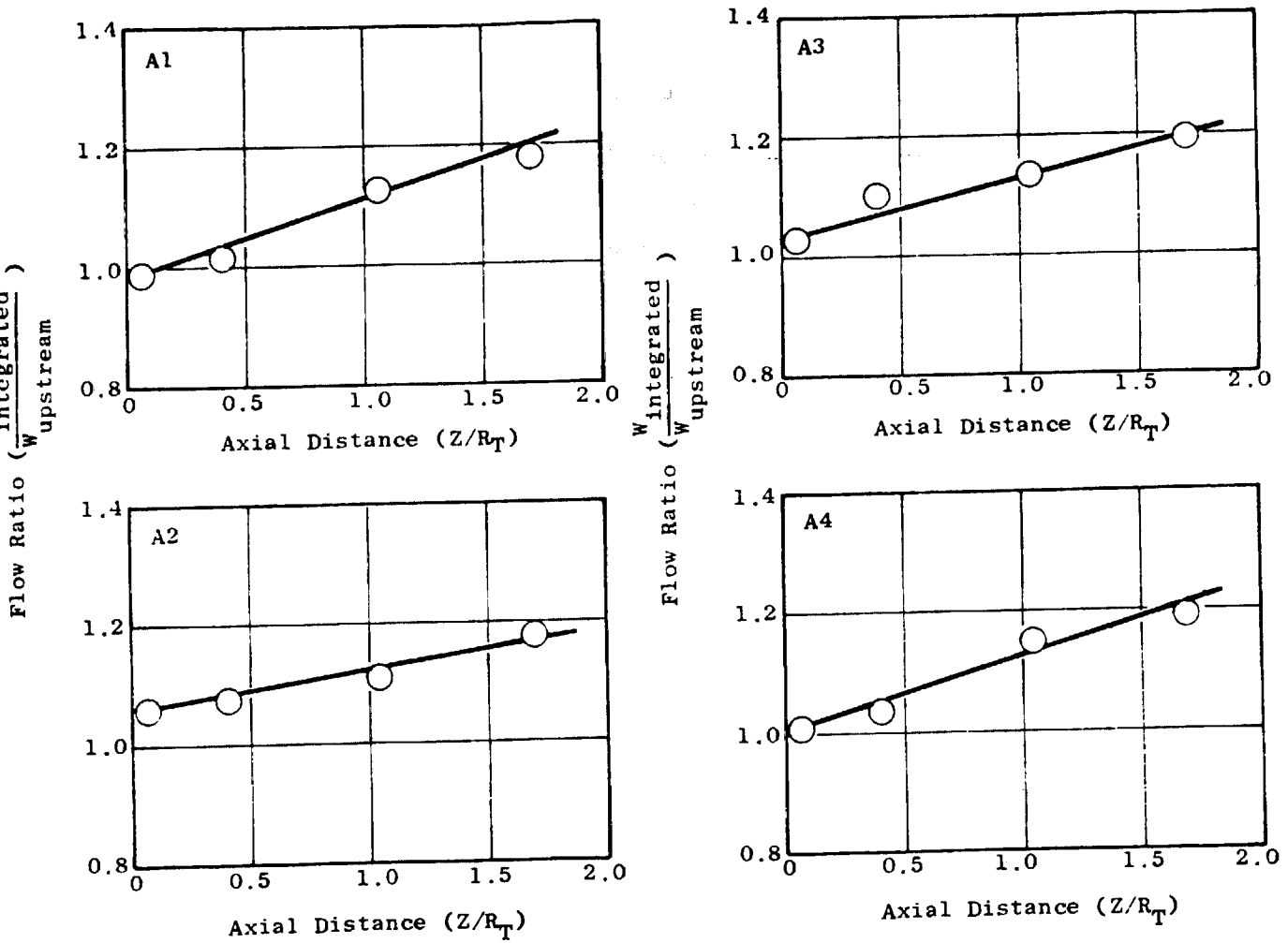

(a) Models A1, A2, A3 and A4

Figure III-4 Flow Entrainment Characteristics for Models with Axial Flow

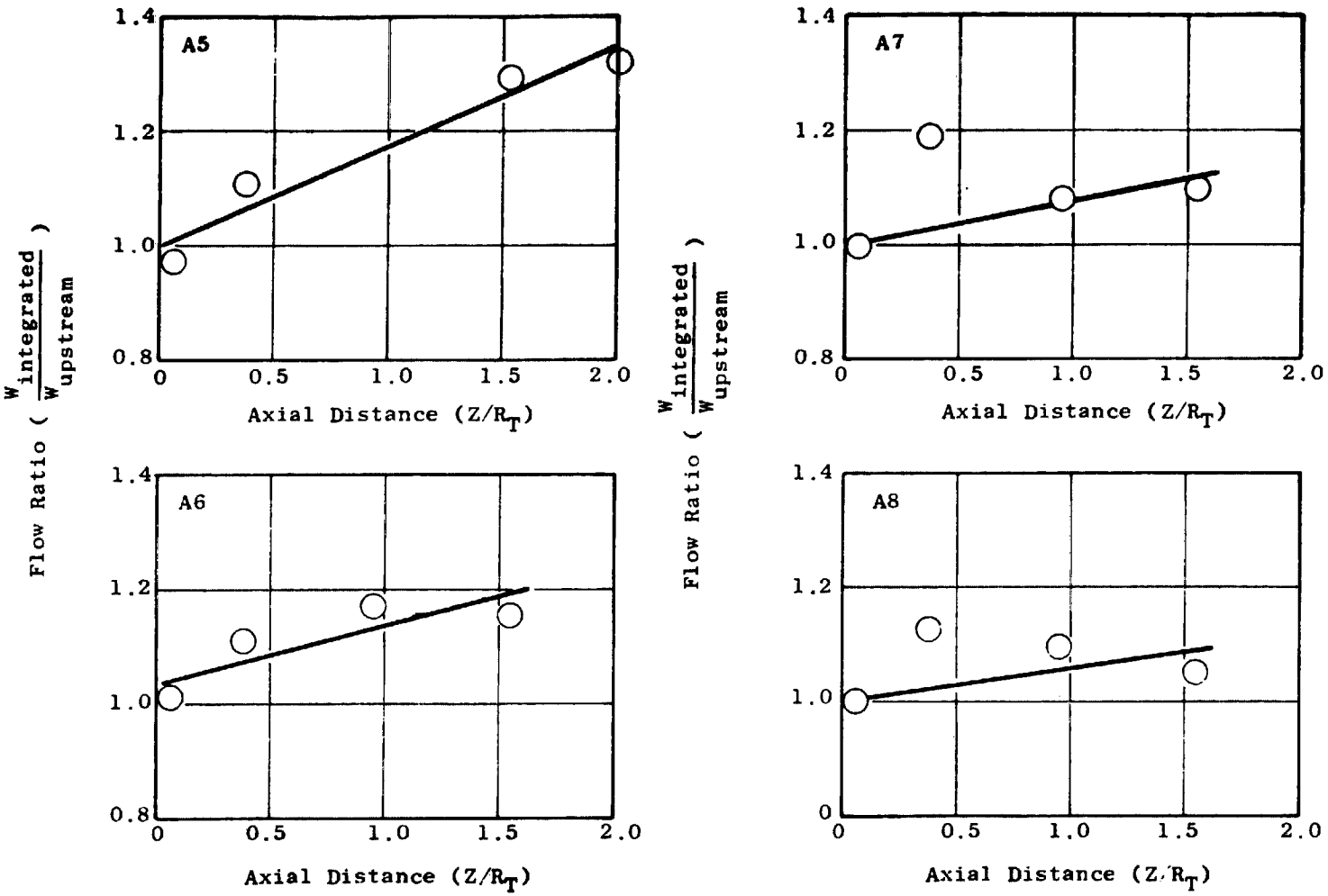

(b) Models A5, A6, A7 and A8

Figure III-4 Flow Entrainment Characteristics for Models with Axial Flow (Continued)

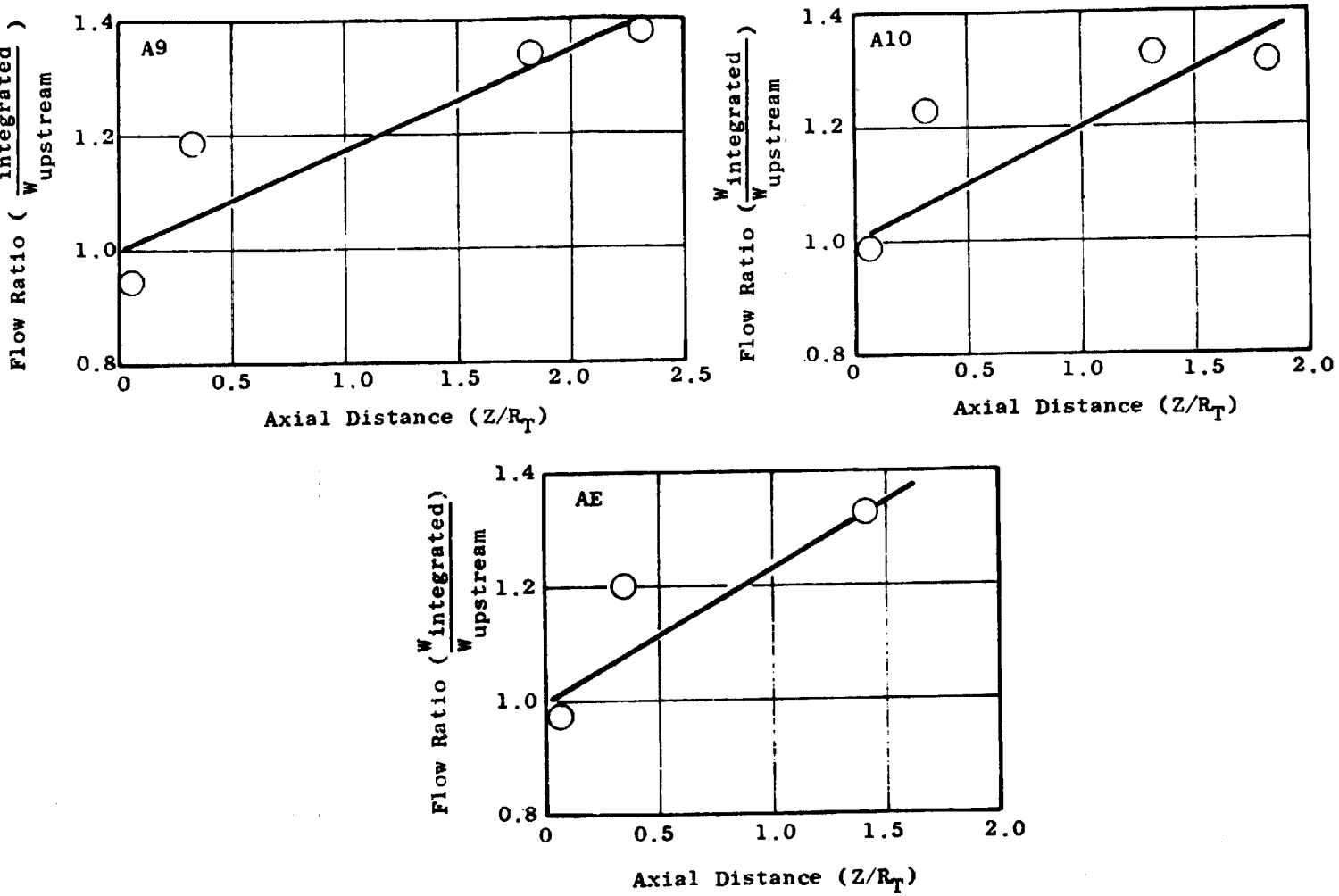

(c) Models A9, A10 and AE

Figure III-4 Flow Entrainment Characteristics for Models with Axial Flow (Concluded)

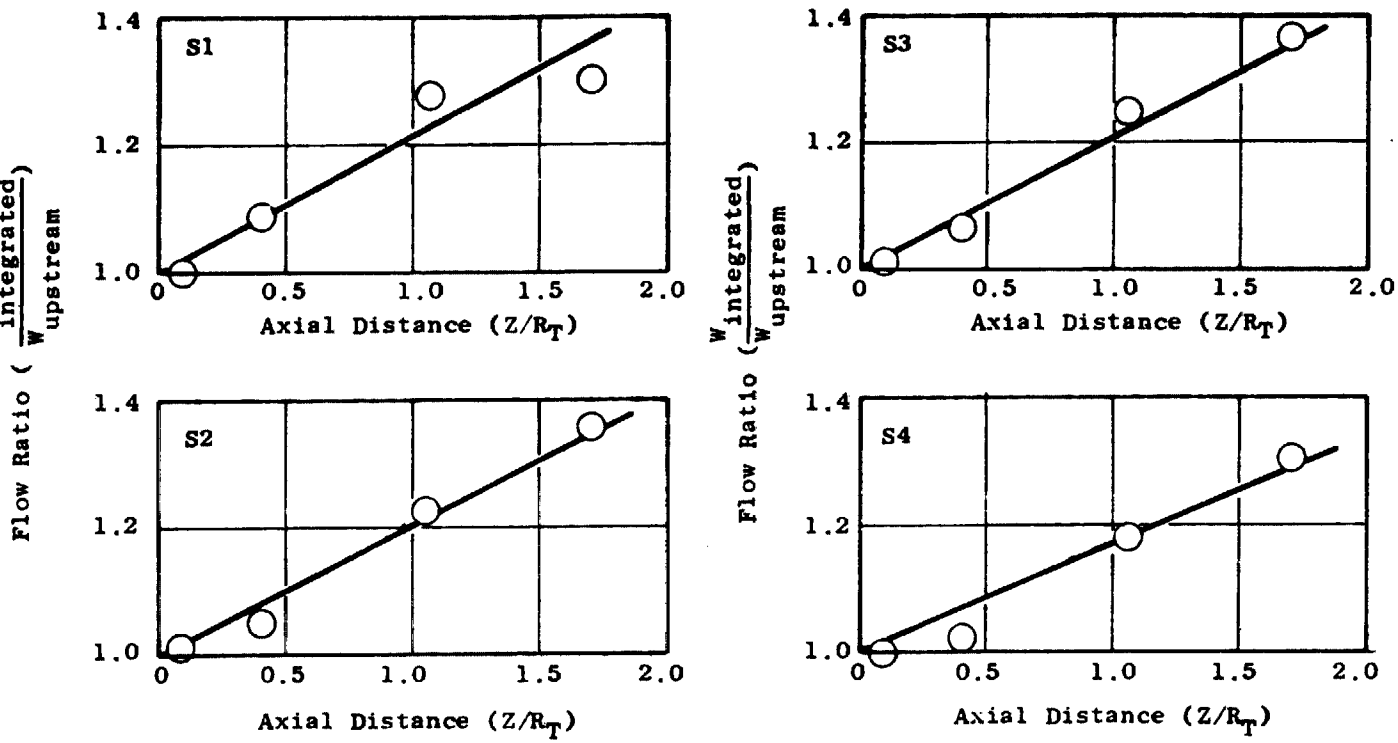

(a) Models S1, S2, S3 and S4

Figure III-5 Flow Entrainment Characteristics for Models with Swirling Flow

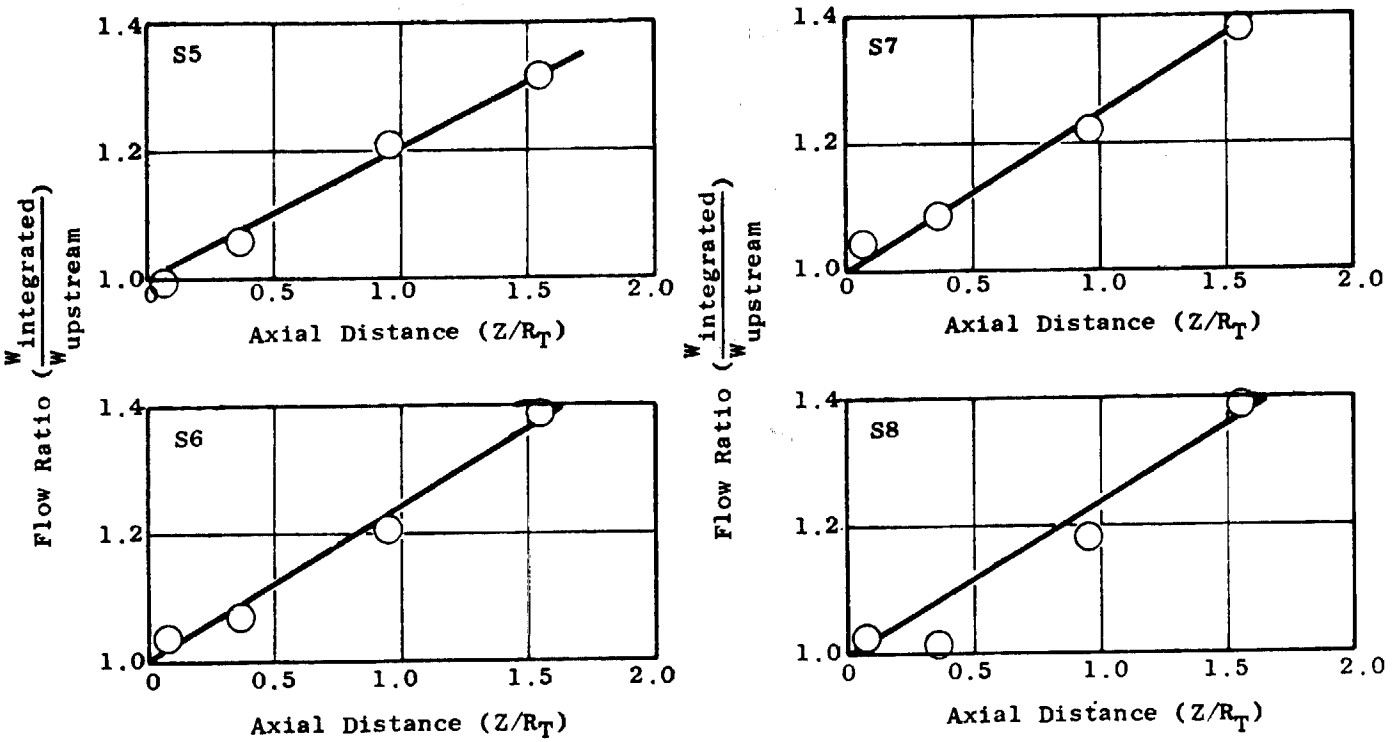

(b) Models S5, S6, S7 and S8

Figure III-5 Flow Entrainment Characteristics for Models with Swirling Flow (Continued)

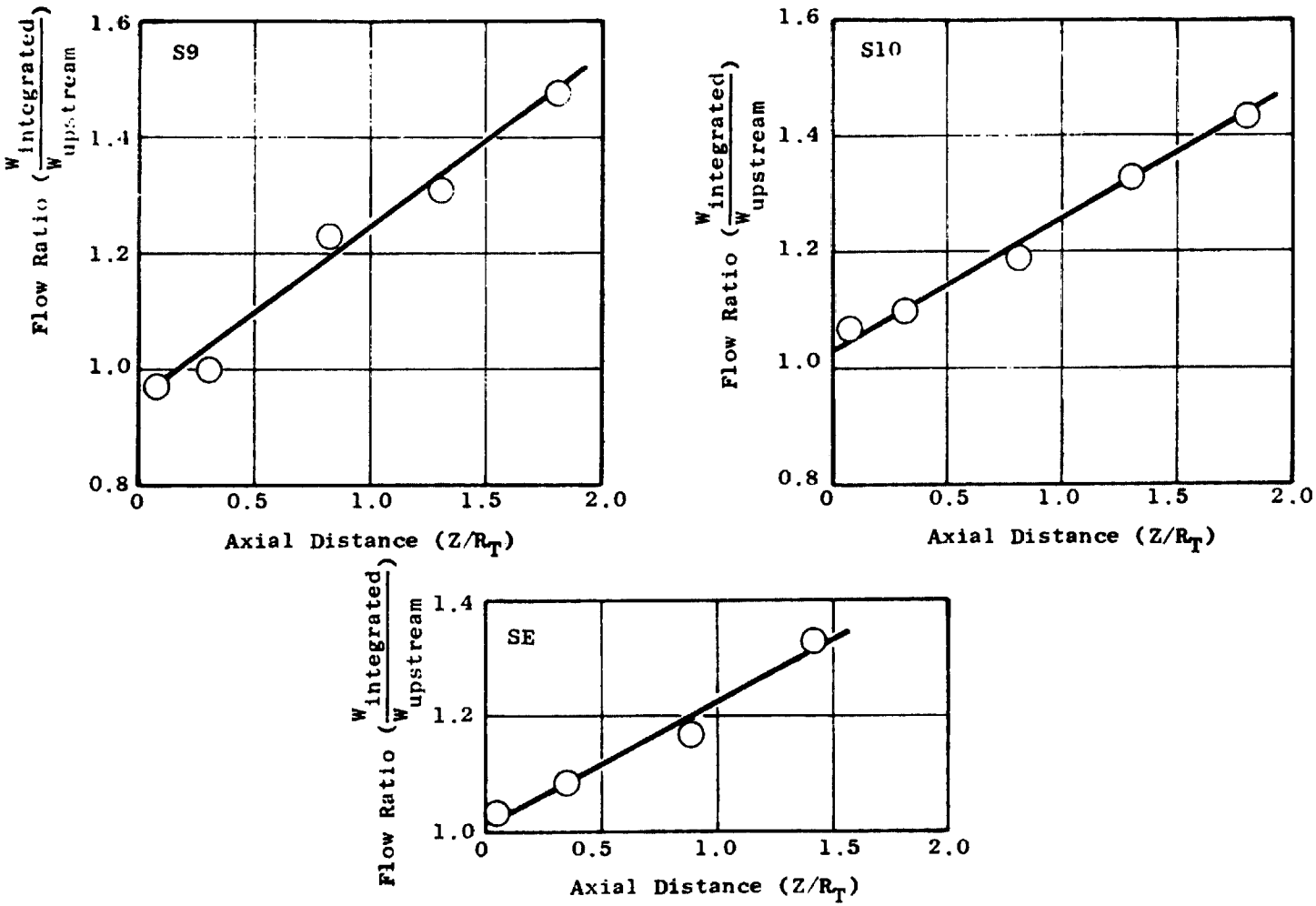

(c) **Models S9, S10 and SE**

Figure III-5 Flow Entrainment Characteristics for Models with Swirling Flow (Concluded)

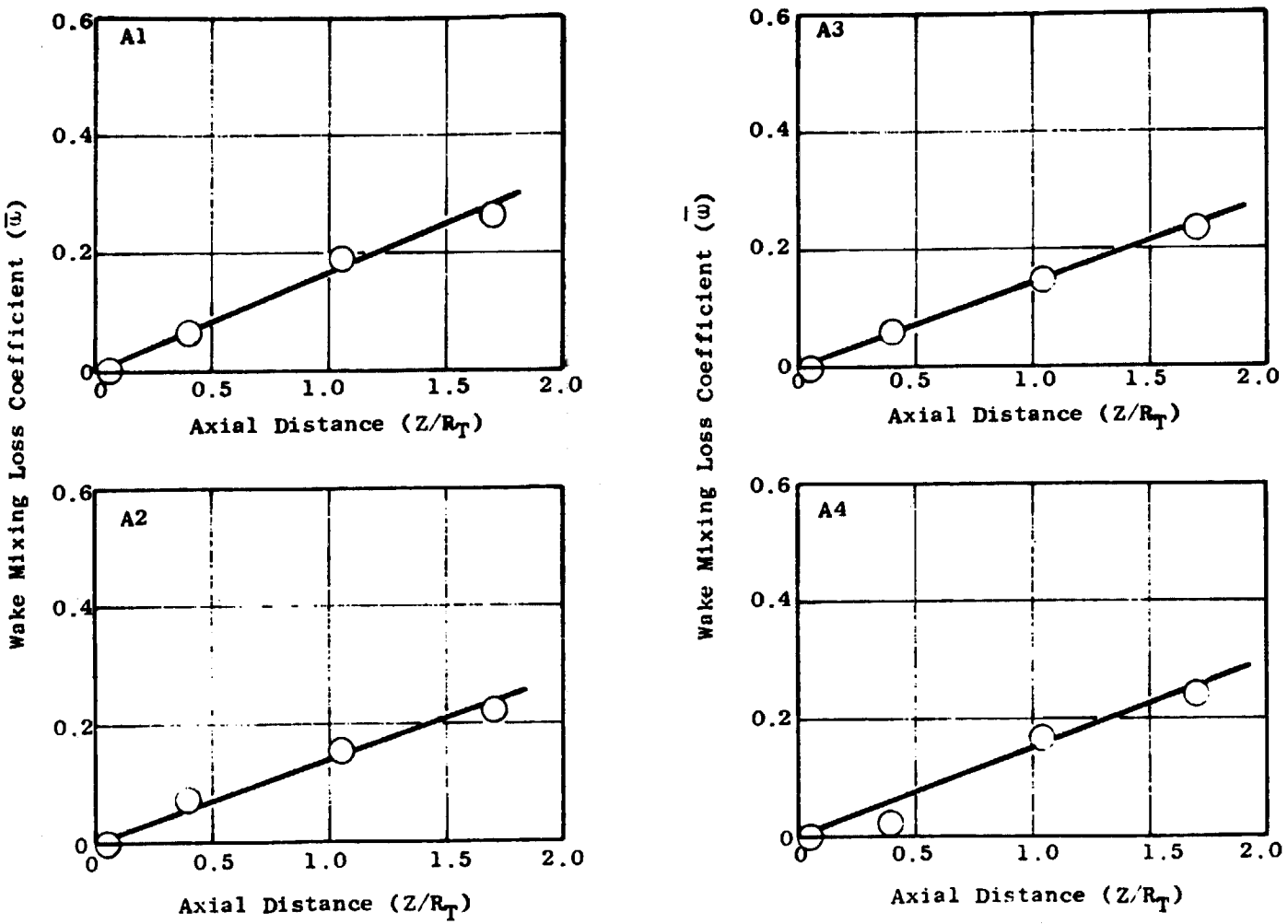

(a) Models A1, A2, A3 and A4

Figure III-6 Wake Mixing Loss Characteristics for Models with Axial Flow

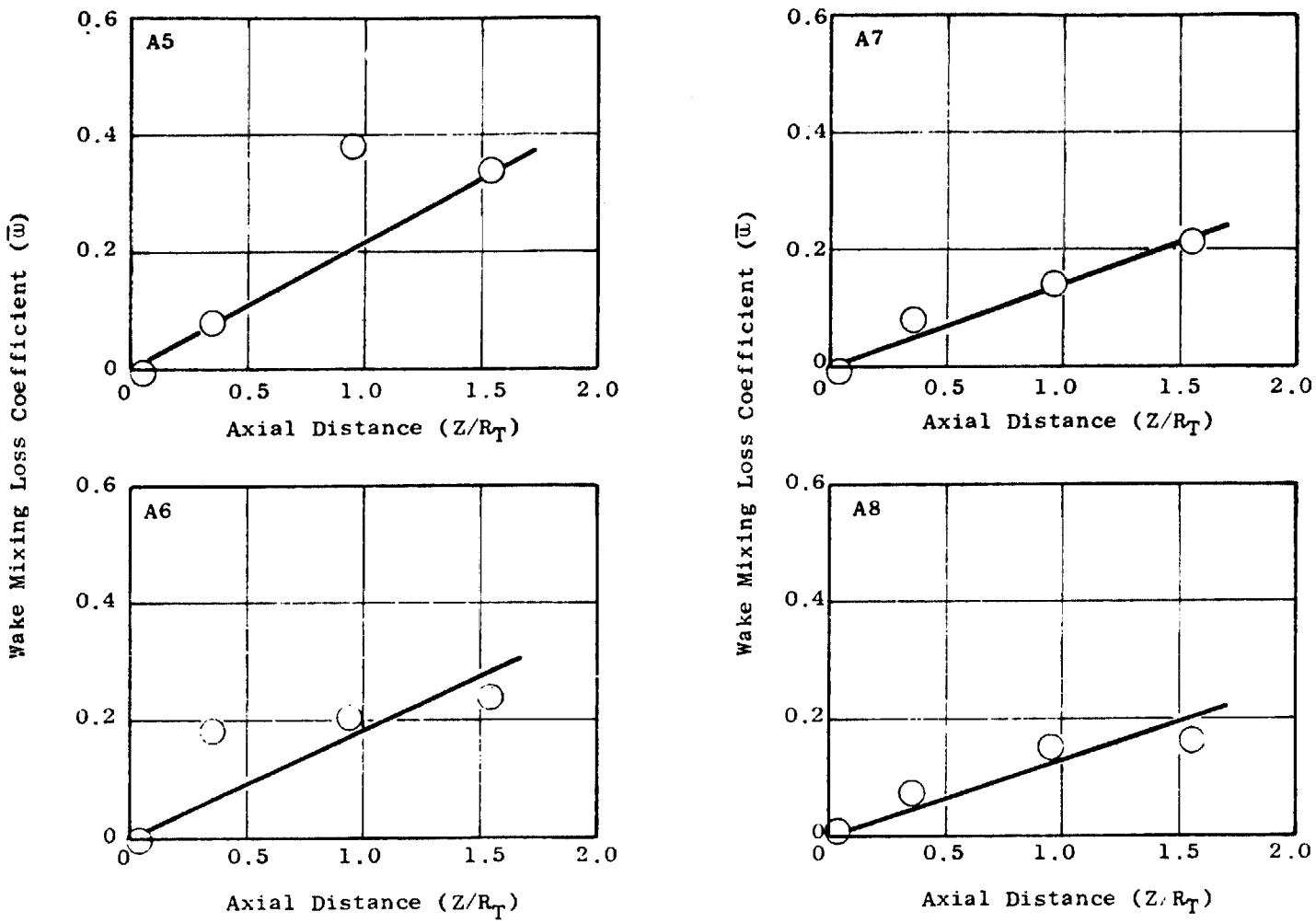

(b) Models A5, A6, A7 and A8

Figure III-6 Wake Mixing Loss Characteristics for Models with Axial Flow (Continued)

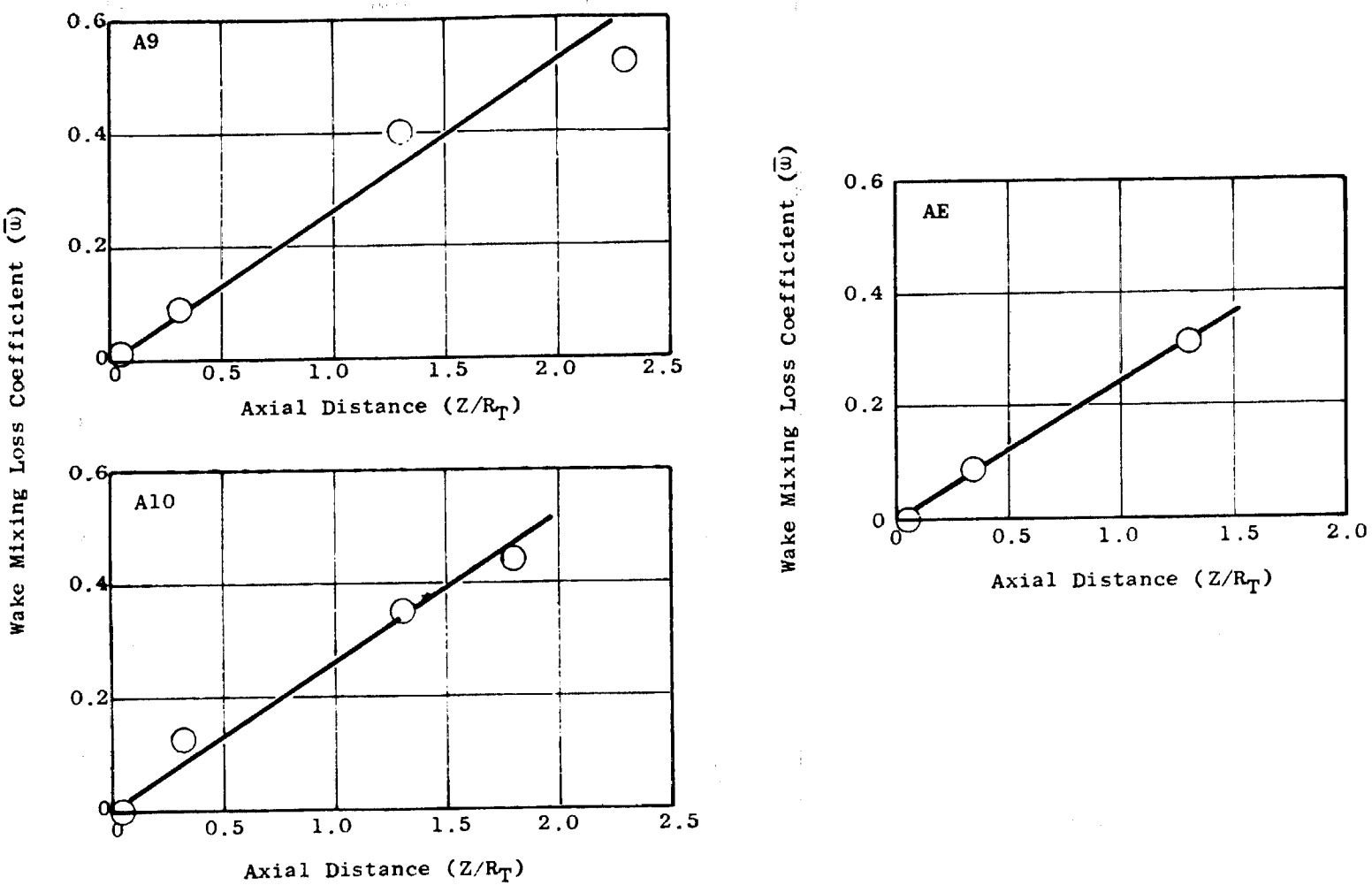

(c) Models A9, A10 and AE

Figure III-6 Wake Mixing Loss Characteristics for Models with Axial Flow (Concluded)

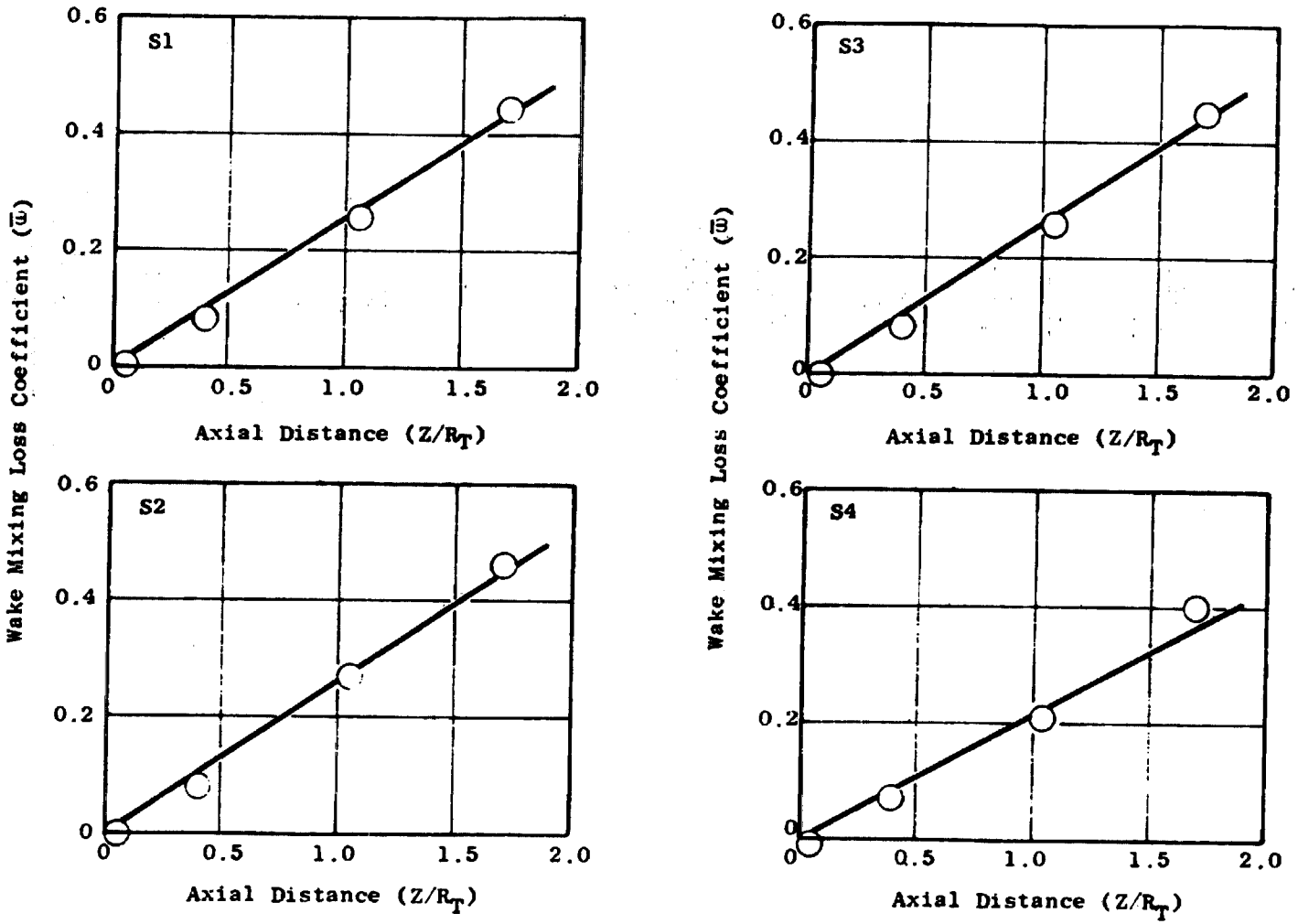

(a) Models S1, S2, S3 and S4

Figure III-7 Wake Mixing Loss Characteristics for Models with Swirling Flow

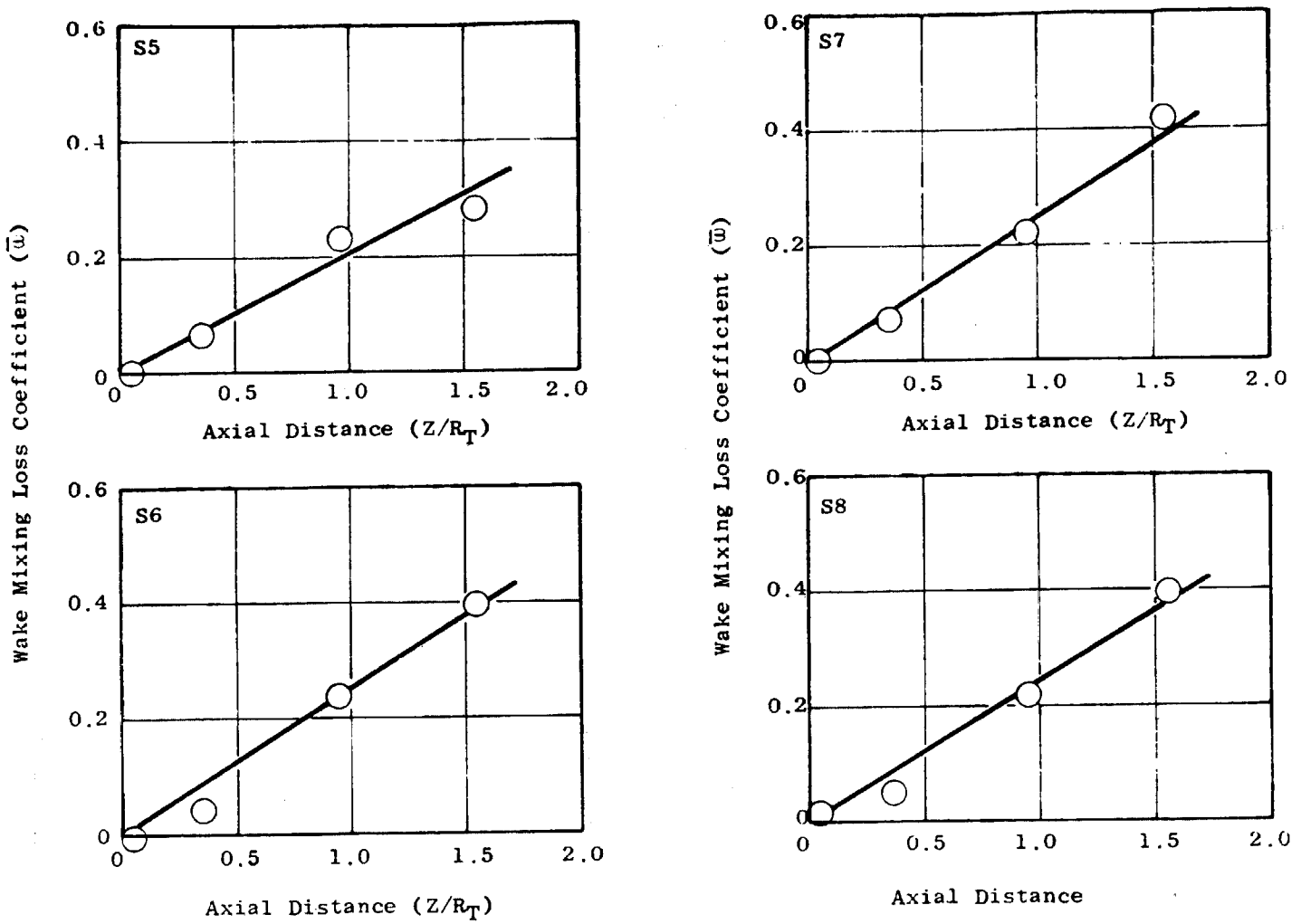

(b) Models S5, S6, S7 and S8

Figure III-7 Wake Mixing Loss Characteristics for Models with Swirling Flow (Continued)

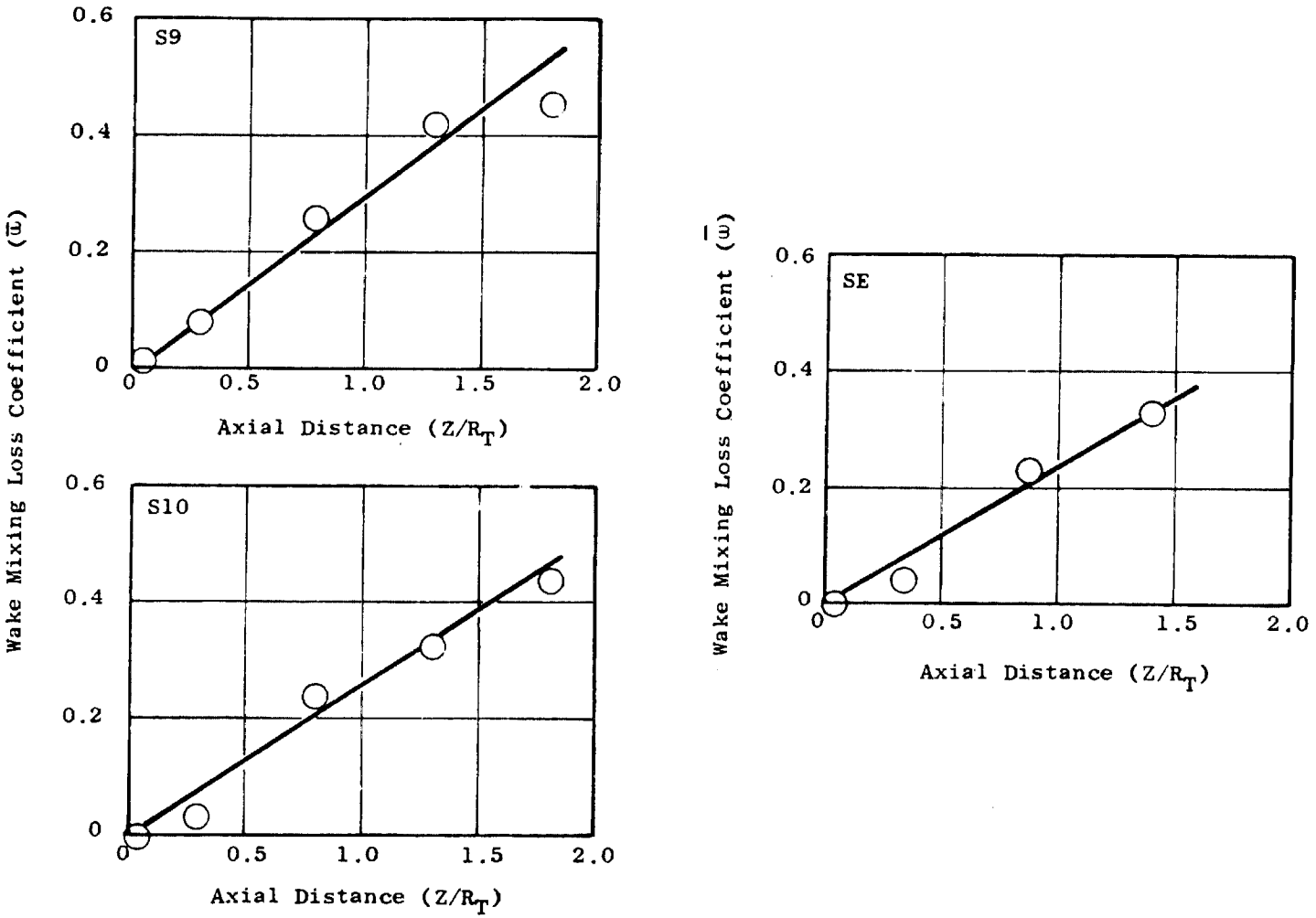

Figure III-7 Wake Mixing Loss Characteristics for Models with Swirling Flow (Concluded)

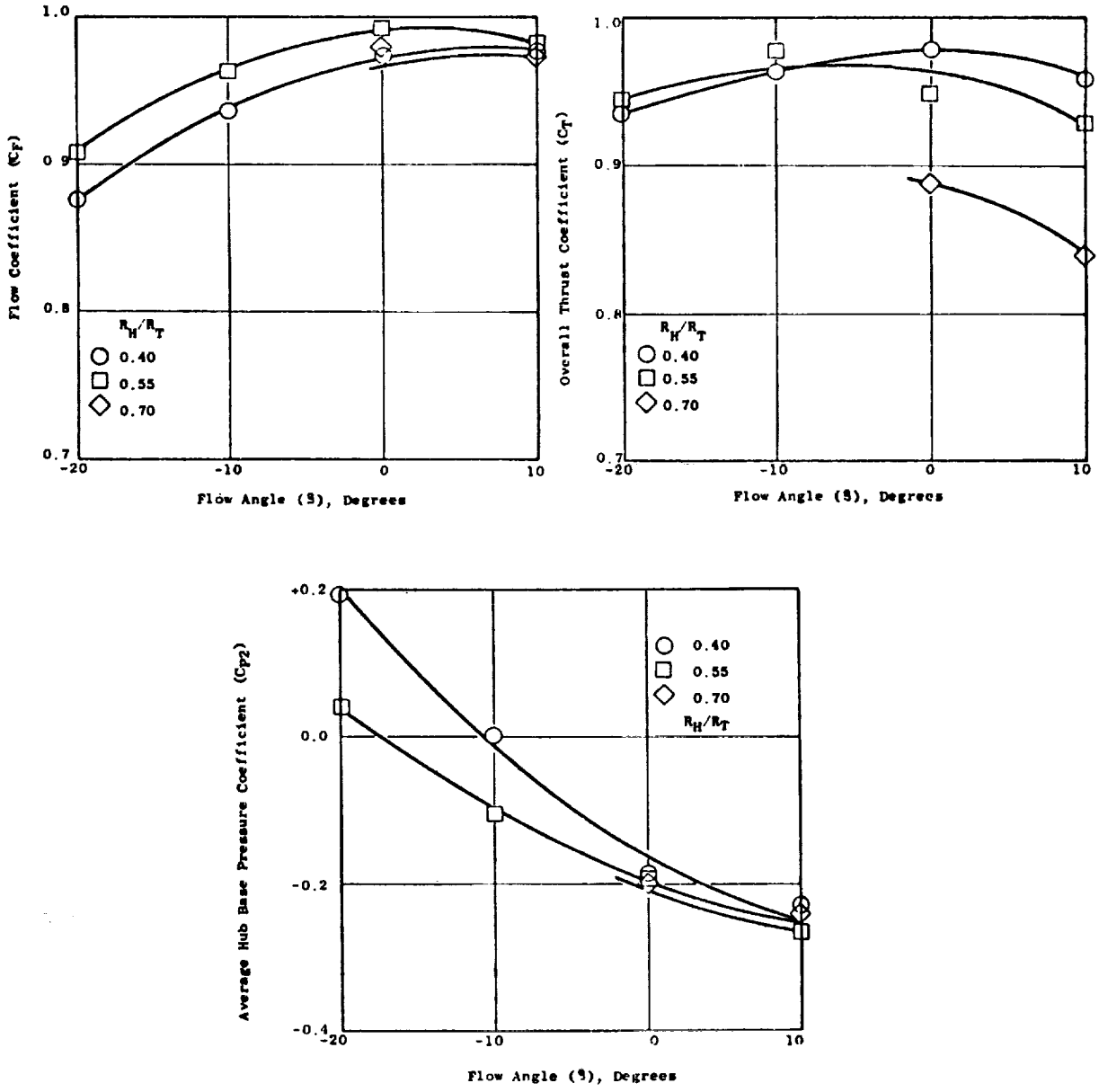

Figure III-8 Overall Performance with Axial Flow

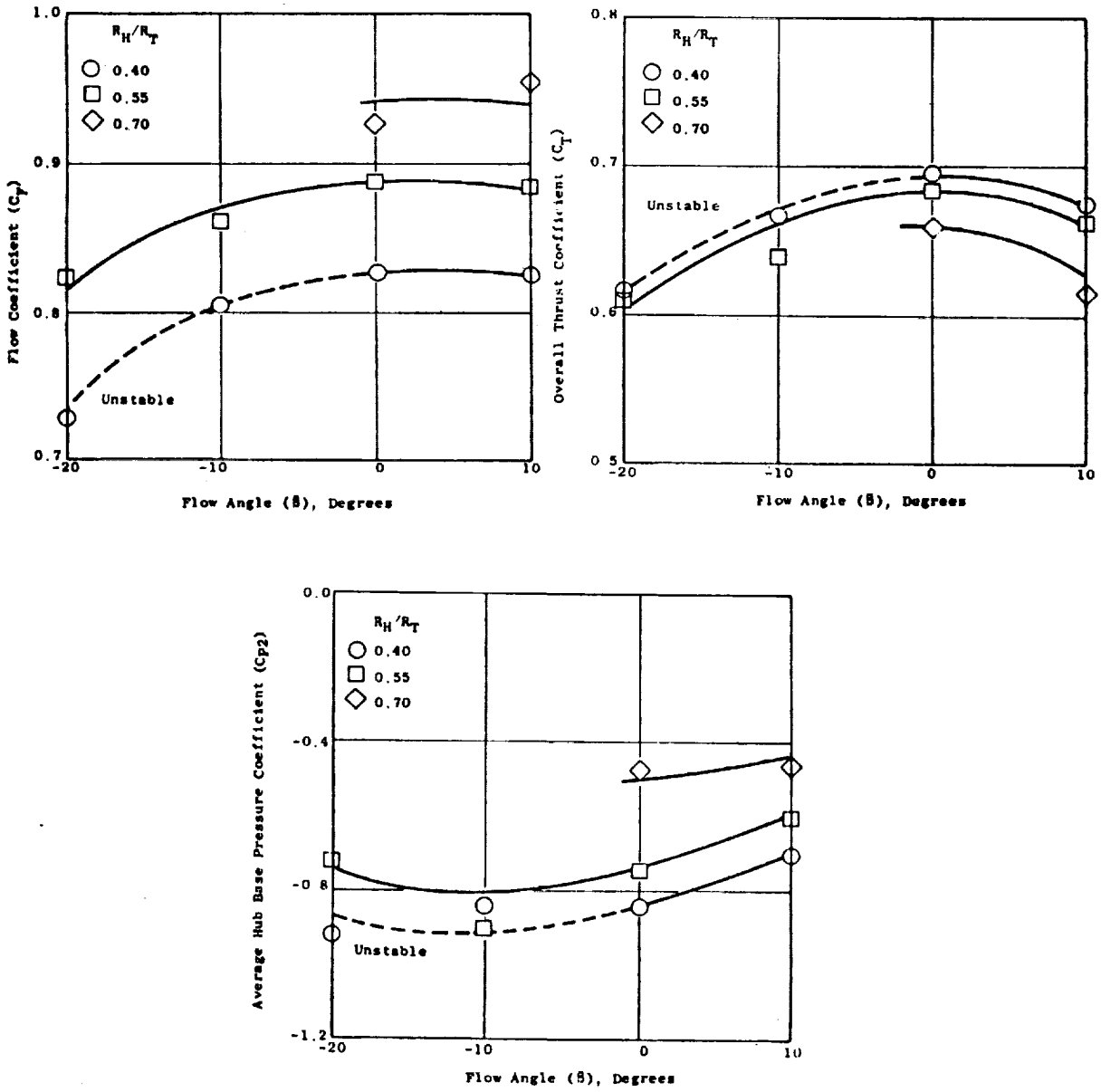

Figure III-9 Overall Performance with Swirling Flow

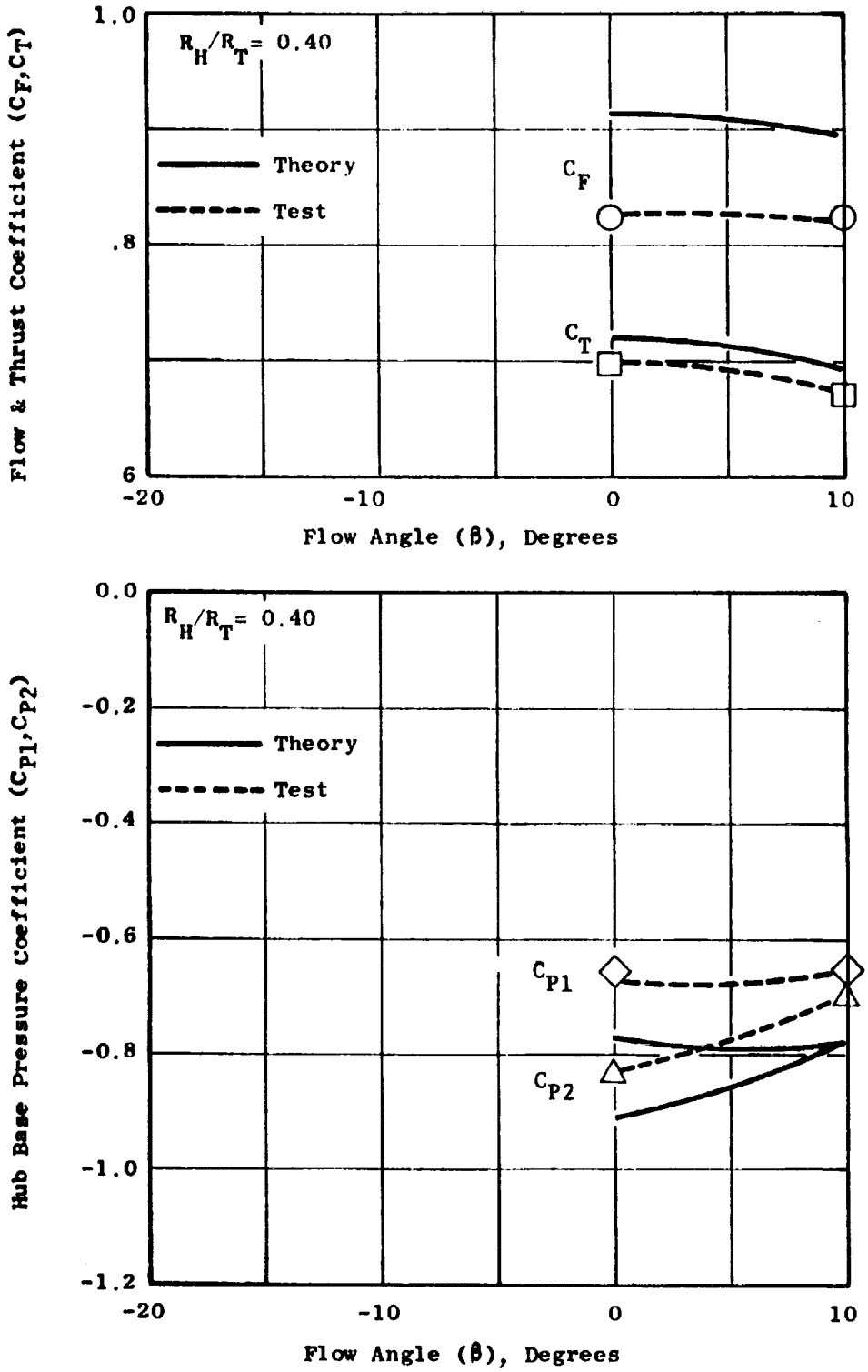

Figure III-10 Comparison of Theoretical Predictions to Test Results for the Base Pressure, Flow and Thrust Coefficients, R_H/R_T = 0.40, Swirling Flow

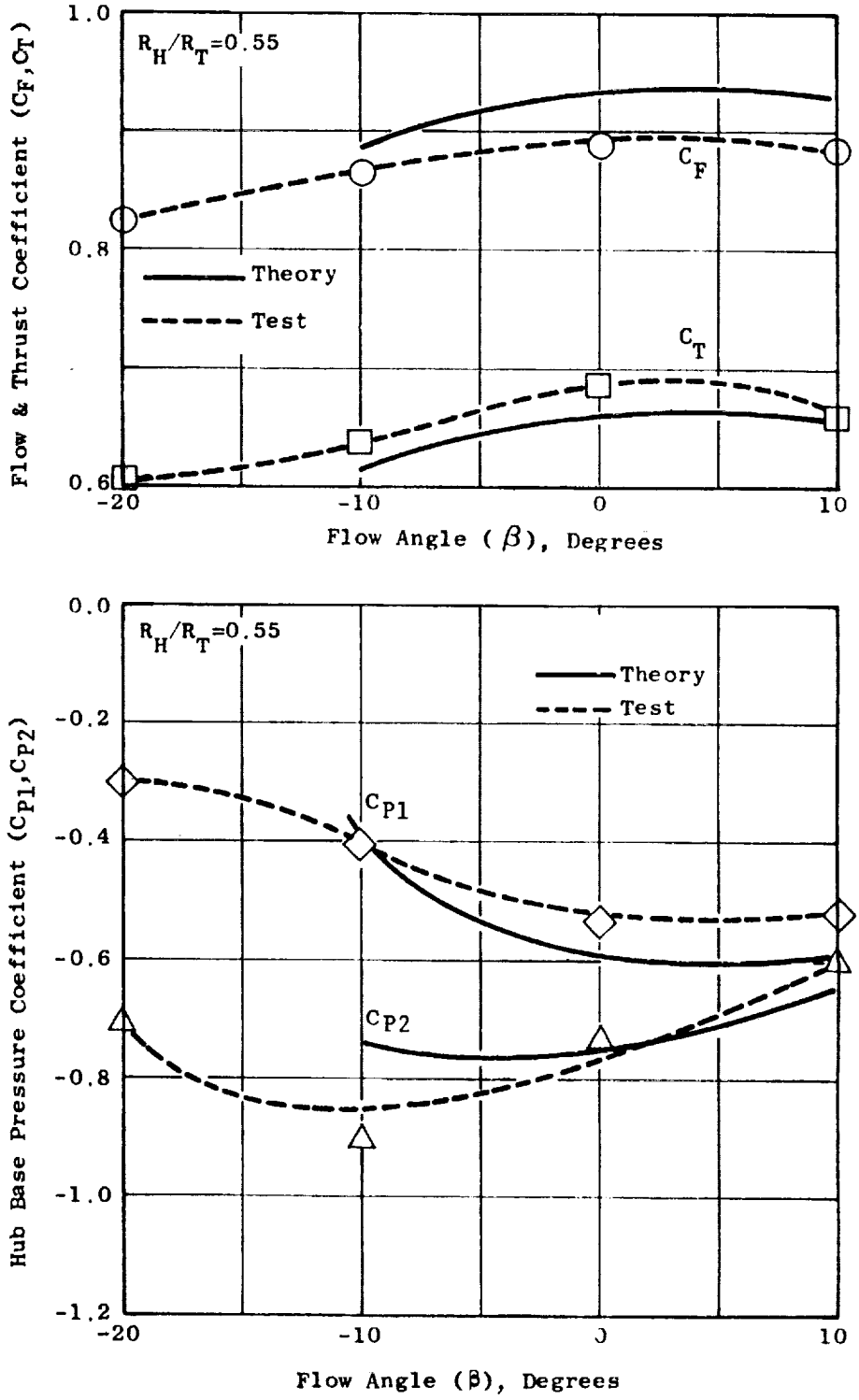

Figure III-11 Comparison of Theoretical Predictions to Test Results for the Base Pressure, Flow and Thrust Coefficients, R_H/R_T = 0.55, Swirling Flow

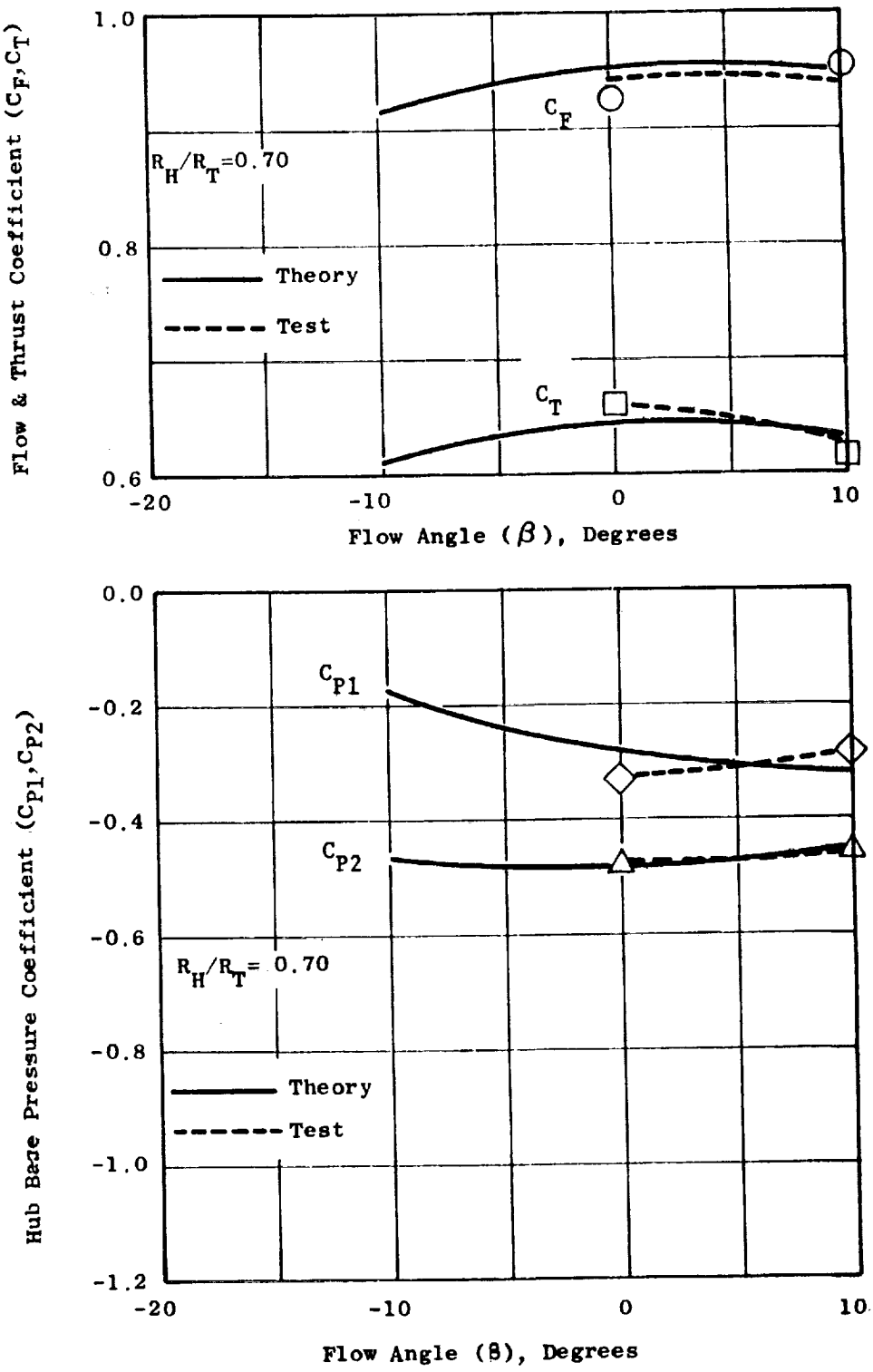

Figure III-12 Comparison of Theoretical Predictions to Test Results for the Base Pressure, Flow and Thrust Coefficients, R_H/R_T = 0.70, Swirling Flow

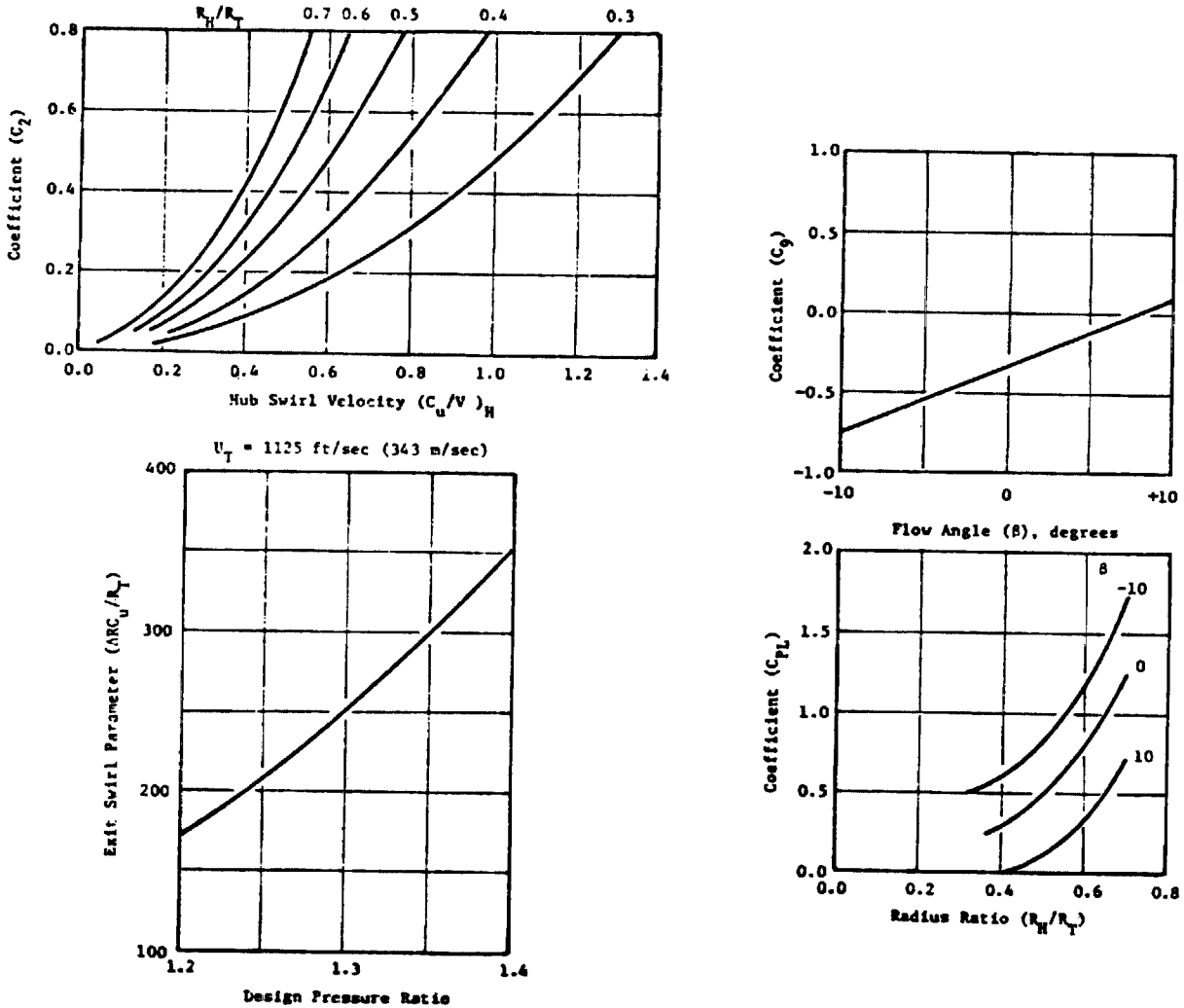

Figure III-13 Design Constants Established by Model Tests

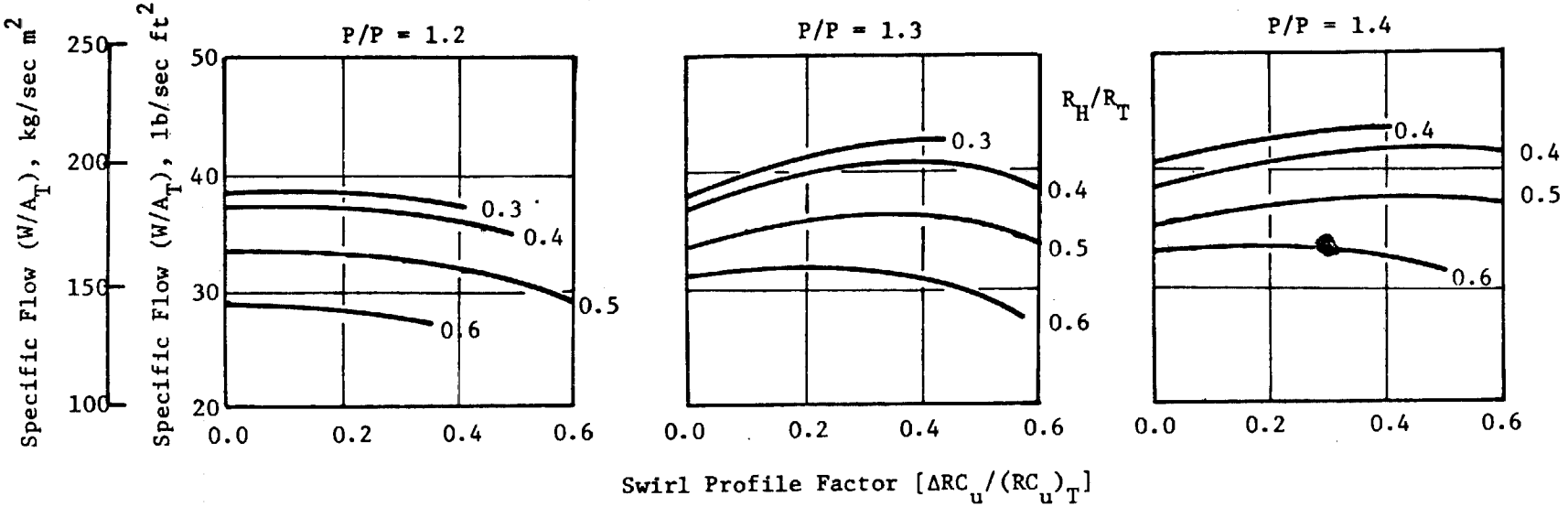

Figure III-14 Effects of Design Parameters on Specific Flow

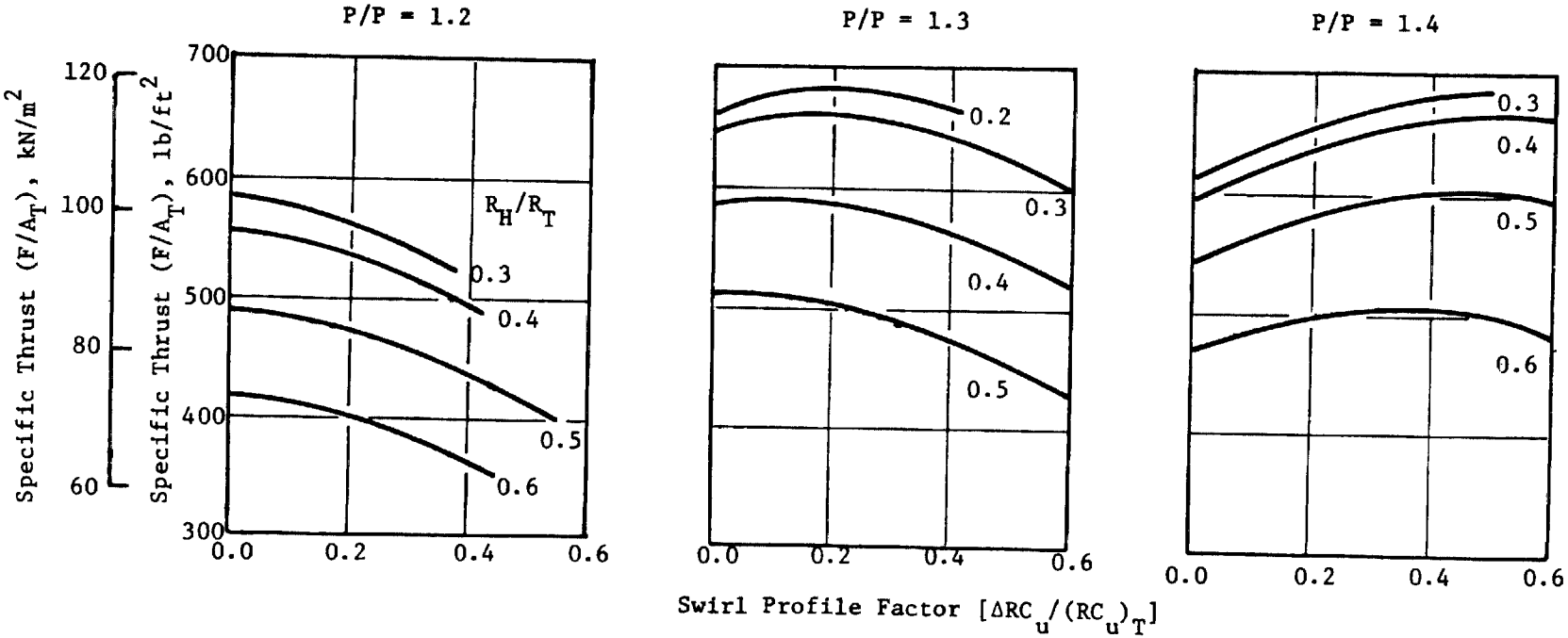

Figure III-15 Effects of Design Parameters on Specific Thrust

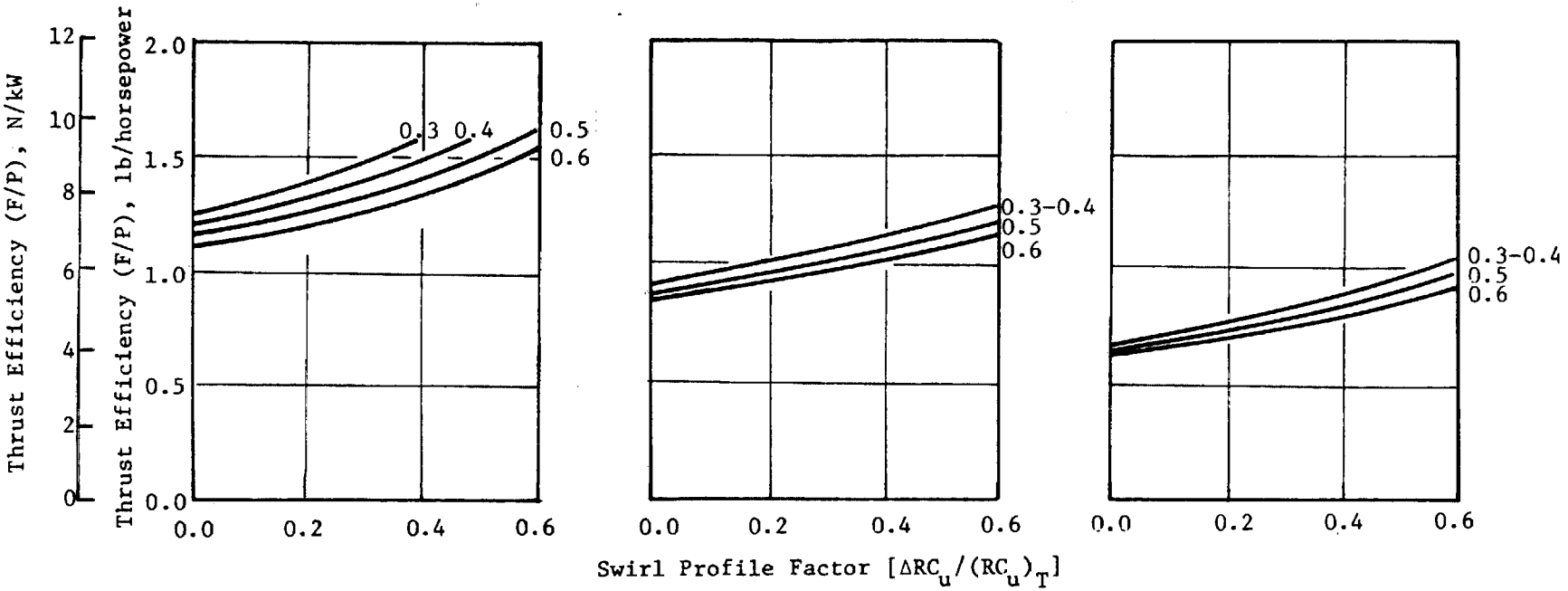

Figure III-16 Effects of Design Parameters on Thrust Efficiency

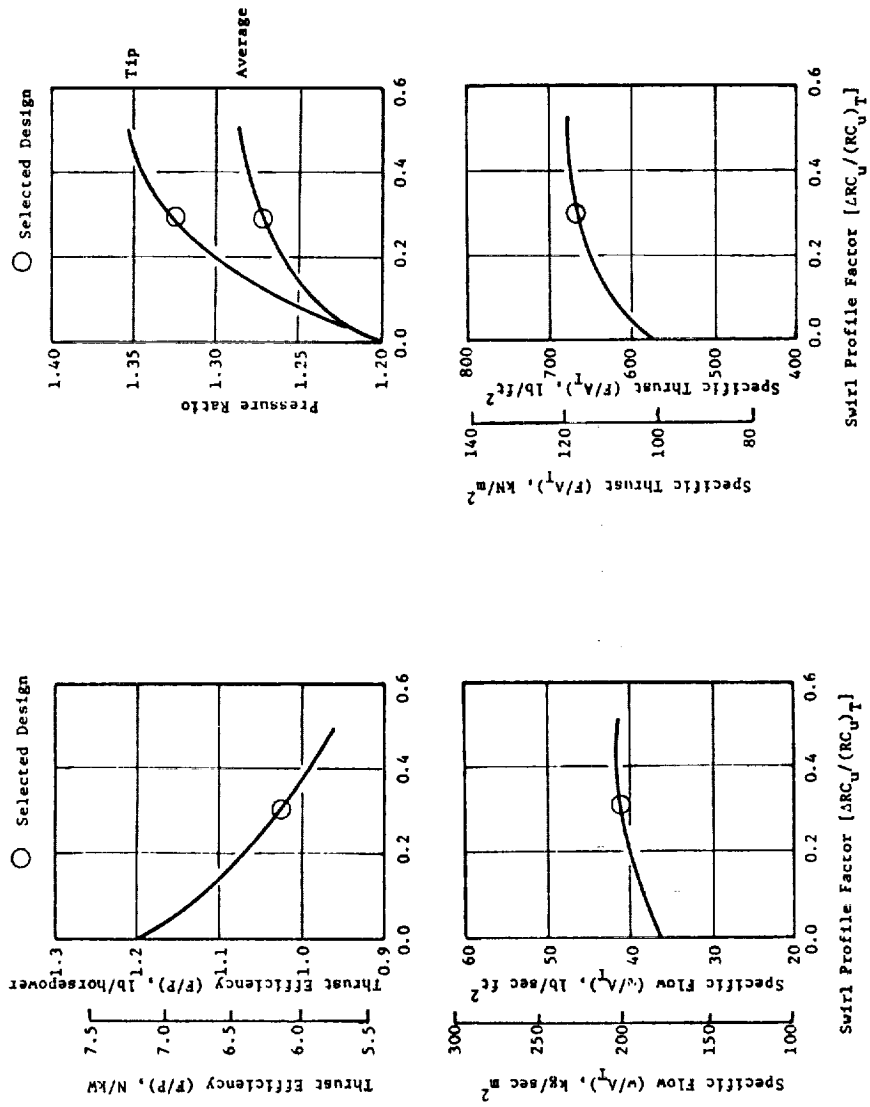

Figure III-17 Effects of Swirl Distribution on Fan Figures of Merit

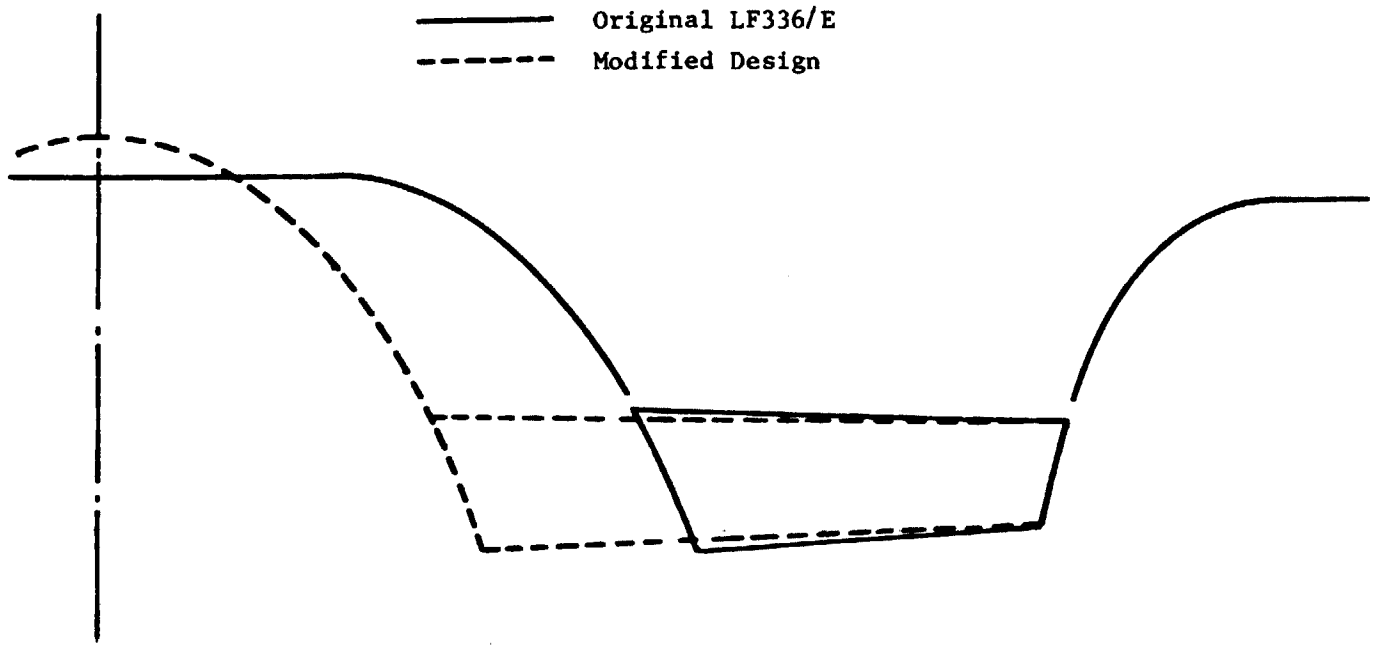

Figure III-18 Comparison of Statorless Fan Flowpaths

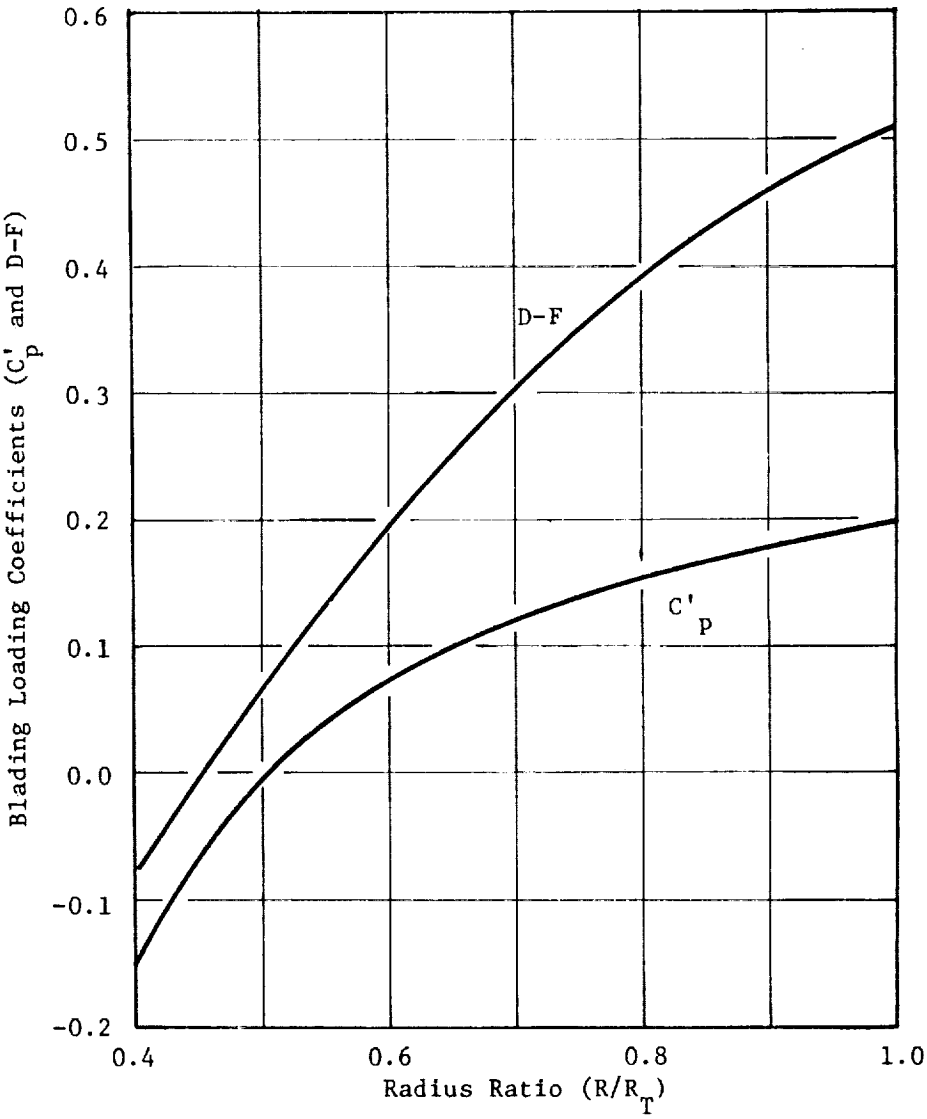

Figure III-19 Rotor Loading Parameters

*U.S. GOVERNMENT PRINTING OFFICE: 1975 - 635-275/25